Estimated Detection Limits of Carboxylates in Palagonite by X-ray Diffraction and Reflectance Spectroscopy

By

Daniel Applin

A Thesis submitted to the Faculty of Graduate Studies in partial fulfilment of the requirements for the Master of Science degree.

Department of Environmental Studies and Sciences and Department of Geography
Master of Science in Environmental and Social Change
The University of Winnipeg
Winnipeg, Manitoba, Canada
September, 2023

Copyright © 2023 Daniel Applin

ABSTRACT

Low molecular weight carboxylates (carbonates, oxalates, formates, and acetates) are either known or are expected to be present on the surface of Mars. Previous work has suggested these phases to be present in Gale Crater materials at nearly the expected detection limit (LOD) for crystalline materials with the Mars Science Laboratory (MSL)Curiosity rover CheMin X-ray diffraction (XRD) instrument. Detection limits of these materials by CheMin-like XRD and reflectance spectroscopy are poorly constrained, thus leading to uncertainties in detectability with these types of instruments. I have filled this knowledge gap by making intimate mixtures of a variety of carboxylates with the JSC Mars-1a regolith analogue material and measured their XRD patterns with a CheMin-like breadboard and reflectance spectra with instruments analogous to the SuperCam instrument on the Mars Perseverance rover. I used simple linear regression to create calibration curves to estimate LODs and compared and contrasted ten different LOD calculations previously used for XRD. I found that the carboxylates measured have LODs near 1.0 wt.% by XRD. Oxalate minerals are likely undetectable by reflectance spectroscopy in bulk materials at expected concentrations, while acetate and formate minerals have relatively low LODs at near-infrared wavelengths due to their sharp and strong absorption bands. Carbonate minerals may show decreasing LODs with increasing grain size in reflectance spectra and have relatively high LODs at near-infrared wavelengths for fine grained powders and relatively low LODs when using the 3950 nm absorption band at all grain sizes. Application of these data to CheMin observations show that my data could accurately detect low concentrations of siderite at nearly the same values determined from previous CheMin data processing within error and within an average of 0.5-1.0 wt.% where siderite was detected. After applying the calibration curves from the other carboxylates, I did not find strong evidence for their detection in any of the CheMin data. Some samples, primarily the Gale crater Rocknest aeolian material may contain some concentration of whewellite which may be consistent with the analysis of the Sample Analysis at Mars (SAM) data, but detection may be complicated by overlapping plagioclase Bragg peaks. I applied the measured reflectance spectra from 350 to 4000 nm to some data collected by the SuperCam instrument at Jezero crater that were implied to contain organic compounds through analysis of Perseverance Scanning Habitable Environments with Raman and Luminescence for Organics and Chemicals (SHERLOC) data. I did not find evidence for carboxylates in the reflectance spectra except for Mg-rich anhydrous carbonates, and I determined the concentration to be between roughly 5.0 and 20.0 wt.%, which is broadly consistent with the previous analyses of these samples by radiative transfer modelling.

ACKNOWLEDGEMENTS

A big thank you to the C-TAPE crew for accommodating me and to Ed for letting me be creative. Most importantly, thanks to Sarah for putting up with the evenings and weekends when I was working on this.

This project was undertaken with the financial support of Research Manitoba and the Canadian Space Agency (CSA: 22EXPCOI4). I wish to thank the National Research Council of Canada (NSERC: RGPIN-2015-04582; RGPIN-2021-02995; RTI-2020-00157), the Canada Foundation for Innovation, the Manitoba Research Innovation Fund (MRIF: CFI-1504, CFI-2450), and the University of Winnipeg for supporting this study.

TABLE OF CONTENTS

LIST OF TABLES

LIST OF FIGURES

Figure 13g. A comparison of several CheMin datasets analyzed here with the JSC Mars-1a analogue collected with the Terra instrument.

Figure 13h. A comparison of several CheMin datasets analyzed here with the JSC Mars-1a analogue collected with the Terra instrument.

Figure 13i. A comparison of several CheMin datasets analyzed here with the JSC Mars-1a analogue collected with the Terra instrument.

Figure 14a. The weak diffraction peak displayed in some CheMin data that could potentially have contribution from whewellite.

Figure 14b. The diffraction peak in some CheMin data that are likely due to a contribution from siderite.

Figure 14c. The weak diffraction peak displayed in some CheMin data that could potentially have contribution from calcium acetate.

Figure 14d. The weak diffraction peak displayed in the Bucksin Drill CheMin data that could potentially be due to magnesite.

Figure 15a. Average reflectance spectra for the targets analyzed here.

Figure 15b. Normalized reflectance for the targets analyzed here.

Figure 15c. Continuum-removed reflectance for the targets analyzed here.

Figure 15d. Comparison of the continuum-removed reflectance for the 2300 nm band between fine grained magnesite and the Penne target.

1.0 Introduction

1.1 Solid carbon-bearing materials on Mars

Both endogenous and exogenous inputs of solid abiotic carbon-bearing compounds to the surface of Mars are known to exist (**Flynn, 1996, Grady et al., 2004; Steele et al., 2016**). Martian meteorites contain endogenous abiotic organics and carbonates, where numerous plausible formation scenarios have been suggested, including but not limited to impact synthesis, primary igneous mechanisms, and secondary hydrothermal alteration (**Anders, 1996**; **Steele et al., 2016**).

The study of impact synthesis production of carbon-bearing compounds often acknowledges the high CO_2 partial pressure of the early martian atmosphere, which probably led to high concentrations of dissolved inorganic carbon such as HCO_3^- within fluids. As an example, Takeuchi et al. (**2020**) demonstrated the synthesis of amino acids by reproducing hypervelocity impacts on inorganic mixtures with dissolved HCO_3- and CO_2. Mukhin et al. (**1989**) showed that impact-induced gases enriched in CO and H_2 could results in the formation of polycyclic aromatic hydrocarbons (PAHs) and other hydrocarbons upon cooling. The distribution of PAHs in the martian meteorite ALH 84001 was shown to possibly have been caused by Fischer-Tropsch type synthesis of trapped carbon oxide (CO, CO_2) in impact-induced gases (**Zolotov and Shock, 1999; Zolotov and Shock, 2000**).

Similar to impact-generation scenarios, magmatic alteration of carbon-rich gases would provide the necessary temperatures for synthesis of reduced solid carbon-bearing compounds from oxidized precursor materials. The low oxygen fugacity of the martian mantle is expected to stabilize graphite at the expense of more oxidized carbon phases, which could reduce the ability for magmatic production of C-O-H phases (**McCubbin et al., 2013**). Steele et al. (**2012**) did find that that much of the PAHs found in martian meteorites are associated with magmatic minerals and thus could have formed during crystallization of the host magma. They suggested that if the martian mantle is graphite saturated, then partial melts could contain substantial C-O-H fluids that could have produced macromolecular carbon and PAHs at 1000 K.

Martian meteorites contain small but significant concentrations of carbonates (**Mittlefehldt, 1994; Bridges and Grady, 2000; Gooding et al., 1988; Wentworth and Good, 1994; Beck et al., 2006**), with which macromolecular carbon and PAHs are often found associated (e.g., **Becker et al., 1999**). In their detailed analyses of several abiotic organic carbon-bearing martian meteorites, Steele et al. (**2018**) found the carbon phases that are not linked to carbonates and are not of igneous origin were to likely have been produced by the interaction of a CO_2-bearing and Cl-rich brine with Fe-rich minerals (sulfides, spinels, titano-magnetite) via electrochemical reduction. This was noted to also be consistent with a number of analyses from the Sample Analysis at Mars (SAM) instrument on the Curiosity rover, in particular the Mojave drill sample.

Another source of solid carbon-bearing materials exists in that the martian latitudinal poles exhibit seasonal CO_2 ice caps (**Kaufmann and Hagermann, 2017**) and massive buried deposits of CO_2 ice (**Phillips et al., 2011**). As described by Applin et al. (**2016**), numerous carboxylate (carbonate, oxalate, acetate, formate; **Figure 1**) formation mechanisms exist that are associated with CO_2 ice, primarily various photochemical and radiochemical pathways (abiotic photosynthesis). Dust interactions with this ice could catalyze these formation scenarios and form salts from produced acids and photochemical products. Resulting seasonal sublimation, dust eruptions, and other geomorphic processes could provide a mechanism for the introduction of CO_2-ice derived carboxylates to become part of the global dust inventory.

Carbonate minerals have been detected at many locations at the surface of Mars, including by most rovers and landers. Data from the Viking lander was used to indirectly suggest carbonate concentrations of <0.5 to 9.0 wt.% in the soils analyzed (**Baird et al., 1976; Hubbard 1979, Banin and Rishpon, 1979**). Interpretations of data from the Thermal and Evolved Gas Analyzer (TEGA) and Wet Chemistry Laboratory (WCL) instruments carried on the Phoenix lander demonstrated calcium carbonate concentrations of 3-5 wt.% at the landing site (**Boynton et al., 2009**). Carbonate-rich outcrops were observed from the Mars Exploration Rover (MER), Spirit (**Morris et al., 2010**). The data showed high concentration (16-34 wt.%) of Mg-rich anhydrous carbonates that were associated with olivine. Further, infrared emittance spectra from the mini-TES instrument on board the MER rovers also supported a minor regolith component of Mg-rich carbonates (**Christensen et al., 2004**).

Data from the SAM instrument on board the Curiosity rover has shown evidence for carbonate minerals at low concentrations (<0.7 wt.%) in numerous samples. The anhydrous Fe^{2+} carbonate, siderite, has been detected by the CheMin X-ray diffraction (XRD) instrument near the typically suggested detection limit (LOD) of 1.0 wt. %. Thorpe et al. (**2022**) detected siderite with CheMin data at concentrations from <1.0 to 3.0 wt.% from the Kilmarie, Mary Anning, Mary Anning 3, and Groken samples, while ankerite was found to be present in the Mary Anning 3 and Groken samples. The SAM data for these samples further supported these measurements (**McAdam et al., 2022**). Schieber et al. (**2022**) indicated the possibility of trace amounts of the carbonates shortite and pirssonite with CheMin data in the Confidence Hills and Telegraph Peak samples, respectively.

Various instruments on board the Perseverance rover have detected significant concentrations of carbonates minerals. For example, interpretation of SuperCam data suggests widespread but low concentrations of carbonates in the magnesite-siderite solid solution series (**Clave et al., 2022**), and data from the Scanning Habitable Environments with Raman and Luminescence for Organics and Chemicals (SHERLOC) instrument have also indicated the presence of carbonates (**Hollis et al., 2022**).

Carbonate minerals have been detected by a number of terrestrial-based, airborne and Mars orbiting spectrometers (**Blaney and McCord, 1989, Pollack et al., 1990, Lellouch et al., 2000, Calvin et al., 1994, Bandfield et al., 2003; Ehlmann et al., 2008, Palomba et al., 2009, Brown et al., 2010; Bishop et al., 2013**). Wray et al., (**2016**) provided a synthesis of detections to that time, while numerous detections have occurred since (e.g, **Horgan et al., 2020**). Clave et al. (**2022**) provided a list of carbonate detections, compositions, and concentrations from both orbital and *in situ* datasets of Mars. The list of detections is relatively extensive and include, but are not limited to, Mg-rich carbonate detections in dust and rock units, Ca-Fe carbonate mixtures, and Mg-rich marginal carbonates found within Jezero crater.

1.2 Organic carbon on Mars

While carbonates have been widely detected by rovers/landers, remote reflectance spectra, and in martian meteorites, non-carbonate abiotic carbon is not observed by reflectance spectra collected from ground/air-based, orbiting, or rover spectrometers (**e.g., Singer et al., 1979**; **Campbell et al., 2016**). Due to interplanetary dust dynamics, the surface of Mars contains some meteoritic component, of which a significant fraction is solid non-carbonate carbon phases, most of which is initially macromolecular. Flynn (**1996**) estimated a rough influx of $12x10^6$ kg/year of interplanetary dust particles, which have a roughly estimated carbon content of 12 wt.% (**Thomas et al., 1993**). The accumulation of meteoritic mass to the martian regolith and soil has a wide range of estimates of between 1 and 20 wt. % (**Flynn and McKay 1990, Morris et al., 2000; Yen et al., 2006**). Accumulated meteoritic carbon therefore also has been estimated with a wide range of between 1 and 500 ppm (**Benner et al., 2000; Fries et al., 2017, Carillo-Sanchez et al., 2020, Fries et al., 2021a, Fries et al., 2021b**).

Ambiguous data from the instruments on the Viking and Phoenix landers led to uncertainties in the non-carbonate carbon concentration of the measured soils (**Biemann and Lavoie 1979, Biemann 2007; Boynton et al., 2009**). The lack of detection of organic carbon compounds had been ascribed to the generally harsh environment of the surface of Mars, where a number of mechanisms could result in complex chemistry of soil carbon, including photochemistry, radiation chemistry, and the resulting complex reduction/oxidation chemistry (**Biemann and Lavoie 1979, Chun et al., 1978, Oro and Holzer 1979, Pavlov et al., 2012, Ten Kate et al., 2010, Pavlov 2002; Poch et al., 2014, Applin et al., 2016; Steele et al., 2018**). Benner et al. (**2000**) suggested that the bulk remnants of the carbon delivered to surface materials would be bound in simple carboxylic acids such as benzenecarboxylic (mellitic), acetic, and oxalic acids, due to the typical oxidation reaction mechanisms that are expected to occur in the soils on Mars.

Subsequent data from MSL has indicated the presence of organic compounds and relatively high concentrations of carboxylates at many of the studied sites (**Friessenet et al., 2015, Eigenbrode et al., 2018, Sutter et al., 2017**), including a number detections of organic compounds that are variably associated with sulphur-bearing phases, which is similar to martian meteorites discussed by Steele et al. (**2020**). The bulk of the carbon detected by SAM has not been associated with these potentially electrochemically-reduced phases, but with the ambiguously identified oxidized-carbon phases that provide mid-temperature CO_2 released in the SAM data, which has been suggested to be possibly attributed to oxalates and acetates (**Sutter et al., 2017, Lewis et al., 2021**).

1.3 The search for non-carbonate carboxylates on Mars

Applin et al. (**2015**) indicated that the carboxylic acids suggested to have formed from meteoritic input by Benner et al. (**2000**) could be present as their Ca-Fe-Mg salts, and suggested that oxalates and carbonates would be the primary metastable and stable end products of the oxidation reaction mechanisms. They re-interpreted the pGCMS and calorimetry data from the Phoenix and Viking missions, and used early MSL SAM data to show that all were consistent with the concentration of roughly 0.1 to 1.0 wt.% oxalate minerals, which was qualitatively consistent with the expected accumulated carbon concentration in martian soils. Franz et al. (**2020**) showed that the evolved CO_2 in SAM measurements could be due to a mixture of exogenous input from meteorites and IDPs, with carbon formed from abiotic photosynthesis and electrochemical reduction. They also suggested the accumulation of oxalates and acetates in the surface materials at concentrations in excess of exogenous input, which implies endogenous formation mechanisms. They indicated the inferred carbonate concentrations could reflect a CO_2 sink of 425-640 millibar of atmospheric CO_2, while an additional 100-170 millibar could be stored in oxalates, formed primarily through abiotic photosynthesis.

Lewis et al. (**2021**) performed extensive experiments with a SAM breadboard instrument and carboxylate-perchlorate mixtures, with the aim of constraining these oxidized-carbon phases and determining concentrations of carboxylates in the materials measured by the SAM pGCMS. They synthesized their results with the SAM data collected by that time and found that martian aeolian materials could have an average concentration of 0.93 and 1.18 wt.% oxalates and acetates, respectively; while the materials drilled from the lithified sediments could have average concentrations of 0.50 and 0.68 wt. % oxalates and acetates, respectively. With this in context, they stated: "...if a crystalline oxalate or acetate was the dominant contributor to CO_2 [in the pGCMS], its abundances would be near or above the CheMin [XRD] detection limit". The LODs of carboxylates with CheMin XRD methods have not been readily established, and some level of empirical experimentation is needed in order to determine if the CheMin instrument could be used to support these ambiguous detections of carboxylate phases on Mars.

Using the data collected by the SHERLOC instrument on Perseverance, Scheller et al. (**2022**) showed that a 340 nm fluorescence feature spatially correlates with a carbonate-phosphate-amorphous silicate alteration zone in Garde, but found no association in Gullaumes and Bellegarde and tentatively assigned this feature to 2-ring aromatic compounds such as naphthalene, and/or potentially Ce-bearing phosphates. Applin et al. (**2016**) found that some carboxylates exhibit relatively strong fluorescence peaks centered near 340 nm, specifically whewellite and its acid. As indicated, these are compounds that are either predicted to be metastable end products of organics on the surface of Mars (**Benner et al., 2000; Applin et al., 2015**), or have been widely suggested to be present throughout Gale Crater based on SAM data interpretations (**Franz et al., 2020, Lewis et al., 2021**). Like naphthalene, broad fluorescence features in oxalates are likely much stronger than Raman scattering, which would explain a non-detection from the Raman data if they were to be the carrier of the 340 nm fluorescence feature.

Aaron et al. (**2019**) looked at Compact Reconnaissance Imaging Spectrometer for Mars (CRISM) regions of interest for possible spectral signatures of magnesium oxalates and found a ~61 km crater located at 37.07°S, 178.23°W that could potentially exhibit oxalate spectral signatures, but the data were ambiguous. As with the CheMin XRD, LODs of carboxylates with reflectance spectroscopy have not been determined experimentally; this is required to constrain the capability of detecting and characterizing these materials with orbiting spectrometers.

Here, I fill this knowledge gap of unknown detectability by making intimate mixtures of carbonates, oxalates, acetates, and formates with a Mars regolith analogue material, and measure XRD patterns and reflectance spectra on these samples. I calculate LODs and use this data to look for these carboxylates in CheMin and SuperCam data, as well as provide a synopsis of their detectability with similar rover and orbital instruments.

2.0 Materials, methods, and methodologies

2.1 Materials and mixtures

An aliquot of JSC Mars-1a palagonitic soil (**Allen et al., 1999**) was dry-sieved to achieve a <45 µm fraction powder. This powder was heated to 130°C for 24 hours, twice, which resulted in mass loss of 11.04 wt.%. This step was performed to remove some adsorbed water, which can complicate LOD studies at wavelengths near 2000 and 3000 nm, where water strongly absorbs (e.g., **Hale and Querry, 1973**). Allen et al. (**1999**) showed the JSC Mars-1 material to be highly hygroscopic, containing up to 20 wt.% H_2O at ambient conditions. Although much wetter, JSC Mars-1a closely resembles the reflectance spectra from the bright surfaces of Mars and, in general, represents a reasonable analogue for the physical and chemical properties of the martian dust (**Evans and Adams, 1979, Bell et al., 1993; Morris et al., 1993, Morris et al., 2001, Allen et al., 1999**). The soil is harvested from a tephra at the Pu'u Nene cinder cone near Mauna Kea, Hawaii, and is dominated by meteorically-altered hydrated and amorphous volcanic ash, and is termed palagonite or palaogonitic soil. Within the palagonitic matrix are crystallites of plagioclase and magnetite (**Stroncik and Schmincke, 2002**). Quantitative XRD analyses of JSC Mars-1a have shown it to be comprised of 82.4 wt.% X-ray amorphous phases, 11.7 wt. % andesine, 3.1 wt.% augite, and 2.8 wt. % olivine (**Moroz et al., 2009**), whereas CheMin results at Gale Crater have repeatedly suggested many of the martian samples are composed of ~40 wt.% amorphous volcanic and phyllosilicate material (**e.g., Bish et al., 2013; Rampe et al., 2020**), the bulk chemistry of JSC Mars-1a is generally similar to other analogue materials and soils of Mars, but is relatively enriched in Al_2O_3 and depleted in MgO (**Carpenter et al., 2003**).

The carboxylates I have focused on for this study have the shortest carbon chains and lowest molecular weights and are most likely to form through various processes on the surface of Mars, as discussed by Applin et al. (**2015**), Sutter et al. (**2017**), and Lewis et al. (**2021**). **Figure 1** demonstrates the similarities and differences between the carboxylate conjugate bases; the two simplest (lowest molecular weight) monocarboxylic acids are formic and acetic, where acetic contains one carbon-carbon bond, whereas formic does not contain carbon bonding. Similarly, the simplest dicarboxylic acids are carbonic and oxalic, where oxalic contains the carbon-carbon bond and carbonate does not. The dicarboxylates contain two carboxyl groups and no hydrogen bonding to their carbons. Geochemically, this is the reason for the argued metastability and stability of carbonates and oxalates compared to acetates and formates on the surface of Mars.

Synthetic formates, acetates, oxalates, and natural carbonates were ground with an alumina mortar and pestle and passed through a <45 µm stainless steel mesh sieve. These carboxylates were weighed, along with sub-aliquots of the dehydrated JSC Mars-1a palagonite and mixed together to produce the mixtures shown in **Table 1**. The acetates, formates, and oxalates were purchased from Alfa Aesar, Amresco, and Sigma Aldrich, and were all described to be at least 98.5% pure on a chemical basis. The natural siderite powder used here (CRB145) was a single crystal sourced from Governador Valadares, Minas Gerais, Brazil. The natural magnesite powder (CRB106) was a granular chunk from Snarum, Norway. The natural calcite powder (CRB131) was precipitated from a spring on Axel Heiberg Island, Nunavut, Canada. The focus was on Ca-, Mg-, and Fe-bearing salts, since these are probably the most geochemically plausible carboxylate salts for martian surface materials, given the elemental composition of basalt (**e.g, Eggleton et**

al., 1987), and that these are the closest matching salts interpreted by Lewis et al. (**2021**). Further, all of the acetates used for this study appear to be quite volatile, as they smell of vinegar at room temperature. Natural acetate and formate minerals do exist, e.g., hoganite and paceite (**Hibbs et al., 2002**), calclacite (**Van Tassel 1958**), formicaite (**Chukanov et al., 1999**), and dashkovaite (**Chukanov et al., 2000**), which should be studied with follow-on work. Each mixture was thoroughly mixed in a borosilicate vial with a glass stir rod for one minute, then ground with an alumina mortar and pestle for 5 minutes to ensure homogenization. Homogenization of the powders can be important for studying LODs, as different mixing scenarios can produce strongly different values of reflectance spectra in mixtures, particularly when there is a significant difference in grain size and refractive indices. **Figure 2a** demonstrates this large contrast in reflectance spectra between mixing methods on the same sample. Aggregates of heterogeneous grains may also result in preferred orientation and/or Laue spotting despite the piezo vibration performed with the transmission XRD described below. Although solvents are sometimes used for sample homogenization, they were not used for the homogenization, as they can contribute to the spectral properties of the materials even after evaporating.

Data from Tarnas et al. (**2021**) were used to further investigate LODs of calcite, in order to supplement the data collected here. In those experiments, the host material was a different analogue powder, with complementary spectral properties; MGS-1, shown in **Figure 2b** (**Cannon et al., 2019**). These mixtures had calcite concentrations of 0, 1, 2.5, 5, 10, 20, 50, and 100 wt.% with grain sizes of 45-75 and 125-250 µm, for the respective two mixture sets. The specific mixings methods for these samples is unknown.

2.2 Data collection methods

2.2.1 X-ray diffraction

X-ray diffraction patterns were acquired using a Terra portable instrument that collects XRD data from 5 to 55° 2θ with a 0.25° FWHM angular resolution and 0.05° angular sampling interval. The instrument also simultaneously collects X-ray fluorescence (XRF) spectra covering 2.5 to 25 keV, which are not used in this study. X-rays are produced with a sealed Co micro-focus tube (Co $K\alpha_{1,2}$ radiation, λ=1.79026 Å) operating at 30 kV and 350 uA. I used a cobalt anode due to the strong interference of Fe fluorescence caused by the more commonly used Cu anode; the same reason CheMin on Mars also uses Co. The produced X-ray beam is passed through a collimating pinhole (~70 μm diameter) before interacting with the sample. About 10 mg of sample is used for the measurements, which is sandwiched between two thin kapton windows that are separated with a ~175 μm spacer. During analysis, the powder is constantly moving like a fluid due to vibration from a piezoelectric actuator attached to a tuning fork that holds the sample, which reduces or eliminates preferred orientation and Laue spotting of the grains as the X-rays transmit through the sample. This also decreases the need for very fine powders (e.g, <20 μm), and is why CheMin can analyze powders passed through a 150 μm sieve. A fraction of a two-dimensional Debye ring is imaged by a 1024×256 pixel (26 μm pitch) Peltier-cooled (-45°C) X-ray sensitive CCD detector placed at a ~30° tilt from the X-ray beam. This angle allows the sensor to be placed at a distance of ~31 mm from the sample. Because the read-out from the CCD is rapid, the pixel charge can be considered to be induced from single photon detection; therefore, photon energy can be measured at a resolution of roughly 230 eV and sampled at 130 eV. For this reason, Co-

Kβ signal can be electronically filtered and removed from the Kα diffraction data. The CCD pixel counts on the two-dimensional image are summed circumferentially at the 0.05º two-theta sampling interval to produce the diffraction pattern of Kα radiation. In my experiments, each exposure consisted of a 10 second integration time, and a total of 500 exposures were collected and averaged to increase signal-to-noise ratio (S/N). Manual inspection of the Debye ring images indicated no significant Laue spots in any of the datasets produced by the samples, an example of which is shown in **Figure 2c**. In most instances, the XRD data were normalized by total Kα counts to better account for X-ray transmittance variability, integration time differences, and other instrument effects such as the difference in source flux, which allows for more accurate comparisons with CheMin data, which are collected with different operational parameters, primarily differences in flux and integration time

The Terra XRD used in this study is a commercial spin-off of the CheMin instrument on the MSL Curiosity rover, which collects diffraction patterns of similar range, resolution, and sampling interval, with similar sensitivity. The powders are moved with the same mechanical method, while the sample holders are similar in configuration. The two instruments are fundamentally similar in design and operation, whereas CheMin patterns are collected at a slightly lower angular resolution (0.35 vs. 0.25 °2-theta Co-Kα) but are sampled with the same interval (0.05 °2-theta Co-Kα). Blake et al. (**2009**) stated: “During its refinement prior to flight, a prototype portable CheMin instrument called “Terra” was developed. Terra shares its diffraction geometry with CheMin, but in many ways exceeds CheMin’s performance. Terra delivers more X-ray flux to the sample, yielding much improved diffraction intensity as well as slightly improved 2θ resolution”.

I did not strip the Co-Kα_2 contribution prior to analyses for either the laboratory patterns nor the CheMin patterns; therefore, each pattern is presented as °2-theta Co-Kα. Ten measurements of the JSC Mars-1a material were collected as a blank, and each mixture and endmember sample was measured one time, with the exception of the 2.53% siderite mixture, which was measured eight times to evaluate LOD statistics.

2.2.2 Visible and Near Infrared Reflectance Spectroscopy

A Malvern-Panalytical Analytical Spectral Devices (ASD) LabSpec 4 Hi-Res reflectance spectrometer was used to collect the reflectance spectra. This ASD spectrometer consists of three separate detectors that cover the 350–1000 nm (Si photodiode array), 1000–1830 nm, and 1830–2500 nm (InGaAs detectors with moving gratings) intervals. A single 2 m long fiber optic cable was used to collect the reflected light from samples. This cable consists of 44 separate silica fibers with internal diameters of 200 μm each. The full diameter of the bundle was 1.85 mm. This fiber optic cable is fed to an optical scrambler that ensured light from each fiber was combined and equally fed to all three optical paths to the detectors. The Si photodiode array was then fed by a fiber optic bundle consisting of 19 separate 100-μm diameter silica fibers. The two InGaAs detectors were fed by separate fiber bundles consisting of 9 separate 200-μm diameter silica fibers. Reflectance offsets at the wavelength boundaries of the three detectors, if existing, were removed by multiplicatively scaling the low (350–1000 nm) and high (1830–2500 nm) wavelength portions of the spectrum to the middle portion. The instrument has a spectral resolution that ranges between 3 nm for the photodiode array and 6 nm for the InGaAs detectors. Dark current signals were subtracted from all spectra during correction to reflectance. These spectra were corrected for the absorption properties of the Fluorilon reflectance standard but were not corrected for the non-Lambertian behavior of Fluorilon. An in-house light source was used for illumination that consists of a quartz-tungsten-halogen (QTH) bulb illuminating a set of reflectors that feed the light through a pipe at a divergence of <1.5 degrees. The filament was operated at a temperature that provided sufficient output over the 350-2500 nm range.

These measurements are highly applicable to interpreting SuperCam data, which carries a NIR reflectance spectrometer (**Fouchet et al., 2022**). The infrared spectrometer measures over a range of 1300-2600 nm at a spectral resolution increasing from 5 to 20 nm (32 cm^{-1} resolution). Between 2000 and 2500 nm, the resolution decreases from ~12 to 20 nm, whereas the spectrometer used in this work has a spectral resolution of ~6 nm at these wavelengths.

Ten measurements of the JSC Mars-1a material were collected as a blank, and each mixture and endmember sample was measured one time. In contrast, I used three measurements from RELAB of the MGS-1 material from Tarnas et al. (**2021**) for the same LOD computations.

2.2.3 Mid-infrared Reflectance Spectroscopy

Mid-infrared (MIR) reflectance spectra were collected with a Bruker (Billerica, MA) Vertex 70 Fourier Transform Infrared (FTIR) spectrometer equipped with an infrared Globar light source, a liquid nitrogen-cooled InSb detector and KBr broadband beamsplitter over the wavelength range of 1.0–5.0 µm, which I define here as MIR. Reflectance spectra were acquired relative to a Labsphere Infragold® 100% reflectance standard measured at *i*=30° and *e*=0° using a SpecAc Monolayer grazing angle specular reflectance accessory. A total of 1500 spectra, collected at a scanner velocity of 40 kHz, were averaged to improve SNR. All measurements were made using an identical viewing geometry, integration time, and number of averaged spectra. For both NIR and MIR reflectance experiments, the samples were packed using the method described by Mustard and Hays (**1997**), which is to gently pour the powder into sample cup and tap it ~5 times. The sample cup was scraped across with a glass slide held at 45° away from the sample to minimize pressing/packing of the powder and to produce a flat matte surface. The samples cups used here were made of 6061 aluminum alloy, with a 13 mm diameter beveled hole, 5 mm deep, and painted black. These methods ensure high quality data by remove ambiguities associated with porosity variation and sample depth from preparation. All MIR data were scaled multiplicatively to the VNIR data at 2000 nm due to the spectral differences between Fluorilon and Infragold.

2.3 Data processing methodologies

2.3.1 Quantitative X-ray diffraction and detection limit calculations

Several methods exist for quantifying mineral concentrations in mixed materials by XRD (**Cullity 1956**; **Pecharskey and Zavalij, 2003**). The most labour-intensive require pure standards and/or doping of samples, such as the internal (**Popovich et al., 1983**) and external (**Leroux et al., 1953**), and reference intensity ratioing (RIR) (**Chung et al., 1975**) standard methods. A number of other methods have been increasingly developed and adopted, such as full pattern summation (**Chipera and Bish, 2002**) and Rietveld refinement (**Rietveld 1967**).

The internal standard method involves the construction of a calibration curve after making several mixtures and measurements. It follows **Equation 1:**

$$\frac{I_a}{I_b} = k\frac{X_a}{Y_b}, \qquad (1),$$

where (***Ia)*** and (***Ib)*** are the intensities of the (usually) strongest Bragg peaks for phase ***a*** (unknown amount) and phase ***b*** (known amount/standard), (***Xa***) is the unknown amount of phase a, (***Yb***) is the amount of the standard, and ***K*** is the slope of the plot. The unknown concentration of phase a can be found by using the constructed calibration curve when applied to successive measurements doped with the standard.

The RIR method is an instrument-dependent analysis derived from the internal standard method where a known weight of a standard material is homogenously mixed with a sample of unknown composition, typically of equal proportions, and typically using corundum. The intensity of the major diffraction line component under study is divided by that for the standard material, which results in an equation that is linear in weight with the phase under study and can be used to create a calibration curve and determine mineral concentrations. For quantification of amorphous component, this method will derive the concentration of the crystalline component relative to the bulk weight of the sample, and the amorphous component can be found by the difference.

Rietveld refinement employs a nonlinear least squares optimization routine to fit a modelled diffraction pattern to that of the sample under investigation. The model includes inputs from theoretical diffraction patterns calculated from the indexed crystal structures of the minerals, and the physical experimental parameters to deal with instrument effects.

Full pattern fitting (FULLPAT) is a method that uses the summation of the mixture component diffraction values in a model to reproduce the observed pattern. The analysis varies the proportion of the components using least-squares minimization, producing a best fit to the observations. An internal standard, typically corundum, is added to reference materials in a library and to the samples under investigation. This allows normalization of the patterns relative to corundum concentration, which removes instrument, absorption, and matrix effects. The quantitative determination of the minerals in the mixtures can be found by calculating the amount that the library standards need to be scaled to match the corundum diffraction intensity in the samples under investigation. One benefit of full pattern fitting is the use of multiple Bragg peaks instead of a single reflection, thus increasing the accuracy. For example, Xiao et al. (**2023**) found full pattern fitting Rietveld refinement to be more accurate than the RIR method; however, Hillier et al. (**2000**) did find Rietveld and RIR methods to be equivalent.

For interpreting my data, I chose not to perform full pattern fitting, as I do not currently have a mineral library constructed of relevant minerals with internal standards and collected with the Terra instrument. Similarly, I chose not to perform Rietveld refinement on CheMin data, as the prime objective of my study is to estimate the LODs of carboxylates by a method that I can quickly use to qualitatively look for carboxylates in CheMin data and determine their detectability. I used a method that involves doping an analogue material (JSC Mars-1a) with known weights of a carboxylate as a doping agent. I am not concerned with determining the concentration of the crystalline components in the JSC Mars-1a analogue or using a peak other than those from the doping agent. Thus, due to the high similarity between the Terra instrument and CheMin, and similar chemical composition of JSC Mars-1a to many martian materials, I created calibration by removing the unknown fraction of *Xa* from **Equation 1,** assuming it is absent, while minimizing but not eliminating instrument and matrix effects. Because my samples are doped with known concentrations of crystalline materials, future processing by other methods can be facilitated.

The laboratory diffraction patterns were first processed by dividing the patterns by the total counts, which minimizes some instrument effects (such as flux difference and CCD efficiency) and facilities comparison between samples and with CheMin data. Peak amplitudes were then calculated by removing a straight-line continuum across the diffraction peak, then isolating that peak by dividing the pattern by the continuum (**Figure 3a, Equation 2**):

$$\boldsymbol{Pa} = \left(\frac{\boldsymbol{Db}}{\boldsymbol{Dc}}\right) \qquad (\mathbf{2}),$$

where (***Pa***) is the peak amplitude, (***Db***) is the maximum normalized count value of the diffraction peak, and (***Dc***) is the normalized count value of the continuum at the same °2-theta Co-Kα as the (***Db***).

The International Union of Pure and Applied Chemistry (IUPAC) defines the LOD to be expressed as a concentration or amount derived from the smallest measure that can be detected with reasonable certainty for a given analytical procedure (**IUPAC 1978; Long and Winedorfer, 1983**). The definition of reasonable certainty is highly variable, and there have been a number of methods used to determine that in XRD measurements, which is often dependent on the data processing methods and number of measurements available for both the sample and background. Long and Winedorfer

(**1983**) demonstrated that a signal value of three times the measured uncertainty, typically the standard deviation of a finite number of blank measurements with normally distributed values, would satisfy the requirement of a reasonably certain signal in the IUPAC model at a confidence of 99.86%. They showed that more accurate determinations of the uncertainty involve the propagation of errors in the slope and intercept, and result in a more liberal determination of the LOD – an order of magnitude lower in their test case. However, the majority of work determining LODs by XRD (and other analytical methods) employ some method of determining the standard deviation of background measurements without propagation of errors in the slope and intercept when constructing calibration curves and commonly adopt a LOD defined as around three times that signal.

The LOD by XRD defined by Davis (**1987**) is the concentration that will produce a signal equivalent to some defined number of standard deviations of the background. The work by Hillier et al. (**1999**), at two standard deviations of the background signal (95% probability of detection) gave:

$$\frac{2\,\sigma_b}{I_j/W_j} \qquad \textbf{(3),}$$

where (σ_b) is the standard deviation of background signal (N) where there is one measurement, and is given as the ($\sqrt{N}$), (I_j) is the measured analyte j signal, and (W_j) is the mass fraction of the analyte j. They further indicated that analyte signal and background signal are required to evaluate ($\boldsymbol{I_p}$), thus further defined a LOD that retains a 95% probability of detection to approximate six standard deviations above background:

$$\frac{4\sqrt{2}\sigma_b}{I_j/W_j} \qquad \textbf{(4).}$$

Ali et al., (**2022**) defined the LOD by XRD to be a concentration of analyte that produces a measurable signal from the analyte ($\boldsymbol{I_j}$) larger than 3 standard deviations ($\boldsymbol{\sigma_b}$) above background signal (N), where ($\boldsymbol{\sigma_b}$) is defined as ($\sqrt{N}$), and $\boldsymbol{W_j}$ is the mass fraction of the analyte $\boldsymbol{j}$. Following **Equation 3**, this can be expressed as:

$$I_j/W_j > 3\sigma_b \qquad \textbf{(5).}$$

Hanchar et al. (**2000**) followed the relation outlined by Lyman et al. (**1990**) for LODs from Electron Dispersive Spectroscopy experiments and defined the XRD LOD as a measured signal equivalent to:

$$\frac{3\sigma_b}{(I_j - I_b)/W_j} \qquad \textbf{(6),}$$

where ($\boldsymbol{\sigma_b}$) is the standard deviation of background signal (N) where there is one measurement, and is given as the ($\sqrt{N}$), $\boldsymbol{I_j}$ is the measured signal of the analyte, $\boldsymbol{I_b}$ is the measured background signal, and $\boldsymbol{W_j}$ is the mass fraction of the analyte $\boldsymbol{j}$.

Vyverberg et al. (**2018**) defined the LOD as the smallest analyte concentration in an unknown sample that can be reliably distinguished from zero with chosen significance (false negative). They outlined several methods for determining LODs with XRD measurements, including using prediction bands from linear regression and as the abscissa of the intersection of the parallel line to the x-axis of a calibration curve passing through the decision limit with the lower one-sided band of the prediction function. They also showed that it can be determined by:

$$\frac{3S_{yx}}{m} \qquad \textbf{(7),}$$

where S_{yx} is the sum of the variance of the samples around the calibration curve, and m is the slope of the regression.

Döbelin (**2020**) defined the LOD by XRD as:

$$I_b + 3\sigma_r \qquad \textbf{(8),}$$

where I_b is the signal of the blank measurement and σ_r is the standard deviation of the determined concentration on 10 analyses of the sample.

Kim et al. (**2012**), following Corley (**2003**), used the root mean square error method to determine LODs by XRD:

$$3\,\frac{R_{mse}}{m} \qquad \textbf{(10),}$$

where $\boldsymbol{R_{mse}}$ is the root mean square error which describes the difference between predicted values and measured ones based on the linear calibration curve, and $\boldsymbol{m}$ is the slope of the regression.

Kontoyannis and Vagenas (**2000**) used a version of the Student's t-test method to determined LODs by XRD:

$$\boldsymbol{t\sigma_b \sqrt{\frac{N+1}{N}}} \qquad \textbf{(11),}$$

where $\boldsymbol{t}$ is the Student's $\boldsymbol{t}$-value they defined as:

$$\frac{(\boldsymbol{x}-\mu)}{\boldsymbol{\sigma_s}} \qquad \textbf{(12),}$$

where $\boldsymbol{\sigma_s}$ is the standard deviation of the measurements and $(\boldsymbol{x}-\mu)$ represents the absolute deviation from the mean value; $\boldsymbol{\sigma_b}$ is the standard deviation of the blank measurements, and $\boldsymbol{N}$ is the number of blank measurements.

The U.S. EPA defined a *method* LOD (MDL) as "the minimum concentration that can be measured and reported with 99% confidence that the analyte concentration is greater than zero" (**EPA, 1984**). Su (**1998**) iterated that this is not the quantitative limit, which can be found by multiplying the $\boldsymbol{\sigma_s}$ of seven replicated measurements of a concentration at or within a factor of 5 of the MDL by ten, or by multiplying the MDL of 7 replicates by 3.18. Zhang (**2007**) indicated that the MDL can be determined by using the Student's t-distribution value ($\mathbf{t_t}$) corresponding to a 99% confidence by:

$$\boldsymbol{\sigma_s\ t_t} \qquad \textbf{(13),}$$

which, in contrast to **Equation 11** does not take into account the blank signal, and the chosen confidence to determine $(\mathbf{t_t})$ can be found with:

$$\boldsymbol{(1-\alpha)100} \qquad \textbf{(14),}$$

for a two-tailed test where is $(\boldsymbol{\alpha})$ the chosen significance level and:

$$\boldsymbol{(1-\alpha/2)100} \qquad \textbf{(15).,}$$

for a one-tailed test.

For this study, I have multiple measurements of my background sample and single measurements of my mixtures; thus, I use:

$$\boldsymbol{\frac{3\sigma_b}{m}} \qquad \textbf{(16).}$$

where $(\boldsymbol{\sigma_b})$ is the standard deviation of the background signal, and $(\boldsymbol{m})$ is the slope derived from constructed calibration curves. Because I constructed calibration curves, $(\boldsymbol{m})$ replaces $(\boldsymbol{I_j/W_j})$ from **Equations 3-6**, and I have chosen to use three standard deviations of the background as a liberal estimation of the LOD, which is evaluated in **section 3.5**.

Derived peak amplitude values (**Equation 2**) were compared to the known concentrations of the analytes in the mixtures in order to perform regression analyses. Simple linear regression was used for each series of mixtures, in order to determine the Y-intercept and the regression slopes, to be used to estimate the LODs with **Equation 16**.

2.3.2 Quantitative reflectance spectroscopy and detection limit calculations

Reflectance spectroscopy is arguably the most widely used analytical technique for studying the composition of planetary surfaces (e.g., **Pieters and Englert, 1993; Bishop et al., 2019**). Methods exist for extracting qualitative to quantitative compositional information from reflectance spectra of some mineral mixtures where they are generally transparent to semi-transparent (e.g., **Clark and Roush 1984, Cloutis et al., 1986; Gaffey et al., 1993**), such as comparisons with empirically calibrated band-area-ratios, band depth analysis, and radiative transfer modelling. In general, materials that have a high imaginary component of the refractive index (*k*) will spectrally mix with abundance near-linearly; an observation that has been demonstrated with some mixtures at ultraviolet and infrared wavelengths where strong light absorbing mechanisms are active (**Lyon 1964; Ramsey and Christensen, 1998; Applin et al., 2018**). In this scenario, reflectance spectra can often be modelled simply by the areal abundance of minerals because the interacting light is absorbed and exhibits limited scattering within the medium. In contrast, materials that exhibit widely different optical properties and/or are relatively transparent will not spectrally mix linearly with abundance due to high multiple scattering within an intimately mixed medium (**Hapke 2012**). This can be observed at VNIR wavelengths where many remote observations are made. Here, it is also often the case that physically impossible work effort is required to produce adequately calibrated parameters for extracting mixture compositions. It is in this scenario where the use of radiative transfer equations have been advocated and can be most useful for extracting quantitative information about planetary surface compositions (**Clark and Roush 1984; Mustard and Pieters 1987; Lucey 2004; Poulet and Erard 2004; Wilcox et al., 2006; Cahill and Lucey 2007; Lawrence and Lucey 2007; Denevi et al., 2007; Denevi et al., 2008, Cahill et al., 2009, Poulet et al., 2009, Yang et al., 2019**).

Chandrasekhar (**1960**) first described computational methods for calculating the interaction of light with particulate media: radiative transfer theory. Early formulations were used for transmittance measurements of planetary and stellar atmospheres (**Goody 1964; Sobolev 1975**). Hapke (**1981; 1986; 1993; 2012**) and Shkuratov et al., (**1999**) described treatments of radiative transfer for the reflectance and emittance of particulate media, which have since been extensively used and revised for the extraction of quantitative parameters from remotely collected spectra. For the Hapke treatment of bidirectional reflectance observations, formulations typically require the conversion of the spectra to single scattering albedo, knowledge of the illumination and emergence angles and the scattering phase functions.

While variations in the equations exist, those below assume the laboratory measurements use a Lambertian scatterer as a reflectance standard. The reflectance factor or radiance coefficient is then defined as:

$$\boldsymbol{REFF(i,e,g) = \frac{w}{4}\frac{1}{\mu_0+\mu}\{[1+B(g)]P(g)+H(\mu_0)H(\mu)-1\}} \qquad \textbf{(17)},$$

where $u_0 = \cos(i)$ *and* $u = \cos(e)$; ***i*** and ***e*** are the incidence and emergence angles, and *g* is the phase angle. Following the results by Mustard and Pieters (**1989**), many researchers set the backscattering function ***B(g)*** to zero if the laboratory measurements are done at phase angles greater than 15°. A two-term Legendre polynomial (below) can be used to approximate the single scattering phase function ***P(g)***:

$$\boldsymbol{P(g) = 1 + b * \cos(g) + c * [1.5cos^2(g) - 0.5]} \qquad \textbf{(18)},$$

where the degree of forward/backward scattering is the phase function coefficient ***b***, and the degree of side scattering is the phase function coefficient ***c***.

For closely-packed particles, the extinction efficiency of a particle (Q_e) can be assumed to be 1, so the single scattering albedo (w) can be defined in this case specifically as:

$$w \cong \boldsymbol{Q_s = S_e + (1 - S_e)\frac{1-S_i}{1-S_i\Theta}\Theta} \qquad \textbf{(19)},$$

where Q_s is the scattering efficiency of a particle, and S_e is the Fresnel reflectance of externally incident light, and S_i is the Fresnel reflectance of internally scattered light. For the purposes of the radiative transfer equations, these variables can be approximated as:

$$\boldsymbol{S_e = \frac{(n-1)^2+k^2}{(n+1)^2+k^2} + 0.05} \qquad \textbf{(20)},$$

and

$$\boldsymbol{S_i = 1.014 - \frac{4}{n(n+1)^2}} \qquad \textbf{(21)}.$$

The internal transmission factor of a grain (Θ) can be expressed as:

$$\boldsymbol{\Theta} = \frac{r_i + exp\left(-\sqrt{a(a+s)\langle D\rangle}\right)}{1 + r_i \exp\left(-\sqrt{a(a+s)\langle D\rangle}\right)} \quad \textbf{(22)},$$

where $\boldsymbol{s}$ is the sum of $\boldsymbol{S_e}$ and $\boldsymbol{S_i}$, and the bihemispherical reflectance of a semi-infinite medium (***r**i*) is:

$$\boldsymbol{r_i} = \frac{1 - \left[\frac{a}{(a+s)}\right]^{1/2}}{1 + \left[\frac{a}{(a+s)}\right]^{1/2}} \quad \textbf{(23)},$$

and where the absorption coefficient ($\boldsymbol{a}$) is defined as:

$$\boldsymbol{a} = \frac{4\pi k}{\lambda}. \quad \textbf{(24)}.$$

The ***H-function***, described by Chandrasekhar (**1960**), can be found in his lookup tables of ***u***, ***w***, and ***H(x)***, or approximated with **Equations 25 and 26** here, which are from Hapke (**2012**):

$$\boldsymbol{H(x) = \left\{1 - wx\left[r_0 + \frac{1-2r_0x}{2}\ln\left(\frac{1+x}{x}\right)\right]\right\}^{-1}} \quad (25),$$

where

$$\boldsymbol{r_0} = \frac{(1-\sqrt{1-w})}{(1+\sqrt{1-w})} \quad \textbf{(26)}.$$

Using one or the other depends on the single scattering albedo of the material; when the value is close to 1 (very bright), the approximation is found to be inadequate, and the exact numbers are required.

The reflectance of materials mix linearly in single scattering albedo and are not grain size dependent, but knowledge of the optical constants *n* (real component) and *k* (imaginary component) are required to accurately perform this. Herein lies a major problem in using radiative transfer modelling for extracting quantitative mineral abundances from planetary surfaces: too few studies have determined the optical constants of rock-forming minerals with appropriate chemical compositions, which is the limiting factor on the application of these methods (**Lucey 1998; Roush and Dalton, 2004; Cruikshank et al., 2005**). The absence of these data is largely due to the difficulty obtaining appropriate volumes of sufficiently pure samples and in generating the required spectroscopic data accurately through laboratory measurements. Below, I describe methods for producing optical constants for radiative transfer modelling.

A common method for indirectly deriving MIR optical constants is to make use of classical dispersion theory, followed by fitting a Fresnel reflectance model to specular reflectance spectra collected on pressed pellets or other flat surfaces such as single crystals (e.g., **Roush et al., 1991, Wenrich and Christensen, 1996; Roush et al., 1996, Lane et al., 1999; Esposito et al., 2000, Glotch and Rossman 2007, Glotch et al., 2009; Zeidler et al., 2015; Sklute et al., 2015; Ye et al., 2021**). This method mathematically defines the fundamental vibrational transitions within a mineral as the sum of lattice harmonic oscillators. For each oscillator, four parameters are defined: center of frequency of oscillation (**ν**), band strength (**$4\pi\rho$**), band width (**γ**), and the frequency dielectric constant, or vacuum permittivity (**ε_0**). The number of oscillators are identified by the number of readily apparent Reststrahlen bands observed in the measured specular reflectance spectra. This number of oscillators is iteratively adjusted during the fitting process. Roush et al. (**1991**) simplified the dielectric constant by showing that it can be approximated by **n^2_{vis}**. As such, the existence of Na D-line (589.29 nm) ***n*** values can be used for the approximation, which is now commonly done. Following this, the refractive indices can be found with one of several iterations of the dispersion equations found in the literature; the following equations were used by Glotch and Rossman (**2007**) and Glotch et al. **(2009**) and were adopted from Spitzer and Kleinman (**1961**):

$$n^2 - k^2 = \varepsilon_0 + \sum_j \frac{4\pi\rho_j v_j^2 (v_j^2 - v^2)}{\left(v_j^2 - v^2\right) + (\gamma_j^2 v_j^2 v^2)} \qquad \textbf{(27)},$$

where j represents the $\boldsymbol{j}$th oscillator, and

$$nk = \sum_j \frac{4\pi\rho_j v_j^2 (\gamma_{j v_j v})}{\left(v_j^2 - v^2\right) + (\gamma_j^2 v_j^2 v^2)} \qquad \textbf{(28)}.$$

Then, the Fresnel reflectance equations can be used to relate the optical constants described here to the total reflectance for non-normal incidence angles:

$$R_T = \frac{R_\perp^2 + R_\parallel^2}{2} \qquad \textbf{(29)},$$

where

$$R_\perp^2 = \frac{\left[(n^2 - k^2)\ cos\emptyset - \mu\right]^2 + (2nk\ cos\emptyset - v)^2}{\left[(n^2 - k^2)\ cos\emptyset + \mu\right]^2 + (2nk\ cos\emptyset + v)^2} \qquad \textbf{(30)},$$

$$R_\parallel^2 = \frac{(cos\emptyset - \mu)^2 + v^2}{(cos\emptyset + \mu)^2 + v^2} \qquad \textbf{(31)},$$

$$\mu = \left(\frac{n^2 - k^2 - sin^2\emptyset + \left[\left(n^2 - k^2 - sin^2\emptyset\right)^2 + 4n^2k^2\right]^{1/2}}{2}\right)^{1/2} \qquad \textbf{(32)},$$

$$v = \left(\frac{-(n^2-k^2-sin^2\emptyset)+\left[(n^2-k^2-sin^2\emptyset)^2+4n^2k^2\right]^{1/2}}{2} \right)^{1/2} \quad \textbf{(33)},$$

and where ∅ is the incidence angle.

From here, some researchers use a non-linear least squares optimization routine (e.g., **Bevington, 1969)** to find the best fit that minimizes the associated errors, and therefore arrive at the best estimated optical constants (**Glotch et al., 2007; Roush et al., 2007**). This method is only valid at wavelengths where materials are opaque and strongly absorbing, and where wavelengths are sufficiently large relative to surface asperities in the measured surfaces. The dispersion technique also deals with fundamental vibrational modes, not electronic transitions. For these reasons, this technique is generally unusable at UV and VNIR wavelengths, and can often lead to significant errors since crystals and the pellet-making process cannot be perfect.

Transmittance spectra can also be used to derive optical constants on thin films and crystals (**Irvine and Pollack, 1968; Warren, 1984; Mooney and Knacke 1985; Roush et al., 2007**). Transmittance measurements of fine particles suspended in KBr matrices have also been used, to varying degrees of success (e.g., **Koike et al., 1989; Marzo et al., 2004**). The theoretical treatment of determining the optical constants from transmittance measurements are described in detail by Heavens (**1970**) and Bohren and Huffman (**1983**), and applied to gypsum crystals by Roush et al. (**2007**), as an example. The light transmitted by a slab of material is given as:

$$T_{slab} = \frac{(1-R)^2+4Rsin^2\varphi}{R^2e^{-ad}+e^{ad}-2Rcos(\delta+2\varphi)} \quad \textbf{(34)},$$

where

$$R = |\tilde{r}|^2 = \left|\frac{m_0 - m_1}{m_0 + m_1}\right|^2, \qquad m = n + ik,$$

and

$$\varphi = tan^{-1}\left(\frac{2n_0k_1}{n_1^2 + k_1^2 - n_0^2}\right), \qquad 0 \leq \varphi \leq \pi, \qquad \delta = \frac{4\pi n_1 d}{\lambda}, \qquad \alpha = \frac{4\pi k_1}{\lambda},$$

where d is the thickness of the sample, m_0 is the absorption coefficient of air, m_1 is the absorption coefficient of the slab, and $\tilde{r}$ is the Fresnel reflectance. Transmittance measurements are of limited use in practice; they are only valid if a measurable amount of light is transmitted at the wavelengths under investigation, and if these values are also below 0.80 (e.g., **Roush et al., 2007 and references therein**). The films and crystals need to be near-perfectly flat without aberrations, which is nearly impossible for most minerals. Although pellets of KBr matrices produce orientation-averaged spectra, they do induce significant scattering which is not accurately accounted for in the theoretical treatments.

Ellipsometric methods are similar to the classical dispersion and Fresnel reflectance combination of methods outlined above and in Glotch et al. (**2007, 2009**), in that the optical constants can be found indirectly by fitting oscillator models to experimentally-measured data (**Fujiwara, 2007; Blake et al., 2017; Spencer 2019; Myers et al., 2020**). The key difference is that ellipsometry measures variations in polarization of reflected light, which is a function of the optical properties of materials. Ellipsometers characterize the optical properties by illuminating the sample with linearly *s*- and *p*-polarized light. The change in polarization by interaction with the sample can be mathematically related to the optical constants; see equations 1 to 3 from Myers et al.

(**2020**). Similar to other techniques, ellipsometry cannot be used for most materials, as the accuracy of the measurements depends on having highly uniform surfaces and the presence of significant ***k*** at the measured wavelengths. As such, its application is generally restricted to thin films, semiconductor layers, and evaporated and deposited materials. However, ellipsometry has been used successfully to determine the optical constants of metals with a focus on space weathering (e.g, **Cahill et al., 2012 and 2019**). Further, recent work has successfully performed ellipsometry on pressed pellets of fine powders (**Myers et al., 2020**); where they stated "spectroscopic ellipsometry should be less sensitive to pellet surface quality since it does not rely on measuring the absolute radiation intensity…". This highlights the need for a direct comparison of ellipsometry with pressed pellets on which other data processing techniques are performed.

Radiative transfer methods have been used to determine optical constants of minerals at VNIR wavelengths by a number of groups (**Roush et al., 1990, Lucey et al., 1998; Roush (2003, 2005); Pitman et al., 2005; Marra et al., 2006; Roush et al., 2007; Dalton and Pitman, 2012; Trang et al., 2013; Pitman et al., 2014, Sklute et al., 2015, Carli et al., 2016; Lucey et al., 2018; Ye et al., 2019; Ye et al., 2021, Roush et al., 2021**). For brevity, here I discuss the Hapke-based models that have found wide application. Other radiative transfer models exist, such as the Skuratov approach, and detailed discussion of their relative benefits can be found in the literature (e.g., **Roush et al., 2007**). The general approach is to first have *a priori* knowledge of *n* at wavelengths under investigation, generally determined at the Na D-line. This value is set as a constant over the entire wavelength range, and *k* is iteratively forced to the point where modelled spectra conform to the measured laboratory spectra. More accurate data is acquired if there are multiple well-defined grain size fractions in the laboratory measurements, since the single scattering albedo does not theoretically change with grain size. With the absence of these measurements, the single scattering albedo and derived optical constants can become grain size dependent (e.g, **Roush et al., 2007 and 2021**). Although approximations exist for the absence of multiple phase angle measurements in the laboratory component (e.g., **Roush et al., 2007**), the existence of the data allow for more accurate phase function determinations, and therefore more accurately derived optical constants.

The radiative transfer method for the determination of optical constants is most useful for weakly-absorbing materials, which is the majority of rock-forming minerals at VNIR wavelengths. For this reason, this method has emerged as the generally preferred framework for deriving optical constants in the VNIR. Because these methods underperform at MIR wavelengths because of high ***k***, researchers generally combine multiple methods to derive wide wavelength range optical constants (**Roush et al., 2007; Pitman et al., 2014; Sklute et al., 2015; Ye et al., 2021**).

Kramers-Kronig analyses have been used in various capacities for determining optical constants of materials in the UV to VNIR (**Calvin, 1990; Roush et al., 1990; Hiroi and Pieters, 1992; Hiroi and Pieters, 1994; Lucey 1998; Cruikshank et al., 2001, Lucarini et al., 2005; Roush et al., 2007; Kitamura et al., 2007**). Variations of this method have previously been used to specifically determine the optical constants of visibly opaque minerals (**Strens et al., 1979, Bell et al., 1985; Querry et al., 1985, 1987**). These equations, in general, derive *n* as a function of wavelength from known ***k*** values. True Kramers-Kronig equations deal with all wavelengths, which is not a measurement that is possible in the laboratory or theoretically. Subtractive Kramers-Kronig analyses use the widest wavelength range accessible (e.g, **Warren 1984, Roush et al., 1991, Roush et al., 1996**). Sklute et al. (**2015**) and Ye et al. (**2021**) have used a singly subtractive Kramers-Kronig measurement to help extend the wavelength range of optical constants determined for classical dispersion theory. The singly subtractive Kramers-Kronig transformation can be written as:

$$\boldsymbol{n(v) = n_0 + \frac{2(v^2 - v_0^2)}{\pi} P\int_0^\infty \frac{v'k(v')}{(v'^2 - v^2)(v'^2 - v_0^2)} dv'} \qquad \textbf{(35)},$$

where ***n(v)*** is the real refractive index at frequency ***v***, and $\boldsymbol{n_0}$ is a known value of the real refractive index at a specific frequency, which is usually at the Na D-line. ***V'*** is a dummy variable, and ***P*** denotes the Cauchy principal value of the integral.

Roush et al. (**2007**) stated: “In respect to ***k***, if 0.01 < ***k*** <1, i.e., in the strong bands then comparison of values derived from dispersion analysis and Kramers-Kronig analysis agree to within a few percent”. As such, the use of singly subtractive Kramers-Kronig analyses to extend MIR optical constants derived from dispersion analyses to overlap with those from VNIR radiative transfer methods is appropriate. The main drawbacks of using Kramers-Kronig analyses are the requirements for existing knowledge of ***k*** values, which are rarely available without already existing *n* values.

Because of the labour intensive nature of producing optical constants to facilitate radiative transfer modelling on my mixtures to derive LODs and to analyze SuperCam data, I have opted to use the simple and common method of continuum-removal and band depth percentage computation. This is a common method for interpreting reflectance spectra (e.g., **Clark and Roush 1984; Cloutis et al., 2004**) and has been noted to be key to successful spectral identification in complex mixtures (**Clark 1999**). First, I calculated a straight line in wavelength space across the absorption band (**Figures 3c and 3d**), then I process the data according to **Equation 37:**

$$\boldsymbol{Bd = \left(1 - \frac{Rb}{Rc}\right)100} \qquad \textbf{(36)},$$

where ***Bd*** is the band depth percentage**,** ***Rb*** is the minimum reflectance value of the absorption band, and ***Rc*** is the value of the continuum at the same wavelength of ***Rb***.

The majority of mineral and cation LODs by reflectance spectroscopy have been qualitative or semi-quantitative (expressed on an ordinal scale; not highly precise or accurate), and based entirely on the visual observation of changes in the reflectance spectrum (e.g., **Scheinost et al., 1998; Gaffey 1985; Lorenz et al., 2018**).

Recent work has attempted to quantify LODs of some materials by reflectance spectroscopy. Kaplan and Milliken (**2016**) looked at the relationship between C-H spectral reflectance band depth (**Eqution 37**) and total organic carbon (TOC) in clay mixtures and estimated a conservative LOD of <1 wt.% for TOC with this relationship. They defined the LOD in this case as the TOC at which spectral evidence (3.4 µm C-H band) was no longer present. They also constructed calibration curves through linear regression to estimate the LOD. They found that applying a 95% confidence to the x-intercept, that in all cases except the darkest montmorillonite sample, the LOD was estimated to be generally between 0.20 and 1.00 wt.% TOC. Kaplan and Milliken (**2018**) extended their sample suite to include a number of Proterozoic shales and kerogen to assess the impact of H/C on the reflectance spectra and LOD of TOC. They found that in general as H/C increases, the LOD of TOC decreases due to the increased absorption strength of the 3.4 µm C-H band. Through visual inspection, they estimated that the LOD of TOC with low H/C to be near 1.0 wt.% and with high H/C to be near 0.1 wt.%. Kaplan et al. (**2019**) applied the similar methods for investigating the reflectance properties of insoluble organic matter from chondritic meteorites in addition to a suite of carbonaceous chondrite meteorites and found that when H/C <0.4 the 3.4 µm C-H band is not readily observable, thus further complicating LOD estimations of TOC when H/C is unknown.

Some work has been done to estimate LODs by reflectance spectroscopy through other methods. Zhang et al. (**2001**) defined LODs of clay minerals by reflectance spectroscopy to be equivalent three standard deviations of the background signal and found that quartz-kaolinite and quartz-dickite mixtures showed detection limits of ~5 wt.% in relative abundance. Tarnas et al. (**2021**) found that dynamic aperture factor analysis/target transformation (DAFA/TT) and factor analysis/target transformation (FA/TT) algorithms on hyperspectral images of mixtures of the MGS-1 Mars analogue materials with the 125-250 µm and 45-75 µm calcite powder had LODs of 10% and 20%, respectively.

For the purposes of this study, I estimate the LOD of carboxylates by using band depth values derived with **Equation 36** and processing these data the same way as those from XRD with **Equation 16**, which is similar to how LODs were determined by Kaplan et al. (**2016**) and Zhang et al. (**2001**).

3.0 Results

3.1 The endmembers by X-ray diffraction

The diffraction patterns collected on the JSC Mars-1a analogue sample are shown in **Figure 4**. The sample is highly amorphous with a broad diffraction hump centered near 30 °2-theta Co-Kα and a strong low angle rise in diffraction. The crystalline component is dominated by andesine with small concentrations of augite and olivine, which is consistent with the XRD analyses by Moroz et al. (**2009**) who showed their aliquot to be composed of 82.4 wt.% X-ray amorphous phases, 11.7 wt. % andesine, 3.1 wt.% augite, and 2.8 wt. % olivine. **Figure 4** also demonstrates the increased S/N with collection time; the average diffraction pattern is plotted against all 10 analyses and shows a significant increase in S/N.

The diffraction patterns on the carbonate powders are shown in **Figure 5a**. These samples are highly crystalline, with XRD peaks with higher amplitudes than those observed in the JSC Mars-1a sample. This further demonstrates the high amorphous content of the analogue sample with its very weak diffraction peaks. The strongest diffraction peaks for the carbonates are listed in **Table 2**; siderite at 37.50, calcite at 34.25, and magnesite at 38.10 °2-theta Co-Kα.

Figure 5b shows the diffraction patterns for the oxalate samples, which are more complex than carbonates, in that they have more diffraction peaks; these carbonates crystallize in the more symmetric trigonal crystal system (**Dufresne et al., 2018**) than these oxalates, which crystallize as monoclinic (**Vlasov et al., 2023**). All of these samples have a number of major diffraction peaks that could be used for identification and discrimination; the strongest of which are listed in **Table 2**. For this study, I make use of three diffraction peaks in humboldtine at 21.45, 34.60, and 39.40 °2-theta Co-Kα. The strongest diffraction peaks for whewellite and glushinskite are situated at 17.35 and 21.00 °2-theta Co-Kα, respectively.

The diffraction patterns for the acetate samples are shown in **Figure 5c**. The Fe^{2+}-acetate sample is X-ray amorphous, with no discernible XRD peaks. The magnesium acetate tetrahydrate shows a much stronger diffraction peak than those exhibited by the calcium acetate monohydrate sample. The peaks I use in this study are listed in **Table 2**, and are situated at 14.75 and 10.50 °2-theta Co-Kα for the magnesium acetate and calcium acetate samples, respectively.

Figure 5d displays the diffraction patterns for the formate samples. **Table 2** shows the major peaks I used in this study, which are found at 18.35 and 20.95 °2-theta Co-Kα for the calcium formate and magnesium formate dihydrate samples, respectively.

3.2 The endmembers by reflectance spectroscopy

The collected reflectance spectra for the JSC Mars-1a analogue powder is shown in **Figure 2a**. The spectra show a Fe^{3+} absorption edge in the visible spectrum and a weak absorption band near 1000 nm. The NIR spectra show a high overall reflectance, which is the reason the analogue material was initially used as a comparison with the bright regions of Mars. The sample shows relatively strong OH and H_2O related absorption nears near 1420, 1920, and 3000 nm, despite baking off ~11 wt.% of water in the sample. There is a very weak Al-OH feature situated near 2200 nm, which is likely contributed from the amorphous phyllosilicate component. This is consistent with the observations that JSC Mars-1a is enriched in Al_2O_3 compared to other analogue materials and much of the martian soils. The overall reflectance and spectral features strongly match those observed in the <40 um particle separate measured by Moroz et al. (**2009**). My sample exhibits observable C-H features related to organic contamination at ~3400 and ~3500 nm (e.g., **Clark et al., 2009, Izawa et al., 2014, Kaplan et al., 2016**) but does not show any observable carbonate contribution (**Figure 2a**).

The reflectance spectra for the MGS-1 material used by Tarnas et al. (**2021**) are contrasted with those from JSC Mars-1a in **Figure 2a**. The sample is significantly darker with more hematite-like contribution in the visible spectrum. The H_2O-associated absorption bands are weaker, and there are fewer weak absorption bands in the NIR. Cannon et al. (**2019**) showed that the MGS-1 material showed broadly similar albedo and spectral shape to the data collected on the Rocknest material at Gale Crater. They indicate that at longer wavelengths, the material is similar to the low albedo regions on Mars.

The reflectance spectra for the carbonate samples are shown in **Figure 6a** in contrast to the spectra from JSC Mars-1a. Reflectance spectra of these minerals have been heavily studied and are well understood (**Hunt and Salisbury, 1971; Gaffey 1985, 1986, 1987; Crowley 1986; Bishop et al., 2021**). The major absorption bands used for detection and discrimination are listed in **Table 2**. For siderite, the major absorption band minima are at ~2322, 2524, and 3964 nm; for magnesite they are situated at 2301, 2502, and 3943 nm; for calcite they are at 2340, 2536, and 2979 nm. The band minima for these are all shifted in wavelength due to the variations in their crystal structures and major cations and provide the ability to discriminate between them and/or interpret where they exist in solid solution. The spectra are very bright at wavelengths outside of the absorption bands, with the exception of a relatively weak split absorption near 1200 nm in the magnesite and siderite samples which is due to the presence of Fe^{2+} in the minerals. Magnesite forms a solid solution with siderite and natural samples typically have small concentrations of Fe^{2+} (e.g., **Gaffey 1987**), and therefore exhibit this weak absorption band. For this study, I do not make use of the ~3400 nm absorption bands, as they overlap with the C-H features found in the JSC Mars-1a sample and have slightly weaker absorption than those situated near 3900 nm.

Figure 6b shows the reflectance spectra of the oxalate samples. These samples have previously been studied in detail (**Applin et al., 2016**). Due to the inclusion of water in the crystal structure, they exhibit more complex reflectance spectra in comparison with anhydrous carbonates, similar to the XRD patterns. Features from H_2O are situated near 1500, 2000, and 3000 nm. Like siderite, the inclusion of Fe^{2+} in humbdoltine causes the presence of the split Fe^{2+} absorption bands in the VNIR. The features of interest used here are listed in **Table 2**. For humboldtine, the strongest and most unique feature is situated at 2048 nm which is due to H_2O. For whewellite and glushinkite, I use weak features situated at 2436 and 2442 nm, respectively. At longer wavelengths, oxalates exhibit weak absorption bands near ~3600 nm, which are not present in most carbonates, and are also listed in **Table 2**. For humboldtine, the band minima are at 3546 and 3606 nm, for whewellite at 3610 nm, and for glushinskite at 3590 nm.

Due to the inclusion of C-H in their structure (e.g., **Figure 1**), acetates and formates exhibit even more complex reflectance spectra (**Figures 6c and 6d; Applin et al., 2017**). In the NIR for acetates, the overtones of the C-H absorption bands are broad doublets centered near 1700 nm. These features are weaker in the formates. Acetates exhibit carbonate-like overtones and combinations near 2300 and 2500 nm, comprised of partially resolved and overlapping absorption bands. The amorphous Fe^{2+} acetate shows a non-split absorption feature near 1000 nm. The features used in this study for detection are listed in **Table 2**. For the X-ray amorphous Fe^{2+} acetate, the features are at 2260 and 4057 nm, for the calcium acetate monohydrate they are at 2263 and 4188 nm, and for the magnesium acetate tetrahydrate they are at 2250 and 4085 nm.

The formate samples show sharp and strong doublet/triplet absorption features in the NIR. The spectra of calcium formate is relatively complex, with numerous weaker absorption bands. The strongest features for the formates are used here and are listed in **Table 2**; these are at 2355 nm for calcium formate and 2340 nm for magnesium formate dihydrate. The formates also exhibit some absorption bands near 3600-3700 nm that could be used for detection and discrimination.

The acetates and formates, with the exception of the anhydrous calcium formate, show characteristic H_2O absorption features near 1400, 1900, and 3000 nm. Due to the inclusion of C-H in their structure, acetates and formates exhibit the C-H features near 3400 and 3500 nm that are characteristic of organic materials (e.g., **Clark et al., 2009, Izawa et al., 2014, Kaplan et al., 2016**).

3.3 The mixtures by X-ray diffraction

The diffraction patterns and the isolated peak amplitude patterns for the carbonate minerals mixed with JSC Mars-1a are shown in **Figures 7a to 7j**. The peak amplitude pattern for the siderite mixtures is shown in **Figure 3b**. The major peak situated at 37.50 °2-theta Co-Kα was detectable above continuum in all of the mixtures. The measured peak amplitudes are listed in **Table 3** and are 1.17, 1.59, 2.78, and 3.69 with increasing siderite content. The peak amplitude of pure siderite was 14.64. Siderite does show other observable diffraction peaks at the higher concentration mixtures. For calcite, the major diffraction peak situated at 34.25 °2-theta Co-Kα overlaps with the weak pyroxene and olivine diffraction peaks in the JSC Mars-1a material, limiting its detectability. Despite this, signal is observed readily at 2.02 wt.% and can be observed slightly at 0.55 wt.%. The peak amplitudes are 1.27 and 1.53 with increasing concentration and 59.04 for pure calcite. The main magnesite peak at 38.10 °2-theta Co-Kα does not overlap with a feature in the JSC Mars-1a material and is therefore more readily detectable at lower concentration. The peak amplitudes are 1.17 and 1.54 with increasing concentration and 37.31 for the pure mineral.

The diffraction patterns and the isolated peak amplitude patterns for the oxalate minerals mixed with JSC Mars-1a are shown in **Figures 8a to 8h**. I analyzed three of the stronger peaks for humboldtine. The first, a doublet situated at 21.45 °2-theta Co-Kα at its strongest amplitude does not overlap with any peaks in the JSC Mars-1a material and is observable at the lowest concentration. The peak amplitudes are 1.19, 1.49, 2.09, and 2.73 with increasing concentration and 13.05 for the pure mineral. The second, situated at 34.60 °2-theta Co-Kα has peak amplitudes of 1.22, 1.27, 1.47, and 2.73 with increasing concentration, while the pure mineral shows a peak amplitude of 5.62. The third, situated at 39.40 °2-theta Co-Kα shows peak amplitudes of 1.25, 1.37, 1.54, and 1.82 with increasing concentration and the pure mineral shows a peak amplitude of 5.44. Both the second and third peaks overlap with weak diffraction peaks found in the JSC Mars-1a material.

For glushinskite, I analyzed the peak situated at 21.00 °2-theta Co-Kα, which does not overlap with another peak in the JSC Mars-1a material. For this sample, the lowest concentration of 0.49 wt.% is observable above continuum, but the peak shape is not recognizable. The peak amplitudes are 1.15 and 1.37 with increasing concentration and 13.20 for the pure mineral. For whewellite, I analyzed the peak situated at 17.35 °2-theta Co-Kα, which is arguably observable above continuum at 0.51 wt.%. The peak amplitudes are 1.08 and 1.23 with increasing concentration and 12.78 for the pure mineral.

The diffraction patterns of the acetates mixtures are shown in **Figures 8i to 8m**. Because the Fe^{2+} acetate sample was X-ray amorphous, I did not do any analysis on the diffraction patterns of those mixtures. For calcium acetate monohydrate I analyzed the 10.50 °2-theta Co-Kα peak, which had peak amplitudes of 1.08 and 1.26 with increasing concentration and 25.13 for the pure material. For magnesium acetate tetrahydrate I analyzed the 14.75 °2-theta Co-Kα peak. At the concentration of 0.59 wt.%, this peak was effectively unobservable. The mixtures showed peak amplitudes of 1.02 and 1.15 with increasing concentration and 25.13 for the pure material.

The diffraction patterns of the formate mixtures are shown in **Figures 8n to 8p**. For the magnesium formate dihydrate, I did not observe any features above continuum at the mixtures concentrations made. For the calcium formate, I analyzed the diffraction peak at 18.35 °2-theta Co-Kα. The peak amplitudes were 1.08 and 1.29 with increasing concentration and 28.88 for the pure material.

3.4 The mixtures by reflectance spectroscopy

The reflectance spectra and the continuum-removed spectra on the mixtures are shown in Figures **9a to 9o**. Because of the weak absorption bands exhibited by carbonates in the NIR, they were not observable in the mixtures with JSC Mars-1a. For example, **Figure 9b** shows that siderite did not contribute any significant absorption to the reflectance spectrum at 2300 and 2500 nm at even the 11.08 wt.% concentration. The absorption bands for carbonates near 3900 nm are much stronger, however. For siderite, there was observable band depth at 3964 nm with the exception of the 0.53 wt.% mixtures. The band depths percentages are listed in **Table 2** and are 0.59, 3.80, and 6.55 with increasing concentration and 57.62 for the pure sample. The absorption band for calcite at 3979 nm was observable even at 0.55 wt.%. The band depth percentages were 0.54 and 2.40 with increasing concentration and 77.76 for the pure sample. Like siderite, the lowest concentration of magnesite (0.65 wt.%) was not observable. The band depth percentage for the 2.00 wt.% mixture was 1.54 and for the pure samples it was 71.13.

I supplemented my carbonate mixture spectra with those collected by Tarnas et al. (**2021**), who used the MGS-1 analogue material, multiple grain size fractions of calcite (45-75 and 125-250 µm) and a more extended concentration suite of samples and measured the spectral reflectance at NIR wavelengths (1.0, 2.5, 5.0, 10.0, 20.0, 50.0 wt.% calcite). Here, I isolated the 2340 nm band of calcite, and the data are shown in **Figures 10a to 10e**. For both grain size fractions, the 2340 nm band is observable at all concentrations. For the calcite sample with a grain size fraction of 45-75 µm, the band depth percentages are 0.30, 0.59, 0.75, 1.07, 2.38, and 5.38 with increasing concentration and 20.16 for the pure sample. For the calcite samples with a grain size fraction of 125-

250 µm, the band depth percentages are 0.55, 0.63, 0.82, 1.13, 4.10, and 10.39 with increasing concentration and 38.76 for the pure sample. **Figure 10e** displays the calcite spectra collected by Tarnas et al. (**2021**) in comparison with those measured here on a small grain size fraction. This demonstrates the strong increase in absorption band strength with increasing grain size fraction.

The reflectance spectra of the oxalate mixtures are shown in **Figures 9h to 9k**. With the exception of humboldtine at concentrations of 5.54 wt.% and higher, none of the spectral features associated with these oxalates were observable. For humboldtine, the H_2O-related feature near 2080 nm had a band depth percentage of 0.77 and 3.60 with increasing concentration and 42.56 for the pure sample.

Figures 9l to 9p show the reflectance spectra of the acetate mixtures. In these samples, absorption bands were only observable at NIR wavelengths. These absorption bands overlap with a very weak band present in JSC Mars-1a, but this doesn't significantly affect their detectability. For the Fe^{2+} acetate sample, the band depth percentages for the absorption band at 2260 nm were 1.25 and 1.86 with increasing concentration and 30.54 for the pure sample. For the magnesium acetate tetrahydrate mixtures, the absorption band at 2259 nm showed band depth percentages of 0.14 and 0.38 with increasing concentration and 26.53 for the pure sample. For the calcium acetate monohydrate, the absorption band at 2263 nm showed band depth percentages of 0.18 and 0.56 with increasing concentration and 46.43 for the pure material.

The reflectance spectra of the formate mixtures are shown in **Figures 9q to 9t**. Like the acetates, discernible absorption bands were only observable at NIR wavelengths. As with the acetate mixtures, JSC Mars-1a display some absorption features that overlap with these formates, but at the concentrations measured it does not significantly affect their detectability. For the calcium formate sample, the absorption band at 2355 nm showed band depth percentages of 0.47 and 2.15 with increasing concentration and 68.28 for the pure sample. For the magnesium formate dihydrate sample, the absorption band at 2340 nm showed band depth percentages of 0.36 and 1.28 with increasing concentration and 40.60 for the pure sample.

3.5 Detection limits by X-ray diffraction

The resulting simple linear regression parameters derived from the peak amplitudes and band depth percentages are listed in **Table 4**.

The computed LODs by XRD of the samples studied here using **Equation 16** are listed in **Table 6**. Some of the linear regression models and resulting R^2 values are shown in Figures **11a to 11e**. For the samples that were only comprised of a set of two mixtures, I assumed a linear relationship and derived the linear regression parameters through that as an estimation of the LODs. This was done because of the relatively high linearity between the lowest two concentrations relative to the measured regression curves for siderite by XRD and calcite by NIR reflectance. For the purposes of this study it provides a reasonable approach for a qualitative estimation of LOD and concentration when unknown, which will be expanded on in future work with multiple measurements of a concentration near the estimated LOD.

Siderite powder with a grain size fraction of <45 µm shows a LOD of 0.65 wt.% when using **Equation 16**. To compare and contrast, I computed LODs for the methods outlined in **Section 2.3.1** (for **Equations 2, 4, 5, 6, 7, 8, 10, 11, and 16**) and these are listed in **Table 5**. For some of these where it was necessary to determine the standard deviation in determined concentration from multiple measurements, I used the approach outlined by Zhang **(2007)** to measure a concentration of the analyte (siderite in this case) at a concentration within a factor of 1-5 of the estimated LOD eight separate times. I used the 2.53 wt.% siderite mixture and found that the standard deviation in concentration derived through regression analysis was 0.48 wt.%, while the range of peak amplitudes from these measurements is graphically shown in **Figure 7b**. The confidence in the determination of this concentration can be evaluated by using a t-distribution, as described in **Section 2.3.1**, and this can be applied to all of the methods outlined in **Section 2.3.1** to qualitatively compare and contrast the confidence levels. This shows the method I used here to determine LODs is a liberal estimation of LOD, producing a 2-sided confidence of 78% (**Figure 7c**), but is more conservative than **Equations 2 and 11**. **Equations 4, 7, 8, 10, and 13** produce LODs greater than the 99% confidence, which is 1.57 wt.% (**Table 5**). The computed confidence of detection for siderite in palagonite with this specific XRD method is shown graphically in **Figure 7c**, which shows that a detection at 0.34 wt.% would contain 50% confidence. **Figure 7d** graphically demonstrates the difference between a confidence of 78% and 99%. Here, I show that the 0.65 wt.% siderite at a confidence of 78% shows a peak amplitude significantly greater than the mean of the background palagonite measurements, and that a concentration between this and the 99% confidence level would likely produce peak amplitudes that are observable by visual inspection. Because in XRD analyses in the context of exploration, specifically in CheMin data, an observable peak by visual inspection would not be ignored and a concentration would be estimated, this generally justifies the use of the liberal **Equation 16** for LOD determination.

I estimated the error in determined concentration for the 2.53 wt.% siderite sample by propagating the standard deviations of the regression slope, intercept, and of the multiple measurements:

$$\sqrt{\left(\mathbf{100}\frac{\sqrt{\boldsymbol{\sigma}_{\mathrm{s}}^{\mathbf{2}}+\boldsymbol{\sigma}_{\mathrm{i}}^{\mathbf{2}}}}{\bar{\boldsymbol{x}}_{\boldsymbol{s}}-\boldsymbol{i}}\right)^{\mathbf{2}}+\left(\mathbf{100}\frac{\boldsymbol{\sigma}_{\mathrm{m}}}{\boldsymbol{m}}\right)^{\mathbf{2}}} \quad \textbf{(37),}$$

where ($\boldsymbol{\sigma}_{\mathbf{s}}$) is the standard deviation in the concentration of the measured 2.53 wt.% siderite sample and ($\bar{\boldsymbol{x}}_{\boldsymbol{s}}$) is the mean concentration determined from those measurements using the regression parameters, ($\boldsymbol{\sigma}_{\mathbf{i}}$) is the standard deviation of the intercept ($\boldsymbol{i}$), and ($\boldsymbol{\sigma}_{\mathbf{m}}$) is the standard deviation of the regression slope ($\boldsymbol{m}$).This produced a relative error of ~22%, or specifically 2.53 ± 0.55 wt.%. These errors can be extended for the range of peak amplitudes from determined siderite concentrations, with the assumption that the standard deviation in peak amplitude of those measurements would remain 0.11. **Figures 7d to 7f** show this for determined concentrations of siderite from 0 to 10 wt.%, and demonstrates that the determined LOD using **Equation 16** would exhibit value of 0.65 ± 0.54 wt.%, or a relative error of ~83%. The error value here nearly converges with the LOD, which may further indicate that any concentration between this LOD and that of 99% confidence should be observable by visual inspection of the diffraction patterns. The standard deviation in peak amplitude for the background JSC Mars-1a material was ~0.05, therefore it may be likely that the standard deviation of multiple measurements at the LOD of 0.65 wt.% would be smaller than that at 2.53 wt.%. However, using the standard deviation for the background results in an error at the LOD of 0.65 ± 0.33 wt.%, which is not very different and would represent a liberal best-case scenario. Future work will determine these values for other carboxylates studied here, but this provides a rough guideline that can be qualitatively applied to measurements with the same method, since the peak amplitudes and concentrations are directly related to Bragg peak strength.

For calcite, the LOD is 0.99 wt.%, and for magnesite the LOD is 0.56 wt. %. The three peaks from humboldtine show LODs of 1.00, 1.86, and 1.89 wt.%, respectfully. The LOD for whewellite is 1.02 wt.% and that of glushinskite is 0.78 wt.%. I did not determine a LOD for Fe^{2+} acetate, as it is X-ray amorphous. Calcium acetate monohydrate had a LOD of 0.93 wt.% and that of magnesium acetate tetrahydrate was 1.25 wt.%. I did not determine the LOD of magnesium formate dihydrate as the diffraction peak of interest was not observable in the mixtures, thus the LOD exceeds the mixture concentrations used. For calcium formate, the LOD was determined to be 0.95 wt.%. Broadly, the LOD for all of these materials when intimately mixed with the JSC Mars-1a analogue material appears to hover near 1.00 wt.%.

3.6 Detection limits by reflectance spectroscopy

The LODs by reflectance spectroscopy for the mixtures are listed in **Table 6** for both NIR and MIR wavelength ranges. Here, I used the same method as with the XRD data; **Equation 16**. As mentioned, the 2322 and 2524 nm absorption bands were not observable for siderite even at the mixture containing 11.08 wt.% siderite. For the 3964 nm band, the LOD is not determined quantitatively but is somewhere between the concentrations of 0.53 and 2.53 wt.%, as the latter was observable in the data. Similarly, for magnesite, the LOD was not determined at these wavelengths, but is somewhere between 0.62 and 2.00 wt. % for the 3943 nm band. Calcite, however, exhibited lower LODs. For the <45 µm particle size fraction at the 2340 nm band, the LOD would be situated somewhere higher than the 2.02 wt.% concentration measured, and should be lower than both magnesite and siderite due to the higher band depth of the pure material. For the 3979 nm band, the LOD was determined to be 0.26 wt.% for the <45 µm particle size fraction. The 125-250 µm particle size fraction exhibited a LOD of between 1.15 and 3.65 wt.%, and the 45-75 µm particle size fraction exhibited a LOD of between 2.31 and 3.01 wt.% for the 2340 nm band. The reason for giving a range here is because I computed LODs for these materials from two different regression slopes (**Figure 11d**), as there was significant non-linearity in the band depth vs. concentration over the full range of concentrations.

The only LOD I could estimate for the oxalates was somewhere between 5.54 wt.% and 10.28 wt.% for the 2048 nm band for humbdoltine. All other features for the oxalate minerals were not observable in the mixtures.

Both acetates and formates exhibited relatively low LODs at NIR wavelengths but were not observable at the measured concentration at the MIR wavelengths. The Fe^{2+} acetate showed a LOD of 0.21 wt. % at 2260 nm, the calcium acetate monohydrate showed a LOD of 0.31 wt.% at 2263 nm, and the magnesium acetate tetrahydrate showed a LOD of 0.43 wt. % at 2259 nm. The calcium formate samples showed a relatively low LOD of 0.04 wt.% at 2355 nm, and the magnesium formate dihydrate showed a LOD of 0.31 wt.% at 2340 nm.

4.0 Discussion

4.1 Difference in detection limits within and between carboxylate groups

My results indicate significant differences in detectability within and between carboxylate groups, as well as between different analytical techniques. Relating to the latter and the majority of the analyses, this is not due to overlapping features found in the JSC Mars-1 and MGS-1 analogue powders, with the exception for diffraction of calcite, where the major Bragg peak significantly overlaps with a weak peak from pyroxene and olivine in JSC Mars-1a. With XRD, carbonates have lower LODs, in general, than oxalates, acetates, and formates. This correlates with the endmember peak amplitude values of the carbonates, which, especially for magnesite and calcite, are higher. If calcite was not masked by the pyroxene/olivine peak, all three carbonates would likely have XRD LODs near 0.60 wt.%. In contrast, the oxalates studied here have XRD LODs near 1.00 wt.%, as do the acetates and formates with the exception of the X-ray amorphous Fe^{2+} acetate and the magnesium formate dihydrate.

With reflectance spectroscopy, there is a marked contrast in LODs between acetates/formates and carbonate/oxalates. Acetates and formates show relatively strong NIR absorption bands, with band depth percentages between 25 and 45 for <45 μm particle size fractions. The LODs of these were roughly near 0.30 wt.%, with the calcium formate sample showing a LOD at 0.04 wt.% due to its strong absorption band. In contrast, the <45 μm particle size fractions of the carbonates showed very weak absorption bands with band depth percentages near 10. For the oxalates, the only LOD that was estimated was for the humboldtine H_2O band near 2040 nm and was found to between 5.0 and 10 .0 wt.%.

At MIR wavelengths shorter than 4000 nm, only the carbonates were detectable, which is expected given their strong absorption bands near 3900 nm. The band depth percentage of calcite was 77.76, magnesite was 71.13, and siderite was 57.62. In particular, the LOD for calcite was found to be only 0.26 wt.%. Some of the oxalates, acetates, and formate mixtures did show observable absorption features at wavelengths longer than 4000 nm, but I opted not to analyze LODs on those because the feature are broad and most observational data do not analyze this wavelength range due to the strong contribution of sample emittance.

4.2 Comparison with previous studies

The LOD of minerals by XRD is instrument, sample, and mixture dependent due to instrument and matrix effects. A LOD of 1.0-2.0 wt.% for crystalline materials for CheMin data has been cited (**Bish et al., 2014; Rampe et al., 2020**). For other instruments, detection limits for crystalline phases in mixed materials have been broadly stated at near ~2.0 wt.%, in general (**Bunaciu et al., 2015**). Xiao et al. (**2023**) performed extensive testing with mixtures of quartz, albite, calcite, dolomite, halite, kaolinite, and montmorillonite with a Panalytical X’pert Pro XRD, using Cu- radiation. They performed similar regression analyses and tested RIR, Rietveld, and FULLPAT methods. They found that the RIR method is the simplest quantitative approach yet is plagued by the caveats discussed in this study. They found that in these mixtures, calcite exhibited a LOD of 0.06 wt.%. Using the RIR method, Hillier (**1999**), using a mixture of quartz, k-feldspar, calcite, dolomite, and pyrite, found a LOD for calcite of 0.22 wt.%. Thus, my calculated LODs are consistent with the known broad LOD suggestions for CheMin-specific instruments. In my mixtures, if the calcite peak did not exhibit strong interference, the LOD would likely approach that found by Hillier (**2000**), since the peak amplitude is higher than the strongest Bragg peak exhibited by siderite (**Table 3**). The major caveat here is that the work by Hillier et al. (**1999**) used **Equation 4** for their analyses, which, in general, produces a LOD an order of magnitude larger than **Equation 16** used here.

Detection limits by reflectance spectroscopy are highly dependent on matrix effects. When significant concentrations of opaque mineral are present in a mixture, absorption bands and features can be strongly masked even at very high concentrations (e.g., **Figure 2a**). Thus, there is no usable reference for LODs of carboxylates or other materials that can be broadly applied to reflectance spectra. Kaplan et al. (**2019**) did estimate the LOD for bulk organic carbon in carbonaceous chondrites when using the ~3400 nm C-H bands to be ~1.0 wt.%, as discussed in **Section 2.3.2**. When studying pyroxene-bearing rocks and mixtures, Pompilio et al. (**2007**) stated:

> "In general, the way to establish detection limits for the absorber-related features, as a function of the relative abundance of the spectroscopically active species randomly distributed within a solid rock surface, is not straightforward."

In comparison with the analyses by Tarnas et al., (**2021**) on the same measurements, I observe a significant difference in LOD estimation. The band depth analyses presented here indicate LODs using the 2300 nm band of relatively large grained calcite mixed with the MGS-1 analogue powder to be near 3 wt.%, whereas the hyperspectral imaging methods used by Tarnas et al., (**2021**) could accurately detect calcite at 10-20 wt.%. I can compare my estimated LODs with data from samples known to contain small concentrations of carbonates to assess the robustness. Alexander et al. (**2015**) found both CI and CM chondrites to have an average of ~0.18 wt.% carbonate concentration, and some CM chondrites exhibit the carbonate absorption band near 3950 nm (**Beck et al., 2018**). Specifically, ALH 83100 was shown by Alexander et al. (**2015**) to have 0.32 wt.% carbonate, and is one of the two CM chondrite found by Beck et al. (**2018**) to show carbonate absorption bands. This exceeds the 0.26 wt.% LOD I determined for calcite in my mixtures, whereas those that had lower carbonate concentrations did not exhibit the 3950 nm absorption band. Thus, my LOD values represent a baseline for understanding carboxylate detectability in similar materials, which are bright, highly amorphous, and highly fine grained with basaltic chemical compositions. Fortunately, this is applicable to many known martian terrains. In particular, the LODs for carbonate at 3950 nm provide input on their high detectability with spectrometers covering this range because most materials are bright and without absorption features over this range.

4.3 Difference in detection limits by powder particle size fraction

With the inclusion of the data presented by Tarnas et al. (**2021**), I have analyzed the effect of grain size distribution on the LOD of calcite at NIR wavelengths. As expected for semi-transparent materials (e.g., **Hapke 2012**), the band depth for calcite at 2340 nm becomes stronger (larger) with increasing grain size (**Figure 10**). The band depth percentage increased from 9.42 for the <45 µm particle size fraction to 38.76 for the 125-250 µm particle size fraction, a four-fold increase. The 2340 nm band was not observable in the <45 µm particle size fraction when mixed with JSC Mars-1a at 2.02 wt.

%, but the LOD for the 45-75 µm particle size fraction when mixed with MGS-1 was 2.31-3.01 wt.% and 1.15-3.65 wt.% for the 125-250 µm particle size fraction. Given the expected formation scenarios for the non-carbonate carboxylates, such as abiotic photosynthesis, their particle sizes on the surface of Mars are likely very small, thus indicating the detectability of oxalates by reflectance spectroscopy would be difficult on the surface of Mars. In contrast, acetates and formates have high detectability at NIR wavelengths even at small grain sizes. Because carbonate minerals have a wide variety of possible formation conditions on the surface of Mars, larger grain sizes could be expected in addition to a relatively higher concentration, and are therefore more accessible to identification by reflectance spectroscopy.

4.4 Implications for exploration and caveats

These results lead to a number implications for Mars exploration that can inform the detection and characterization of these materials with XRD instruments and reflectance spectrometers on the surface. Acetate and formate minerals can be detected at relatively low concentrations with NIR reflectance spectrometers when mixed with relatively bright materials such as the JSC Mars-1a analogue material, even at fine grain sizes. In particular, the anhydrous calcium formate exhibited a very sharp and strong absorption band on which I calculated a LOD of only 0.04 wt.%. Oxalates will likely not be detected by orbital spectrometers or in situ reflectance spectrometers if the concentration of these minerals is at or below the LODs by XRD and at the concentrations suggested by SAM data. These are not expected to be rock-forming minerals, thus their concentration is not expected to exceed the LODs by reflectance. Oxalates can be identified by XRD at concentrations detected by SAM, and further analyses by CheMin may provide opportunities for their detection and characterization. In contrast, carbonates can be detected and have been detected at NIR wavelengths when the concentration is significant and/or the particle sizes are large. For larger grain sizes they could be detected at concentrations much lower than 5.0 wt.%. At MIR wavelengths, carbonates are readily detectable even at small grain sizes. This is consistent with the observation of carbonates at wavelengths of ~3900 nm in various carbonaceous chondrite meteorites where the concentration is not high and their particle sizes are small.

I have confirmed that the LOD for these minerals is very close to the often cited concentration of 1.0 wt.% by CheMin XRD. The exception, in general, is anhydrous carbonates which can be observed at lower concentrations because of their stronger diffraction peaks, but the error in the regression curves overlap with the 1.0 wt.% value.

One large caveat is that my LOD calculations are based on the standard deviation of measurements taken on the pure JSC Mars-1a material. This introduces an unrealistic low-noise component when comparing my experimental procedures with the data collected on the surface of Mars, e.g., CheMin and SuperCam. Thus, when data are noisier, the LODs will be higher; therefore, these numbers represent best-case-scenarios. Another caveat is that the CheMin XRD measurements are not relative measurements. Therefore, instrument effects are not removed from comparative measurements such as they are with ratioed reflectance spectra. The Terra breadboard is an excellent analogue for CheMin, and the normalization procedure to minimize differences in incident X-ray flux and quantum efficiency of the CCDs did help, but do not completely eliminate instrument effects that could change peak amplitudes between instruments.

Matrix effects are important when considering both XRD and reflectance spectroscopy measurement and are not removed by relative measurements. In particular, for CheMin-like XRD, the grain size distribution, sample composition, microabsorption, and bulk chemical composition, can have strong effects on detectability and LODs. Similarly, for reflectance spectroscopy, the grain size distribution, sample composition (not least opaque mineral composition), can strongly affect the band depths of the target materials. Thus, my results provide a rough guideline for detectability where these caveats need to be considered.

5.0 Application to rover data

5.1 Application to CheMin data

Because of the strong similarities between my Terra instrument and CheMin, the data I collected facilitates interpretation of CheMin data without necessarily performing FULLPAT or Rietveld analysis. There is precedent for using these commercial breadboards for building usable databases and interpreting CheMin data. For example, Blake et al. (**2012**) stated:

"Several Terra® instruments (a commercial spinoff instrument of CheMin, manufactured by inXitu, Inc., Campbell, CA) are in use at Ames Research Center, Jet Propulsion Laboratory, Los Alamos National Laboratory, Johnson Space Center and Goddard Space Flight Center. They are battery-operated, field-portable instruments designed with enough fidelity to the CheMin FM to allow practical evaluation of how the CheMin design functions in field situations and for the development of XRD libraries. The Terra® instrument at GSFC is being used for direct comparisons of mineral and rock analyses between SAM and CheMin testbeds. The Terra instrument at JSC is likewise being used for direct comparisons of mineral and rock analyses between CheMin and the ChemCam testbed at LANL."

To demonstrate the accuracy of the calibration curves here to detect and discriminate carboxylates, I have compared analyses of recent CheMin data that have detected siderite with the application of my mixtures series with siderite. **Figure 12a** demonstrates the °2-theta Co-Kα accuracy of my Terra instrument, showing a normalized plot of quartz powder measured by the Terra in comparison with the quartz:beryl standard carried on CheMin. For all of my analyses, I used Kapton windows; **Figure 12b** shows the diffraction patterns for both Kapton and mylar windows, both of which were used for CheMin analyses (**Table 7**). These can be used to eliminate false detections of minerals at regions of °2-theta Co-Kα where these materials can contribute to diffraction.

Archer et al. (**2020**) demonstrated a potential detection of siderite in the Kilmarie and Glen Etive 1 samples near the stated CheMin LOD of 1.0 wt.%. Thorpe et al. (**2022**) showed siderite and/or ankerite detections in several samples by CheMin; concentrations in the bulk material materials to be 0.8 ± 0.9 wt. % for Glen Etive 1, 2.2 ± 1 wt. % for Kilmarie, 1.4 ± 0.9 wt. % for Mary Anning, 1.1 ± 1.7 wt. % for Mary Anning 3, and 3.2 ± 2.6 wt. % for Groken. **Table 8** shows a comparison of my application of the calibration curves derived from my mixtures to the results presented by Thorpe et al. (**2022**). I find that my determined concentrations of siderite for these samples closely match those determined by Thorpe et al. (**2022**), all within error. Here, I used the error derived in my siderite mixtures from propagating errors, described in **Section 3.5**. The estimated siderite concentrations display a difference from the CheMin values of only 0.16, 0.30, 0.26, and 1.84 wt.% for the Kilmarie, Mary Anning 3, Glen Etive 1, and Groken samples, respectively. The Groken and Mary Anning 3 samples were suggested to contain concentrations of ankerite, but the tabulated values were not separated from siderite, my measurements are therefore likely closer than the difference of 1.84 wt.% for the relative siderite concentrations for Groken. Thus, for all samples, my analyses are within an average of roughly 0.50-1.00 wt.% of the derived values from the FULLPAT analyses outlined in previous work. This may demonstrate the robustness of the FULLPAT methods used for determining concentrations of minor phases in bulk samples on Mars with CheMin data and the applicability of my method for analyzing isolated peaks with the same data. The likelihood that both methods correctly determine the same compositions rests on both methods using Bragg reflection strength underpinning the concentration estimations.

This indicates that my simple continuum-removal method for determining the peak amplitudes and calibration cures for estimating LODs of the carboxylates can be applied to CheMin data to quickly identify potential identifications of other carboxylates. The CheMin files I used are listed in **Table 7**, and span data collected from sol 77 to sol 2921. The quantified mineral abundances for the crystalline component of each sample are listed in **Table 9**. **Figures 13a to 13i** show the CheMin data analyzed in comparison with the JSC Mars-1a sample, after normalization to reduce instrument effects. I have also listed major peak positions in °2-theta Co-Kα for these minerals, and have identified which overlap with the major peaks for the carboxylates studied here (**Table 10**). To identify potential detections, I processed the CheMin files with the simple linear regression parameters listed in **Table 4**, and computed concentrations. Carboxylate peaks that overlapped with the minerals listed in **Table 10** were eliminated, as were those that overlapped with secondary and minor peaks not identified in that table. I also eliminated peak analysis where the determined concentrations were significantly below the LODs determined in this study for the respective carboxylate. My results are listed in **Table 11**, which show that for the majority of the samples analyzed by CheMin, carbonates, oxalates, and acetates are either not present or below the LODs determined in this study.

Figures 14a to 14d show diffraction patterns where most detections and false detections occurred. Here, the only carboxylates that produced detections or false detections were siderite, magnesite, whewellite, and calcium acetate monohydrate. **Figure 14b** clearly shows the siderite diffraction peaks are observable above noise. In addition to the samples identified as siderite-bearing by Thorpe et al. **(2022**), my analyses also indicate that Aberlady and Greenhorn samples exhibit siderite concentrations at 2.11 and 0.68 wt.%, respectively, which are near or above the LOD. Very weak peaks that are below or near the noise floor that are consistent with whewellite are observable in the Rocknest diffraction patterns (**Figure 14a**). A number of other samples also show possible evidence for this weak peak: Ogunquit Beach, John Klein, Cumberland, Windjaana, Confidence Hill, Mojave, Telegraph Peak, Glen Etive, Glasgow, Mary Anning 3, Kilmarie, and Big Sky. The major peak for calcium acetate monohydrate overlaps with the broad amorphous phyllosilicate peaks near 10° 2-theta Co-Kα in many samples (**Figure 14c**), which produced a number of false detections.

If the peak in the Rocknest material is due to whewellite, it would indicate an average of 1.22 wt.%, which is close to the oxalate value of 1.10 wt.% determined by Lewis et al. (**2021**) with SAM data. Complicating this identification is a variable peak position attributed to plagioclase minerals, specifically fit to andesine for the Rocknest material. However, all of the samples measured by both CheMin and SAM contain relative large concentrations of plagioclase, and only about half of these samples show this peak. The average oxalate value determined by SAM on samples that show this peak in CheMin data is 0.74 wt.%, and the average value on samples that do not show this peak is 0.28 wt.%. This may indicate that oxalate is indeed in these samples at higher concentrations and observable by CheMin, but further analyses are needed for confirmation. If the false detections of oxalate and acetate in my analyses did contribute to the XRD patterns, it may indicate that the aeolian materials are enriched in carboxylates, which was the conclusion determined by Lewis et al. (**2021**), who showed that the aeolian materials could have an average concentration of 0.93 and 1.18 wt.% oxalates and acetates, respectfully; while the materials drilled from the lithified sediments could have average concentrations of 0.50 and 0.68 wt. % oxalates and acetates.

However, none of the other samples with suggested oxalate and acetate concentrations near or above the LODs determined in this study were confidently identified in the CheMin data. This could be due to decreased LODs in CheMin data due to the higher noise floor stemming from the lower X-ray flux from the tube in comparison to the Terra. The non-detection could also indicate that the concentrations of oxalate and acetate are closer to the minimum values determined by Lewis et al. (**2021**) which would be below the CheMin LOD for the carboxylates, that other materials are responsible for the CO_2 release in the SAM data, that oxalate and acetate phases may be amorphous, or that other oxalate and acetate minerals that were not studied here or by Lewis et al. (**2021**) are present. As indicated by Applin et al. (**2015**), isomorphous substitution of metals in oxalate minerals can occur; oxalate can also form in double and triple metal and multi-anion minerals that include sulphate and chloride, bioxalate and hydroxide phases, including formation alumino-silicate minerals. Further, the oxidation of organic-bearing clays can form trioxalato-complexes. Due to the presence of perchlorate on the surface, it could be possible for chlorinated carboxylates to form and significantly contribute to SAM data. Most of these materials have not been studied and may contribute to the observed CO_2 released in SAM data ascribed to carboxylates.

5.2 Application to SuperCam data

In general, reflectance spectra are relative measurements and are calibrated to remove instruments effects, which the general exception of systemic noise, spectral resolution, sampling interval, and other discrepancies not accounted for by ratioing. As such, my reflectance spectra can be used to interpret those from the SuperCam IRS instrument. The SuperCam files I used are listed in **Table 12**. These targets, Guillaumes, Garde, and Bellegarde were chosen because they represent the targets that Scheller et al. (**2022**) identified as exhibiting the 340 nm fluorescence feature in the SHERLOC data that could be due to organic materials. I complemented these targets with the data collected by SuperCam on the Penne target, which was shown by Wiens et al. (**2022**) to display NIR carbonate features. The NIR reflectance spectra for these targets are shown in **Figure 15a**, and the normalized reflectance spectra are shown in **Figure 15b**. The spectra show overall reflectance that are not highly different than my JSC Mars-1a or MGS-1 samples in the NIR, thereby facilitating my calibration curves to measure at least order of magnitude accurate concentrations for any potential identification. As can be seen in **Figure 15b**, there does not appear to be any significant absorption near 2260 nm where acetates absorb strongly. The features observed at 2340 nm are indicative of Fe^{3+} phyllosilicates (**Wiens et al., 2022**) rather than formates. There does not appear to be any indication for the presence of oxalates. These samples do appear to show absorption bands that are consistent with an Mg-rich carbonate near 2305 nm. Clave et al. (**2022**) showed that these absorption bands are consistent with carbonates on the magnesite-siderite solid solution. In their analyses, they determine there to be 3.0 to 20.0 vol.% carbonate for the Garde abraded patch at the mm scale, acknowledging the difficulty in accurately determining concentration due to the number of variables that affect the 2300 nm band depth. Continuum-removed reflectance for the samples analyzed here are shown in **Figure 15c**. This shows that for the Guillaume and Bellegard targets, there does not appear to be a significant contribution from carbonates. Normalized continuum-removed reflectance spectra of the Penne target compared with my magnesite spectra are shown in **Figure 15d**. This demonstrates that magnesite is not a perfect match; the center of the absorption band for Penne is shifted to longer wavelengths, thus suggesting the carbonate shifted towards siderite in the solid solution. I applied my calibration curves derived from the calcite spectra collected by Tarnas et al. (**2021**), with the assumption that the same regression parameters could be used for magnesite because they have very similar band depths at the same grain size distribution; **Table 3** shows the 2340 nm band depth percentage for calcite at a <45 µm particle size to be 9.42 and magnesite at 2301 nm to be 10.42. Note that as the mineral progressively moves towards siderite in solution, the band depth would progressively become smaller when all other variables are similar, as the band depth percentage is 4.31 for siderite. The concentrations I produced for these targets are listed in **Table 13**. For the Garde abrasion patch, I show a carbonate concentration of

9.75 wt.% if the particle size fraction was 125-150 µm, and a concentration of 18.74 wt.% if the particle size fraction was 45-75 µm. The concentration would be higher for finer particles. These values are consistent with the 3.0-20.0 vol.% suggested by Clave et al. (**2022**). Further, the Garde cuttings show a lower concentration when assuming the same particle size fraction; 6.12 to 11.48 wt.%. This would be consistent with the carbonate particles becoming finer during abrasion and therefore the sample exhibited a shallower band depth (**Figure 15c**). Due to the large number of variables that affect band depth in intimate mixtures and not knowing the grain size distribution of the carbonates, these represent only an estimated range of carbonate concentration for these samples.

6.0 Summary and conclusions

I have measured a series of intimate mixtures of carboxylates (carbonates, oxalates, acetates, and formats) with Mars analogue materials and collected CheMin-like XRD and reflectance spectra from 350 to 5000 nm. I processed these data to determine LODs of carboxylates and applied these results to some CheMin and SuperCam data in order to determine whether carboxylates were present and at what concentrations.

I found that most of these carboxylate minerals have LODs that hover near 1.0 wt.% with CheMin-like measurements, which is consistent with previous suggestions for CheMin LODs. In particular, carbonate minerals have LODs near 0.60 wt.%, lower than the other minerals studies here. Acetate and formate minerals can be detected at relatively low concentrations at NIR wavelengths due to their strong and sharp absorption bands. Calcium formate exhibited a NIR LOD of 0.04 wt.%, much lower than the other minerals studied here. In contrast, oxalate minerals will not likely be detected by orbiting spectrometers due to their weak absorption bands and likely presence below LODs by reflectance spectroscopy. Anhydrous carbonates minerals have relatively low LODs at NIR wavelengths, which may decrease with increasing grain size. At 3950 nm, relatively low (<<1.0 wt.%) concentrations of carbonates can be detected at all grain sizes. I found that my resulting LOD for calcite at 3950 nm was consistent with the threshold for the detection of carbonate minerals in carbonaceous chondrites at this wavelength.

I found that the XRD calibration curve method detected siderite concentrations within 0.50-1.00 wt.% on average, similar to previous analyses using FULLPAT processing of CheMin data for the Kilamarie, Mary Anning 1, Mary Anning 3, Glen Etive 1, and Groken samples, thus demonstrating robustness for both methods. I further detected siderite in the Aberlady and Greenhorn samples. After processing all of the diffraction patterns available to compare with the SAM results by Lewis et al. (**2021**), I found that there was no strong evidence for the contribution of oxalates, acetate, and formate minerals in CheMin data, with the exception of potentially 1.22 wt.% whewellite in the averaged Rocknest data, and the possibility of a number of other samples showing weak evidence for the same mineral. Plausible scenarios that could explain the absence of carboxylate detection at or near the derived XRD LODs include other materials being responsible for the CO_2 release in the SAM data, that oxalate and acetate phases may be amorphous, or that other oxalate and acetate minerals not included in this study are present. Isomorphous substation of metals in oxalate minerals can occur; oxalate can also form in double and triple metal and multi-anion minerals that include sulphate and chloride, bioxalate and hydroxide phases, including formation of alumino-silicate minerals. Trioxalato and chlorinated carboxylates could potentially form. Most of these materials have not been studied and may contribute to the observed CO_2 released in SAM data ascribed to carboxylates.

Similarly, I looked for the presence of carboxylate minerals in data from SuperCam on samples that were suggested to have the presence of organic materials by Scheller et al. (**2022**). I did not observe any absorption bands that could be associated with oxalates, acetates, and formate minerals. I did observe the ~2300 nm absorption band that has been ascribed to the magnestite-siderite solid solution mineral and found that when my calibration curves are crudely applied, I derived concentrations of roughly 5.0-20.0 wt.%, which are highly dependent on grain size, where the mineral is situated on the solid solution, and the usual radiative transfer matrix effects. These results were consistent with the results by Clave et al. (**2022**), who suggested the absorption band could indicate 3.0 to 20.0 vol.% carbonate.

Thus, my results provide a baseline for the detection, discrimination, and concentration estimation of carboxylate minerals on the surface of Mars with XRD and reflectance spectroscopy instruments. These results can inform processing of data collected by CheMin and future XRD systems in the context of carboxylate detection. As SuperCam continues to operate, these data can be used for organic compounds in combination with SHERLOC data.

7.0 References

Aaron, L. M., Steele, A., Shkolyar, S., Seelos, K., Viviano, C., Applin, D., & Cloutis, E. (2019, March). Detecting Oxalate Minerals on Mars Using CRISM and In-Situ Spectroscopy. In *50th Annual Lunar and Planetary Science Conference* (No. 2132, p. 3125).

Alexander, C. O. D., Bowden, R., Fogel, M. L., & Howard, K. T. (2015). Carbonate abundances and isotopic compositions in chondrites. Meteoritics & Planetary *Science*, 50(4), 810-833.

Ali, A., Chiang, Y. W., & Santos, R. M. (2022). X-ray diffraction techniques for mineral characterization: A review for engineers of the fundamentals, applications, and research directions. *Minerals*, 12(2), 205.

Allen, C. C., Jager, K. M., Morris, R. V., Lindstrom, D. J., Lindstrom, M. M., & Lockwood, J. P. (1998). JSC Mars-1: a Martian soil simulant. *In Space* 98 (pp. 469-476).

Anders, E. (1996). Evaluating the evidence for past life on Mars. *Science*, 274(5295), 2119-2121.

Applin, D. M., Izawa, M. R. M., Cloutis, E. A., Goltz, D., & Johnson, J. R. (2015). Oxalate minerals on Mars?. *Earth and Planetary Science Letters*, *420*, 127-139.

Applin, D. M., Izawa, M. R., & Cloutis, E. A. (2016). Reflectance spectroscopy of oxalate minerals and relevance to Solar System carbon inventories. *Icarus*, *278*, 7-30.

Applin, D. M., & Cloutis, E. A. (2017, March). Spectral Reflectance of Formates, Acetates, and Some Other Carboxylates. *In 48th Annual Lunar and Planetary Science Conference (No. 1964, p. 2073).*

Applin, D. M., Izawa, M. R., Cloutis, E. A., Gillis-Davis, J. J., Pitman, K. M., Roush, T. L., ... & Lucey, P. G. (2018). Ultraviolet spectral reflectance of carbonaceous materials. *Icarus, 307*, 40-82.

Archer, P. D., Rampe, E. B., Clark, J. V., Tu, V., Sutter, B., Vaniman, D., ... & Yen, A. S. (2020, March). Detection of siderite (FeCO3) in glen torridon samples by the Mars science laboratory rover. In *Lunar and Planetary Science Conference* (No. JSC-E-DAA-TN78281).

Baird, A. K., Toulmin III, P., Clark, B. C., Rose Jr, H. J., Keil, K., Christian, R. P., & Gooding, J. L. (1976). Mineralogic and petrologic implications of Viking geochemical results from Mars: Interim report. *Science*, 194(4271), 1288-1293.

Bandfield, J. L., Glotch, T. D., & Christensen, P. R. (2003). Spectroscopic identification of carbonate minerals in the Martian dust. *Science*, 301(5636), 1084-1087.

Banin, A., and J. Rishpon. (1989). "Smectite clays in Mars soil: Evidence for their presence and role in Viking biology experimental results." *Journal of Molecular Evolution* 14: 133-152.

Beck, P., Barrat, J. A., Gillet, P., Wadhwa, M., Franchi, I. A., Greenwood, R. C., ... & Reynard, B. (2006). Petrography and geochemistry of the chassignite Northwest Africa 2737 (NWA 2737). *Geochimica et Cosmochimica Acta*, 70(8), 2127-2139.

Beck, P., Maturilli, A., Garenne, A., Vernazza, P., Helbert, J., Quirico, E., & Schmitt, B. (2018). What is controlling the reflectance spectra (0.35–150 µm) of hydrated (and dehydrated) carbonaceous chondrites?. *Icarus*, 313, 124-138.

Becker, L., Popp, B., Rust, T., & Bada, J. L. (1999). The origin of organic matter in the Martian meteorite ALH84001. *Advances in Space Research*, 24(4), 477-488.

Bell III, J. F., Morris, R. V., & Adams, J. B. (1993). Thermally altered palagonitic tephra: A spectral and process analog to the soil and dust of Mars. *Journal of Geophysical Research: Planets*, 98(E2), 3373-3385.

Bell, R. J., Alexander Jr, R. W., Long, L. L., Ordal, M. A., Paul, R., & Peacher, J. (1985). The Optical Constants of Smoke Materials (Naturally Occurring Minerals) Plus Iron and Graphite in the Millimeter and Submillimeter. *Missouri University Department of Physics*.

Benner, S. A., Devine, K. G., Matveeva, L. N., & Powell, D. H. (2000). The missing organic molecules on Mars. *Proceedings of the National Academy of Sciences*, *97*(6), 2425-2430.

Bevington, P. R., & Reduction, D. (1969). Error Analysis for the Physical Sciences. *Editorial McGraw-Hill*.

Biemann, K., & Lavoie Jr, J. M. (1979). Some final conclusions and supporting experiments related to the search for organic compounds on the surface of Mars. *Journal of Geophysical Research: Solid Earth*, *84*(B14), 8385-8390.

Biemann, K. (2007). On the ability of the Viking gas chromatograph–mass spectrometer to detect organic matter. *Proceedings of the National Academy of Sciences*, *104*(25), 10310-10313.

Bish, D. L., Blake, D. F., Vaniman, D. T., Chipera, S. J., Morris, R. V., Ming, D. W., ... & Gaboriaud, A. (2013). X-ray diffraction results from Mars Science Laboratory: Mineralogy of Rocknest at Gale crater. *Science*, *341*(6153), 1238932.

Bishop, J. L., Perry, K. A., Darby Dyar, M., Bristow, T. F., Blake, D. F., Brown, A. J., & Peel, S. E. (2013). Coordinated spectral and XRD analyses of magnesite-nontronite-forsterite mixtures and implications for carbonates on Mars. *Journal of Geophysical Research: Planets*, 118(4), 635-650.

Bishop, J. L., Bell III, J. F., & Moersch, J. E. (Eds.). (2019). *Remote compositional analysis: Techniques for understanding spectroscopy, mineralogy, and geochemistry of planetary surfaces* (Vol. 24). Cambridge University Press.

Bishop, J. L., King, S. J., Lane, M. D., Brown, A. J., Lafuente, B., Hiroi, T., ... & Sánchez Román, M. (2021). Spectral properties of anhydrous carbonates and nitrates. *Earth and Space Science*, 8(10), e2021EA001844.

Blake, D. F., Vaniman, D. T., Anderson, R., Bish, D., Chipera, S., Chemtob, S., ... & Yen, A. (2009, March). The CheMin mineralogical instrument on the Mars Science Laboratory mission. *In 40th Annual Lunar and Planetary Science Conference (p. 1484).*

Blake, D., Vaniman, D., Achilles, C., Anderson, R., Bish, D., Bristow, T., ... & Yen, A. (2012). Characterization and calibration of the CheMin mineralogical instrument on Mars Science Laboratory. *Space Science Reviews, 170*(1), 341-399.

Blake, T. A., Brauer, C. S., Kelly-Gorham, M. R., Burton, S. D., Bliss, M., Myers, T. L., ... & Tiwald, T. E. (2017, May). Measurement of optical constants for spectral modeling: n and k values for ammonium sulfate via single-angle and ellipsometric methods. In Algorithms and Technologies for Multispectral, Hyperspectral, and Ultraspectral Imagery XXIII (Vol. 10198, p. 101980J*). International Society for Optics and Photonics.*

Blaney, D. L., & McCord, T. B. (1989). An observational search for carbonates on Mars. *Journal of Geophysical Research: Solid Earth*, 94(B8), 10159-10166.

Bohren, C. F., & Huffman, D. R. (1983). Absorption and scattering of light by small particles. John Wiley & Sons.

Bridges, J. C., & Grady, M. M. (2000). Evaporite mineral assemblages in the nakhlite (martian) meteorites. Earth and Planetary Science Letters, 176(3-4), 267-279.

Brown, G.E., Prewitt, C.T. "High-temperature crystal chemistry of hortonolite". *Am. Mineral*. 1973, 58, 577.

Brown, A. J., Hook, S. J., Baldridge, A. M., Crowley, J. K., Bridges, N. T., Thomson, B. J., ... & Bishop, J. L. (2010). Hydrothermal formation of clay-carbonate alteration assemblages in the Nili Fossae region of Mars. *Earth and Planetary Science Letters*, 297(1-2), 174-182.

Boynton, W. V., Ming, D. W., Kounaves, S. P., Young, S. M. M., Arvidson, R. E., Hecht, M. H., ... & Morris, R. V. (2009). Evidence for calcium carbonate at the Mars Phoenix landing site. *Science*, *325*(5936), 61-64.

Bunaciu, A. A., UdriŞTioiu, E. G., & Aboul-Enein, H. Y. (2015). X-ray diffraction: instrumentation and applications. *Critical reviews in analytical chemistry*, 45(4), 289-299.

Bushuev, N., Borisov. (1982). *Russ. J. Inorg. Chem. (Engl. Transl.).*, 27, 341.

Cahill, J. T., & Lucey, P. G. (2007). Radiative transfer modeling of lunar highlands spectral classes and relationship to lunar samples. *Journal of Geophysical Research: Planets, 112*(E10).

Cahill, J. T. S., Lucey, P. G., & Wieczorek, M. A. (2009). Compositional variations of the lunar crust: Results from radiative transfer modeling of central peak spectra. *Journal of Geophysical Research: Planets*, *114*(E9).

Cahill, J. T., Blewett, D. T., Nguyen, N. V., Xu, K., Kirillov, O. A., Lawrence, S. J., ... & Coman, E. I. (2012). Determination of iron metal optical constants: Implications for ultraviolet, visible, and near-infrared remote sensing of airless bodies. *Geophysical research letters*, *39*(10).

Cahill, J. T., Blewett, D. T., Nguyen, N. V., Boosalis, A., Lawrence, S. J., & Denevi, B. W. (2019). Optical constants of iron and nickel metal and an assessment of their relative influences on silicate mixture spectra from the FUV to the NIR. *Icarus*, *317*, 229-241.

Calvin, W. M. (1990). Additions and corrections to the absorption coefficients of CO2 ice: Applications to the Martian south polar cap. *Journal of Geophysical Research: Solid Earth*, *95*(B9), 14743-14750.

Calvin, W. M., King, T. V., & Clark, R. N. (1994). Hydrous carbonates on Mars?: Evidence from Mariner 6/7 infrared spectrometer and ground-based telescopic spectra. *Journal of Geophysical Research: Planets*, 99(E7), 14659-14675.

Campbell, J., Sidiropoulos, P., & Muller, J. P. (2016, March). The Search for Polycyclic Aromatic Hydrocarbons in the Martian South Polar Residual Cap Using CRISM Infrared Spectra. In *47th Annual Lunar and Planetary Science Conference* (No. 1903, p. 2110).

Cannon, K. M., Britt, D. T., Smith, T. M., Fritsche, R. F., & Batcheldor, D. (2019). Mars global simulant MGS-1: A Rocknest-based open standard for basaltic martian regolith simulants. *Icarus*, *317*, 470-478.

Carli, C., Roush, T. L., Pedrazzi, G., & Capaccioni, F. (2016). Visible and Near-Infrared (VNIR) reflectance spectroscopy of glassy igneous material: Spectral variation, retrieving optical constants and particle sizes by Hapke model. *Icarus*, 266, 267-278.

Carpenter, P., Sebille, L., Boles, W., Chadwell, M., & Schwarz, L. (2003). JSC Mars-1 martian soil simulant: Melting experiments and electron microprobe studies. *Microscopy and Microanalysis*, 9(S02), 30-31.

Carrillo-Sánchez, J. D., Gómez-Martín, J. C., Bones, D. L., Nesvorný, D., Pokorný, P., Benna, M., ... & Plane, J. M. (2020). Cosmic dust fluxes in the atmospheres of Earth, Mars, and Venus. Icarus, 335, 113395.

Chandrasekhar, S. (1960). *Radiative transfer*. Courier Corporation.

Chipera, S. J., & Bish, D. L. (2002). FULLPAT: a full-pattern quantitative analysis program for X-ray powder diffraction using measured and calculated patterns. *Journal of Applied Crystallography*, *35*(6), 744-749.

Christensen, P. R., Ruff, S. W., Fergason, R. L., Knudson, A. T., Anwar, S., Arvidson, R. E., ... & Wyatt, M. B. (2004). Initial results from the Mini-TES experiment in Gusev Crater from the Spirit Rover. *Science*, 305(5685), 837-842.

Chun, S. F., Pang, K. D., Cutts, J. A., & AJELLO, J. M. (1978). Photocatalytic oxidation of organic compounds on Mars. *Nature*, *274*(5674), 875-876.

Chukanov, N. V. (1999). Formicaite Ca (HCO_2) _2, a new mineral. *Zap. Vseross. Mineral. Obshch.*, 128, 43-47.

Chukanov, N. V. (2000). Dashkovaite Mg (HCO_3) _2 2H_2O-A new formate mineral. *Zap. Vseross. Mineral. Obshch.*, 129, 49-53.

Clark, R. N., & Roush, T. L. (1984). Reflectance spectroscopy: Quantitative analysis techniques for remote sensing applications. *Journal of Geophysical Research: Solid Earth*, *89*(B7), 6329-6340.

Clark, R. N. (1999). Spectroscopy of rocks and minerals, and principles of spectroscopy. In: Rencz, A.N., Ed., *Manual of Remote Sensing, Volume 3, Remote Sensing for the Earth Sciences*, John Wiley and Sons, New York, 3-58.

Clark, R. N., Curchin, J. M., Hoefen, T. M., & Swayze, G. A. (2009). Reflectance spectroscopy of organic compounds: 1. Alkanes. *Journal of Geophysical Research: Planets*, 114(E3).

Clavé, E., Benzerara, K., Meslin, P. Y., Forni, O., Royer, C., Mandon, L., ... & SuperCam team. (2023). Carbonate detection with SuperCam in igneous rocks on the floor of Jezero Crater, Mars. *Journal of Geophysical Research: Planets*, 128(6), e2022JE007463.

Cloutis, E. A., Gaffey, M. J., Jackowski, T. L., & Reed, K. L. (1986). Calibrations of phase abundance, composition, and particle size distribution for olivine-orthopyroxene mixtures from reflectance spectra. *Journal of Geophysical Research: Solid Earth, 91*(B11), 11641-11653.

Cloutis, E. A., Sunshine, J. M., & Morris, R. V. (2004). Spectral reflectance-compositional properties of spinels and chromites: Implications for planetary remote sensing and geothermometry. *Meteoritics & Planetary Science*, 39(4), 545-565.

Chung, F. H. (1975). Quantitative interpretation of X-ray diffraction patterns of mixtures.

III. Simultaneous determination of a set of reference intensities. *Journal of Applied Crystallography*, 8(1), 17-19.

Corley, J. (2003). Best practices in establishing detection and quantification limits for pesticide residues in foods. *Handbook of residue analytical methods for agrochemicals*, 1, 0471491942-4.

Crowley, J. K. (1986). Visible and near-infrared spectra of carbonate rocks: Reflectance variations related to petrographic texture and impurities. *Journal of Geophysical Research: Solid Earth*, 91(B5), 5001-5012.

Cruikshank, D. P., Dalle Ore, C. M., Roush, T. L., Geballe, T. R., Owen, T. C., de Bergh, C., ... & Hartmann, W. K. (2001). Constraints on the composition of Trojan asteroid 624 Hektor. *Icarus*, *153*(2), 348-360.

Cruikshank, D. P., Imanaka, H., & Dalle Ore, C. M. (2005). Tholins as coloring agents on outer Solar System bodies. *Advances in Space Research*, *36*(2), 178-183.

Cullity, B. D. (1956). Elements of X-ray Diffraction. Addison-Wesley Publishing.

Dalton III, J. B., & Pitman, K. M. (2012). Low temperature optical constants of some hydrated sulfates relevant to planetary surfaces. *Journal of Geophysical Research: Planets*, *117*(E9).

Davis, B. L. (1987). The estimation of limits of detection in RIM quantitative X-ray diffraction analysis. *Advances in X-Ray Analysis*, 31, 317-323.

Denevi, B. W., Lucey, P. G., Hochberg, E. J., & Steutel, D. (2007). Near-infrared optical constants of pyroxene as a function of iron and calcium content. *Journal of Geophysical Research: Planets*, *112*(E5).

Denevi, B. W., Lucey, P. G., & Sherman, S. B. (2008). Radiative transfer modeling of near-infrared spectra of lunar mare soils: Theory and measurement. *Journal of Geophysical Research: Planets*, *113*(E2).

de Wolff, P., (1959). Technisch Physische Dienst, Delft Netherlands. ICDD Grant-in-Aid.

de Wolff, P., (1957). Technisch Physische Dienst, Delft, The Netherlands. ICDD Grant-in-Aid.

Döbelin, N. (2020). Validation of XRD phase quantification using semi-synthetic data. *Powder Diffraction*, 35(4), 262-275.

Donnay, Donnay. (1952). *Am. J. Sci. Bowen.*, 115.

Dufresne, W. J., Rufledt, C. J., & Marshall, C. P. (2018). Raman spectroscopy of the eight natural carbonate minerals of calcite structure. *Journal of Raman Spectroscopy*, 49(12), 1999-2007.

Eggleton, R. A., Foudoulis, C., & Varkevisser, D. (1987). Weathering of basalt: changes in rock chemistry and mineralogy. *Clays and Clay Minerals*, *35*(3), 161-169.

Ehlmann, B. L., Mustard, J. F., Murchie, S. L., Poulet, F., Bishop, J. L., Brown, A. J., ... & Wray, J. J. (2008). Orbital identification of carbonate-bearing rocks on Mars. *Science*, 322(5909), 1828-1832.

Eigenbrode, J. L., Summons, R. E., Steele, A., Freissinet, C., Millan, M., Navarro-González, R., ... & Coll, P. (2018). Organic matter preserved in 3-billion-year-old mudstones at Gale crater, Mars. *Science*, *360*(6393), 1096-1101.

Environmental Protection Agency. 1984. Definition and Procedure for the Determination of the Method Detection Limit, Revision 1.11. Federal Register, 49, 43430.

Esposito, F., Colangeli, L., & Palomba, E. (2000). Infrared reflectance spectroscopy of Martian analogues. *Journal of Geophysical Research: Planets*, *105*(E7), 17643-17654.

Evans, D. L., & Adams, J. B. (1979). Comparison of Viking Lander multispectral images and laboratory reflectance spectra of terrestrial samples. In In: Lunar and Planetary Science Conference, 10th, Houston, Tex., March 19-23, 1979, Proceedings. Volume 2.(A80-23617 08-91) New York, Pergamon Press, Inc., 1979, p. 1829-1834. (Vol. 10, pp. 1829-1834).

Flynn, G. J., & McKay, D. S. (1990). An assessment of the meteoritic contribution to the Martian soil. *Journal of Geophysical Research: Solid Earth*, 95(B9), 14497-14509.

Flynn, G. J. (1996). The delivery of organic matter from asteroids and comets to the early surface of Mars. *Earth, Moon, and Planets*, 72(1-3), 469-474.

Fouchet, T., Reess, J. M., Montmessin, F., Hassen-Khodja, R., Nguyen-Tuong, N., Humeau, O., ... & Wiens, R. C. (2022). The SuperCam infrared spectrometer for the perseverance rover of the Mars2020 mission. *Icarus*, 373, 114773.

Franz, H. B., Mahaffy, P. R., Webster, C. R., Flesch, G. J., Raaen, E., Freissinet, C., ... & Summons, R. E. (2020). Indigenous and exogenous organics and surface–atmosphere cycling inferred from carbon and oxygen isotopes at Gale crater. *Nature Astronomy*, 4(5), 526-532.

Freissinet, C., Glavin, D. P., Mahaffy, P. R., Miller, K. E., Eigenbrode, J. L., Summons,

R. E., ... & MSL Science Team. (2015). Organic molecules in the sheepbed mudstone, gale crater, mars. *Journal of Geophysical Research: Planets*, *120*(3), 495-514.

Fries, M., Cintala, M., Steele, A., & Welzenbach, L. C. (2017, March). Dust Infall Onto Phobos and Deimos Can Explain Their Carbonaceous Reflectance Signature, Perhaps Overlying a Mars-Impact-Origin Core: A Hypothesis. In *Lunar and Planetary Science Conference* (No. JSC-CN-38696).

Fries, M., Ashley, J., Beegle, L., Bhartia, R., Bland, P., Burton, A., ... & Zolensky, M. (2021a). The Scientific Need for a Dedicated Interplanetary Dust Instrument at Mars. *Bulletin of the American Astronomical Society*, *53*(4), 097.

Fries, M. (2021b). A review of the meteor shower hypothesis for methane on Mars. *Mars Geological Enigmas*, 175-203.

Fujiwara, H. (2007). Spectroscopic ellipsometry: principles and applications. John Wiley & Sons.

Gaffey, S. J. (1985). Reflectance spectroscopy in the visible and near-infrared (0.35–2.55 µm): Applications in carbonate petrology. *Geology*, 13(4), 270-273.

Gaffey, S. J. (1986). Spectral reflectance of carbonate minerals in the visible and near infrared (0.35-2.55 microns); calcite, aragonite, and dolomite. *American Mineralogist*, 71(1-2), 151-162.

Gaffey, S. J. (1987). Spectral reflectance of carbonate minerals in the visible and near infrared (0.35–2.55 um): Anhydrous carbonate minerals. *Journal of Geophysical Research: Solid Earth*, 92(B2), 1429-1440.

Gaffey, M. J., Bell, J. F., Brown, R. H., Burbine, T. H., Piatek, J. L., Reed, K. L., &

Chaky, D. A. (1993). Mineralogical variations within the S-type asteroid class. *Icarus*, *106*(2), 573-602.

Glotch, T. D., Rossman, G. R., & Aharonson, O. (2007). Mid-infrared (5–100 μm) reflectance spectra and optical constants of ten phyllosilicate minerals. *Icarus*, *192*(2), 605-622.

Glotch, Timothy D., and George R. Rossman. "Mid-infrared reflectance spectra and optical constants of six iron oxide/oxyhydroxide phases." *Icarus* 204.2 (2009): 663-671.

Gooding, J. L., Wentworth, S. J., & Zolensky, M. E. (1988). Calcium carbonate and sulfate of possible extraterrestrial origin in the EETA 79001 meteorite. *Geochimica et Cosmochimica Acta*, 52(4), 909-915.

Goody, R. (1964). The transmission of radiation through an inhomogeneous atmosphere. *Journal of Atmospheric Sciences*, *21*(6), 575-581.

Grady, M. M., Verchovsky, A. B., & Wright, I. P. (2004). Magmatic carbon in Martian meteorites: attempts to constrain the carbon cycle on Mars. *International Journal of Astrobiology*, *3*(2), 117-124.

Guideline, I. H. T. (2005). Validation of analytical procedures: text and methodology. *Q2 (R1)*, *1*(20), 05.

Hale, George M., and Marvin R. Querry. "Optical constants of water in the 200-nm to 200-μm wavelength region." *Applied optics* 12.3 (1973): 555-563.

Hanchar, J. M., Nagy, K. L., Fenter, P., Finch, R. J., Beno, D. J., & Sturchio, N. C. (2000). Quantification of minor phases in growth kinetics experiments with powder X-ray diffraction. *American Mineralogist*, 85(9), 1217-1222.

Hapke, B. (1981). Bidirectional reflectance spectroscopy: 1. Theory. *Journal of Geophysical Research: Solid Earth*, *86*(B4), 3039-3054.

Hapke, B. (1986). Bidirectional reflectance spectroscopy: 4. The extinction coefficient and the opposition effect. *Icarus*, *67*(2), 264-280.

Hapke, B. W., Nelson, R. M., & Smythe, W. D. (1993). The opposition effect of the moon: the contribution of coherent backscatter. *Science*, 260(5107), 509-511.

Hapke, B. (2012). *Theory of reflectance and emittance spectroscopy*. Cambridge university press.

Hibbs, D. E., Kolitsch, U., Leverett, P., Sharpe, J. L., & Williams, P. A. (2002). Hoganite and paceite, two new acetate minerals from the Potosi mine, Broken Hill, Australia. *Mineralogical magazine,* 66(3), 459-464.

Hillier, S. (1999). Quantitative analysis of clay and other minerals in sandstones by X-ray powder diffraction (XRPD). *Clay mineral cements in sandstones*, 213-251.

Hillier, S. (2000). Accurate quantitative analysis of clay and other minerals in sandstones by XRD: comparison of a Rietveld and a reference intensity ratio (RIR) method and the importance of sample preparation. *Clay minerals*, 35(1), 291-302.

Hiroi, T., & Pieters, C. M. (1992). Effects of grain size and shape in modeling reflectance spectra of mineral mixtures. In *Lunar and Planetary Science Conference Proceedings* (Vol. 22, pp. 313-325).

Hiroi, T., & Pieters, C. M. (1994). Estimation of grain sizes and mixing ratios of fine powder mixtures of common geologic minerals. *Journal of Geophysical Research: Planets, 99*(E5), 10867-10879.

Hollis, J. R., Moore, K. R., Sharma, S., Beegle, L., Grotzinger, J. P., Allwood, A., ... &

Yanchilina, A. (2022). The power of paired proximity science observations: Co-located data from SHERLOC and PIXL on Mars. *Icarus*, 387, 115179.

Horgan, B. H., Anderson, R. B., Dromart, G., Amador, E. S., & Rice, M. S. (2020). The mineral diversity of Jezero crater: Evidence for possible lacustrine carbonates on Mars. *Icarus*, 339, 113526.

Hubbard, J. S. (1979). Laboratory simulations of the pyrolytic release experiments: An interim report. *Journal of Molecular Evolution*, 14, 211-221.

Hunt and Salisbury, 1971; Visible and near-infrared spectra of minerals and rocks: II. Carbonates: *Modern Geology*, v. 2, p. 23-30.

Irvine, W. M., & Pollack, J. B. (1968). Infrared optical properties of water and ice spheres. *Icarus*, *8*(1-3), 324-360.

IUPAC. (1978). “Nomenclature, symbols, units and their usage in spectrochemical analysis— II, *Spectrochim. Acta B.*,33B, 242.

Izawa, M. R. M., Applin, D. M., Norman, L., & Cloutis, E. A. (2014). Reflectance spectroscopy (350–2500 nm) of solid-state polycyclic aromatic hydrocarbons (PAHs). *Icarus*, 237, 159-181.

Kaplan, H. H., & Milliken, R. E. (2016). Reflectance spectroscopy for organic detection and quantification in clay-bearing samples: Effects of albedo, clay type, and water content. Clays and Clay Minerals, 64(2), 167-184.

Kaplan, H. H., & Milliken, R. E. (2018). Reflectance spectroscopy of organic matter in sedimentary rocks at mid-infrared wavelengths. *Clays and Clay Minerals*, 66(2), 173-189.

Kaplan, H. H., Milliken, R. E., Alexander, C. M. O. D., & Herd, C. D. (2019).

Reflectance spectroscopy of insoluble organic matter (IOM) and carbonaceous meteorites. *Meteoritics & Planetary Science*, 54(5), 1051-1068.

Kaufmann, E., & Hagermann, A. (2017). Experimental investigation of insolation-driven dust ejection from Mars' CO2 ice caps. *Icarus*, 282, 118-126.

Keller, l., McCarthy, G. (1985). North Dakota State University, Fargo, Nd, USA ICDD grant-in-aid.

Kim, W., Suh, C. Y., Cho, S. W., Roh, K. M., Kwon, H., Song, K., & Shon, I. J. (2012). A new method for the identification and quantification of magnetite–maghemite mixture using conventional X-ray diffraction technique. *Talanta*, 94, 348-352.

Kitamura, R., Pilon, L., & Jonasz, M. (2007). Optical constants of silica glass from extreme ultraviolet to far infrared at near room temperature. *Applied optics*, *46*(33), 8118-8133.

Koike, C., Hasegawa, H., Asada, N., & Komatuzaki, T. (1989). Optical constants of fine particles for the infrared region. *Monthly Notices of the Royal Astronomical Society*, *239*(1), 127-137.

Kontoyannis, C. G., & Vagenas, N. V. (2000). Calcium carbonate phase analysis using XRD and FT-Raman spectroscopy. *Analyst*, 125(2), 251-255.

Lane, M. D. (1999). Midinfrared optical constants of calcite and their relationship to particle size effects in thermal emission spectra of granular calcite. *Journal of Geophysical Research: Planets*, *104*(E6), 14099-14108

Lawrence, S. J., & Lucey, P. G. (2007). Radiative transfer mixing models of meteoritic assemblages. *Journal of Geophysical Research: Planets*, *112*(E7).

Kern, A., Eysel, W.. (1993). Mineralogisch-Petrograph. Inst., Univ. Heidelberg, Germany. ICDD Grant-in-Aid.

Lellouch, E., Encrenaz, T., de Graauw, T., Erard, S., Morris, P., Crovisier, J., ... & Burgdorf, M. (2000). The 2.4–45µm spectrum of Mars observed with the infrared space observatory. *Planetary and Space Science*, 48(12-14), 1393-1405.

LeRoux, J., Lennox, D. H., & Kay, K. (1953). Direct quantitative X-ray analysis by diffraction-absorption technique. *Analytical Chemistry*, 25(5), 740-743.

Lewis, J. M. T., Eigenbrode, J. L., Wong, G. M., McAdam, A. C., Archer, P. D., Sutter, B., ... & Mahaffy, P. R. (2021). Pyrolysis of oxalate, acetate, and perchlorate mixtures and the implications for organic salts on Mars. *Journal of Geophysical Research: Planets*, *126*(4), e2020JE006803.

Lucarini, V., Saarinen, J. J., Peiponen, K. E., & Vartiainen, E. M. (2005). *Kramers-Kronig relations in optical materials research* (Vol. 110). Springer Science & Business Media.

Lucey, P. G. (1998). Model near-infrared optical constants of olivine and pyroxene as a function of iron content. *Journal of Geophysical Research: Planets*, *103*(E1), 1703-1713.

Long, G. L., & Winefordner, J. D. (1983). Limit of detection. A closer look at the IUPAC definition. *Analytical chemistry*, 55(7), 712A-724A.

Lorenz, S., Beyer, J., Fuchs, M., Seidel, P., Turner, D., Heitmann, J., & Gloaguen, R. (2018). The potential of reflectance and laser induced luminescence spectroscopy for near-field rare earth element detection in mineral exploration. *Remote Sensing*, 11(1), 21.

Lyman, C.E., Newbury, D.E., Goldstein, J.I., D.B. Williams, A.D. Romig Jr., J. Armstrong, P. Echlin, C. Fiori, D.C. Joy, E. Lifshin, and Peters, K-R. (1990) *Scanning Electron Microscopy, X-Ray Microanalysis, and Analytical Electron Microscopy: A Laboratory Workbook*, 420 p. Plenum Press, New York

Lucey, P. G. (2004). Mineral maps of the Moon. *Geophysical Research Letters, 31*(8).

Lucey, P. G., Trang, D., Johnson, J. R., & Glotch, T. D. (2018). Derivation of optical constants for nanophase hematite and application to modeled abundances from in-situ Martian reflectance spectra. *Icarus*, *300*, 167-173.

Lyon, R. J. P. (1964). Evaluation of infrared spectrophotometry for compositional analysis of lunar and planetary soils. *part ii-rough and powdered surfaces* (No. NASA-CR-100).

Marra, A. C., Politi, R., Blanco, A., Brunetto, R., Fonti, S., Marzo, G. A., & Orofino, V. (2006). Optical constants of particulate minerals from reflectance measurements: The case of calcite. *Journal of Quantitative Spectroscopy and Radiative Transfer, 100*(1-3), 250-255.

Marzo, G. A., Blanco, A., De Carlo, F., D'Elia, M., Fonti, S., Marra, A. C., ... & Politi, R. (2004). The optical constants of gypsum particles as analog of Martian sulfates. *Advances in Space Research*, *33*(12), 2246-2251.

McAdam, A. C., Sutter, B., Archer, P. D., Franz, H. B., Wong, G. M., Lewis, J. M., ... & Johnson, S. S. (2020). Constraints on the mineralogy and geochemistry of Vera Rubin ridge, Gale crater, Mars, from Mars Science Laboratory Sample Analysis at Mars evolved gas analyses. *Journal of Geophysical Research: Planets*, 125(11), e2019JE006309.

McAdam, A. C., Sutter, B., Archer, P. D., Franz, H. B., Wong, G. M., Lewis, J. M. T., ... & Malespin, C. A. (2022). Evolved gas analyses of sedimentary rocks from the Glen Torridon clay-bearing unit, Gale crater, Mars: Results from the Mars Science Laboratory Sample Analysis at Mars instrument suite. *Journal of Geophysical Research: Planets*, 127(9), e2022JE007179.

McCubbin, F. M., Elardo, S. M., Shearer Jr, C. K., Smirnov, A., Hauri, E. H., & Draper, D. S. (2013). A petrogenetic model for the comagmatic origin of chassignites and nakhlites: Inferences from chlorine-rich minerals, petrology, and geochemistry. *Meteoritics & Planetary Science*, 48(5), 819-853.

McMurdie, H., Morris, M., Evans, E., Paretzkin, B., Wong-Ng, W., Hubbard, C. *(1986). Powder Diffr*., 1, 267.

Mittlefehldt, D. W. (1994). ALH84001, a cumulate orthopyroxenite member of the Martian meteorite clan. *Meteoritics*, 29(2), 214-221.

Mooney, T., & Knacke, R. F. (1985). Optical constants of chlorite and serpentine between 2.5 and 50 µm. *Icarus*, 64(3), 493-502.

Morimoto, N., Gueven, N. "Refinement of the crystal structure of pigeonite". *Am. Mineral*. 1970, 55, 1195.

Moroz, L. V., Basilevsky, A. T., Hiroi, T., Rout, S. S., Baither, D., Van Der Bogert, C. H., ... & Pieters, C. M. (2009). Spectral properties of simulated impact glasses produced from Martian soil analogue JSC Mars-1. *Icarus*, 202(1), 336-353.

Morris, R. V., Golden, D. C., Bell III, J. F., Lauer Jr, H. V., & Adams, J. B. (1993).

Pigmenting agents in Martian soils: Inferences from spectral, Mössbauer, and magnetic properties of nanophase and other iron oxides in Hawaiian palagonitic soil PN-9. *Geochimica et cosmochimica acta*, 57(19), 4597-4609.

Morris, R. V., Golden, D. C., Bell III, J. F., Shelfer, T. D., Scheinost, A. C., Hinman, N. W., ... & Britt, D. T. (2000). Mineralogy, composition, and alteration of Mars Pathfinder rocks and soils: Evidence from multispectral, elemental, and magnetic data on terrestrial analogue, SNC meteorite, and Pathfinder samples. *Journal of Geophysical Research: Planets*, 105(E1), 1757-1817.

Morris, R. V., Golden, D. C., Ming, D. W., Shelfer, T. D., Jørgensen, L. C., Bell III, J. F., ... & Mertzman, S. A. (2001). Phyllosilicate-poor palagonitic dust from Mauna Kea Volcano (Hawaii): A mineralogical analogue for magnetic Martian dust?. *Journal of Geophysical Research: Planets*, 106(E3), 5057-5083.

Mukherjee. (1969). Acta Crystallogr., Sect. B: Struct. *Crystallogr. Cryst*. Chem, 25, 675.

Mukhin, L. M., Gerasimov, M. V., & Safonova, E. N. (1989). Origin of precursors of organic molecules during evaporation of meteorites and mafic terrestrial rocks. *Nature*, 340(6228), 46-48.

Mustard, J. F., & Pieters, C. M. (1987). Quantitative abundance estimates from bidirectional reflectance measurements. *Journal of Geophysical Research: Solid Earth*, *92*(B4), E617-E626.

Mustard, J. F., & Pieters, C. M. (1989). Photometric phase functions of common geologic minerals and applications to quantitative analysis of mineral mixture reflectance spectra. *Journal of Geophysical Research: Solid Earth*, 94(B10), 13619-13634.

Mustard, J. F., & Hays, J. E. (1997). Effects of hyperfine particles on reflectance spectra from 0.3 to 25 μm. *Icarus*, *125*(1), 145-163.

Myers, T. L., Blake, T. A., Yokosuk, M. O., Fortin, G., & Johnson, T. J. (2020). Improved infrared optical constants from pressed pellets: II. Ellipsometric n and k values for ammonium sulfate with variability analysis. *Applied spectroscopy*, *74*(8), 868-882.

Pavlov, A. K., Blinov, A. V., & Konstantinov, A. N. (2002). Sterilization of Martian surface by cosmic radiation. *Planetary and Space Science*, 50(7-8), 669-673.

Pavlov, A. A., Vasilyev, G., Ostryakov, V. M., Pavlov, A. K., & Mahaffy, P. (2012). Degradation of the organic molecules in the shallow subsurface of Mars due to irradiation by cosmic rays. *Geophysical research letters*, 39(13).

Pecharsky, V. K., & Zavalij, P. Y. (2003). Fundamentals of diffraction (pp. 99-260). Springer US.

Phillips, R. J., Davis, B. J., Tanaka, K. L., Byrne, S., Mellon, M. T., Putzig, N. E., ... & Seu, R. (2011). Massive CO2 ice deposits sequestered in the south polar layered deposits of Mars. *Science*, 332(6031), 838-841.

Pieters, C. M., & Englert, P. A. (1993). *Remote geochemical analysis, elemental and mineralogical composition*.

Pitman, K. M., Wolff, M. J., & Clayton, G. C. (2005). Application of modern radiative transfer tools to model laboratory quartz emissivity. *Journal of Geophysical Research: Planets*, *110*(E8).

Pitman, K. M., Noe Dobrea, E. Z., Jamieson, C. S., Dalton III, J. B., Abbey, W. J., & Joseph, E. C. (2014). Reflectance spectroscopy and optical functions for hydrated Fe-sulfates. *American Mineralogist*, *99*(8-9), 1593-1603.

Poch, O., Kaci, S., Stalport, F., Szopa, C., & Coll, P. (2014). Laboratory insights into the chemical and kinetic evolution of several organic molecules under simulated Mars surface UV radiation conditions. *Icarus*, 242, 50-63.

Pollack, J. B., Roush, T., Witteborn, F., Bregman, J., Wooden, D., Stoker, C., ... & Freedman, R. (1990). Thermal emission spectra of Mars (5.4–10.5 μm): Evidence for sulfates, carbonates, and hydrates. *Journal of Geophysical Research: Solid Earth*, 95(B9), 14595-14627.

Pompilio, L., Sgavetti, M., & Pedrazzi, G. (2007). Visible and near-infrared reflectance spectroscopy of pyroxene-bearing rocks: New constraints for understanding planetary surface compositions. *Journal of Geophysical Research: Planets*, 112(E1).

Poulet, F., & Erard, S. (2004). Nonlinear spectral mixing: Quantitative analysis of laboratory mineral mixtures. *Journal of Geophysical Research: Planets*, *109*(E2).

Poulet, F., Mangold, N., Platevoet, B., Bardintzeff, J. M., Sautter, V., Mustard, J. F., ... & Aléon-Toppani, A. (2009). Quantitative compositional analysis of Martian mafic regions using the MEx/OMEGA reflectance data: 2. Petrological implications. *Icarus, 201*(1), 84-101.

Nagelschmidt. Z. (1937). Kristallogr., Kristallgeom., Kristallphys., Kristallchem, 97, 518.

Natl. Acad. Sci. U. S. A. (2013). 110 (16), 6292.

Natl. Bur. Stand. (U. S.), (1956). Circ. 539, 6.

Natl. Bur. Stand. (U. S.). (1967) Monogr. 25, 5, 31.

Natl. Bur. Stand. (U. S.). (1953). Circ. 539, 1, 39.

Natl. Bur. Stand. (U. S.). (1980). Monogr. 25, 17, 16.

Natl. Bur. Stand. (U. S.). (1978). Monogr. 25, 15, 32.

Natl. Bur. Stand. (U. S.). (1978). Monogr. 25, 15, 34.

Nodland, D., Syvinski, W., McCarthy, G., Bayliss, P., (1989).North Dakota State Univ., Fargo, North Dakota, USA. ICDD Grant-in-Aid.

Oro, J., & Holzer, G. (1979). The photolytic degradation and oxidation of organic compounds under simulated martian conditions. *Journal of Molecular Evolution*, *14*(1), 153-160.

Palomba, E., Zinzi, A., Cloutis, E. A., d'Amore, M., Grassi, D., & Maturilli, A. (2009). Evidence for Mg-rich carbonates on Mars from a 3.9 μm absorption feature. *Icarus*, 203(1), 58-65.

Pavlov, A. K., Blinov, A. V., & Konstantinov, A. N. (2002). Sterilization of Martian surface by cosmic radiation. *Planetary and Space Science*, *50*(7-8), 669-673.

Pavlov, A. A., Vasilyev, G., Ostryakov, V. M., Pavlov, A. K., & Mahaffy, P. (2012). Degradation of the organic molecules in the shallow subsurface of Mars due to irradiation by cosmic rays. *Geophysical research letters*, *39*(13).

Pieters, C. M. (1983). Strength of mineral absorption features in the transmitted component of near-infrared reflected light: First results from RELAB. *Journal of Geophysical Research: Solid Earth*, *88*(B11), 9534-9544.

Poch, O., Kaci, S., Stalport, F., Szopa, C., & Coll, P. (2014). Laboratory insights into the chemical and kinetic evolution of several organic molecules under simulated Mars surface UV radiation conditions. *Icarus*, *242*, 50-63.

Popović, S. (2020). Quantitative Phase Analysis by X-ray Diffraction—Doping Methods and Applications. *Crystals*, 10(1), 27.

Post, J.E., Heaney, P.J., von Dreele, R.B., Hanson, J.C. "Neutron and temperature-resolved synchrotron X-ray powder diffraction study of akaganeite". *Am. Mineral*. 2003, 88, 782.

Querry, M. R. (1985). Optical constants (pp. 237-302). US Army Armament, Munitions & Chemical Command, Chemical Research & Development Center.

Querry, M. (1987). Optical constants of minerals and other materials from the millimeter to the ultraviolet. (Contractor Report, Jun. 1985- May 1987).

Rampe, E. B., Bristow, T. F., Morris, R. V., Morrison, S. M., Achilles, C. N., Ming, D. W., ... & Salvatore, M. R. (2020). Mineralogy of Vera Rubin ridge from the Mars science laboratory CheMin instrument. *Journal of Geophysical Research: Planets*, *125*(9), e2019JE006306.

Ramsey, M. S., & Christensen, P. R. (1998). Mineral abundance determination: Quantitative deconvolution of thermal emission spectra. *Journal of Geophysical Research: Solid Earth*, *103*(B1), 577-596.

Redfern, S.A.T., Artioli, G., Rinaldi, R., Henderson, C.M.B., Knight, K.S., Wood, B.J. "Octahedral cation ordering in olivine at high temperature. II: an in situ neutron powder diffraction study on synthetic Mg Fe Si O4 (Fa50)". *Phys. Chem. Miner*. 2000, 27, 630.

Rietveld, H. M. (1967). Line profiles of neutron powder-diffraction peaks for structure refinement. *Acta Crystallographica*, 22(1), 151-152.

Roush, T. L., Pollack, J. B., Witteborn, F. C., Bregman, J. D., & Simpson, J. P. (1990). Ice and minerals on Callisto: A reassessment of the reflectance spectra. *Icarus*, *86*(2), 355-382.

Roush, T., Pollack, J., & Orenberg, J. (1991). Derivation of midinfrared (5–25 μm) optical constants of some silicates and palagonite. *Icarus*, *94*(1), 191-208.

Roush, T. L. (1996). Midinfrared (5.0–25 μm, 2000–400 cm− 1) optical constants of hydrous carbonate, sulfate, and nitrate. *Journal of Geophysical Research: Planets*, *101*(E1), 2215-2224.

Roush, T. L. (2003). Estimated optical constants of the Tagish Lake meteorite. *Meteoritics & Planetary Science*, 38(3), 419-426.

Roush, T. L., & Dalton, J. B. (2004). Reflectance spectra of hydrated Titan tholins at cryogenic temperatures and implications for compositional interpretation of red objects in the outer Solar System. *Icarus*, 168(1), 158-162.

Roush, T. L. (2005). Near-infrared (0.67–4.7 μm) optical constants estimated for montmorillonite. *Icarus*, 179(1), 259-264.

Roush, T. L., Esposito, F., Rossman, G. R., & Colangeli, L. (2007). Estimated optical constants of gypsum in the regions of weak absorptions: Application of scattering theories and comparisons to independent measurements. *Journal of Geophysical Research: Planets*, *112(E10).*

Roush, T. L., Teodoro, L. F., Blewett, D. T., & Cahill, J. T. (2021). Optical constants and diffuse reflectance of opaque minerals: A modeling study using magnetite. *Icarus*, *361*, 114331.

Scheller, E. L., Hollis, J. R., Cardarelli, E. L., Steele, A., Beegle, L. W., Bhartia, R., ... & Wiens, R. C. (2022). First-results from the Perseverance SHERLOC investigation: Aqueous alteration processes and implications for organic geochemistry in Jezero crater, Mars. In *LPSC 2022*.

Schieber, J., Bohacs, K. M., Coleman, M., Bish, D., Reed, M. H., Thompson, L., ... & Yawar, Z. (2022). Mars is a mirror–Understanding the Pahrump Hills mudstones from a perspective of Earth analogues. *Sedimentology*, 69(6), 2371-2435.

Scheinost, A. C., Chavernas, A., Barrón, V., & Torrent, J. (1998). Use and limitations of second-derivative diffuse reflectance spectroscopy in the visible to near-infrared range to identify and quantify Fe oxide minerals in soils. *Clays and Clay Minerals*, 46, 528-536.

Shkuratov, Y., Starukhina, L., Hoffmann, H., & Arnold, G. (1999). A model of spectral albedo of particulate surfaces: Implications for optical properties of the Moon. *Icarus*, 137(2), 235-246.

Sklute, E. C., Glotch, T. D., Piatek, J. L., Woerner, W. R., Martone, A. A., & Kraner, M. L. (2015). Optical constants of synthetic potassium, sodium, and hydronium jarosite. *American Mineralogist*, *100*(5-6), 1110-1122.

Sato. (1964). *Mineral. J.* 4, 215.

Singer, R. B., McCord, T. B., Clark, R. N., Adams, J. B., & Huguenin, R. L. (1979). Mars surface composition from reflectance spectroscopy: A summary. *Journal of Geophysical Research: Solid Earth*, *84*(B14), 8415-8426.

Smith. *Mineral. Mag*. 1956, 31, 47.

Smith, D., Auh, (1971). Penn State University, University Park, Pennsylvania, USA. ICDD Grant-in-Aid

Sobolev, V. V. (1975). Light scattering in planetary atmospheres. *International series of monographs in natural philosophy* (Vol. 76).

Spencer, C. (2019). Application of ellipsometry to the identification of ore minerals. *Rocks & Minerals*, 94(4), 344-347.

Spitzer, W. G., & Kleinman, D. A. (1961). Infrared lattice bands of quartz. *Physical Review*, 121(5), 1324.

Steele, A., McCubbin, F. M., Fries, M., Kater, L., Boctor, N. Z., Fogel, M. L., ... & Jull, A. J. T. (2012). A reduced organic carbon component in martian basalts. *Science*, 337(6091), 212-215.

Steele, A., McCubbin, F. M., & Fries, M. D. (2016). The provenance, formation, and implications of reduced carbon phases in Martian meteorites. *Meteoritics & Planetary Science*, 51(11), 2203-2225.

Steele, A., Benning, L. G., Wirth, R., Siljeström, S., Fries, M. D., Hauri, E., ... & Rodriguez Blanco, J. D. (2018). Organic synthesis on Mars by electrochemical reduction of CO2. *Science advances*, *4*(10), eaat5118.

Strens, R. G. (1979). Determining the optical constants of opaque minerals. *Bulletin de Minéralogie*, *102*(4), 308-313.

Stroncik, N. A., & Schmincke, H. U. (2002). Palagonite–a review. *International Journal of Earth Sciences*, 91, 680-697.

Su, G. C. (1998). A comparison of statistical and empirical detection limits. *Journal of AOAC International*, 81(1), 105-110.

Sutter, B., Mcadam, A. C., Mahaffy, P. R., Ming, D. W., Edgett, K. S., Rampe, E. B., ... & Yen, A. S. (2017). Evolved gas analyses of sedimentary rocks and eolian sediment in Gale Crater, Mars: Results of the Curiosity rover's sample analysis at Mars instrument from Yellowknife Bay to the Namib Dune. *Journal of Geophysical Research: Planets*, *122*(12), 2574-2609.

Swanson and Tatge. (1951). *J. Res. Natl. Bur. Stand. (U. S.)*, 46, 325.

Takeuchi, Y., Furukawa, Y., Kobayashi, T., Sekine, T., Terada, N., & Kakegawa, T. (2020). Impact-induced amino acid formation on Hadean Earth and Noachian Mars. *Scientific reports*, 10(1), 9220.

Tarnas, J. D., Mustard, J. F., Wu, X., Das, E., Cannon, K. M., Hundal, C. B., ... & Parente, M. (2021). Successes and challenges of factor analysis/target transformation application to visible-to-near-infrared hyperspectral data. *Icarus*, *365*, 114402.

ten Kate, I. L. (2010). Organics on Mars?. *Astrobiology*, *10*(6), 589-603.

Thomas, K. L., Blanford, G. E., Keller, L. P., Klöck, W., & McKay, D. S. (1993). Carbon abundance and silicate mineralogy of anhydrous interplanetary dust particles. *Geochimica et Cosmochimica Acta*, 57(7), 1551-1566.

Thorpe, M. T., Bristow, T. F., Rampe, E. B., Tosca, N. J., Grotzinger, J. P., Bennett, K. A., ... & Fedo, C. M. (2022). Mars Science Laboratory CheMin data from the Glen Torridon region and the significance of lake-groundwater interactions in interpreting mineralogy and sedimentary history. *Journal of Geophysical Research: Planets*, 127(11), e2021JE007099.

Trang, D., Lucey, P. G., Gillis-Davis, J. J., Cahill, J. T., Klima, R. L., & Isaacson, P. J. (2013). Near-infrared optical constants of naturally occurring olivine and synthetic pyroxene as a function of mineral composition. *Journal of Geophysical Research: Planets*, 118(4), 708-732.

Van Tassel, R. (1958). On the crystallography of calclacite, Ca (CH3COO) Cl. 5H2O. *Acta Crystallographica*, 11(10), 745-746.

Vlasov, D. Y., Zelenskaya, M. S., Izatulina, A. R., Janson, S. Y., & Frank-Kamenetskaya, O. V. (2023). Oxalate Crystallization under the Action of Brown Rot Fungi. *Crystals*, 13(3), 432.

Vyverberg, Karen L., John M. Jaeger, and Andrea Dutton. "Quantifying detection limits and uncertainty in X-ray diffraction mineralogical assessments of biogenic carbonates." *Journal of Sedimentary Research* 88.11 (2018): 1261-1275

Warren, S. G. (1984). Optical constants of ice from the ultraviolet to the microwave. *Applied optics*, *23*(8), 1206-1225.

Wenrich, M. L., & Christensen, P. R. (1996). Optical constants of minerals derived from emission spectroscopy: Application to quartz. *Journal of Geophysical Research: Solid Earth*, *101*(B7), 15921-15931.

Wentworth, S. J., & Gooding, J. L. (1994). Carbonates and sulfates in the Chassigny meteorite: Further evidence for aqueous chemistry on the SNC parent planet. *Meteoritics*, 29(6), 860-863.

Wiens, R. C., Udry, A., Beyssac, O., Quantin-Nataf, C., Mangold, N., Cousin, A., ... & SuperCam Team. (2022). Compositionally and density stratified igneous terrain in Jezero crater, Mars. *Science Advances*, 8(34), eabo3399.

Wilcox, B. B., Lucey, P. G., & Hawke, B. R. (2006). Radiative transfer modeling of compositions of lunar pyroclastic deposits. *Journal of Geophysical Research: Planets*, *111*(E9).

Wenk, H.R., Joswig, W., Tagai, T., Korekawa, M., Smith, B.K. "The average structure of An 62-66 labradorite". Am. Mineral. 1980, 65, 81.

Wolska, E., Schwertmann, U. "Nonstoichiometric structures during dehydroxylation of goethite". *Z. Kristallogr*. 1989, 189, 223.

Wray, J. J., Murchie, S. L., Bishop, J. L., Ehlmann, B. L., Milliken, R. E., Wilhelm, M. B., ... & Chojnacki, M. (2016). Orbital evidence for more widespread carbonate-bearing rocks on Mars. *Journal of Geophysical Research: Planets*, 121(4), 652-677.

Xiao, J., Song, Y., & Li, Y. (2023). Comparison of Quantitative X-ray Diffraction Mineral Analysis Methods. *Minerals*, 13(4), 566.

Xu, H., Jin, S. and Noll, B. C. "Incommensurate density modulation in a Na-rich plagioclase feldspar: Z-contrast imaging and single-crystal X-ray diffraction study". *Acta Crystallogr., Sect. B: Struct. Sci., Cryst. Eng. Mater*. 2016, 72, 904-915.

Yang, Y., Li, S., Milliken, R. E., Zhang, H., Robertson, K., & Hiroi, T. (2019). Phase Functions of Typical Lunar Surface Minerals Derived for the Hapke Model and Implications for Visible to Near-Infrared Spectral Unmixing. *Journal of Geophysical Research: Planets*, 124(1), 31-60.

Ye, C., Rucks, M. J., Arnold, J. A., & Glotch, T. D. (2019). Mid-infrared optical constants of labradorite, a triclinic plagioclase mineral. Earth and Space *Science,* 6(12), 2410-2422.

Ye, C., Sklute, E. C., & Glotch, T. D. (2021). Orientation Averaged Visible/Near-Infrared and Mid-Infrared Optical Constants of Hydrous Ca-Sulfates: Gypsum and Bassanite. *Earth and Space Science,* 8(10), e2021EA001834.

Yen, A. S., Mittlefehldt, D. W., McLennan, S. M., Gellert, R., Bell III, J. F., McSween Jr,

H. Y., ... & Squyres, S. W. (2006). Nickel on Mars: Constraints on meteoritic material at the surface. *Journal of Geophysical Research: Planets*, 111(E12).

Zeidler, S., Mutschke, H., & Posch, T. (2015). Temperature-dependent infrared optical constants of olivine and enstatite. *The Astrophysical Journal*, 798(2), 125.

Zhang, C. (2007). *Fundamentals of environmental sampling and analysis*. John Wiley & Sons.

Zhang, Li, Meng, Yue, Dera, Przemyslaw, Yang, Wenge, Mao, Wendy L., Mao, Ho-Kwang "Single- crystal structure determination of (Mg,Fe) Si O3 postperovskite". *Proc. Swanson, Fuyat. Natl. Bur. Stand. (U. S.)*, Circ. 539 1953, II, 41.

Zhang, G., Wasyliuk, K., & Pan, Y. (2001). The characterization and quantitative analysis of clay minerals in the Athabasca Basin, Saskatchewan: Application of shortwave infrared reflectance spectroscopy. *The Canadian Mineralogist*, 39(5), 1347-1363.

Zolotov, M., & Shock, E. (1999). Abiotic synthesis of polycyclic aromatic hydrocarbons on Mars. *Journal of Geophysical Research: Planets*, 104(E6), 14033-14049.

Zolotov, M. Y., & Shock, E. L. (2000). An abiotic origin for hydrocarbons in the Allan Hills 84001 martian meteorite through cooling of magmatic and impact-generated gases. *Meteoritics & Planetary Science*, 35(3), 629-638.

5.0 Supplemental Material

5.1 Python script for retrieving I/F data from PDS archived SuperCam files

```
from astropy.io import fits
import pandas as pd
# open fits file
hdulist=fits.open('INPUT FITS FILE NAME.fits)
x = hdulist[7].data['Wavelength (um)']
y = hdulist[6].data['I_F_atm']
df = pd.DataFrame({"Wavelength" : x, "I_F_ATM_CORR" : y})
df.to_csv("OUPUT CSV FILE NAME.csv",index=False)
```

5.2 Excel file with reflectance spectra

5.3 Excel file X-ray diffraction patterns

Table List

Table 1. Samples used in this study. See Table 2 for chemical formulas.

Sample ID	Wt. % carboxylate	Wt. % Mars analogue	carboxylate sample ID	carboxylate
CBXMIX001	0.00	100.00	none	none
CBXMIX002	2.50	97.50	ACT006	calcium acetate monohydrate
CBXMIX003	2.33	97.67	ACT005	magnesium acetate tetrahydrate
CBXMIX004	2.02	97.98	ACT004	ferrous acetate
CBXMIX005	2.12	97.88	FRM001	formicaite
CBXMIX006	1.98	98.02	FRM003	magnesium formate
CBXMIX007	1.98	98.02	ART003	whewellite
CBXMIX008	2.05	97.95	CRB715	humboldtine
CBXMIX009	1.98	98.02	CRB720	glushinskite
CBXMIX010	2.02	97.98	CRB131	calcite
CBXMIX011	2.00	98.00	CRB106	magnesite
CBXMIX012	2.53	97.47	CRB145	siderite
CBXMIX013	0.53	99.47	ACT006	calcium acetate monohydrate
CBXMIX014	0.59	99.41	ACT005	magnesium acetate tetrahydrate
CBXMIX015	0.53	99.47	ACT004	ferrous acetate
CBXMIX016	0.60	99.40	FRM001	formicaite
CBXMIX017	0.61	99.39	FRM003	magnesium formate
CBXMIX018	0.51	99.49	ART003	whewellite
CBXMIX019	0.59	99.41	CRB715	humboldtine
CBXMIX020	0.49	99.51	CRB720	glushinskite
CBXMIX021	0.55	99.45	CRB131	calcite
CBXMIX022	0.62	99.38	CRB106	magnesite
CBXMIX023	0.53	99.47	CRB145	siderite
CBXMIX024	6.90	93.10	CRB145	siderite
CBXMIX025	5.54	94.46	CRB715	humboldtine
CBXMIX026	11.08	88.92	CRB145	siderite
CBXMIX027	10.28	89.72	CRB715	humboldtine
FRM001	100.00	0.00	FRM001	formicaite

FRM003	100.00	0.00	FRM003	magnesium formate
ACT005	100.00	0.00	ACT005	magnesium acetate tetrahydrate
ACT004	100.00	0.00	ACT004	ferrous acetate
CRB105	100.00	0.00	CRB106	magnesite
CRB131	100.00	0.00	CRB131	calcite
CRB145	100.00	0.00	CRB145	siderite
ART003	100.00	0.00	ART003	whewellite
CRB715	100.00	0.00	CRB715	humboldtine
CRB720	100.00	0.00	CRB720	glushinskite
ACT006	100.00	0.00	ACT006	calcium acetate monohydrate
C3JT101	0.00	100.00	none	none
C1JT110	1.00	99.00	C1JT120	calcite
C1JT109	2.50	97.50	C1JT120	calcite
C1JT108	5.00	95.00	C1JT120	calcite
C1JT107	10.00	90.00	C1JT120	calcite
C1JT185	20.00	80.00	C1JT120	calcite
C1JT184	50.00	50.00	C1JT120	calcite
C1JT120	100.00	0.00	C1JT120	calcite
C2JT105	1.00	99.00	C2JT106	calcite
C2JT104	2.50	97.50	C2JT106	calcite
C2JT103	5.00	95.00	C2JT106	calcite
C2JT102	10.00	90.00	C2JT106	calcite
C2JT183	20.00	80.00	C2JT106	calcite
C2JT182	50.00	50.00	C2JT106	calcite
C2JT106	100.00	0.00	C2JT106	calcite

Table 2. Absorption band minima and diffraction peak maxima for endmember samples used in this study.

Sample number	Chemical formula	phases identified XRD	Particle size (μm)	VNIR band minima (nm)	MIR band minima (nm)	XRD peak maxima (°2-theta; Co Ka)
CRB145	$Fe^{2+}CO_3$	siderite	<45	2322, 2524	3964	37.50
CRB131	$CaCO_3$	calcite	<45	2340, 2536	3979	34.25
C2JT106	$CaCO_3$	[nm]	45-75	2340, [nm]	[nm]	[nm]
C1JT120	$CaCO_3$	[nm]	125-250	2340, [nm]	[nm]	[nm]
CRB106	$MgCO_3$	magnesite	<45	2301, 2502	3943	38.1
CRB715	$Fe^{2+}C_2O_4 \cdot 2H_2O$	humboldtine	<45	2048	3546, 3606	21.45[a], 34.60[b], 39.40[c]
ART003	$CaC_2O_4 \cdot H_2O$	whewellite	<45	2436	3610	17.35
CRB720	$MgC_2O_4 \cdot 2H_2O$	glushinskite	<45	2442	3590	21.00
ACT004	$Fe^{2+}(CH_3CO_2)_2$	X-ray amorphous	<45	2260	4057	none
ACT005	$Mg(CH_3CO_2)_2 \cdot 4H_2O$	magnesium acetate tetrahydrate	<45	2259	4085	14.75
ACT006	$Ca(CH_3CO_2)_2 \cdot H_2O$	calcium acetate monohydrate	<45	2263	4188	10.50
FRM001	$Ca(HCO_2)_2$	formicaite	<45	2355	various	18.35
FRM003	$Mg(HCO_2)_2 \cdot 2H_2O$	magnesium formate	<45	2340	various	20.95

[nm] not measured

[a] The 21.45 °2-theta Co Ka peak

[b] The 34.60 °2-theta Co Ka peak

[c] The 39.40 °2-theta Co Ka peak

Table 3. Measured and depths and peak amplitudes for samples used in this study.

Sample ID	Wt. % carboxylate	Wt. % Mars analogue	Carboxylate sample ID	VNIR band depth	MIR band depth	XRD peak amplitude
CBXMIX001	0.00	100.00[a]	none	nm	nm	nm
CBXMIX002	2.5	97.50[a]	ACT006	0.56	0.00	1.26
CBXMIX003	2.33	97.67[a]	ACT005	0.38	0.00	1.15
CBXMIX004	2.02	97.98[a]	ACT004	1.86	0.00	0.00
CBXMIX005	2.12	97.88[a]	FRM001	2.15	0.00	1.29
CBXMIX006	1.98	98.02[a]	FRM003	1.28	0.00	0.00
CBXMIX007	1.98	98.02[a]	ART003	0.00	0.00	1.23
CBXMIX008	2.05	97.95[a]	CRB715	0.00	0.00	1.49[b], 1.27[c], 1.37[d]
CBXMIX009	1.98	98.02[a]	CRB720	0.00	0.00	1.37
CBXMIX010	2.02	97.98[a]	CRB131	0.00	2.40	1.53
CBXMIX011	2.00	98.00[a]	CRB106	0.00	1.54	1.54
CBXMIX012	2.53	97.47[a]	CRB145	0.00	0.59	1.59
CBXMIX013	0.53	99.47[a]	ACT006	0.18	0.00	1.08
CBXMIX014	0.59	99.41[a]	ACT005	0.14	0.00	1.02
CBXMIX015	0.53	99.47[a]	ACT004	1.25	0.00	0.00
CBXMIX016	0.60	99.40[a]	FRM001	0.47	nd	1.08
CBXMIX017	0.61	99.39[a]	FRM003	0.36	nd	0.00
CBXMIX018	0.51	99.49[a]	ART003	0.00	0.00	1.08
CBXMIX019	0.59	99.41[a]	CRB715	0.00	0.00	1.19[b], 1.22[c], 1.25[d]
CBXMIX020	0.49	99.51[a]	CRB720	0.00	0.00	1.15
CBXMIX021	0.55	99.45[a]	CRB131	0.00	0.54	1.27
CBXMIX022	0.62	99.38[a]	CRB106	0.00	0.00	1.17
CBXMIX023	0.53	99.47[a]	CRB145	0.00	0.00	1.17
CBXMIX024	6.90	93.10[a]	CRB145	0.00	3.80	2.78
CBXMIX025	5.54	94.46[a]	CRB715	0.77	0.00	2.09[b], 1.47[c], 1.54[d]
CBXMIX026	11.08	88.92[a]	CRB145	0.00	6.55	3.69
CBXMIX027	10.28	89.72[a]	CRB715	3.60	0.00	2.73[b], 2.10[c], 1.82[d]
FRM001	100.00	0.00	FRM001	68.28	nd	28.88
FRM003	100.00	0.00	FRM003	40.60	nd	14.61

ACT005	100.00	0.00	ACT005	26.53	[nd]	25.13
ACT004	100.00	0.00	ACT004	30.54	[nd]	0.00
CRB106	100.00	0.00	CRB106	19.03[b], 10.43[c]	71.13	37.31
CRB131	100.00	0.00	CRB131	18.54[b], 9.42[c],	77.76	59.04
CRB145	100.00	0.00	CRB145	11.06[b], 4.31[c]	57.62	14.64
ART003	100.00	0.00	ART003	16.67	[nd]	12.78
CRB715	100.00	0.00	CRB715	42.56	[nd]	13.05[d], 5.62[e], 5.44[f]
CRB720	100.00	0.00	CRB720	19.14	[nd]	13.20
ACT006	100.00	0.00	ACT006	46.43	[nd]	25.13
C3JT101	0.00	100.00[g]	none	[nm]	[nm]	[nm]
C1JT110	1.00	99.00[g]	C3JT101[h]	0.55	[nm]	[nm]
C1JT109	2.50	97.50[g]	C3JT101[h]	0.63	[nm]	[nm]
C1JT108	5.00	95.00[g]	C3JT101[h]	0.82	[nm]	[nm]
C1JT107	10.00	90.00[g]	C3JT101[h]	1.13	[nm]	[nm]
C1JT185	20.00	80.00[g]	C3JT101[h]	4.10	[nm]	[nm]
C1JT184	50.00	50.00[g]	C3JT101[h]	10.39	[nm]	[nm]
C1JT120	100.00	0.00	C3JT101[h]	38.76	[nm]	[nm]
C2JT105	1.00	99.00[g]	C2JT106[i]	0.30	[nm]	[nm]
C2JT104	2.50	97.50[g]	C2JT106[i]	0.59	[nm]	[nm]
C2JT103	5.00	95.00[g]	C2JT106[i]	0.75	[nm]	[nm]
C2JT102	10.00	90.00[g]	C2JT106[i]	1.07	[nm]	[nm]
C2JT183	20.00	80.00[g]	C2JT106[i]	2.38	[nm]	[nm]
C2JT182	50.00	50.00[g]	C2JT106[i]	5.38	[nm]	[nm]
C2JT106	100.00	0.00	C2JT106[i]	20.16	[nm]	[nm]

[nm] Not measured.

[nd] Not determined.

[a] JSC Mars-1a.

[b] The 2.5 µm band with continuum wavelength extending short of the 2.3 µm band.

[c] The 2.3 µm band only.

[d] The 21.45 °2-theta Co Ka peak

[e] The 34.60 °2-theta Co Ka peak

[f] The 39.40 °2-theta Co Ka peak

[g] MGS-1

[h] 125-250 µm

[i] 45-75 µm

Table 4. Parameters derived from linear regression for samples used in this study.

Sample number	carboxylate	Particle size (μm)	XRD m	XRD b	VNIR m	VNIR b	MIR m	MIR b
CRB145	siderite	<45	0.2435	1.0256	nd	nd	0.6501	0.7046
CRB131	calcite	<45	0.1772	1.1749	nd	nd	1.2651	0.1529
C2JT106	calcite	45-75	nd	nd	0.1033	0.224	nd	nd
C1JT120	calcite	125-250	nd	nd	0.0656	0.4777	nd	nd
CRB106	magnesite	<45	0.2698	1.0008	nd	nd	nd	nd
CRB715[a]	humboldtine	<45	0.1581	1.1428	nd	nd	nd	nd
CRB715[b]	humboldtine	<45	0.0913	1.0913	nd	nd	nd	nd
CRB715[c]	humboldtine	<45	0.057	1.2352	nd	nd	nd	nd
ART003	whewellite	<45	0.1022	1.0257	nd	nd	nd	nd
CRB720	glushinskite	<45	0.1477	1.0732	nd	nd	nd	nd
ACT004	ferrous acetate	<45	nd	nd	0.4074	1.035	nd	nd
ACT005	magnesium acetate tetrahydrate	<45	0.0734	0.9798	0.1392	0.0593	nd	nd
ACT006	calcium acetate monohydrate	<45	0.0883	1.038	0.1914	0.0801	nd	nd
FRM001	formicaite	<45	0.1384	0.9952	1.0995	0.1834	nd	nd
FRM003	magnesium formate	<45	nd	nd	0.3566	-0.096	nd	nd

[nd] not determined

[a] The 21.45 °2-theta Co Ka peak

[b] The 34.60 °2-theta Co Ka peak

[c] The 39.40 °2-theta Co Ka peak

Table 5. Detection limits of CRB145 siderite on palagonite determined by different methods.

Reference	Uncertainty method	Equation	LOD	2-sided confidence %
Kontonyannis and Vagenas 2000	t-test; sample and background standard deviation	11	0.29	60
Hillier 1999	2(standard deviation of background)	2	0.43	64
Ali et al., 2022, Hanchar et al., 2000, this work	3(standard deviation of background)	5, 6, 16	0.65	78
Dobelin 2020	(background signal) + 3(standard deviation in determined concentration)	8	1.67	99
Zhang 2007	t-test; standard deviation in determined concentration	13	1.69	99
Vyverberg et al., (2018)	3(sum of variance around regression curve)	7	2.18	>99
Kim et al., 2012	3(root mean square error of regression curve)	10	2.59	>99
Hillier 1999	~6(standard deviations of background)	4	5.34	>99

Table 6. Calculated LODs for samples used in this study.

Sample number	Carboxylate	Particle size (µm)	XRD LOD (wt. %)	VNIR LOD (wt. %)	MIR LOD (wt. %)
CRB145	siderite	<45	0.65	>11.08	>0.65
CRB131	calcite	<45	0.99	>2.02	0.26
CRB131	calcite	45-75	[nm]	2.31-3.01	[nm]
CRB131	calcite	125-250	[nm]	1.15-3.65	[nm]
CRB106	magnesite	<45	0.56	[nd]	>0.65
CRB715[a]	humboldtine	<45	1.00	>5.00	[nd]
CRB715[b]	humboldtine	<45	1.86	[nm]	[nm]
CRB715[c]	humboldtine	<45	1.89	[nm]	[nm]
ART003	whewellite	<45	1.02	[nd]	[nd]
CRB720	glushinskite	<45	0.78	[nd]	[nd]
ACT004	ferrous acetate	<45	[nd]	0.21	[nd]
ACT005	magnesium acetate tetrahydrate	<45	1.25	0.43	[nd]
ACT006	calcium acetate monohydrate	<45	0.93	0.31	[nd]
FRM001	formicaite	<45	0.95	0.04	[nd]
FRM003	magnesium formate	<45	[nd]	0.31	[nd]

[nd] not determined

[nm] not measured

[a] The 21.45 °2-theta Co Ka peak

[b] The 34.60 °2-theta Co Ka peak

[c] The 39.40 °2-theta Co Ka peak

Table 7. CheMin files used in this study.

Sample name	**File name**	**Sol**	**Window**	**Integration time (minutes)**
4th scooped soil; Rocknest	CMA_404470826rda00790050104ch11503p1	0077-0088	1a (kapton)	1140
5th scooped soil, Rocknest (a)	CMA_405889312RDA00950050104CH11504P1	0094-0119	7a (mylar)	1578
John Klein drill	CMA_414856883RDA01960060000CH12240P1	0196-0269	13b (mylar)	1590
John Klein Drill	CMA_414856883MIN01960060000CH12240P2	0196-?	13b (mylar)	2034
Highfield drill	CMA_595174954RDA22270730550CH00111P1	0226-0237	10a (mylar)	1350
Rock Hall drill	CMA_598547494RDA22650731206CH00111P1	264	7b (mylar)	120
Cumberland drill	CMB_434685266RDA04190180786CH00113P1	0418-0432	12b (mylar)	1247
John Klein drill	CMB_439549561RDA04740240192CH00111P1	0473-0488	13b (mylar)	1348
Windjana	CMB_452848863RDA06240311330CH00111P1	0623-0632	13a (mylar)	1320
Confidence Hill drill (b)	CMB_465487684RDA07660421020CH00113P2	0765-0785	12a (mylar)	2246
Mojave2 drill (b)	CMB_476051894RDA08850450000CH00113P2	0884-0894	6a (kapton)	1348
Telegraph Peak drill	CMB_479423416RDA09230450450CH00113P2	0923-0949	5b (kapton)	2247
Buckskin drill	CMB_492814566RDA10740490642CH00111P1	1073-1079	14b (kapton)	899
Big Sky drill	CMB_497096076RDA11220500592CH00113P1	1121-1129	7b (mylar)	1348

Greenhorn drill	CMB_498699740RDA11400500676CH00113P1	1139-1148	8a (mylar)	1348
Gobabed dune scoop	CMB_509595663RDA12630530000CH00111P1	1262-1279	7a (mylar)	1350
Lubango drill	CMB_515083970RDA13250540746CH00113P1	1323-1330	8a (mylar)	1350
Okoruso drill	CMB_515987369RDA13350540938CH00111P1	1334-1347	7b (mylar)	1727
Oudam drill	CMB_518482923RDA13630542280CH00113P1	1361-1364	12a (mylar)	900
Marimba2 drill	CMB_524082694RDA14260561236CH00113P1	1426	8b (mylar)	450
Quela drill	CMB_528182076RDA14720580642CH00113P1	1470-1480	5a (kapton)	1800
Sebina drill	CMB_530590971RDA14990582136CH00113P1	1496	4b (kapton)	450
Ogunquit Beach scoop © (OG3)	CMB_569138401RDA19340672420CH00113P1	1931	1a (kapton)	450
Duluth drill	CMB_581124537RDA20690701752CH00111P1	2068-1095	13b (mylar)	1350
Stoer drill	CMB_587626717RDA21420721316CH00111P1	2141-2151	10a (mylar)	1350
Aberlady drill	CMB_608205076RDA23740751386CH00111P1	2373-2383	8a (mylar)	1350
Kilmarie drill	CMB_609535789RDA23890751398CH00111P1	2388-2400	9b (mylar)	1800
Glen Etive drill	CMB_618807226RDA24920763002CH00113P1	2492-2502	8b (mylar)	1350
Glen Etive drill 2nd	CMB_623314115RDA25430763002CH00111P1	2543-2553	8a (mylar)	1350
Hutton drill	CMB_634766364RDA26720790000CH00111P1	2672-2676	12a (mylar)	900

Edinburgh drill	CMB_638579868RDA27150790654CH00111P1	2715-2722	7b (mylar)	1350
Glasgow drill	CMB_642400648RDA27580792008CH00111P1	2758-2771	7b (mylar)	1350
Mary Anning drill	CMB_649856565RDA28420822176CH00111P1	2841-2853	7a (mylar)	1350
Mary Anning 3	CMB_653942038RDA28880822176CH00111P1	2887-2894	7a (mylar)	1350
Groken	CMB_656073671RDA29120822188CH00111P1	2912-2921	9a (mylar)	1350

Table 8. Comparison of determined siderite concentrations by CheMin with those from my regression analysis.

Sample	Siderite CheMin	Siderite Terra
Glen Etive 1	0.8 ± 0.9	0.50 ± 0.54
Mary Anning	1.4 ± 0.9	0.00 ± 0.54
Mary Anning 3	1.1 ± 1.7	0.84 ± 0.54
Groken	3.2 ± 2.6	1.36 ± 0.54
Kilmarie	2.2 ± 1.0	2.04 ± 0.55

Table 9. Mineral concentrations determined by CheMin of Gale Crater samples.

Mineral	**RN scooped soil 4th**	**RN scooped soil 5th**	**JK drill a**	**JK drill b**	**HF drill**	**RH drill**	**CL drill a**	**CL drill b**	**JK drill c**
andesine	45.8	40.8	43.8	43.5			43.6	43.2	
feldspar									46.5
k-feldspar									
plagioclase					47.3	38.2			
pyroxene					10.1	17.1			25.3
forsterite	18.2	22.4	5.1	5.7			1.8	1.8	6.9
olivine									
Fe-forsterite									
augite	18.1	14.6	8.5	7.6			8.1	6.5	
pigeonite	11.4	13.8	12.7	11.3			15.6	13.4	
enstatite									
magnetite	2.7	2.1	7.0	7.6	1.4		8.7	8.7	6.4
anhydrite	2.1	1.5	3.3	5.3	8.2	21.2	1.6	1.8	4.6
quartz	1.6	1.4	0.6	0.9	1.3		0.2		0.8
cristobalite									
opal-CT									
tridymite									
sanidine		1.3	1.7	2.4	3.7		3.2	3.4	
hematite		1.1	1.2	1.2	20.0	5.4	1.3	1.1	0.9
ilmenite		0.9					1.0	0.5	0.7
akaganeite			2.4	2.3		11.3	3.4	3.6	2.2
orthopyroxene			6.8	6.1			8.1	11.1	
halite			0.2	0.3			0.2	0.1	0.7
pyrite			0.4	0.6					
pyrrhotite			1.5	2.0			1.9	2.1	2.0
basanite			2.0	2.1	2.6		1.4	2.5	2.3
gypsum					5.2				
ankerite									
siderite									
jarosite						4.3			
apatite						2.5			
SUM	**99.9**	**99.9**	**97.2**	**98.9**	**99.8**	**100.0**	**100.1**	**99.8**	**99.3**

Table 9 (cont.). Mineral concentrations determined by CheMin of Gale Crater samples.

Mineral	**WJ**	**CH drill a**	**CH drill b**	**MO2 drill a**	**MO2 drill b**	**TP drill**	**BK drill**	**BS drill**	**GH drill**
andesine									
feldspar									
k-feldspar	21.1	8.0	9.4			5.9			
plagioclase	5.6	38	38.3	55.1	55.5	38.0	42.8	46.7	42.4
pyroxene									
forsterite	5.2	3.3	2.3		0.4				
olivine									
Fe-forsterite				2.0					
augite	29.0	11.4	12	2.6	5.2	2.1			
pigeonite	16.7	9.9	9.9	12.7	10.9	7.0		19.1	5.0
enstatite	1.0	5.4				2.8			
magnetite	13.8	6.9	5.6	6.8	7.1	10.9	6.9	13.1	17.0
anhydrite	1.4					0.5	1.8	1.1	16.1
quartz	0.2	0.8	1.3	1.5	1.9	1.2		1.5	2.4
cristobalite						8.7	6.0		
opal-CT						14.5			
tridymite							34.1	1.7	
sanidine							8.4		
hematite	0.9	13.4	12.8	7.4	7.1	1.6		2.8	5.5
ilmenite	1.1	1.4		0.9		0.9			
akaganeite	2.5								
orthopyroxene			3.9					13.9	7.6
halite									
pyrite									
pyrrhotite	1.3								
basanite	0.2					0.5			3.9
gypsum									
ankerite									
siderite									
jarosite		1.5	2.1	6.8	7.6	2.4			
apatite			2.4	4.2	4.3	3.0			
SUM	**100.0**	**100.0**	**100.0**	**100.0**	**100.0**	**100.0**	**100.0**	**99.9**	**99.9**

Table 9 (cont.). Mineral concentrations determined by CheMin of Gale Crater samples.

Mineral	**GD scoop a**	**GD scoop b**	**LB drill**	**OK drill**	**OD drill**	**MR2 drill**	**QU drill**	**SB drill**	**OB scoop a**
andesine									
feldspar									
k-feldspar				2.9					
plagioclase	35.8	50.3	43.2	41.9	51.1	45.8	44	38.4	47.1
pyroxene					9.7	3.6	5.3	6.8	
forsterite						5.3	5.1	3.0	18.2
olivine	28.0	10.7							
Fe-forsterite									
augite	20.2	8.6							15.7
pigeonite	10.9	6.9	5.9	20.8					10.2
enstatite									
magnetite	2.8	8.5	11.1	17.3					2.5
anhydrite	1.0	6.0	12.3	0.8	5.8	10.2	10.7	16.9	2.3
quartz	0.7	2.3	3.5	1.4	1.9	1.2	1.1	1.2	1.6
cristobalite									
opal-CT									
tridymite									
sanidine						7.7	6.1	5.1	
hematite	0.5	6.8	2.3	1.1	26.0	16.4	20.0	20.4	2.3
ilmenite									
akaganeite									
orthopyroxene			10.4	11					
halite									
pyrite									
pyrrhotite									
basanite			9.0	1.2		1.9	4.5	1.8	
gypsum			2.3		5.5	6.4	1.8	3.8	
ankerite									
siderite									
jarosite						1.5	1.4	2.6	
apatite				1.6					
SUM	**99.9**	**100.1**	**100.0**	**100.0**	**100.0**	**100.0**	**100.0**	**100.0**	**99.9**

Table 9 (cont.). Mineral concentrations determined by CheMin of Gale Crater samples.

Mineral	**OB scoop b**	**DL drill**	**ST drill**	**AL drill**	**KM drill**	**GE drill**	**GE drill**	**HT drill**	**EB drill**
andesine									
feldspar									
k-feldspar									
plagioclase	53.1	55.8	44.1	34.7	32.5	40.0	63.0	49.7	39.6
pyroxene		9.0	7.3	14.7	13.4	6.0	11.0	14.1	27.6
forsterite	10.4								
olivine									
Fe-forsterite									11.5
augite	13.2								
pigeonite	8.5								
enstatite									
magnetite	2.4	1.6	0.7	1.9				12.4	14.0
anhydrite	3.1	3.0	5.3	18.9	29.3	34.0	10.0	1.2	
quartz	2.5	1.3	1.5	2.1	0.8	2.0	2.0		0.2
cristobalite								9.3	
opal-CT									
tridymite									
sanidine		9.0	4.0	3.9	2.3	5.0	6.0	4.7	4.6
hematite	6.8	13	28.3	5.5	3.8	7.0	4.0	4.8	0.5
ilmenite									
akaganeite			1.6						
orthopyroxene									
halite									
pyrite									
pyrrhotite									
basanite		5.4	0.8	18.4	10.0	3.0	3.0		
gypsum		1.8	4.2						
ankerite									
siderite					8.0	3.0			
jarosite			2.2						
apatite								3.8	2.0
SUM	**100.0**	**99.9**	**100.0**	**100.1**	**100.1**	**100.0**	**99**	**100.0**	**100.0**

Table 9 (cont.). Mineral concentrations determined by CheMin of Gale Crater samples.

Mineral	GG drill	MA drill	MA 3
andesine			
feldspar			
k-feldspar			
plagioclase	50.4	70.5	63.7
pyroxene	5.8	11.6	13.9
forsterite			
olivine			
Fe-forsterite			
augite			
pigeonite			
enstatite			
magnetite			
anhydrite	18.5	3.9	4.6
quartz	3.3	2.1	2.3
cristobalite	0.7		
opal-CT			
tridymite			
sanidine	3.7	6.3	6.3
hematite	13.4	2.5	1.9
ilmenite			
akaganeite			
orthopyroxene			
halite			
pyrite			
pyrrhotite			
basanite	3.2		4.8
gypsum			
ankerite		3.1	2.3
siderite			
jarosite			
apatite	1.0		
SUM	**100.0**	**100.0**	**99.8**

Table 10. Major d-spacings converted to °2-theta Co Ka for minerals identified by CheMin, for assessment of overlapping diffraction peaks with those identified with carboxylates.

Mineral	**°2-theta Co Ka 1**	**°2-theta Co Ka 2**	**°2-theta Co Ka 3**	**Reference**	**Overlapping carboxylate**
andesine	32.38	32.64	25.58	Xu et al., 2016	
feldspar	32.51	27.38	16.09	Smith 1956	whewellite[c]
K-feldspar	31.36	27.45	24.48	Nagelschmidt 1937	
plagioclase	32.54	32.78	25.65	Wenk et al., 1980	
pyroxene	34.8	41.44	36.02	De Wolff 1959	calcite[a], humboldtine[a]
forsterite	42.68	41.70	26.66	Swanson and Tatge 1951	
olivine	42.18	37.20	41.16	Redfern et al., 2000	
Fe-forsterite	42.25	41.25	37.29	Brown 1973	siderite[c]
augite	34.71	41.48	35.17	Smith 1971	calcite[a], humboldtine[a]
pigeonite	34.48	32.39	35.92	Moromoto 1970	calcite[a], humboldtine[a]
enstatite	32.81	36.29	42.04	NBS 1956	
magnetite	41.38	74.11	35.09	NBS 1967	
anhydrite	29.63	36.59	45.19	McMurdie et al., 1986	
quartz	31.04	24.27	58.95	Kern 1993	
cristobalite	25.58	44.91	42.12	NBS 1953	
opal-CT	25.20	23.90	41.93	Wilson 2014	
tridymite	25.16	23.86	27.10	Sato 1964	
sanidine	31.18	27.31	32.23	Donnay 1952	
hematite	38.71	41.59	63.72	Wolska 1989	magnesite[a], humboldtine[a]
ilmenite	37.91	41.17	62.42	NBS 1978	siderite[a]

akageneite	13.77	41.09	31.18	Post et al., 2003	magnesium acetate tetrahydrate[a]
orthopyroxene	42.98	58.74	61.57	Zhang et al., 2013	
halite	36.97	53.31	66.66	Swanson 1953	
pyrite	38.61	66.41	43.37	Nodland et al., 1989	magnesite[a], humboldtine[a]
pyrrhotite	51.36	39.61	34.94	Mukherjee 1969	calcite[c], humboldtine[b]
bassanite	29.87	34.64	17.09	Busheuv 1982	calcite[b], humboldtine[b], whewellite[c], formicaite[c]
gypsum	13.47	24.11	33.94	NBS 1980	calcite[c], magnesium acetate tetrahydrate[a]
ankerite	35.85	59.69	47.91	Keller and McCarthy 1985	
siderite	37.33	62.21	61.94	NBS 1978	magnesite[a]
jarosite	33.82	33.36	20.28	Keller and McCarthy 1985	calcite[ab], magnesite[a], humboldtine[a], glushinskite[c], magnesium formate[c]
apatite	37.07	37.47	38.4	de Wolff 1957	siderite[a]

[a] Overlaps with a D1 peak.

[b] Overlaps with a D2 peak.

[c] Overlaps with a D3 peak.

Table 11. Concentrations of carboxylates derived by SAM studies and by CheMin data analyzed here.

	oxalate wt. % SAM	**oxalate wt. % SAM min**	**oxalate wt. % SAM max**	**acetate wt. % SAM**	**acetate wt. % SAM min**	**acetate wt. % SAM max**	**Oxalate wt. % XRD**	**Acetate wt. % XRD**	**Magnesite wt. % XRD**	**Siderite wt. % XRD**
FEST[a]										
Edinburgh	0.75	0.00	1.54	0.96	0.00	1.99	<LOD	<LOD	<LOD	<LOD
Hutton 2	0.53	0.00	1.12	0.77	0.00	1.66	<LOD	<LOD	<LOD	<LOD
Glasgow	0.24	0.00	0.66	0.35	0.00	0.98	<LOD	<LOD	<LOD	<LOD
Mary Anning	1.13	0.30	1.96	1.64	0.35	2.93	<LOD	<LOD	<LOD	0.84
Glen Etive 2	0.95	0.13	1.77	1.39	0.13	2.65	<LOD	<LOD	<LOD	<LOD
Kilmarie	2.45	0.83	4.07	3.56	1.01	6.11	<LOD	<LOD	<LOD	2.04
Rock Hall	0.20	0.00	0.65	0.26	0.00	0.83	<LOD	<LOD	<LOD	<LOD
Highfield	0.21	0.00	0.81	0.31	0.00	1.21	<LOD	<LOD	<LOD	<LOD
Stoer	0.23	0.00	0.79	0.33	0.00	1.16	<LOD	<LOD	<LOD	<LOD
Duluths	0.14	0.00	0.28	0.2	0.00	0.42	<LOD	<LOD	<LOD	<LOD
Avg.	0.68	0.13	1.37	0.98	0.15	2.00	0.00	0.00	0.00	0.34
CHIMRA[b]										
Marimba	0.06	0.00	0.34	0.09	0.00	0.49	<LOD	<LOD	<LOD	<LOD
Oudam	0.04	0.00	0.23	0.06	0.00	0.33	<LOD	<LOD	<LOD	<LOD
Greenhorn 2	0.12	0.03	0.21	0.16	0.05	0.27	<LOD	<LOD	<LOD	0.68
Big Sky	0.24	0.01	0.47	0.31	0.01	0.61	<LOD	<LOD	<LOD	<LOD
Buckskin	0.14	0.00	0.28	0.17	0.00	0.36	<LOD	<LOD	0.98	<LOD
Telegraph Peak	0.08	0.00	0.25	0.10	0.00	0.31	<LOD	<LOD	<LOD	<LOD
Mojave	0.22	0.00	0.62	0.28	0.00	0.80	<LOD	<LOD	<LOD	<LOD
Confidence Hills	0.46	0.01	0.91	0.59	0.00	1.18	<LOD	<LOD	<LOD	<LOD
Windjana	1.21	0.45	1.97	1.54	0.53	2.55	<LOD	<LOD	<LOD	<LOD
Cumberland 3	0.30	0.06	0.54	0.38	0.06	0.70	<LOD	<LOD	<LOD	<LOD
John Klein 4	0.65	0.12	1.18	0.83	0.13	1.53	<LOD	<LOD	<LOD	<LOD

Avg.	0.32	0.06	0.64	0.41	0.07	0.83	0.00	0.00	0.09	0.06
Aeolian										
OG3	0.65	0.25	1.05	0.83	0.29	1.37	<LOD	<LOD	<LOD	<LOD
Gobabeb	1.03	0.34	1.72	1.32	0.40	2.24	<LOD	<LOD	<LOD	<LOD
Rocknest average	1.10	0.54	1.66	1.40	0.65	2.15	1.22	<LOD	<LOD	<LOD
Avg.	0.93	0.38	1.48	1.18	0.45	1.92	0.41	0.00	0.00	0.00

[a] feed-extended sample transfer

[b] Collection and Handling for Interior Martian Rock Analysis

Table 12. SuperCam files used in this study.

SuperCam file	Target	Sol
scam_0162_0681322341_713_cp2_scam02162_guillaumes_162_scam__02p03.fits	Guillaumes	162
scam_0162_0681322556_728_cp2_scam02162_guillaumes_162_scam__03p03.fits	Guillaumes	162
scam_0162_0681323109_713_cp2_scam02162_guillaumes_162_scam__05p03.fits	Guillaumes	162
scam_0168_0681855158_102_cp2_scam02168_guillaumes_168_scam__01p03.fits	Guillaumes	168
scam_0168_0681855379_093_cp2_scam02168_guillaumes_168_scam__02p03.fits	Guillaumes	168
scam_0168_0681855595_093_cp2_scam02168_guillaumes_168_scam__03p03.fits	Guillaumes	168
scam_0168_0681855849_114_cp2_scam02168_guillaumes_168_scam__04p03.fits	Guillaumes	168
scam_0168_0681856065_072_cp2_scam02168_guillaumes_168_scam__05p03.fits	Guillaumes	168
scam_0168_0681856282_117_cp2_scam02168_guillaumes_168_scam__06p03.fits	Guillaumes	168
scam_0168_0681856539_088_cp2_scam02168_guillaumes_168_scam__07p03.fits	Guillaumes	168
scam_0168_0681856755_310_cp2_scam02168_guillaumes_168_scam__08p03.fits	Guillaumes	168
scam_0168_0681857052_182_cp2_scam02168_guillaumes_168_scam__09p03.fits	Guillaumes	168
scam_0187_0683540867_823_cp2_scam01187_bellegarde_187_scam__01p02.fits	Bellegarde	187
scam_0187_0683541086_999_cp2_scam01187_bellegarde_187_scam__02p02.fits	Bellegarde	187
scam_0187_0683541303_089_cp2_scam01187_bellegarde_187_scam__03p02.fits	Bellegarde	187
scam_0187_0683541565_982_cp2_scam01187_bellegarde_187_scam__04p02.fits	Bellegarde	187
scam_0187_0683541875_859_cp2_scam01187_bellegarde_187_scam__05p02.fits	Bellegarde	187
scam_0187_0683542090_838_cp2_scam01187_bellegarde_187_scam__06p02.fits	Bellegarde	187
scam_0187_0683542353_070_cp2_scam01187_bellegarde_187_scam__07p02.fits	Bellegarde	187
scam_0187_0683542569_046_cp2_scam01187_bellegarde_187_scam__08p02.fits	Bellegarde	187
scam_0187_0683542867_857_cp2_scam01187_bellegarde_187_scam__09p02.fits	Bellegarde	187
scam_0188_0683628754_979_cp2_scam01188_bellegarde_188_scam__01p02.fits	Bellegarde	188
scam_0188_0683628984_953_cp2_scam01188_bellegarde_188_scam__02p02.fits	Bellegarde	188
scam_0188_0683629210_919_cp2_scam01188_bellegarde_188_scam__03p02.fits	Bellegarde	188
scam_0188_0683629474_948_cp2_scam01188_bellegarde_188_scam__04p02.fits	Bellegarde	188
scam_0188_0683629700_915_cp2_scam01188_bellegarde_188_scam__05p02.fits	Bellegarde	188

scam_0188_0683629926_917_cp2_scam01188_bellegarde_188_scam__06p02.fits	Bellegarde	188
scam_0188_0683630194_898_cp2_scam01188_bellegarde_188_scam__07p02.fits	Bellegarde	188
scam_0188_0683630420_961_cp2_scam01188_bellegarde_188_scam__08p02.fits	Bellegarde	188
scam_0188_0683630728_916_cp2_scam01188_bellegarde_188_scam__09p02.fits	Bellegarde	188
scam_0191_0683893869_697_cp2_scam01191_bellegarde_191a_scam_01p02.fits	Bellegarde	191
scam_0191_0683894117_654_cp2_scam01191_bellegarde_191a_scam_02p02.fits	Bellegarde	191
scam_0191_0683894361_718_cp2_scam01191_bellegarde_191a_scam_03p02.fits	Bellegarde	191
scam_0191_0683894651_805_cp2_scam01191_bellegarde_191a_scam_04p02.fits	Bellegarde	191
scam_0191_0683894895_671_cp2_scam01191_bellegarde_191a_scam_05p02.fits	Bellegarde	191
scam_0191_0683895139_666_cp2_scam01191_bellegarde_191a_scam_06p02.fits	Bellegarde	191
scam_0191_0683895429_666_cp2_scam01191_bellegarde_191a_scam_07p02.fits	Bellegarde	191
scam_0191_0683895672_681_cp2_scam01191_bellegarde_191a_scam_08p02.fits	Bellegarde	191
scam_0191_0683896001_698_cp2_scam01191_bellegarde_191a_scam_09p02.fits	Bellegarde	191
scam_0207_0685310942_124_cp2_scam01207_garde_207_scam_______01p02.fits	Garde	207
scam_0207_0685311141_198_cp2_scam01207_garde_207_scam_______02p02.fits	Garde	207
scam_0207_0685311338_224_cp2_scam01207_garde_207_scam_______03p02.fits	Garde	207
scam_0207_0685311576_165_cp2_scam01207_garde_207_scam_______04p02.fits	Garde	207
scam_0207_0685311775_184_cp2_scam01207_garde_207_scam_______05p02.fits	Garde	207
scam_0207_0685311972_226_cp2_scam01207_garde_207_scam_______06p02.fits	Garde	207
scam_0207_0685312212_211_cp2_scam01207_garde_207_scam_______07p02.fits	Garde	207
scam_0207_0685312409_194_cp2_scam01207_garde_207_scam_______08p02.fits	Garde	207
scam_0207_0685312681_197_cp2_scam01207_garde_207_scam_______09p02.fits	Garde	207
scam_0208_0685405541_839_cp2_scam01208_garde_cuttings_208___01p02.fits	Garde cuttings	208
scam_0208_0685405672_836_cp2_scam01208_garde_cuttings_208___02p02.fits	Garde cuttings	208
scam_0208_0685405802_827_cp2_scam01208_garde_cuttings_208___03p02.fits	Garde cuttings	208
scam_0208_0685405932_796_cp2_scam01208_garde_cuttings_208___04p02.fits	Garde cuttings	208
scam_0208_0685406063_819_cp2_scam01208_garde_cuttings_208___05p02.fits	Garde cuttings	208
scam_0208_0685406192_819_cp2_scam01208_garde_cuttings_208___06p02.fits	Garde cuttings	208
scam_0208_0685406322_917_cp2_scam01208_garde_cuttings_208___07p02.fits	Garde cuttings	208
scam_0208_0685406452_841_cp2_scam01208_garde_cuttings_208___08p02.fits	Garde cuttings	208

scam_0208_0685406582_796_cp2_scam01208_garde_cuttings_208___09p02.fits	Garde cuttings	208
scam_0208_0685406792_807_cp2_scam01208_garde_cuttings_208___10p02.fits	Garde cuttings	208
scam_0209_0685487671_795_cp2_scam01209_garde_209a_scam______01p02.fits	Garde	209
scam_0209_0685487916_851_cp2_scam01209_garde_209a_scam______02p02.fits	Garde	209
scam_0209_0685488157_866_cp2_scam01209_garde_209a_scam______03p02.fits	Garde	209
scam_0209_0685488437_857_cp2_scam01209_garde_209a_scam______04p02.fits	Garde	209
scam_0209_0685488758_977_cp2_scam01209_garde_209a_scam______05p02.fits	Garde	209
scam_0209_0685488998_790_cp2_scam01209_garde_209a_scam______06p02.fits	Garde	209
scam_0209_0685489277_906_cp2_scam01209_garde_209a_scam______07p02.fits	Garde	209
scam_0209_0685489517_937_cp2_scam01209_garde_209a_scam______08p02.fits	Garde	209
scam_0209_0685489838_789_cp2_scam01209_garde_209a_scam______09p02.fits	Garde	209
scam_0210_0685577665_463_cp2_scam01210_garde_210_scam_______01p02.fits	Garde	210
scam_0210_0685577900_430_cp2_scam01210_garde_210_scam_______02p02.fits	Garde	210
scam_0210_0685578130_405_cp2_scam01210_garde_210_scam_______03p02.fits	Garde	210
scam_0210_0685578396_399_cp2_scam01210_garde_210_scam_______04p02.fits	Garde	210
scam_0210_0685578628_366_cp2_scam01210_garde_210_scam_______05p02.fits	Garde	210
scam_0210_0685578860_411_cp2_scam01210_garde_210_scam_______06p02.fits	Garde	210
scam_0210_0685579125_412_cp2_scam01210_garde_210_scam_______07p02.fits	Garde	210
scam_0210_0685579355_357_cp2_scam01210_garde_210_scam_______08p02.fits	Garde	210
scam_0210_0685579666_464_cp2_scam01210_garde_210_scam_______09p02.fits	Garde	210
scam_0211_0685666430_321_cp2_scam04211_penne________________01p02.fits	Penne	211
scam_0211_0685666730_416_cp2_scam04211_penne________________02p02.fits	Penne	211
scam_0211_0685667025_444_cp2_scam04211_penne________________03p02.fits	Penne	211
scam_0211_0685667481_337_cp2_scam04211_penne________________04p02.fits	Penne	211
scam_0211_0685667779_368_cp2_scam04211_penne________________05p02.fits	Penne	211
scam_0211_0685668073_399_cp2_scam04211_penne________________06p02.fits	Penne	211
scam_0211_0685668528_311_cp2_scam04211_penne________________07p02.fits	Penne	211
scam_0211_0685668825_364_cp2_scam04211_penne________________08p02.fits	Penne	211
scam_0211_0685669120_324_cp2_scam04211_penne________________09p02.fits	Penne	211
scam_0211_0685669488_336_cp2_scam04211_penne________________10p02.fits	Penne	211

Table 13. Concentrations of carboxylates derived from SuperCam data analyzed here.

Target	**wt. % oxalate <45 µm**	**wt. % acetate <45 µm**	**wt. % formate <45 µm**	**wt. % carbonate[a] <45 µm**	**wt. % carbonate[a] 45-75 µm**	**wt. % carbonate[a] 125-250**
Bellegarde	< LOD	< LOD	< LOD	< LOD	< LOD	< LOD
Guillaume	< LOD	< LOD	< LOD	< LOD	< LOD	< LOD
Garde	< LOD	< LOD	< LOD	>> 18.74	18.74	9.75
Garde cuttings	< LOD	< LOD	< LOD	>> 11.48	11.48	6.12
Penne	< LOD	< LOD	< LOD	>>21.19	21.19	10.96

[a] The carbonate is assumed to be magnesite, a combination of magnesite and siderite, or a Fe-rich phase like breunnerite. The linear regression parameters of the calcite mixtures were used, as the absorption strength of magnesite and calcite are similar, and therefore have similar refractive indices and LODs.

List of Figures

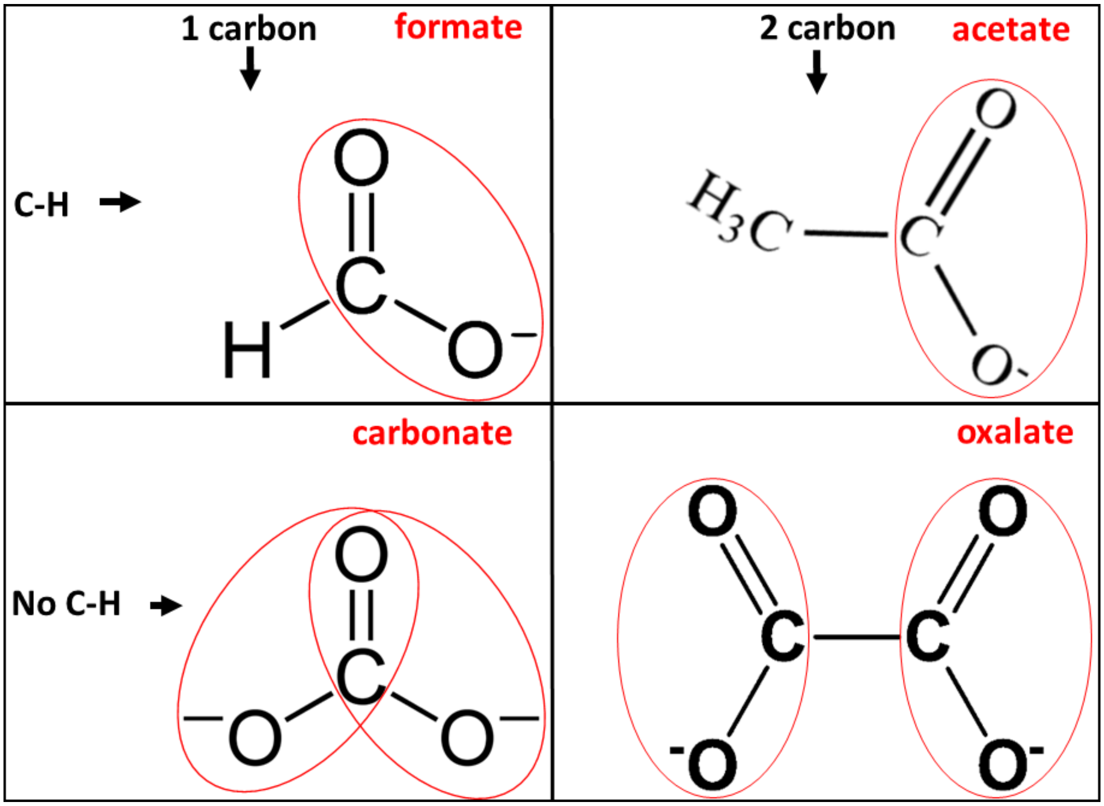

Figure 1. Molecular comparison of the carboxylate conjugate bases that form the minerals used in this study. The carboxyl groups are encircled in red.

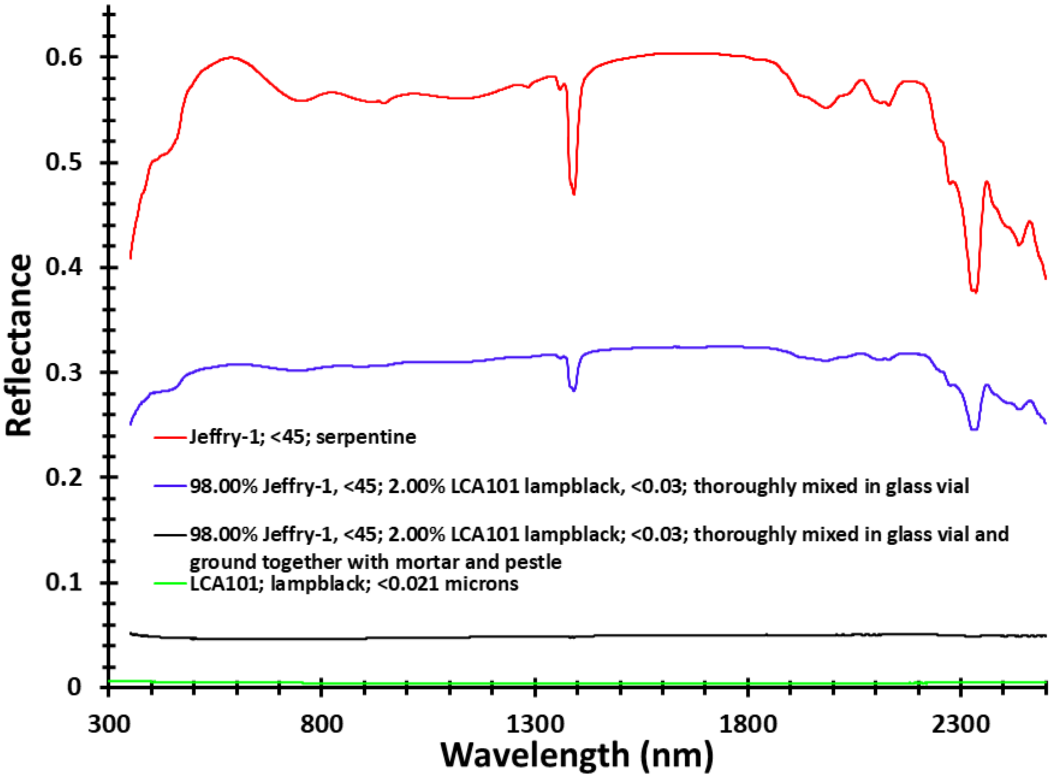

Figure 2a. A comparison of visible and near-infrared reflectance spectra of the same mixture with different mixing techniques. Grinding the samples together produced a much more intimate mixture.

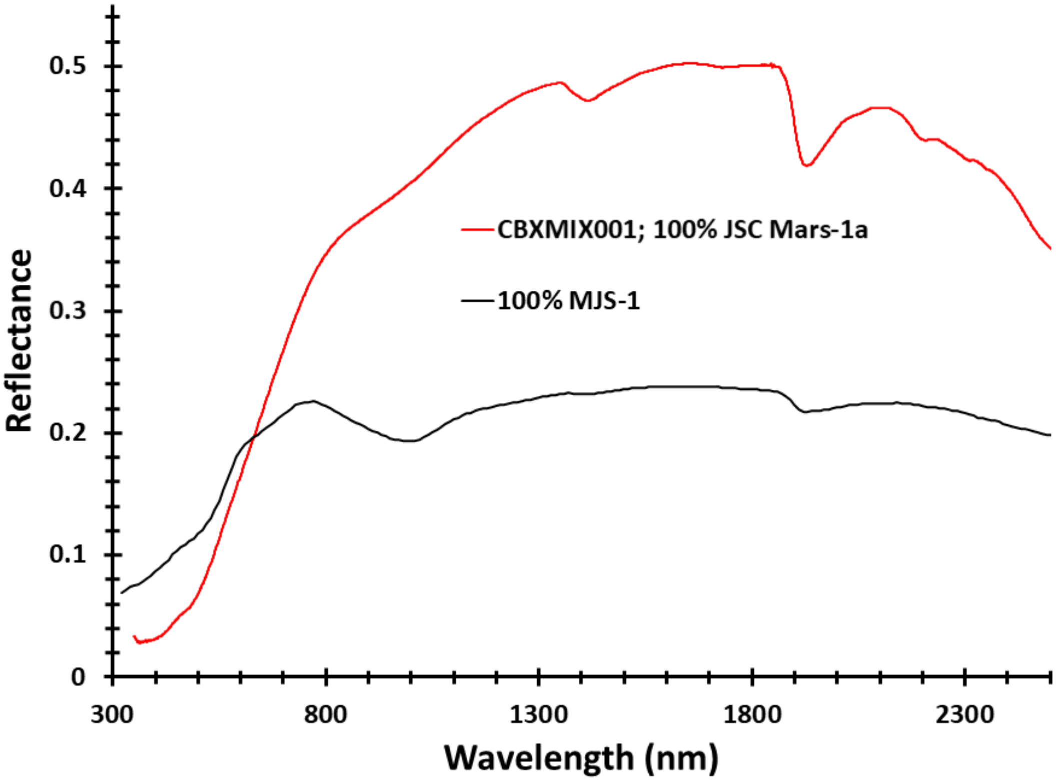

Figure 2b. A comparison of the spectral reflectance characteristics of the two Mars analogue materials used in this study.

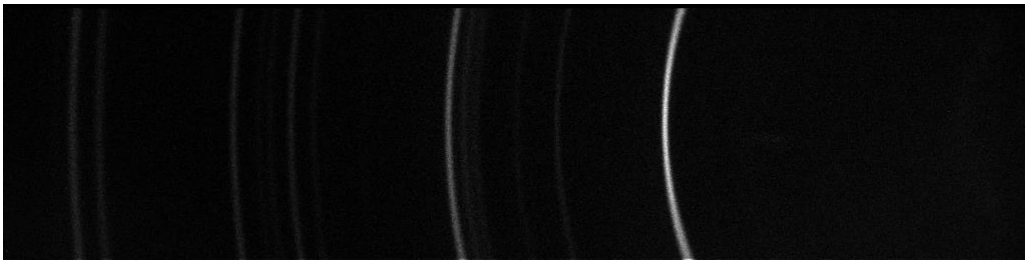

Figure 2c. A 2 dimensional image from the Terra CCD showing the diffraction pattern collected on FRM001 (calcium formate) before circumferential summing.

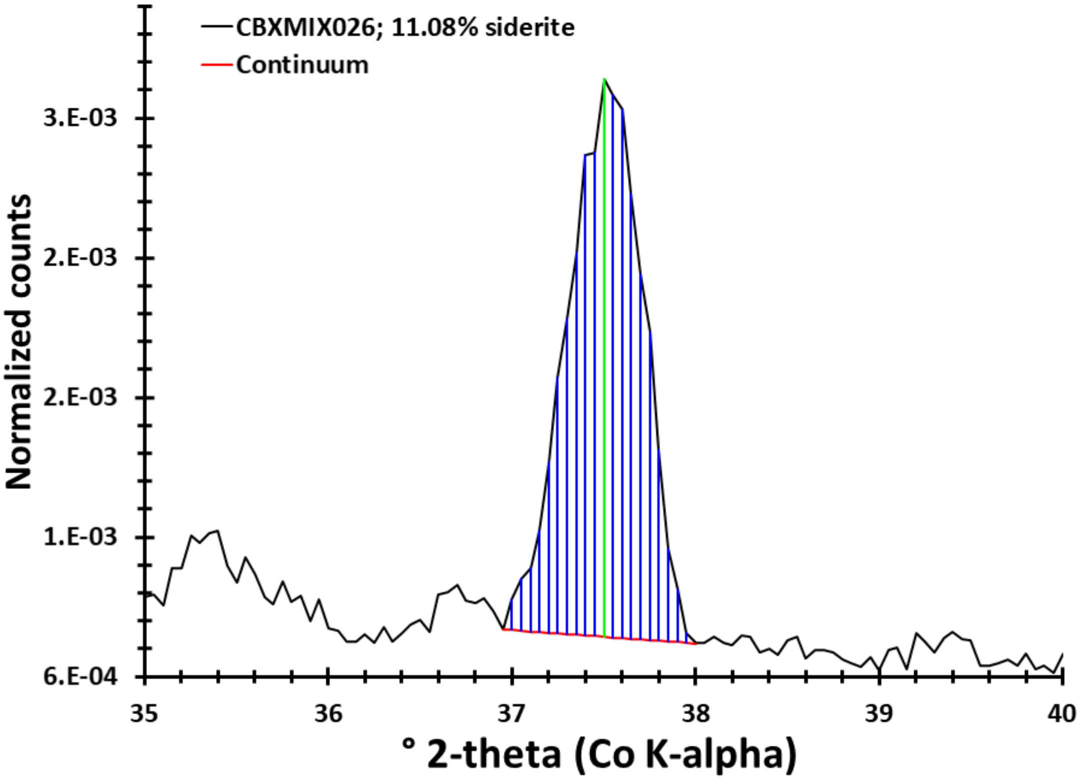

Figure 3a. Representation of the computed straight-line continuum and line of maximum peak amplitude (green) in an X-ray diffractogram.

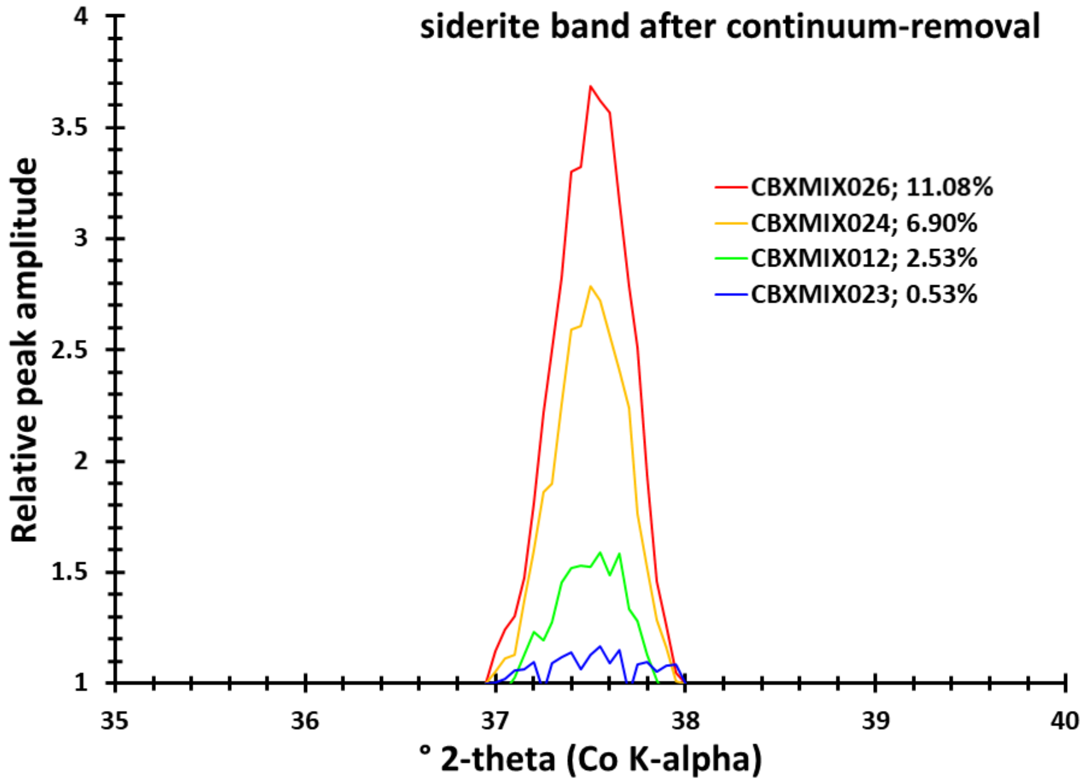

Figure 3b. Relative diffraction peaks after continuum-removal for the JSC Mars 1a and siderite mixtures. The maximum value for each pattern is used for computing LODs.

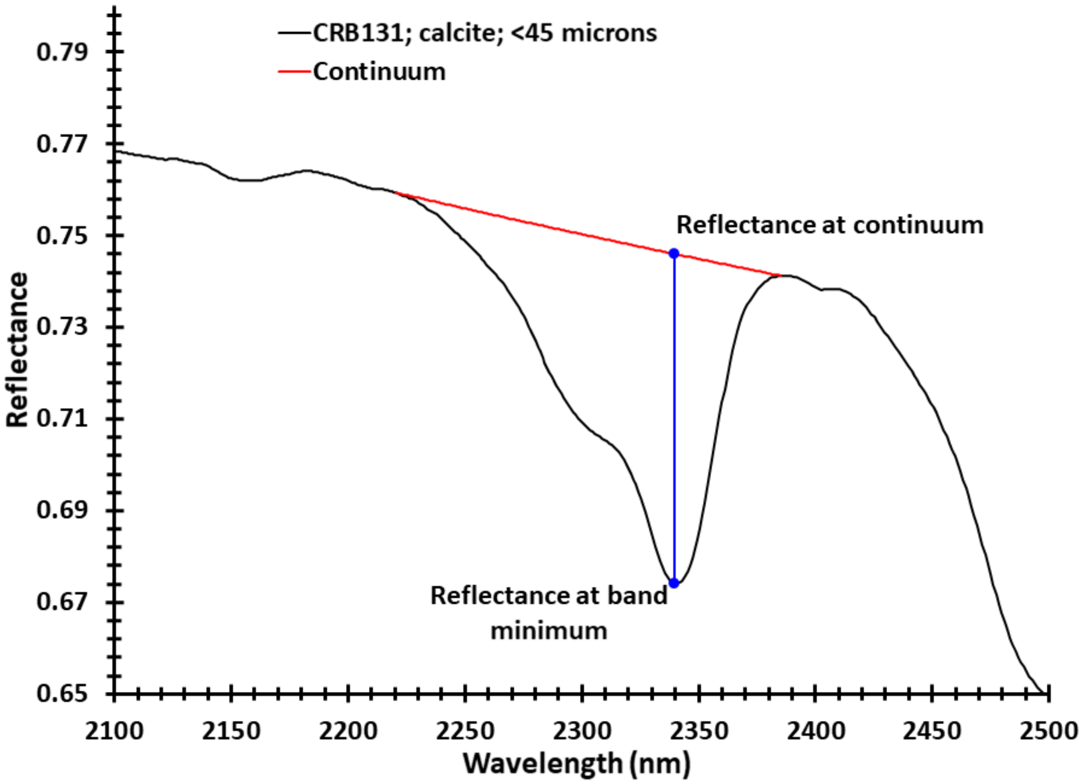

Figure 3c. An example of the continuum across an absorption feature, the band minimum, and the reflectance at the computed straight line continuum.

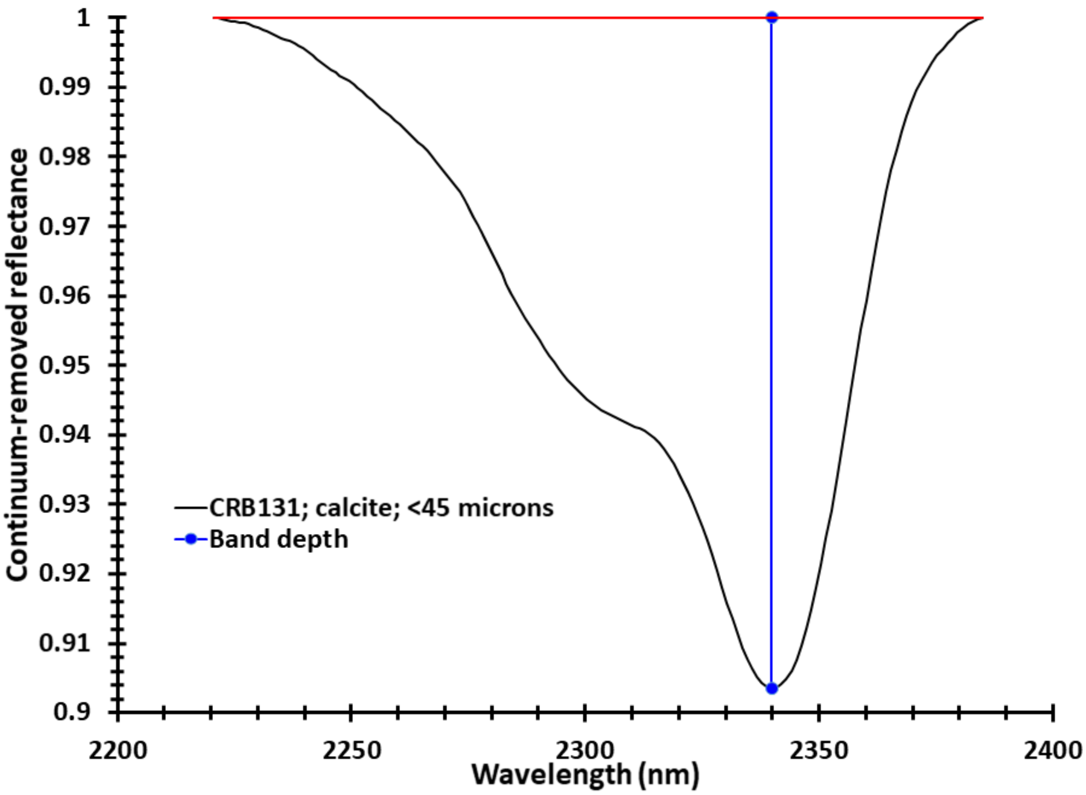

Figure 3d. The absorption band after division by the straight line continuum. This shows how the band depth is calculated by using the two points at the wavelengths where the band minimum is situated.

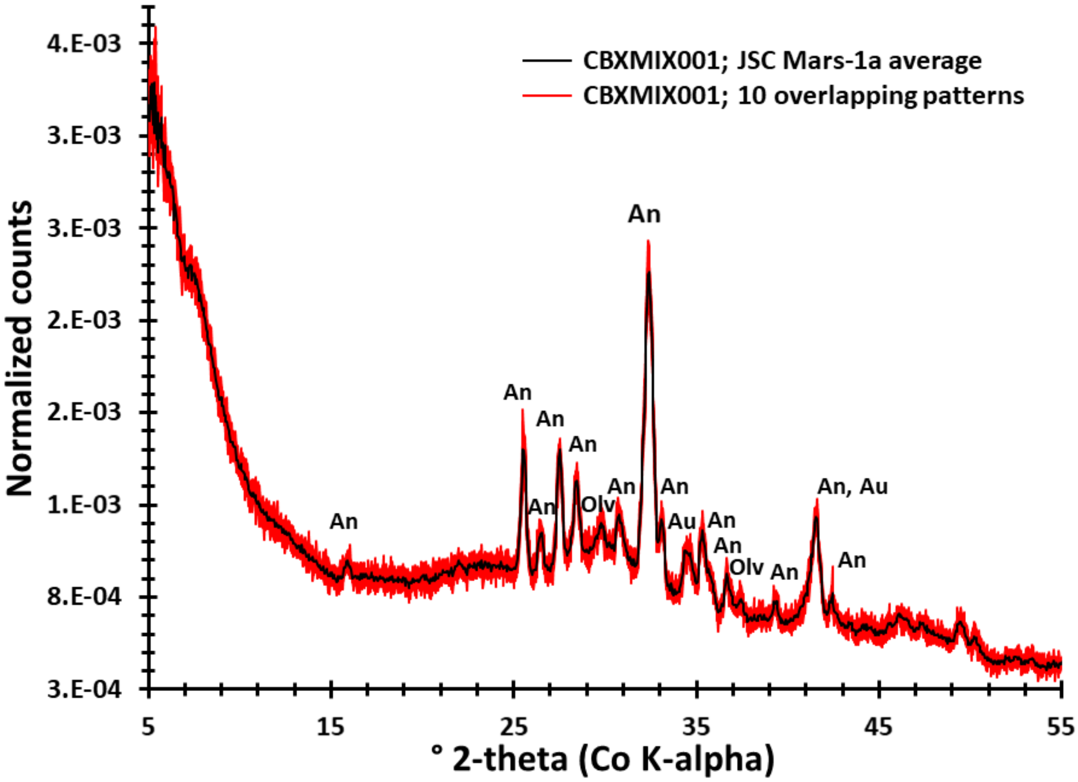

Figure 4. X-ray diffraction patterns for JSC Mars-1a, illustrating the increased S/N with a tenfold increased collection time. An = andesine, Au = augite, Olv = olivine.

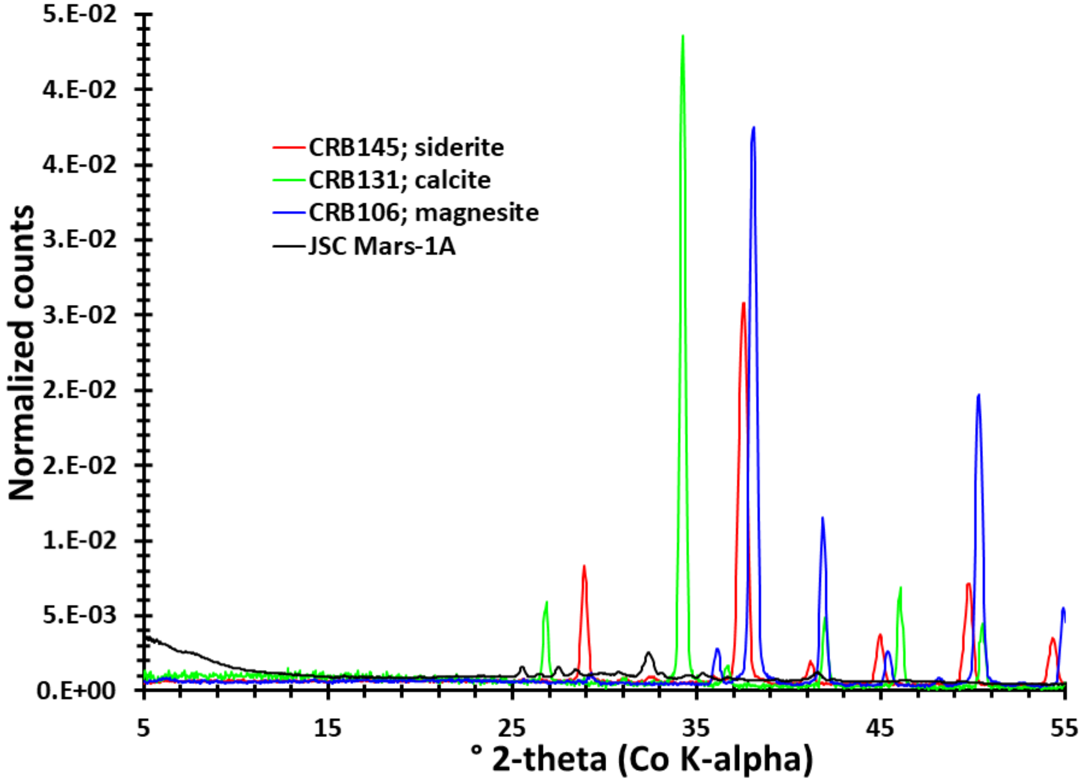

Figure 5a. X-ray diffraction patterns for the carbonate minerals used in this study.

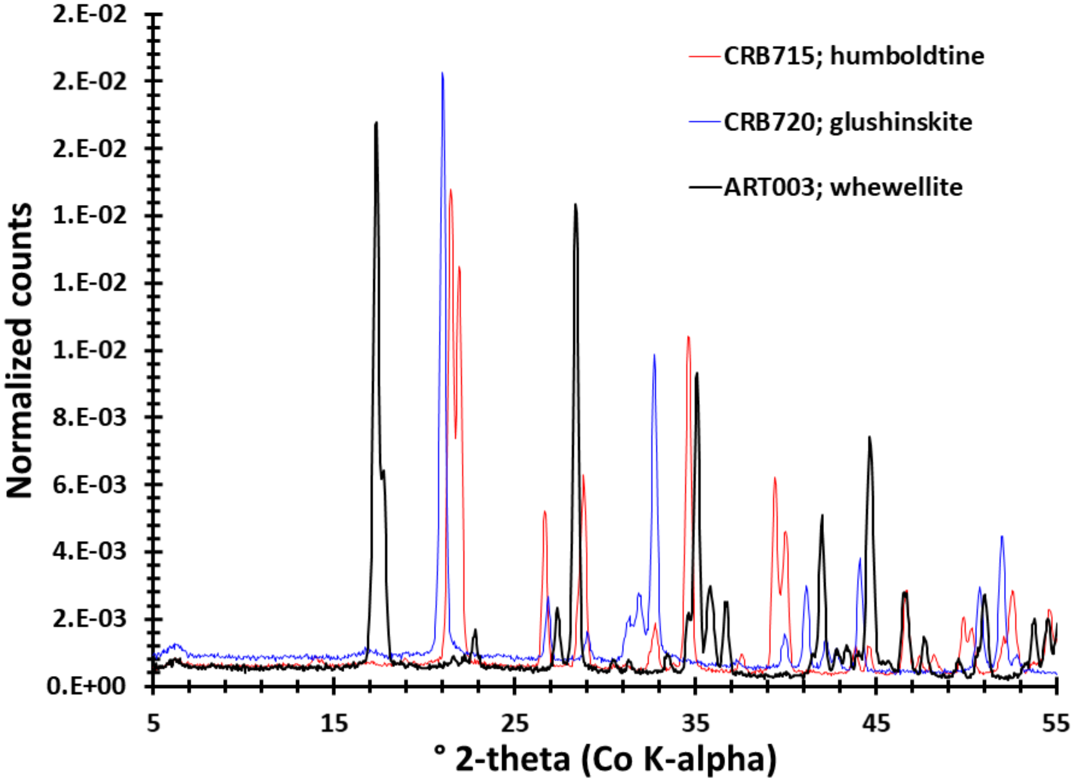

Figure 5b. X-ray diffraction patterns for the oxalate minerals used in this study.

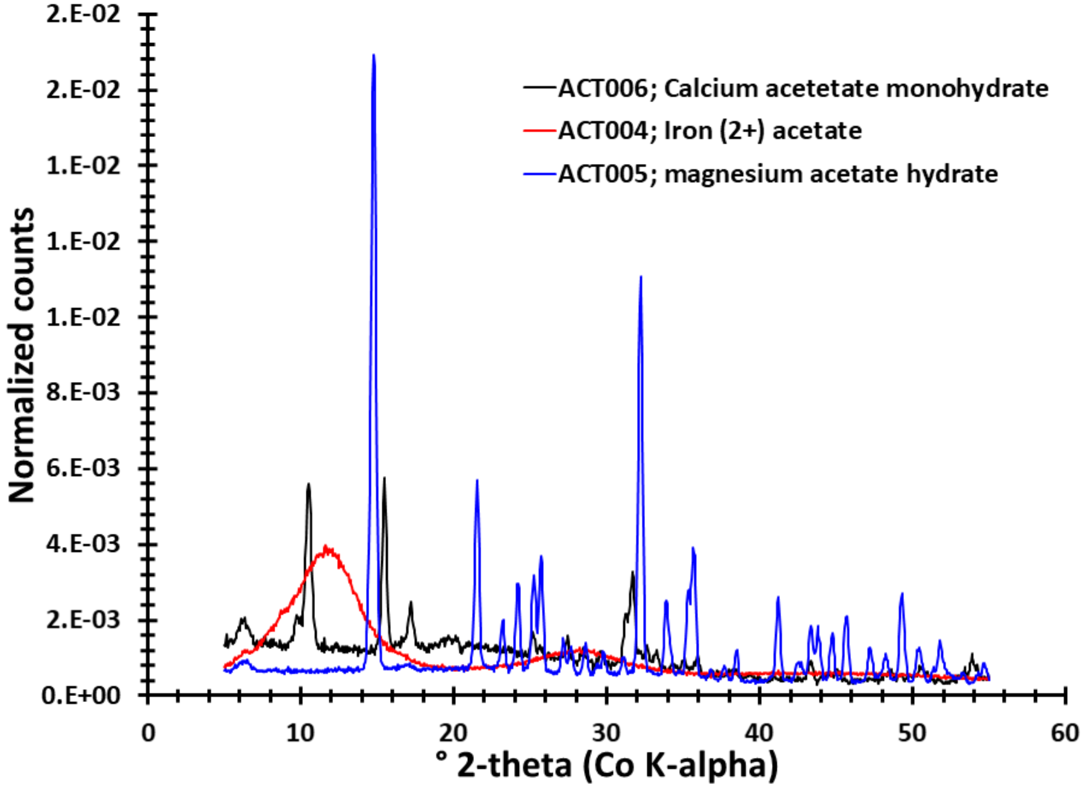

Figure 5c. X-ray diffraction patterns for the acetate minerals used in this study.

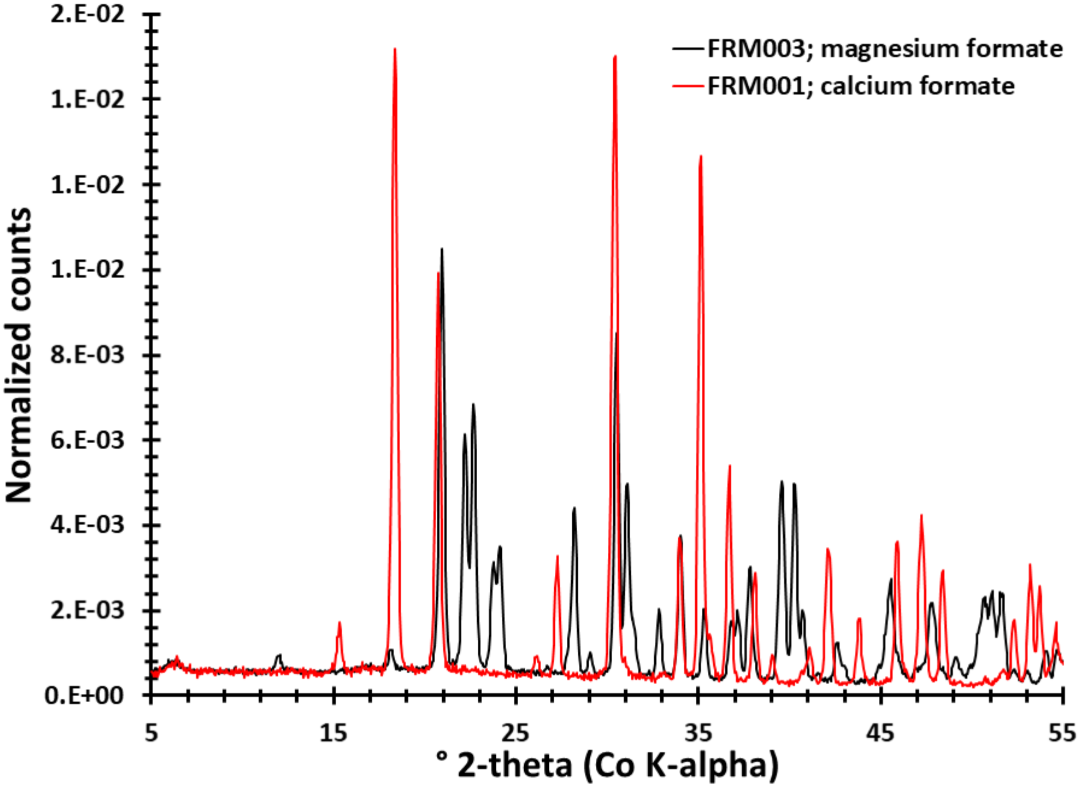

Figure 5d. X-ray diffraction patterns for the formate minerals used in this study.

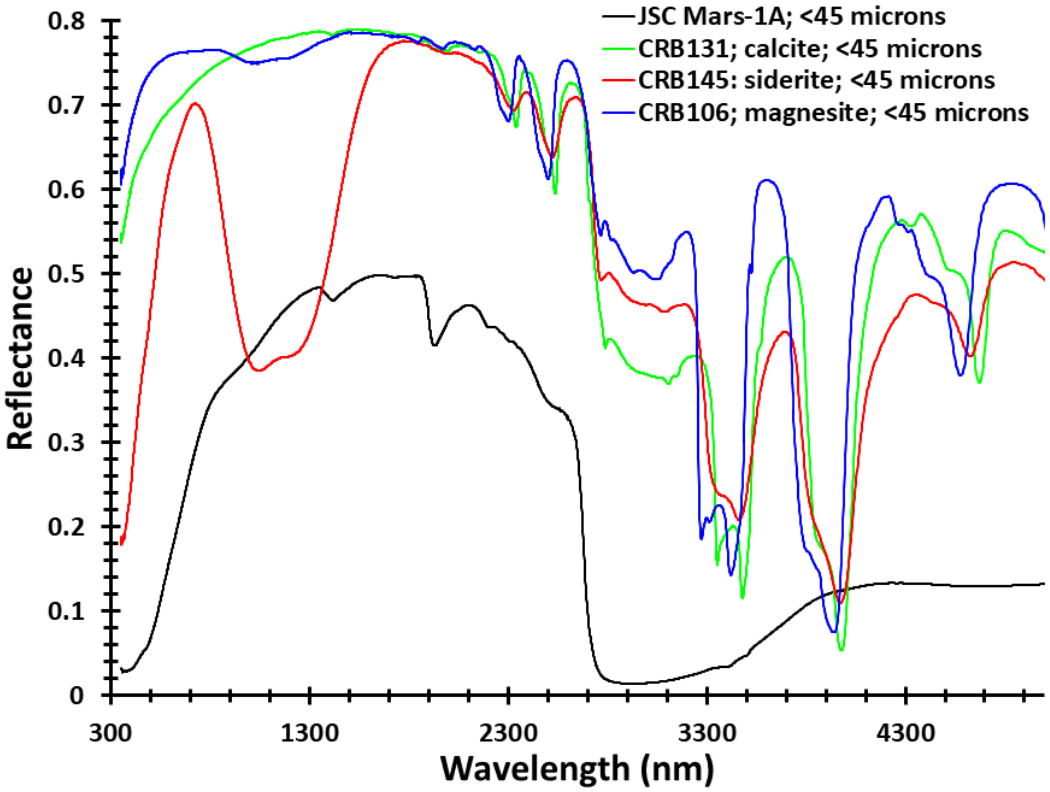

Figure 6a. Reflectance spectra of the JSC Mars-1A analogue and carbonate mineral powders used in this study.

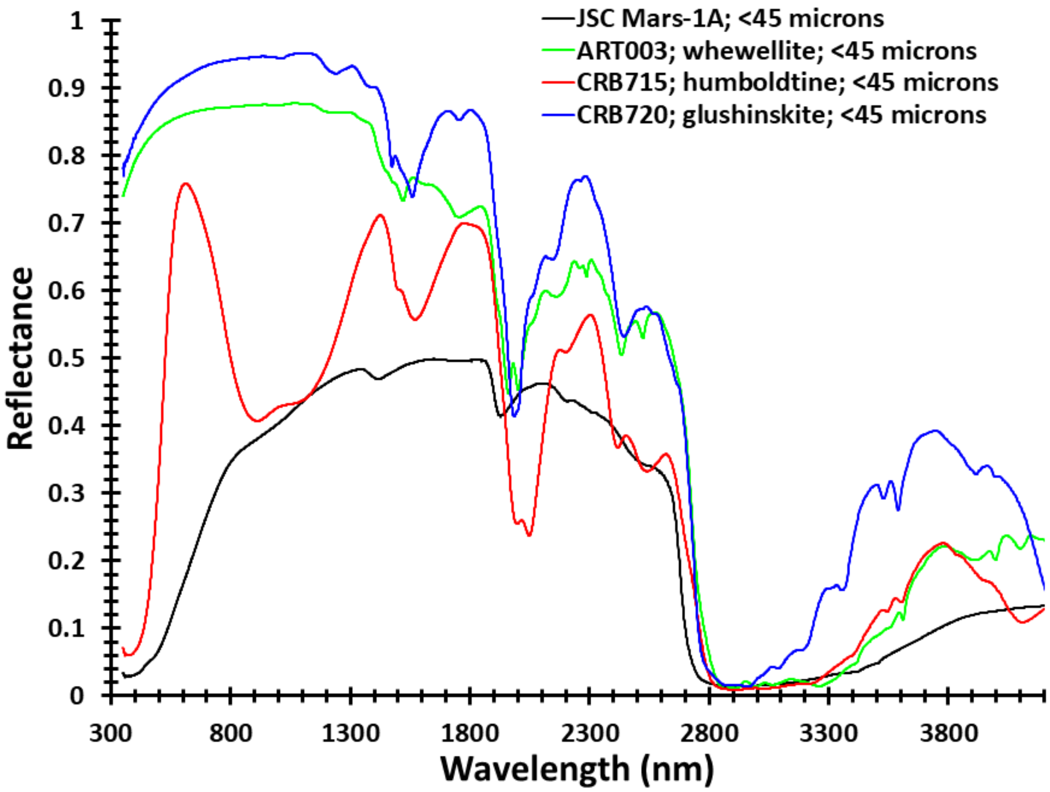

Figure 6b. Reflectance spectra of the JSC Mars-1A analogue and oxalate mineral powders used in this study.

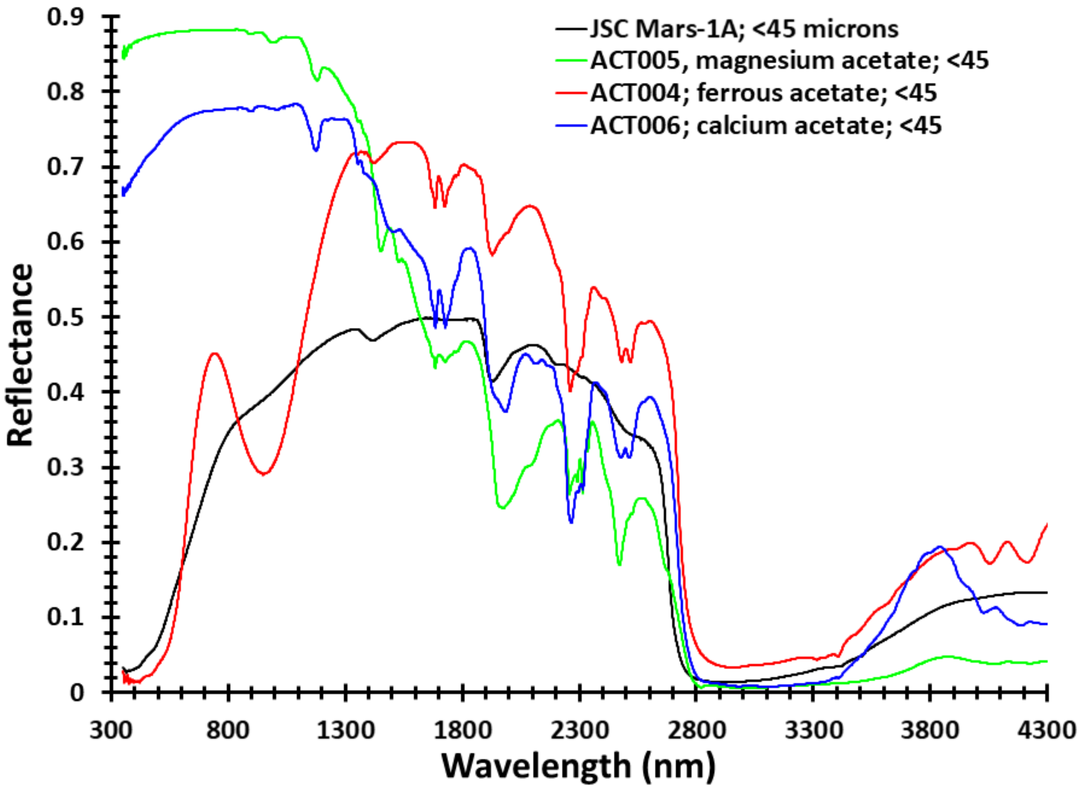

Figure 6c. Reflectance spectra of the JSC Mars-1A analogue and acetate mineral powders used in this study.

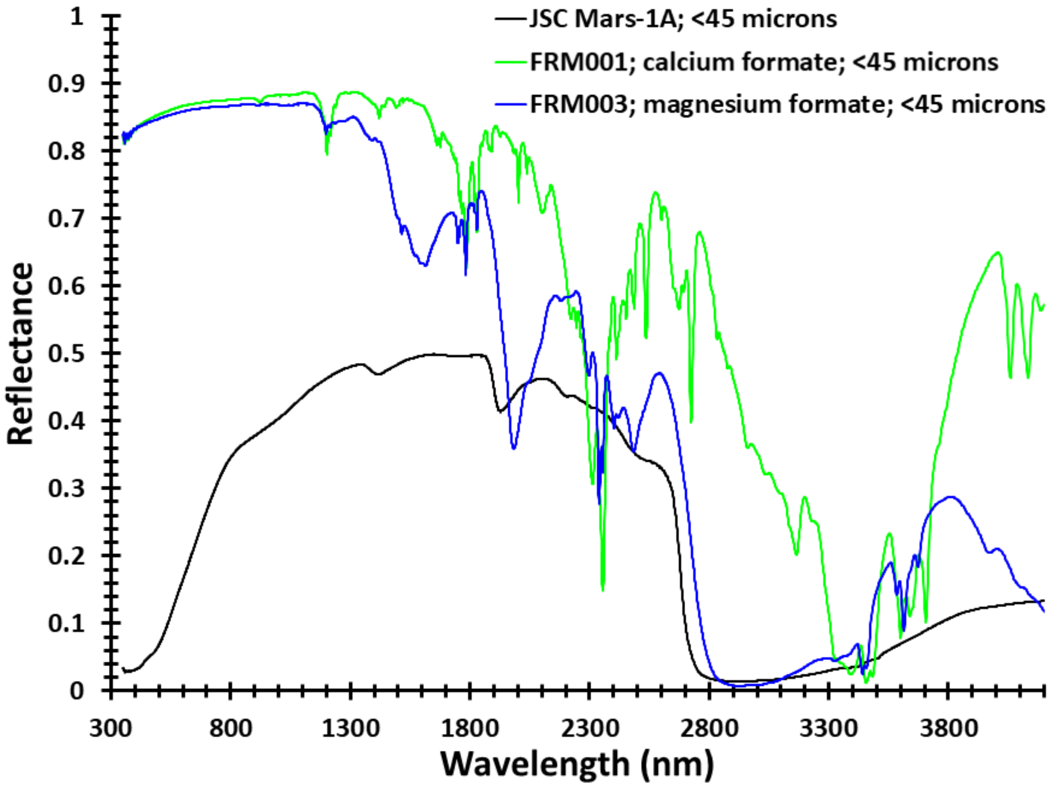

Figure 6d. Reflectance spectra of the JSC Mars-1A analogue and formate mineral powders used in this study.

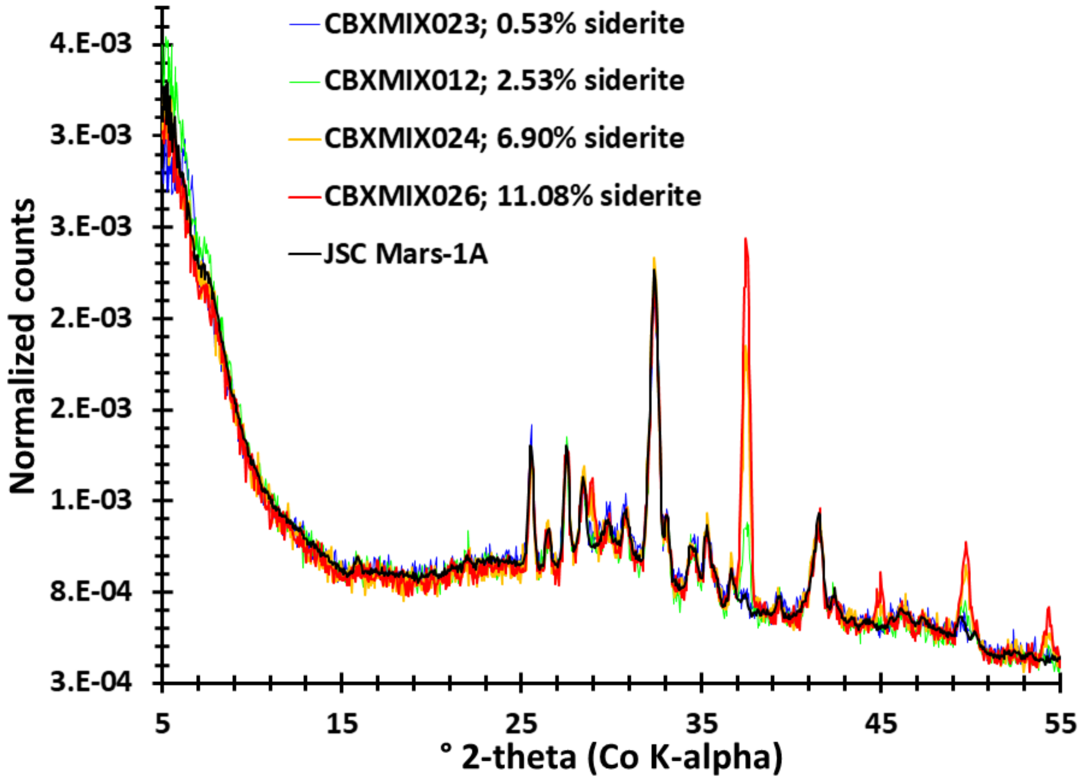

Figure 7a. X-ray diffraction patterns of the JSC Mars-1a + siderite mixtures.

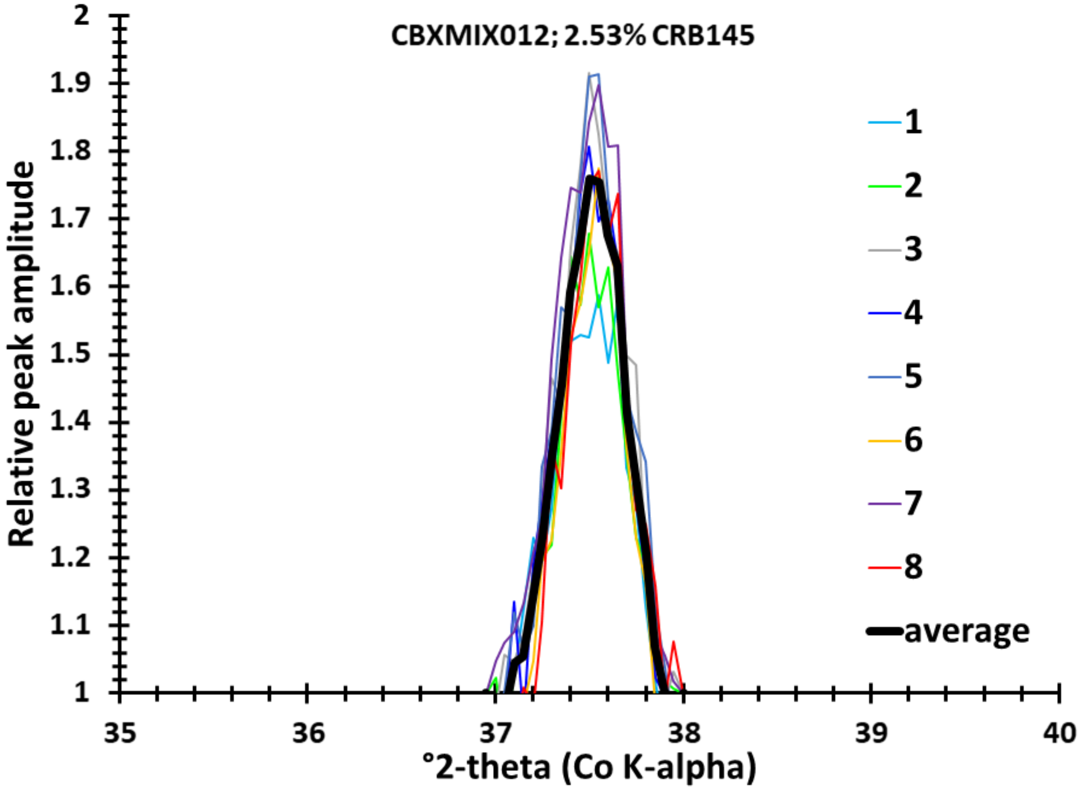

Figure 7b. X-ray diffraction patterns of the JSC Mars-1a + 2.53 wt.% mixture, demonstrating the variance in measured signal between scans.

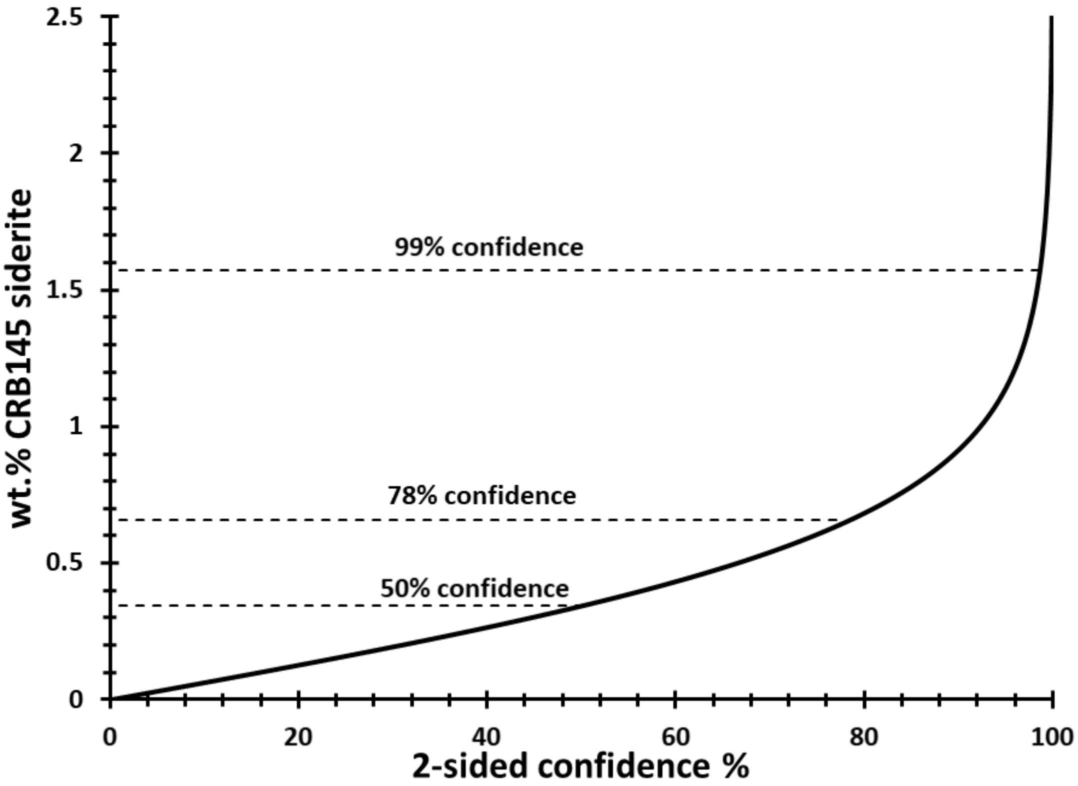

Figure 7c. Graphical demonstration of confidence levels in siderite concentrations determined with this specific method.

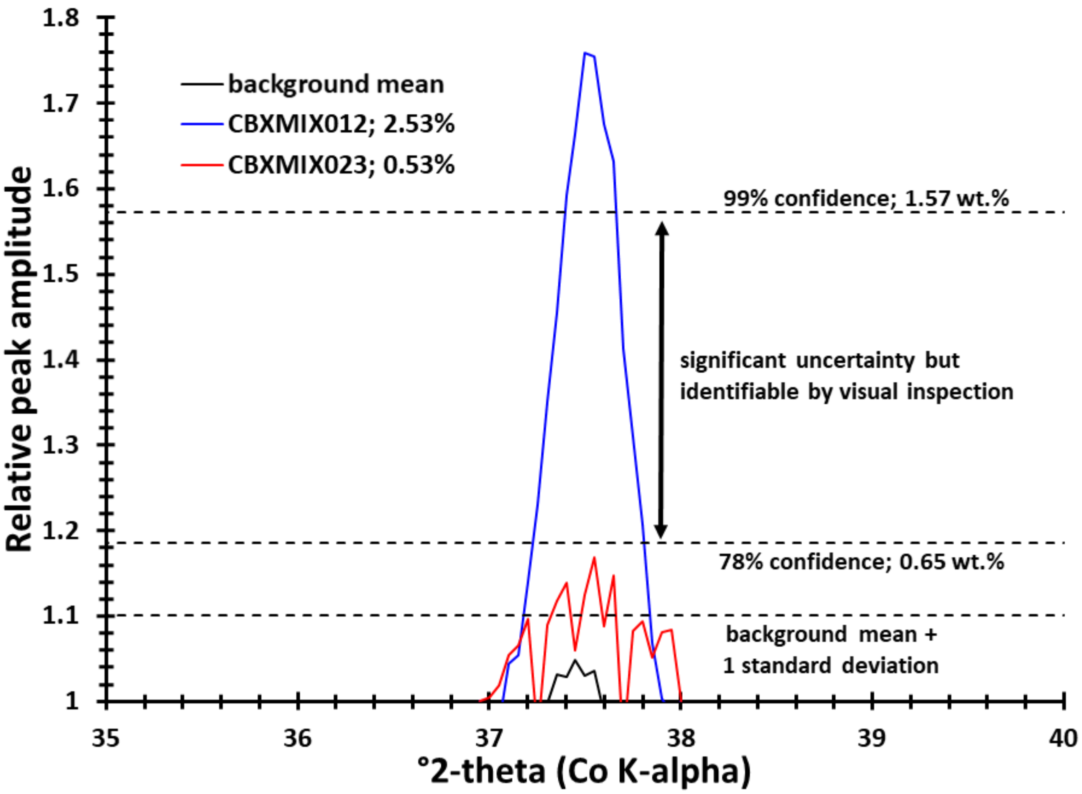

Figure 7d. Graphical demonstration of confidence levels in LOD determinations for CRB145 siderite by XRD.

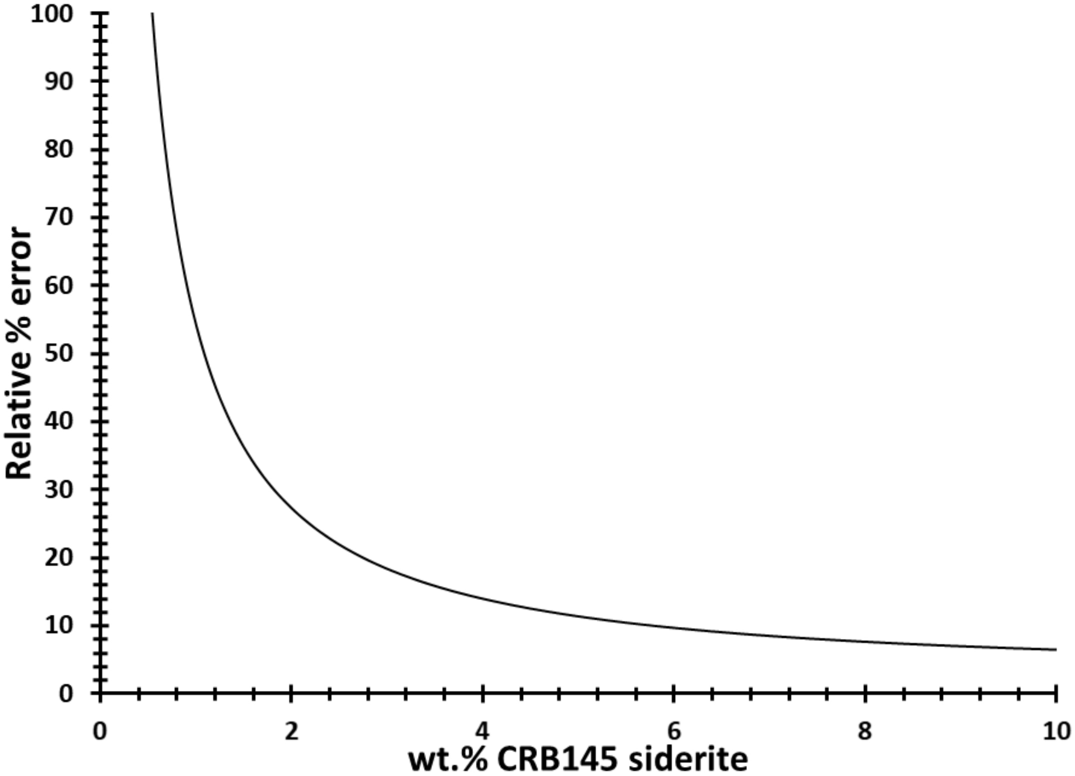

Figure 7e. Relative error percentage for given determined concentrations of siderite by XRD.

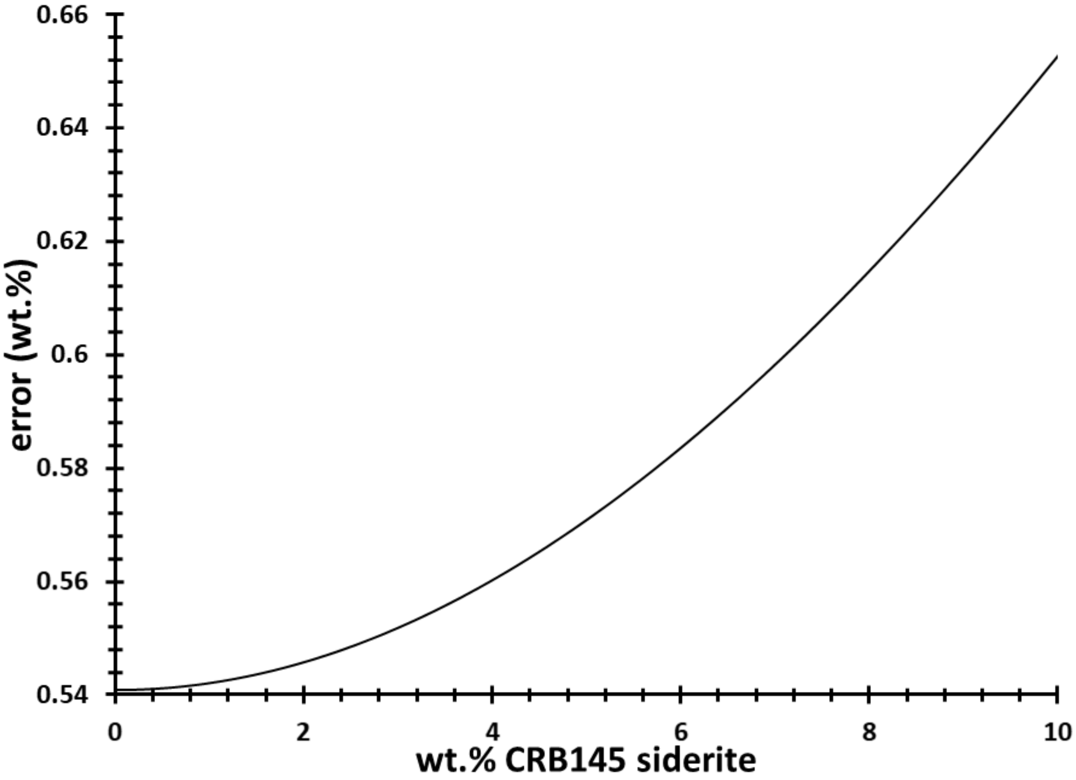

Figure 7f. Error (wt.%) of determined siderite concentration by XRD.

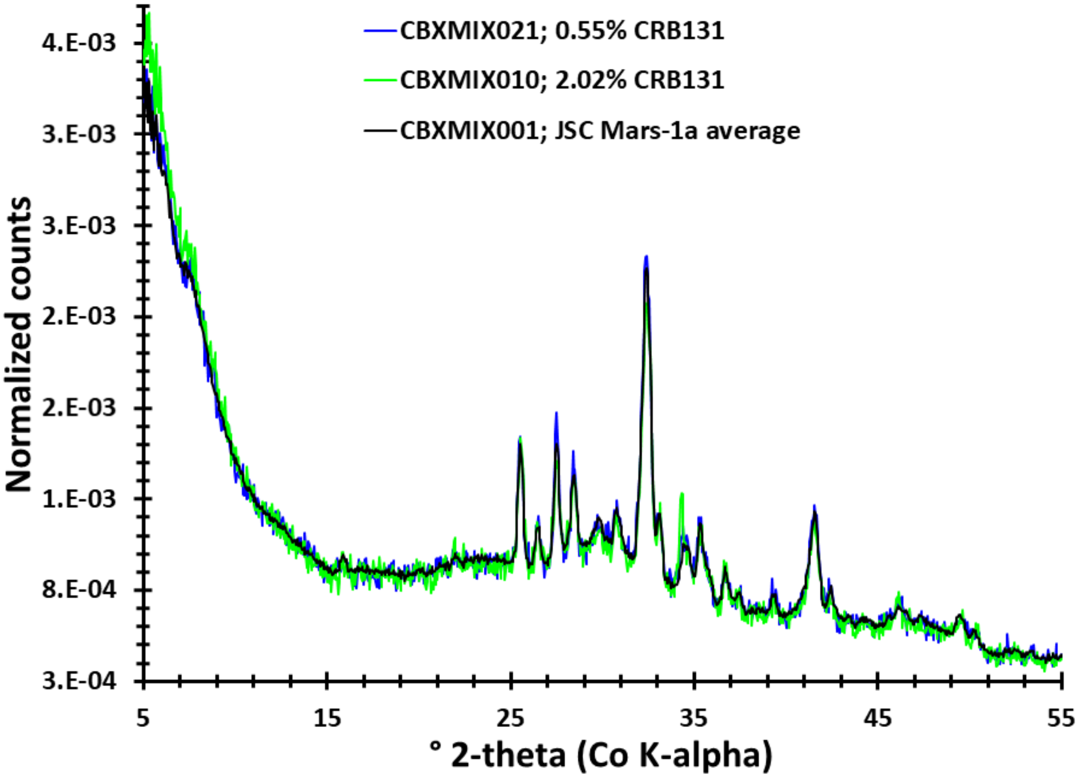

Figure 7g. X-ray diffraction patterns of the JSC Mars-1a + calcite mixtures.

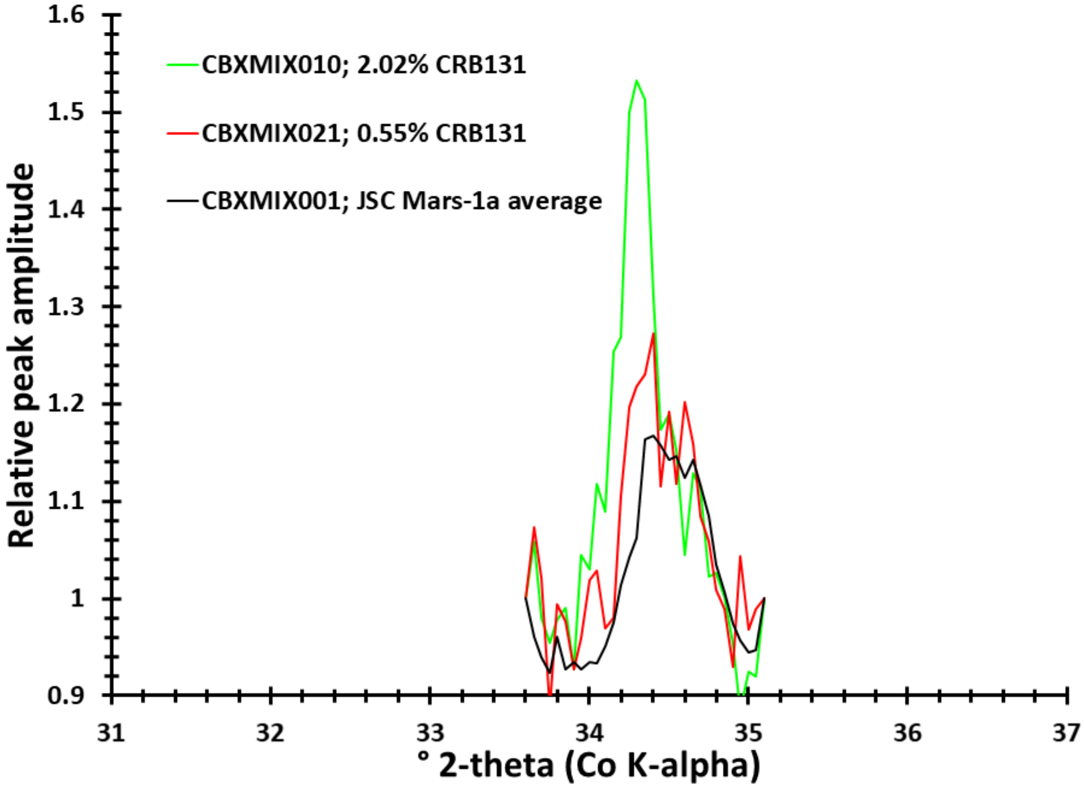

Figure 7h. Continuum-removed XRD patterns of the JSC Mars-1a + calcite mixtures.

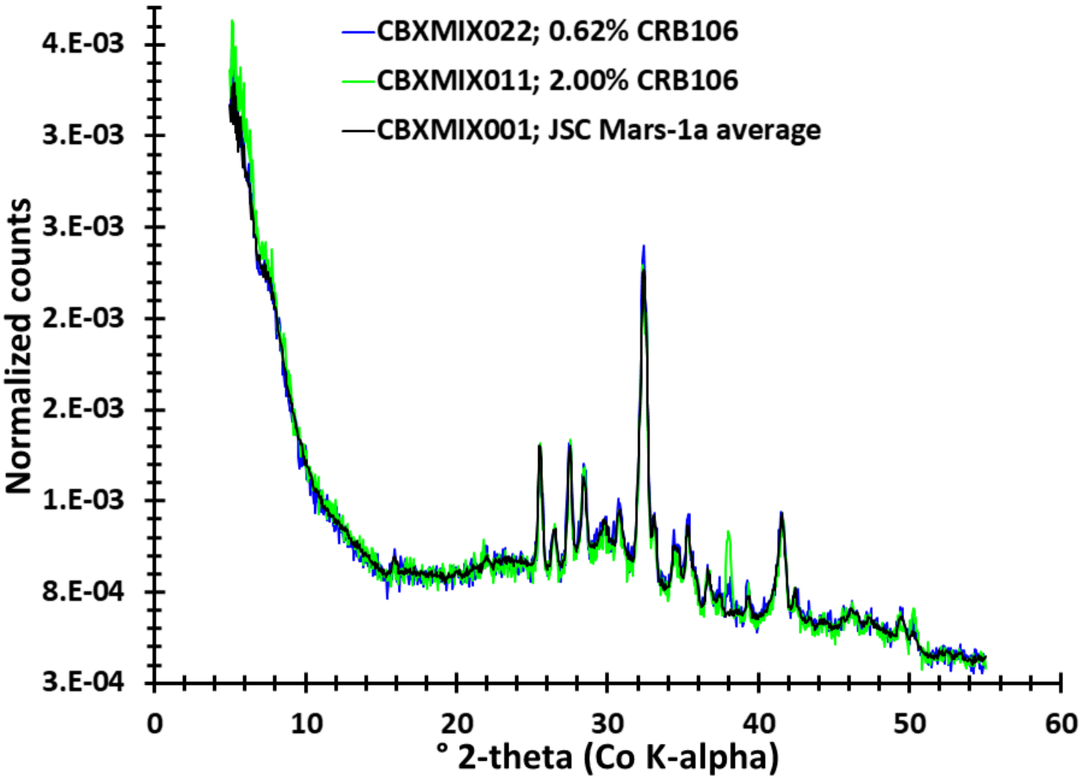

Figure 7i. X-ray diffraction patterns of the JSC Mars-1a + magnesite mixtures.

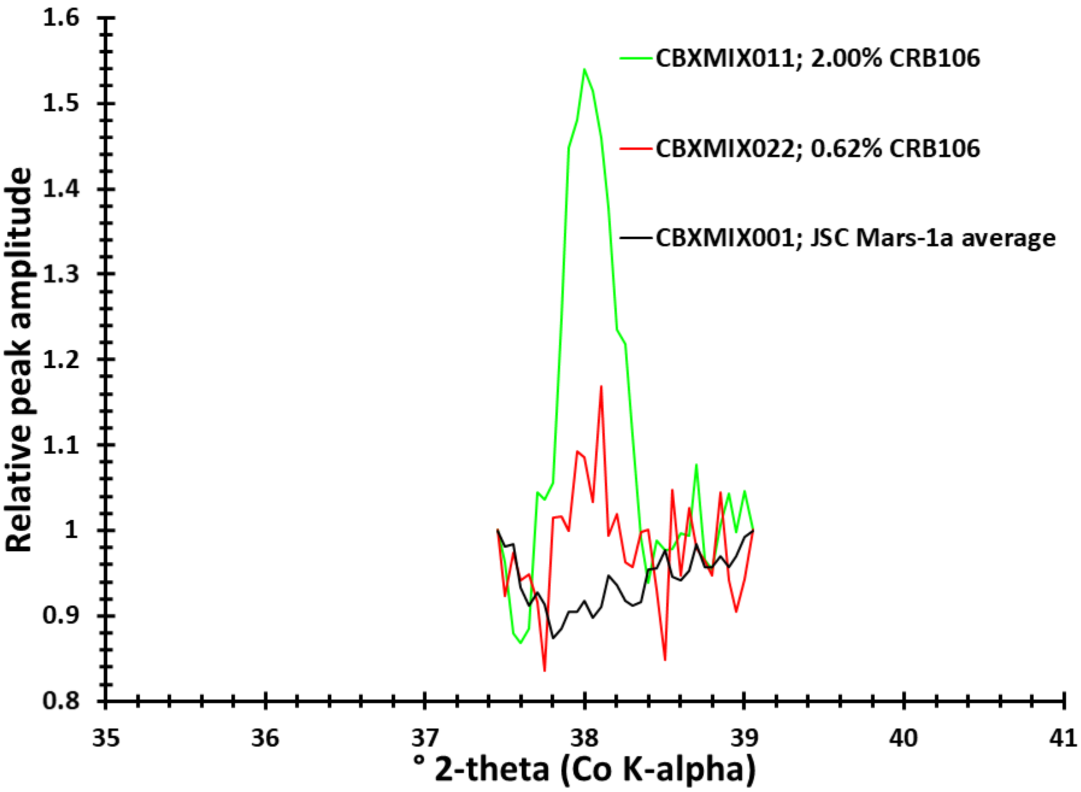

Figure 7j. Continuum-removed XRD patterns of the JSC Mars-1a + magnesite mixtures.

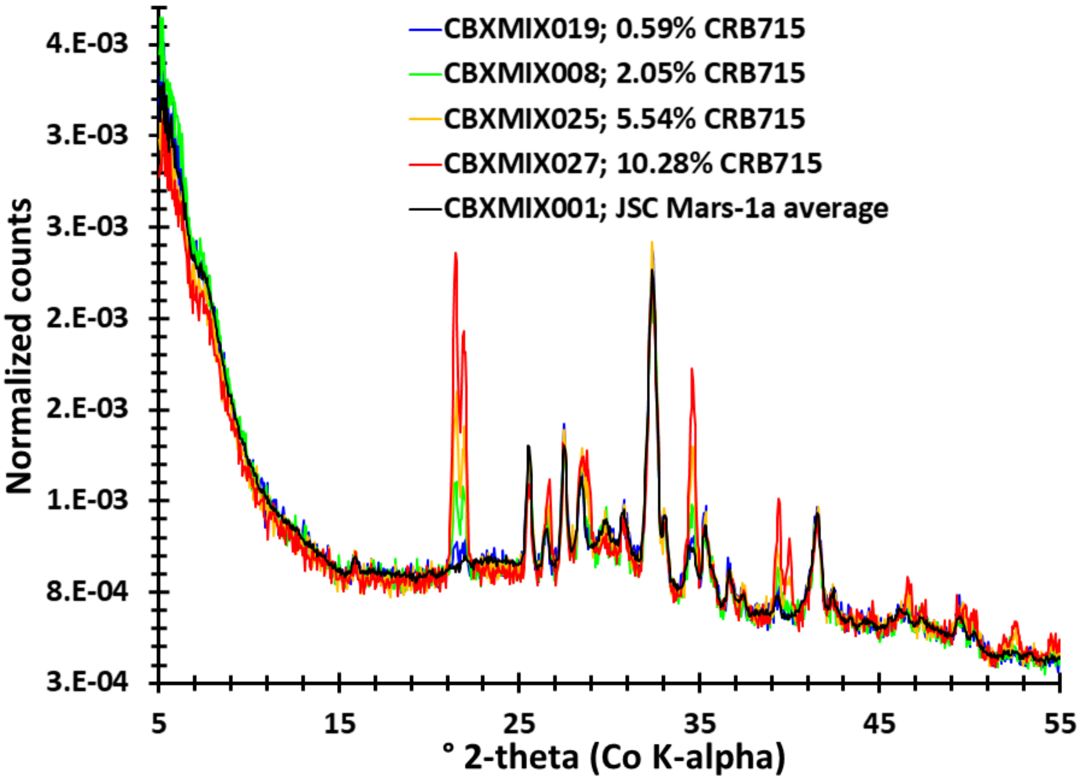

Figure 8a. X-ray diffraction patterns of the JSC Mars-1a + humboldtine mixtures.

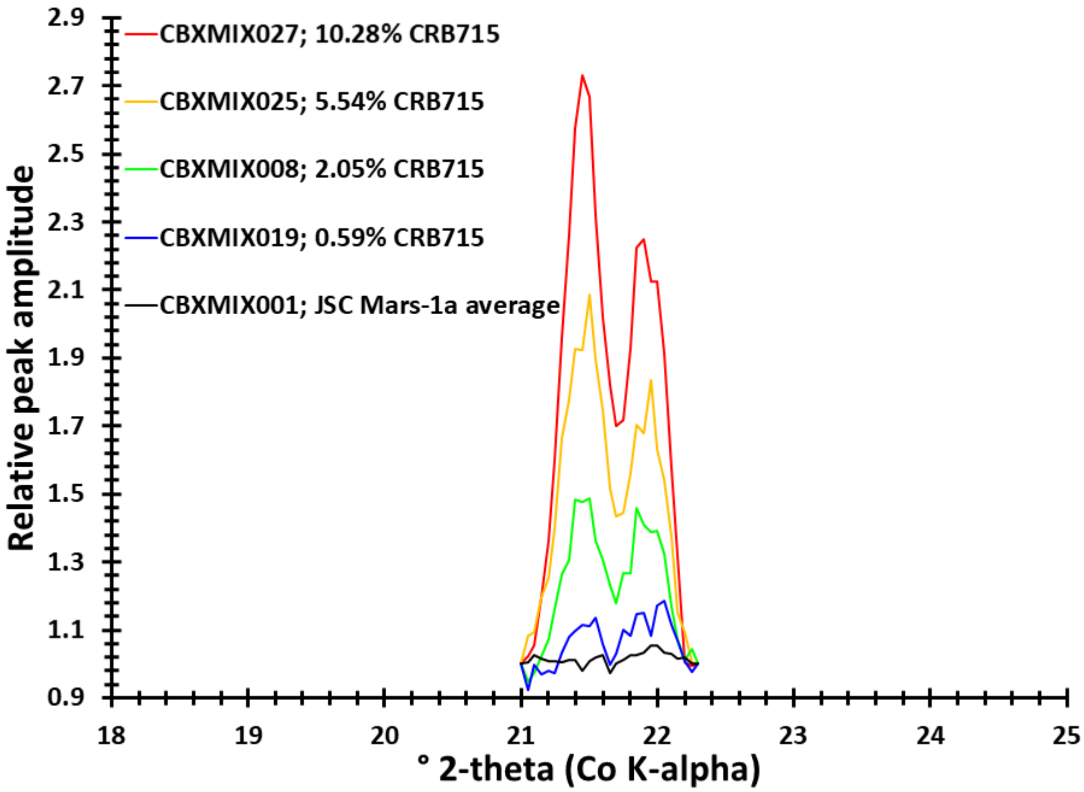

Figure 8b. Continuum-removed XRD patterns of the JSC Mars-1a + humboldtine mixtures.

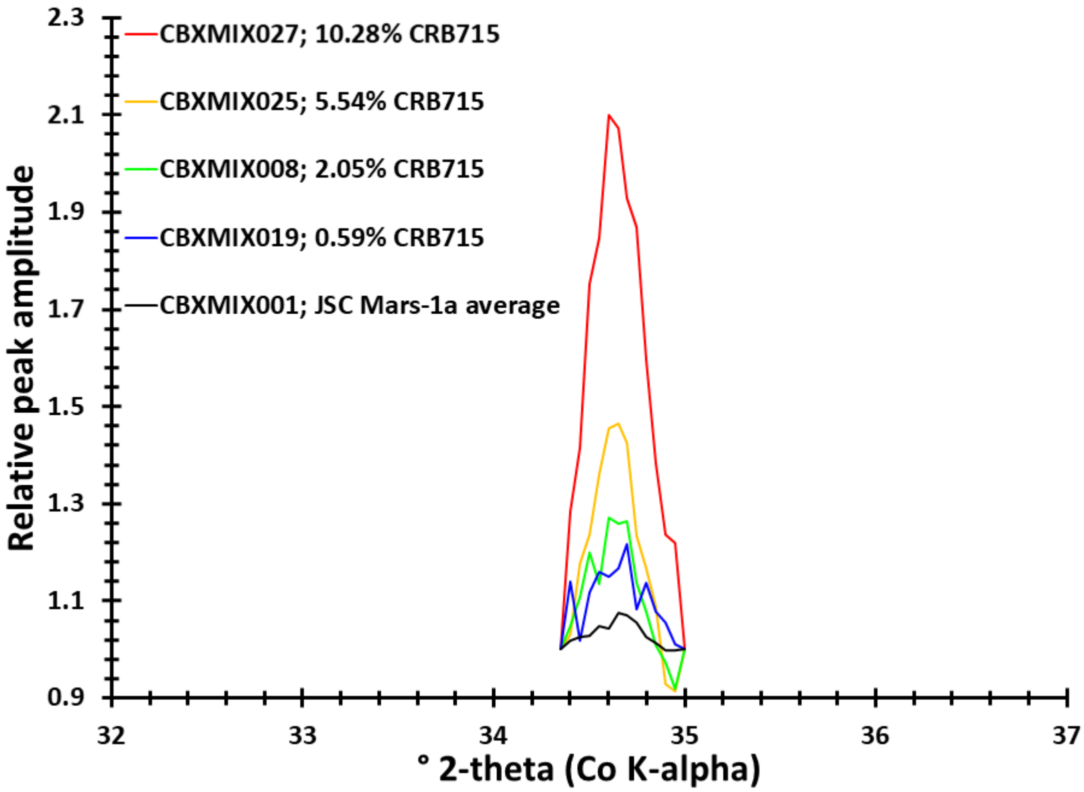

Figure 8c. Continuum-removed XRD patterns of the JSC Mars-1a + humboldtine mixtures.

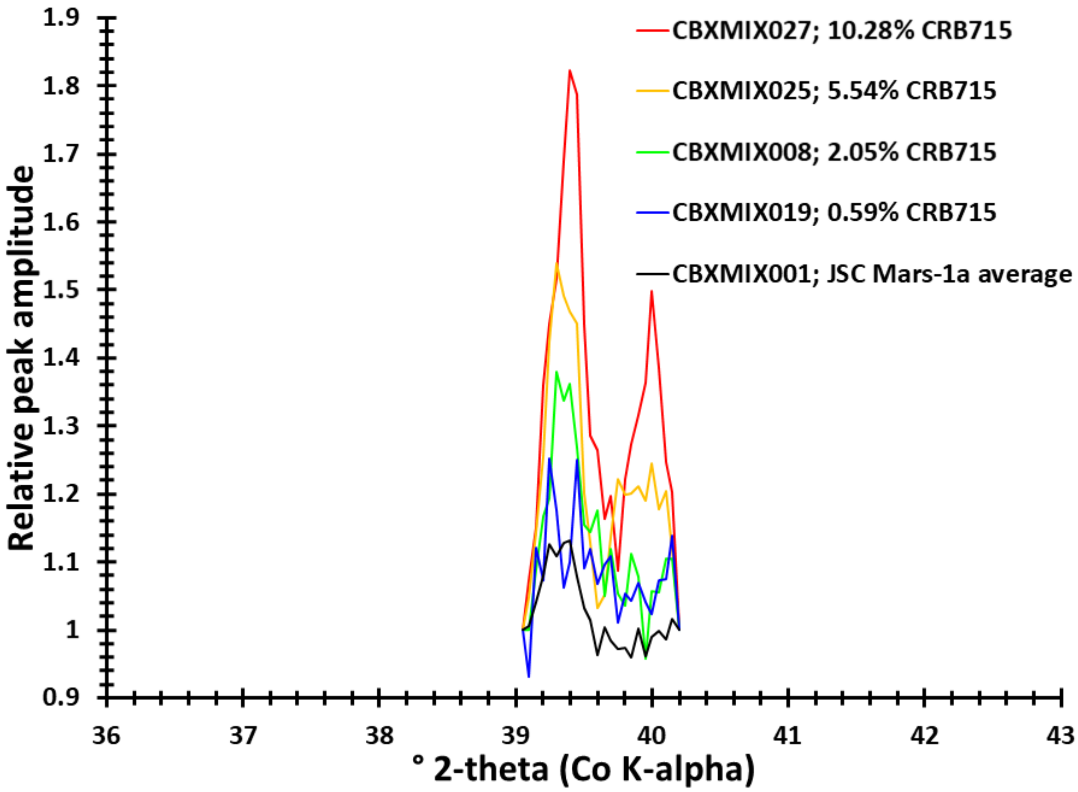

Figure 8d. Continuum-removed XRD patterns of the JSC Mars-1a + humboldtine mixtures.

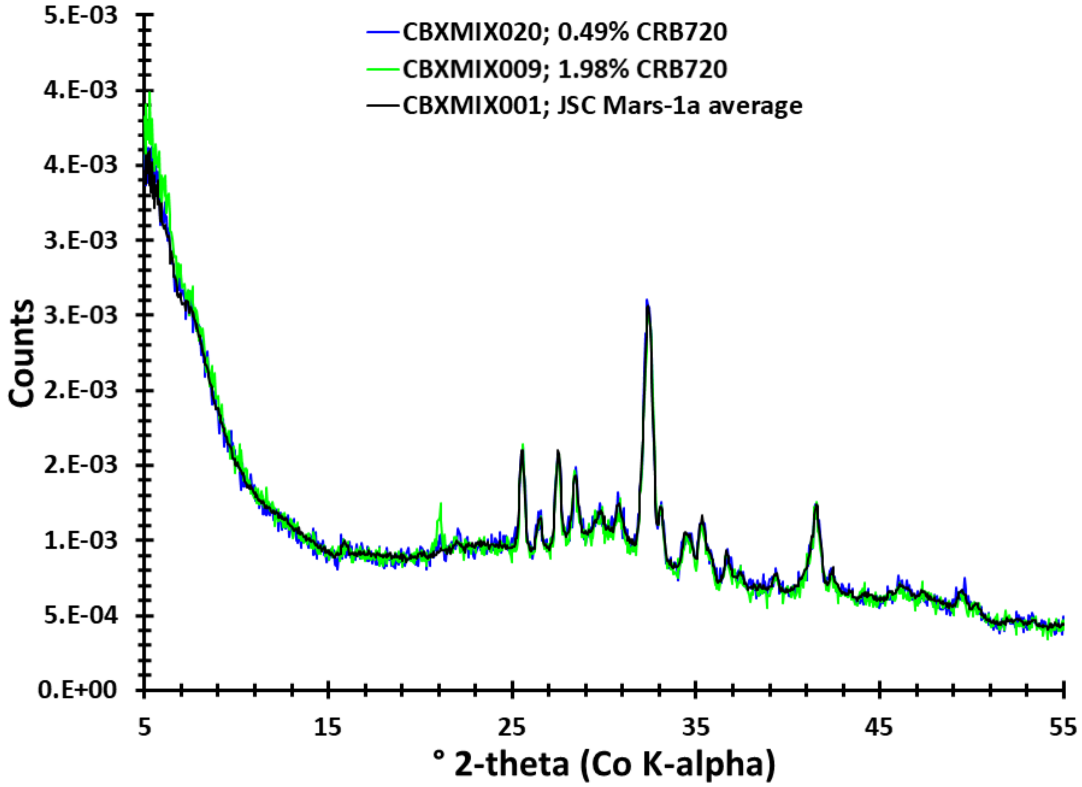

Figure 8e. X-ray diffraction patterns of the JSC Mars-1a + glushinskite mixtures.

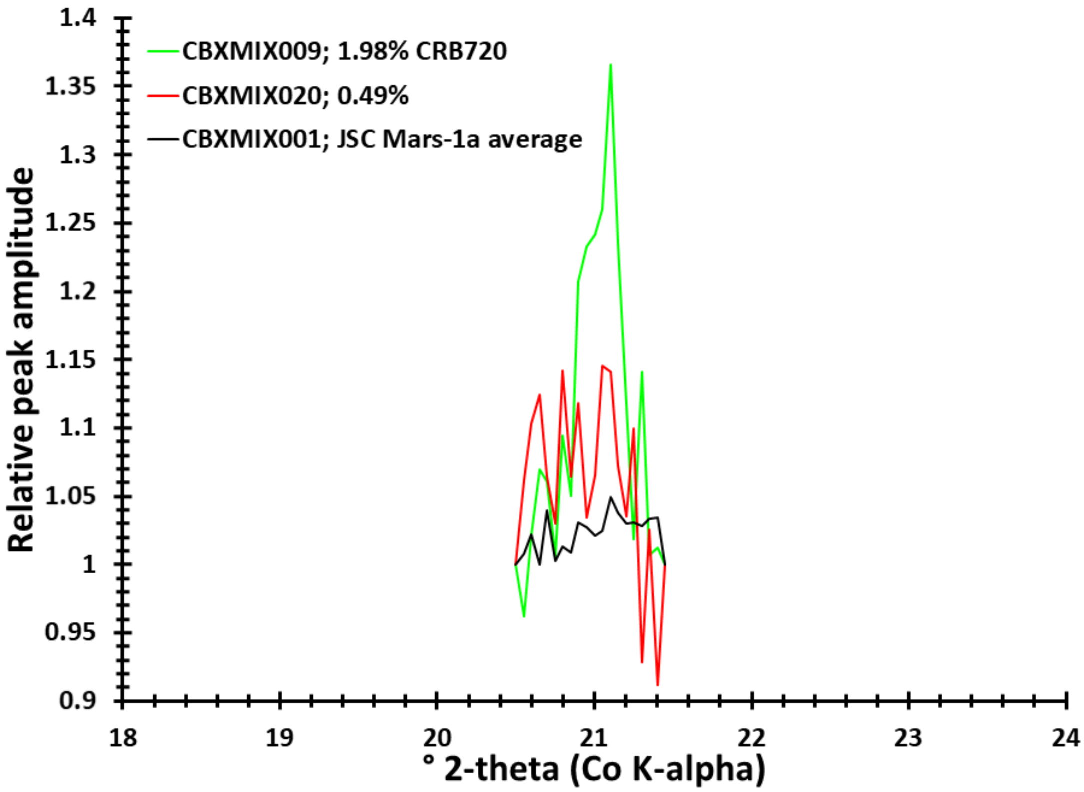

Figure 8f. Continuum-removed XRD patterns of the JSC Mars-1a + glushinskite mixtures.

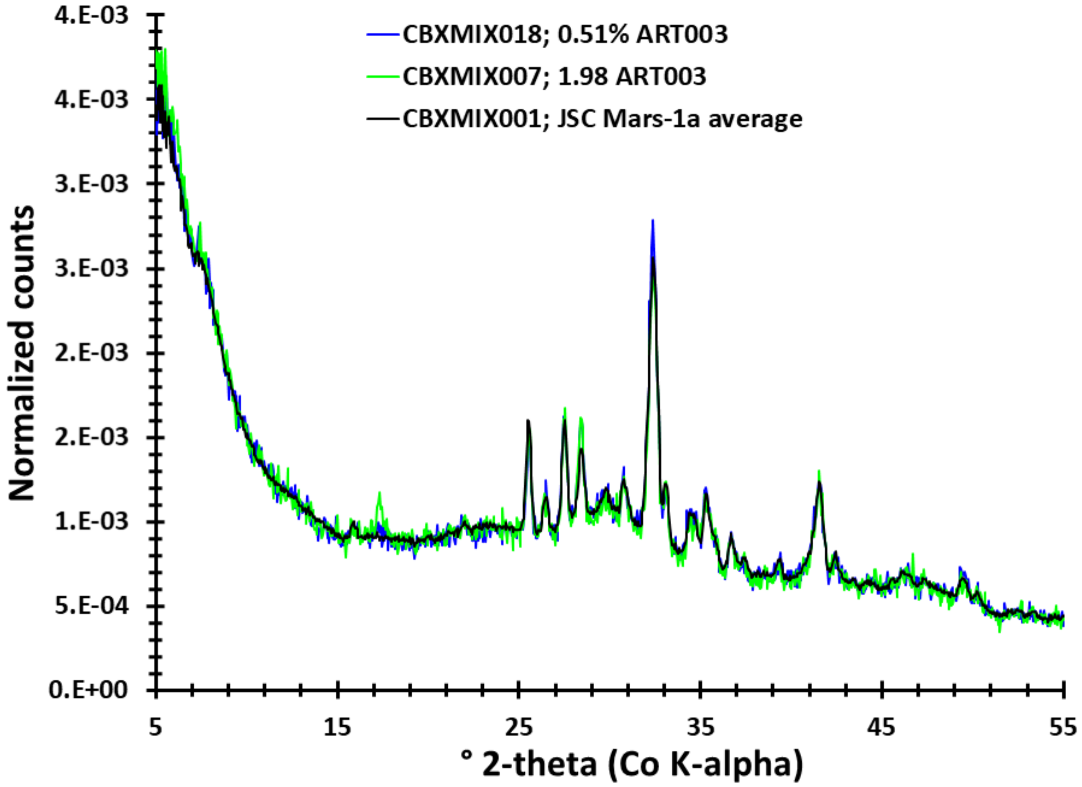

Figure 8g. X-ray diffraction patterns of the JSC Mars-1a + whewellite mixtures.

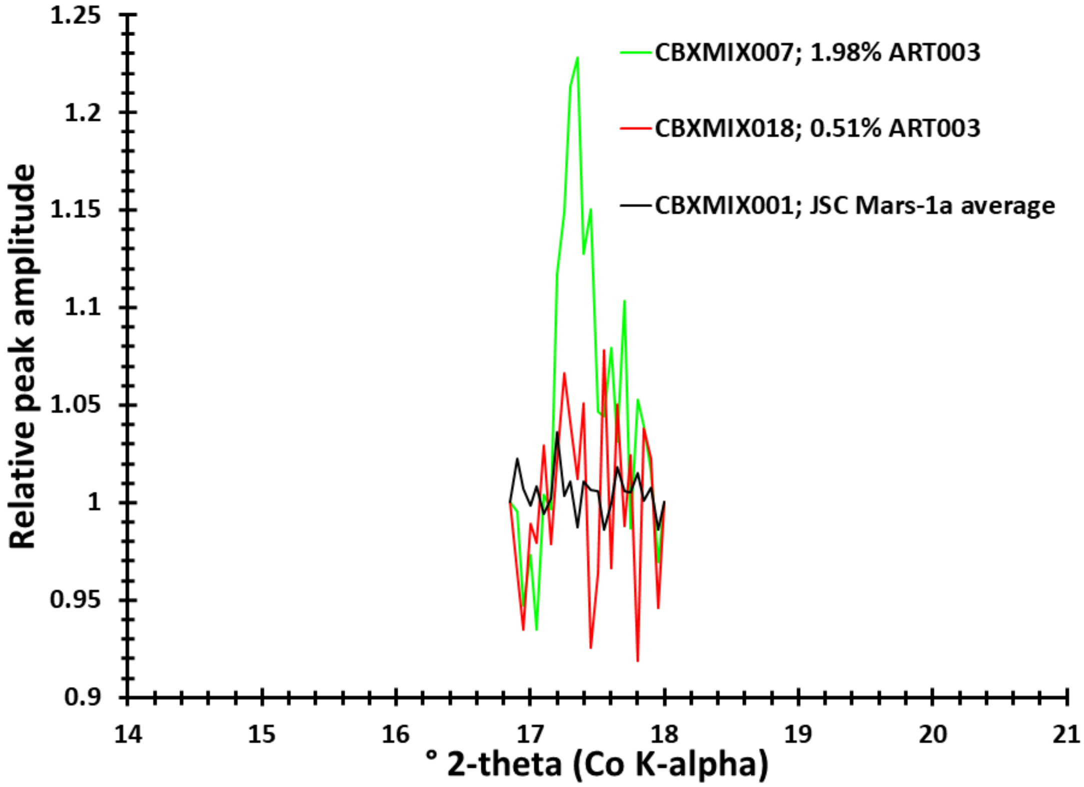

Figure 8h. Continuum-removed XRD patterns of the JSC Mars-1a + whewellite mixtures.

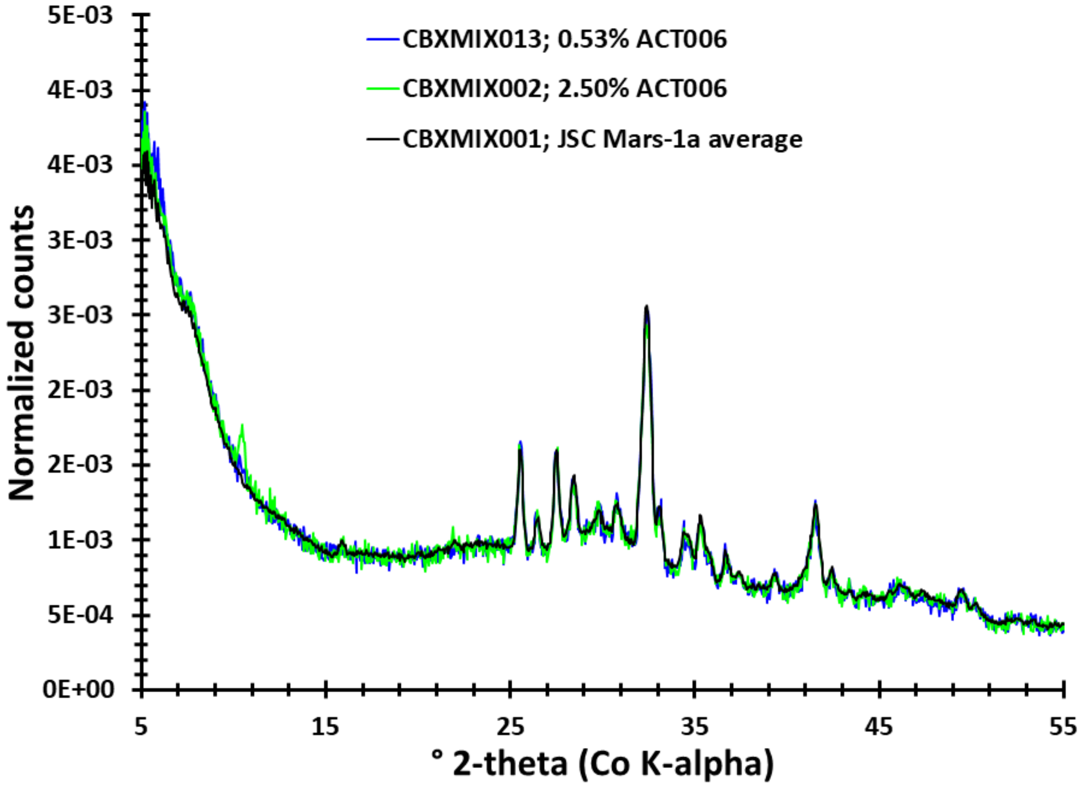

Figure 8i. X-ray diffraction patterns of the JSC Mars-1a + calcium acetate monohydrate mixtures.

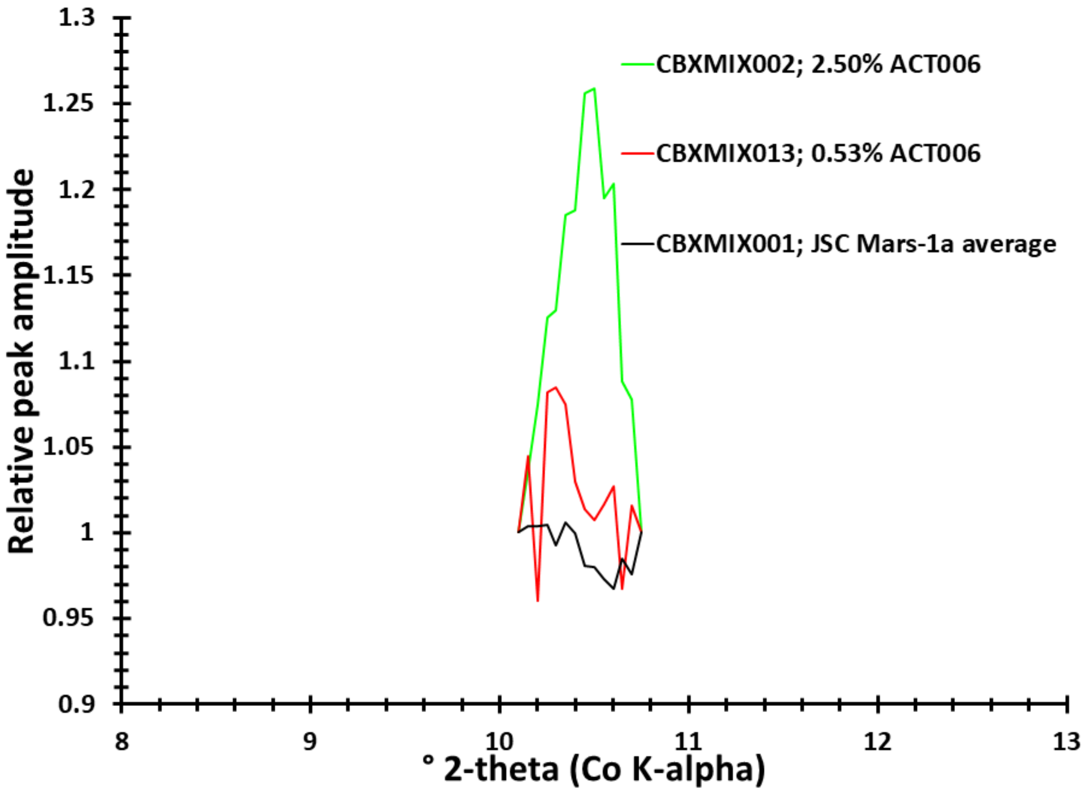

Figure 8j. Continuum-removed XRD patterns of the JSC Mars-1a + calcium acetate monohydrate mixtures.

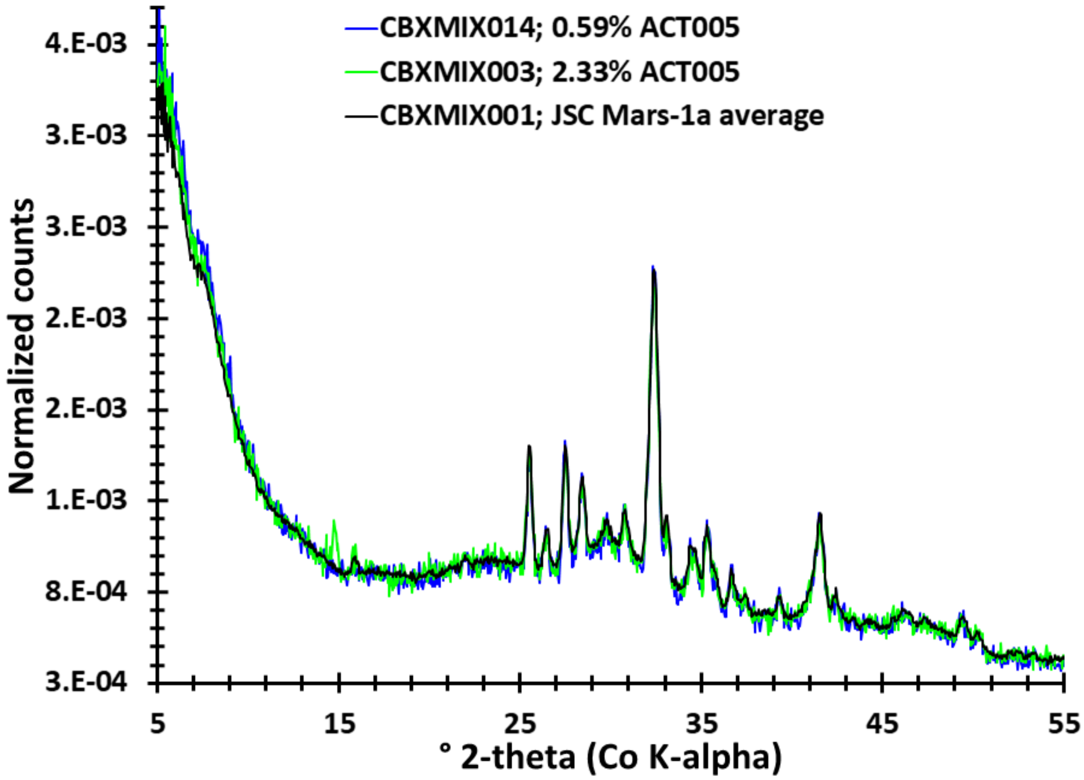

Figure 8k. X-ray diffraction patterns of the JSC Mars-1a + magnesium acetate tetrahydrate mixtures.

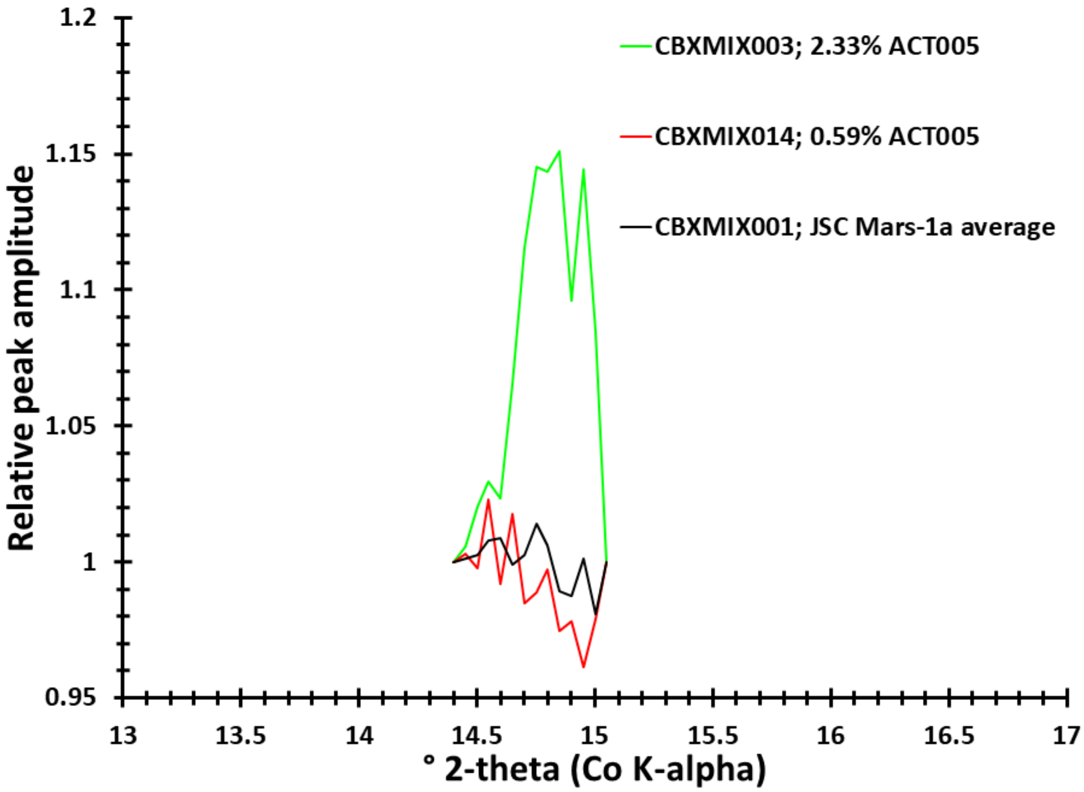

Figure 8l. Continuum-removed XRD patterns of the JSC Mars-1a + magnesium acetate tetrahydrate mixtures.

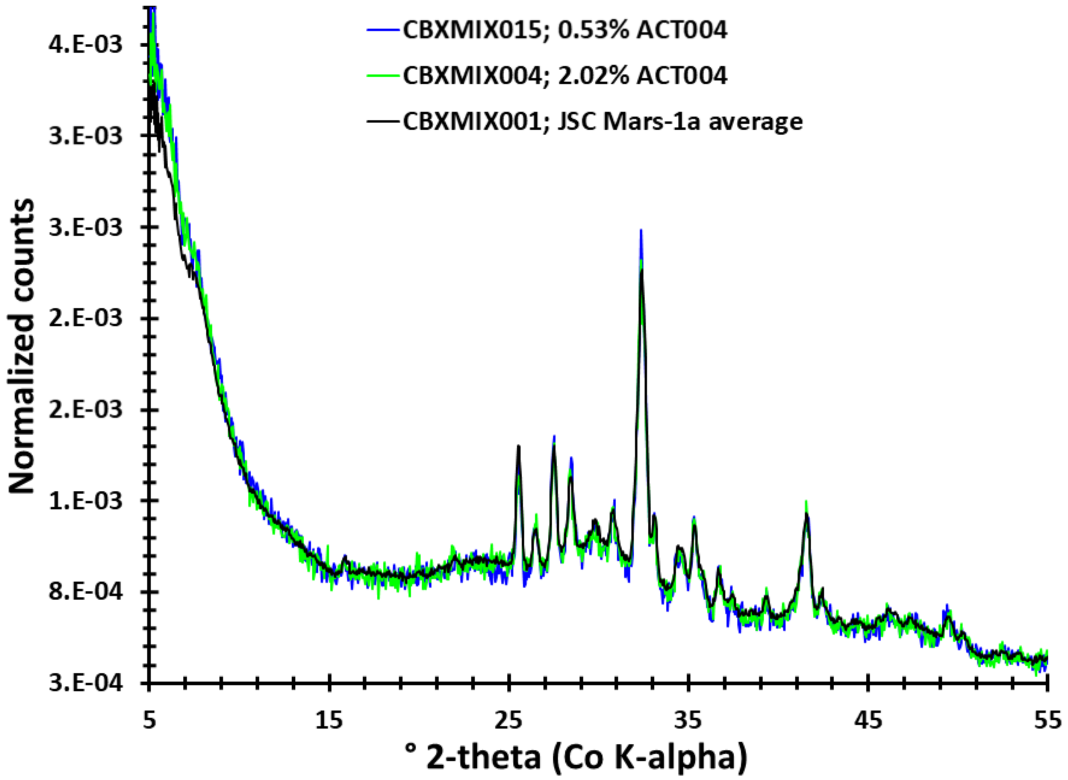

Figure 8m. X-ray diffraction patterns of the JSC Mars-1a + ferrous acetate mixtures.

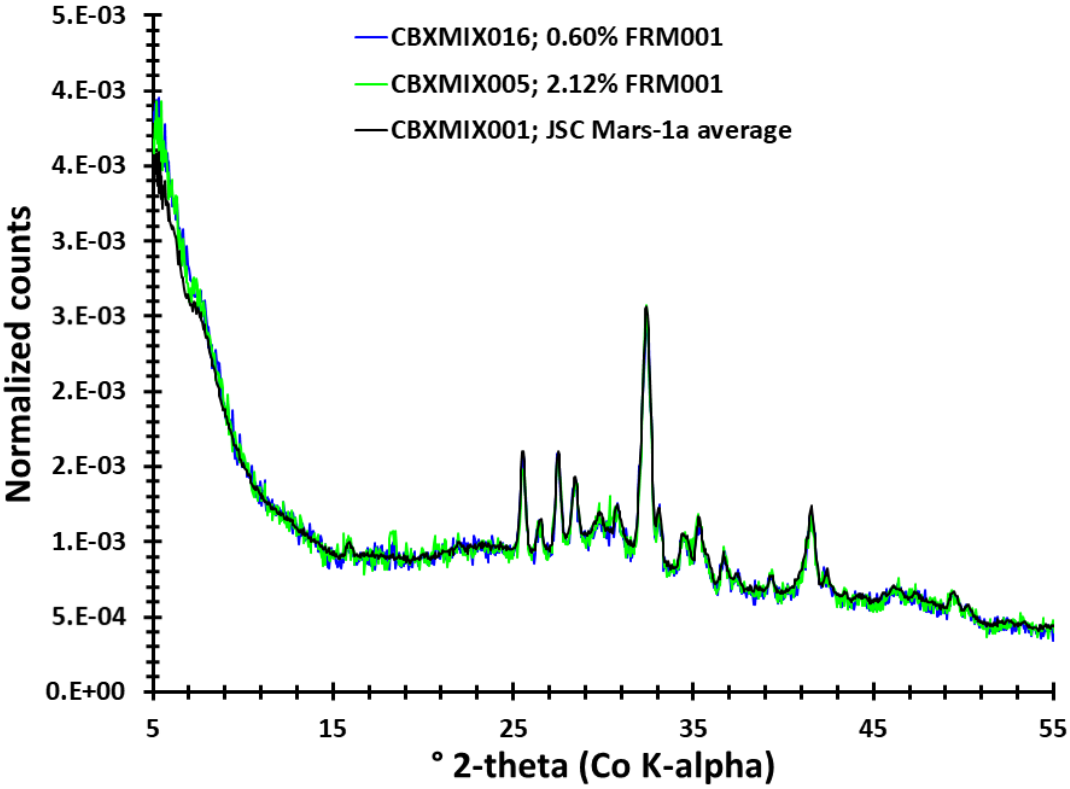

Figure 8n. X-ray diffraction patterns of the JSC Mars-1a + calcium formate mixtures.

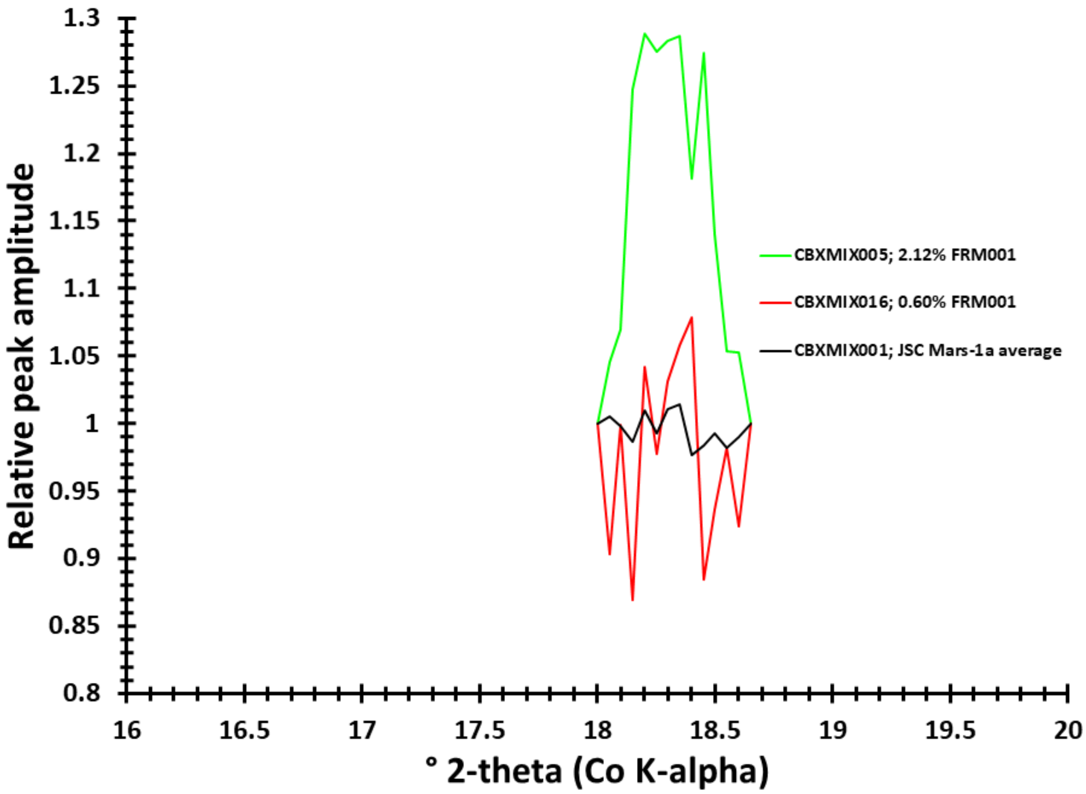

Figure 8o. Continuum-removed XRD patterns of the JSC Mars-1a + calcium formate mixtures.

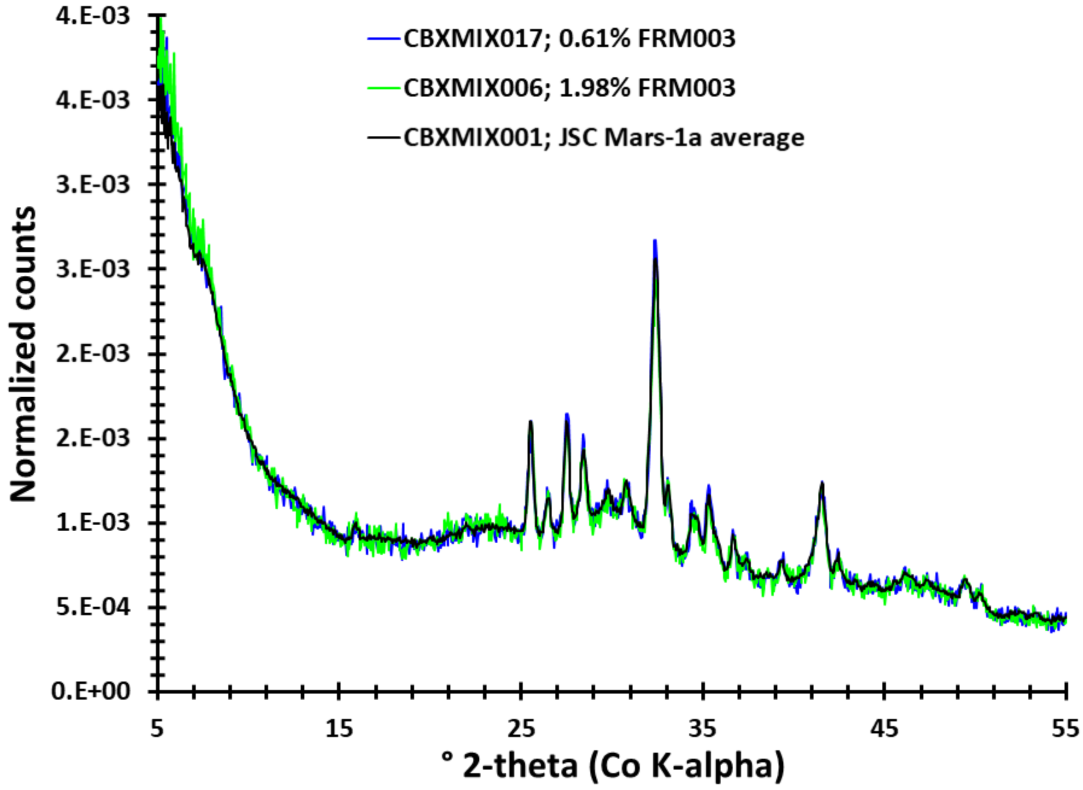

Figure 8p. X-ray diffraction patterns of the JSC Mars-1a + magnesium formate dihydrate mixtures.

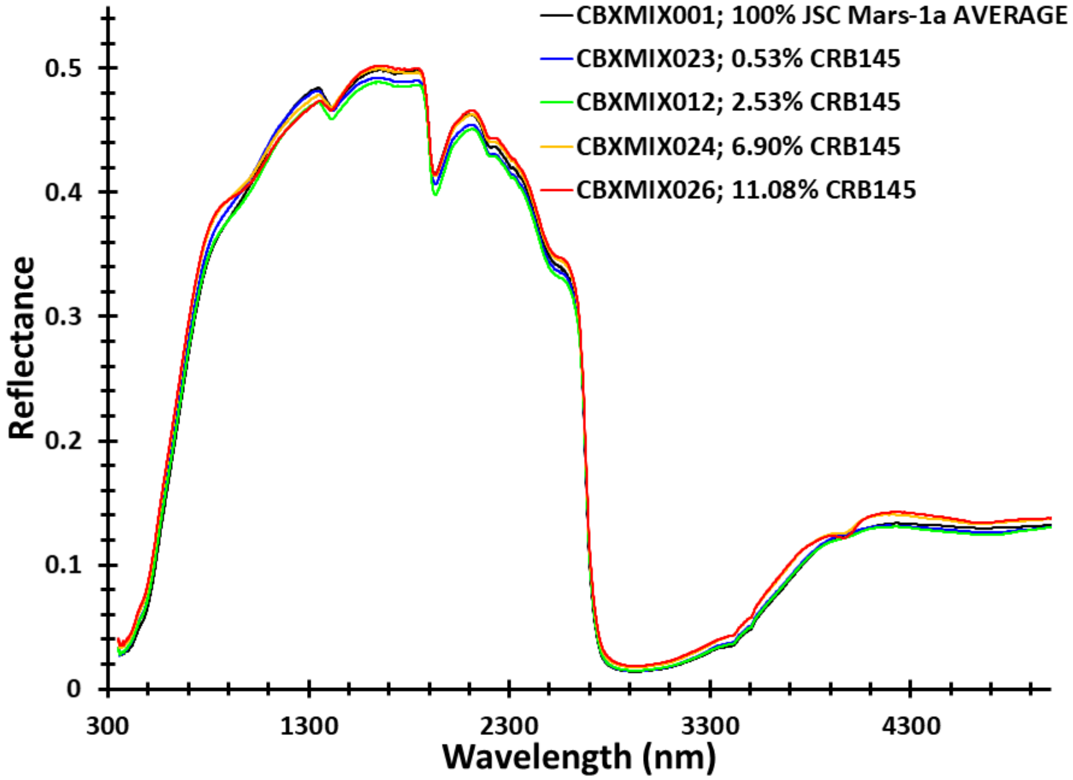

Figure 9a. Reflectance spectra of the siderite + JSC Mars-1a mixtures compared with pure JSC Mars-1a.

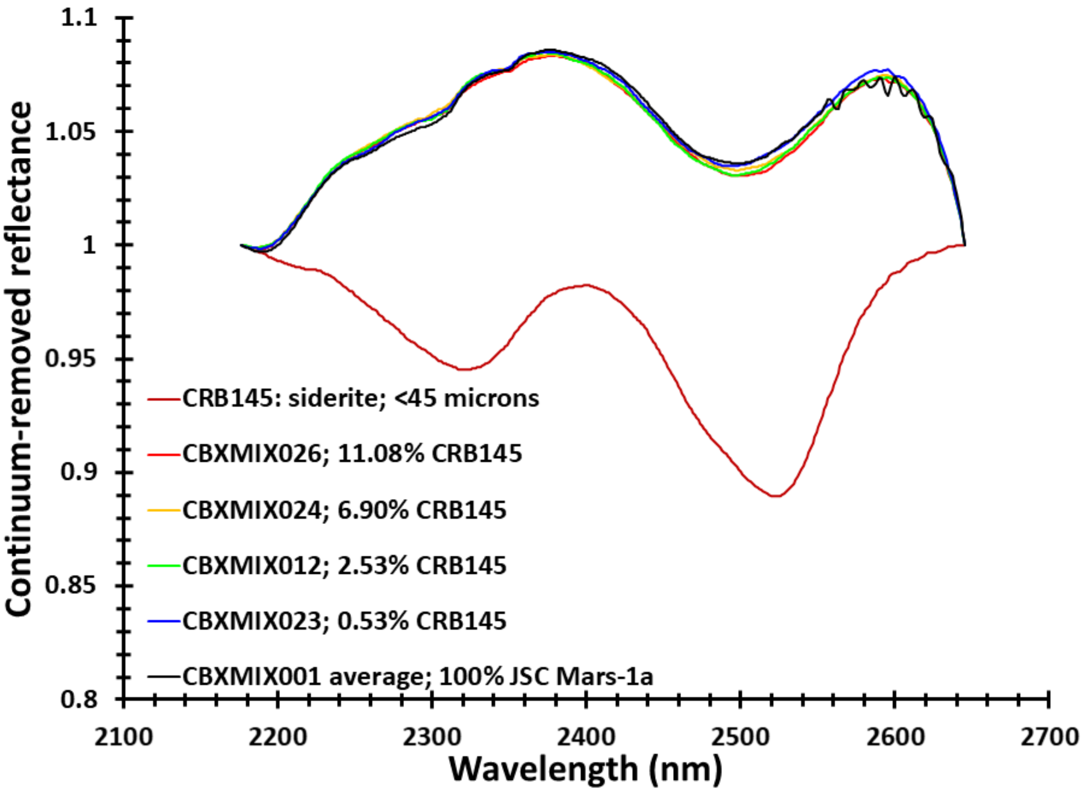

Figure 9b. Continuum-removed reflectance of the NIR band of the siderite + JSC Mars-1a mixtures compared with pure JSC Mars-1a.

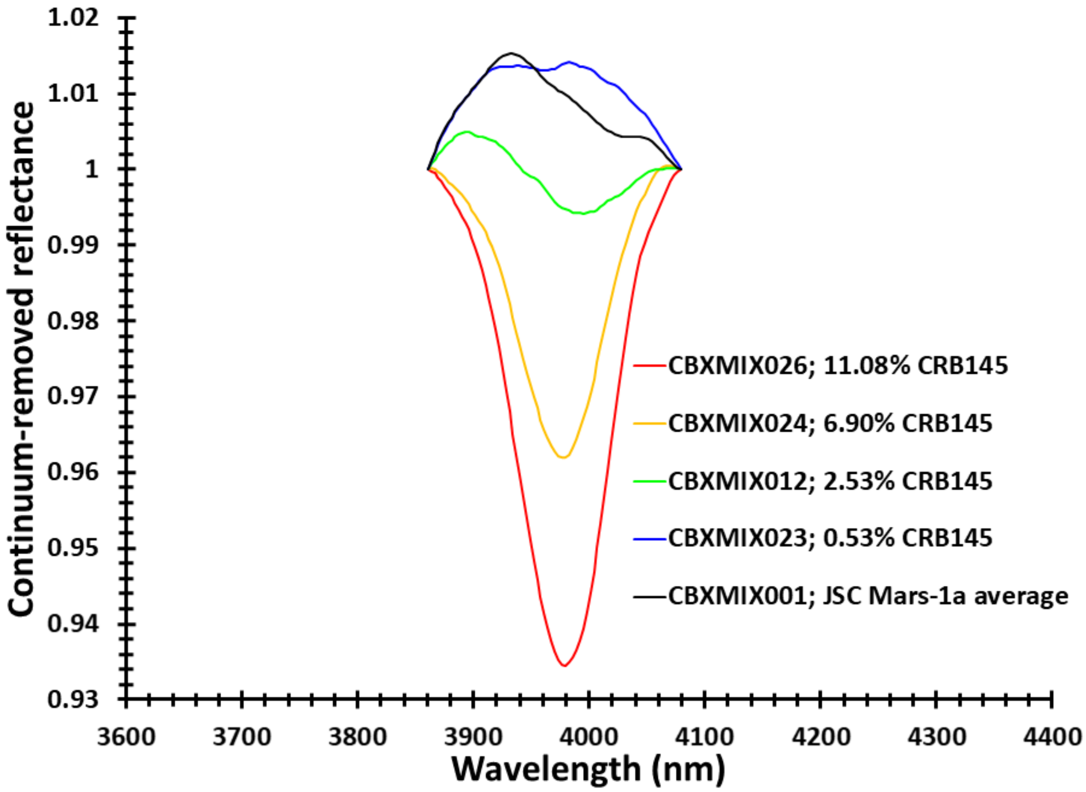

Figure 9c. Continuum-removed reflectance of the MIR band of the siderite + JSC Mars-1a mixtures compared with pure JSC Mars-1a.

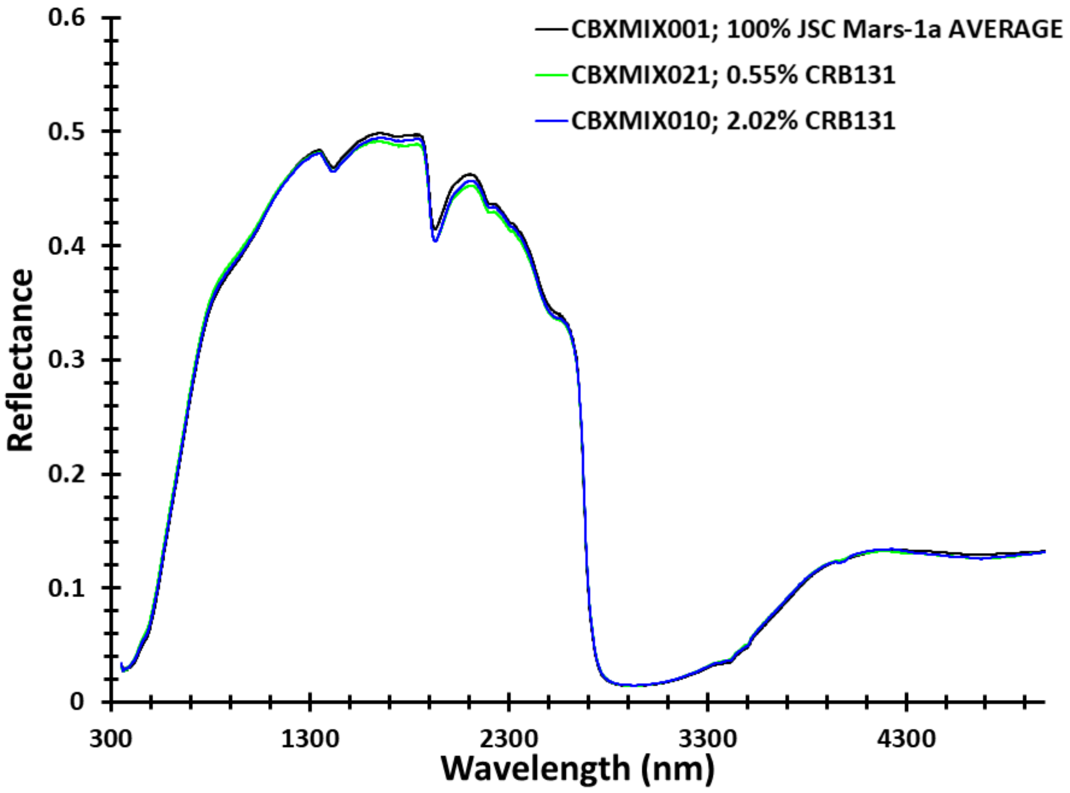

Figure 9d. Reflectance spectra of the calcite + JSC Mars-1a mixtures compared with pure JSC Mars-1a.

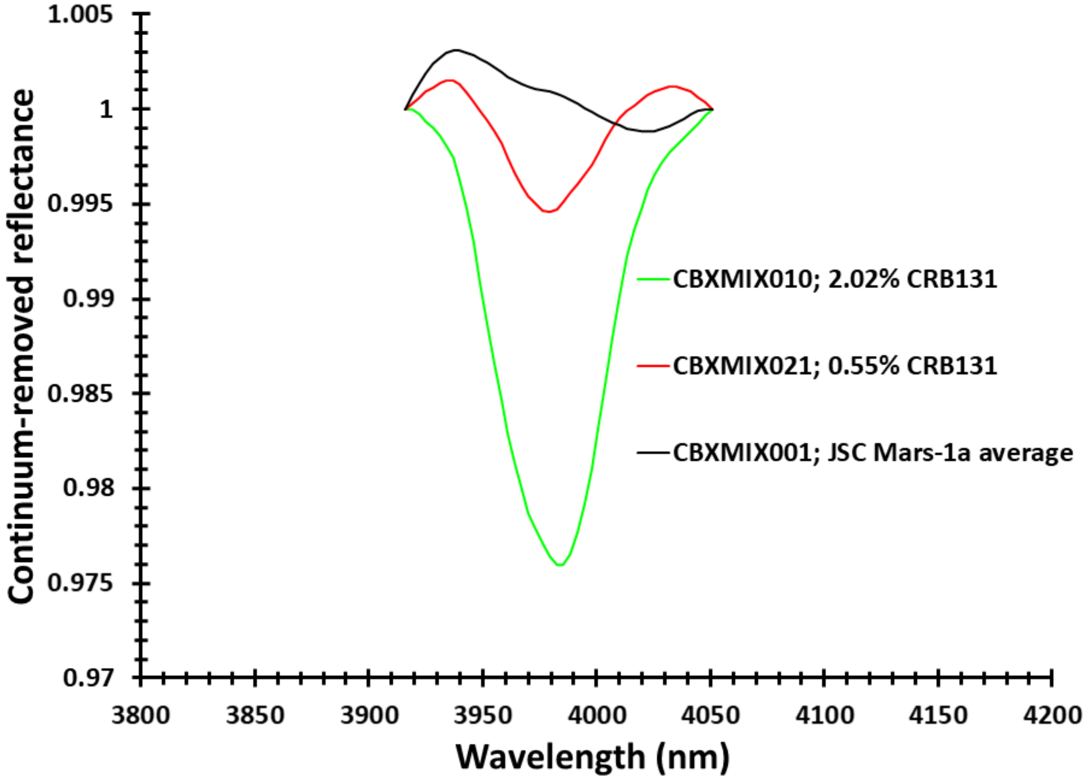

Figure 9e. Continuum-removed reflectance of the MIR band of the calcite + JSC Mars-1a mixtures compared with pure JSC Mars-1a.

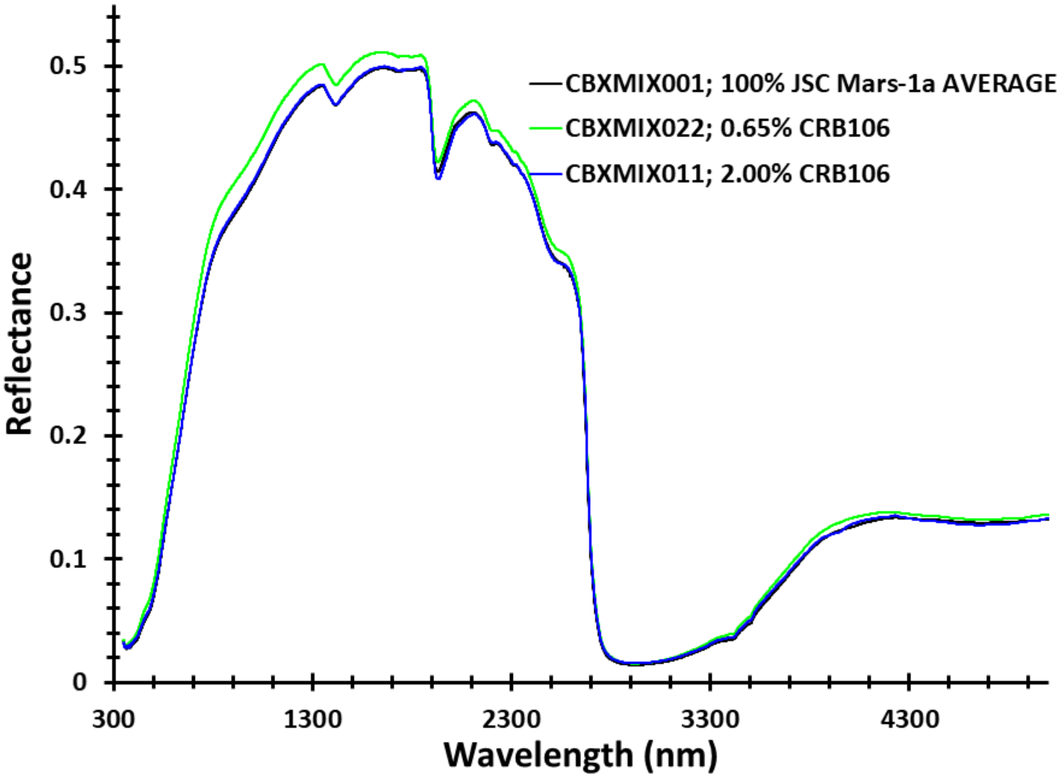

Figure 9f. Reflectance spectra of the magnesite + JSC Mars-1a mixtures compared with pure JSC Mars-1a.

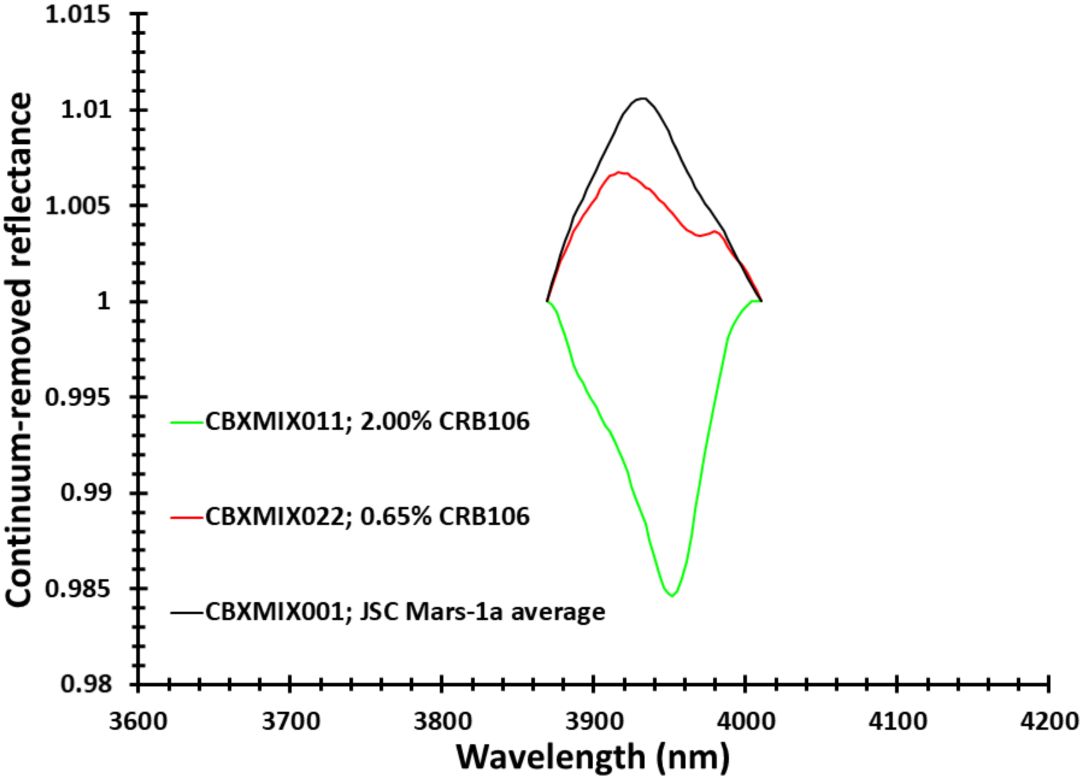

Figure 9g. Continuum-removed reflectance of the MIR band of the magnesite + JSC Mars-1a mixtures compared with pure JSC Mars-1a.

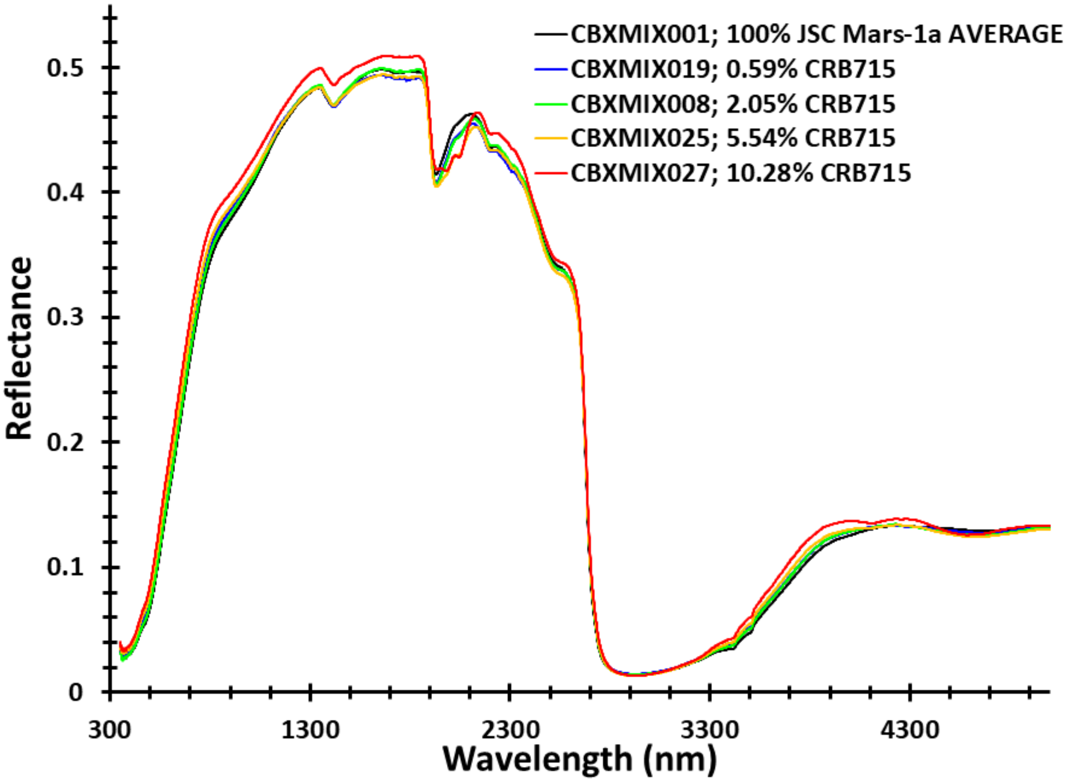

Figure 9h. Reflectance spectra of the humboldtine + JSC Mars-1a mixtures compared with pure JSC Mars-1a.

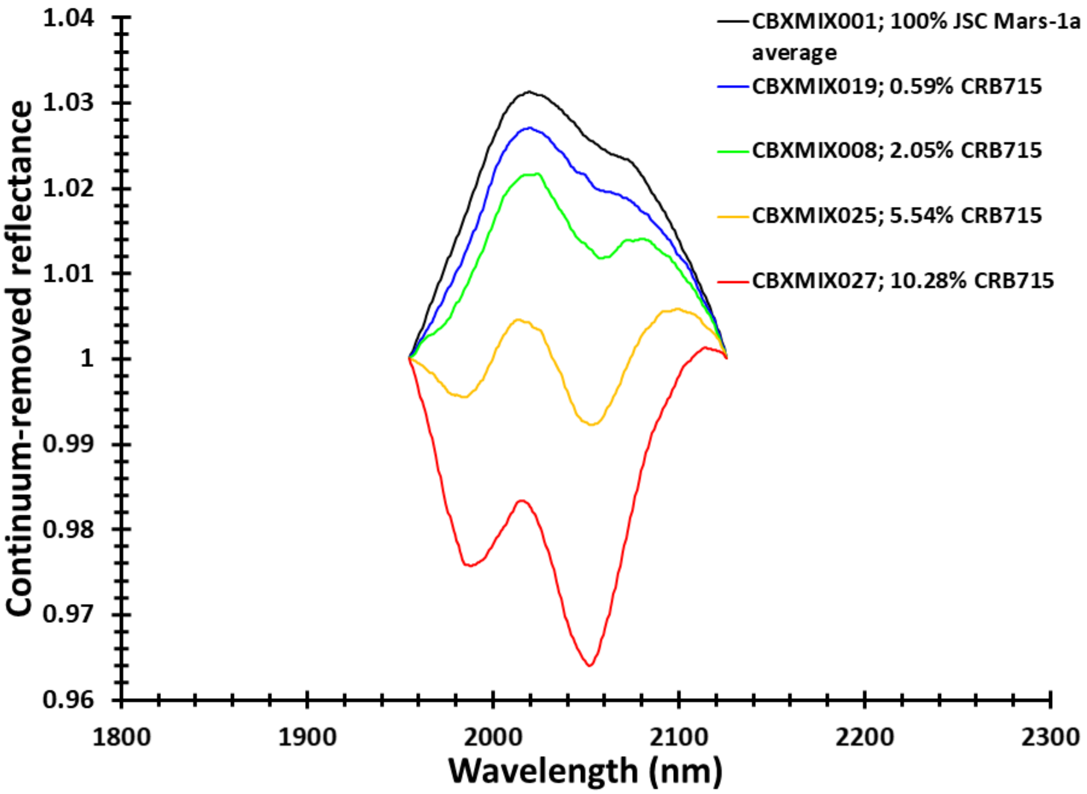

Figure 9i. Continuum-removed reflectance spectra of the humboldtine + JSC Mars-1a mixtures compared with pure JSC Mars-1a.

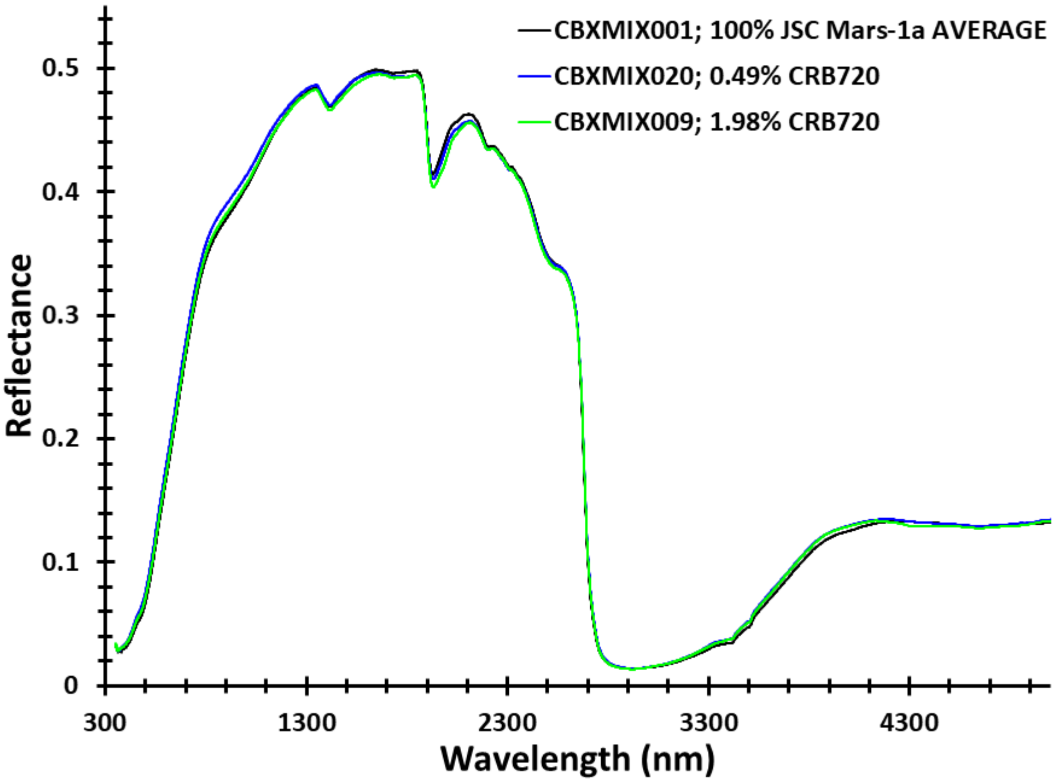

Figure 9j. Reflectance spectra of the glushinskite + JSC Mars-1a mixtures compared with pure JSC Mars-1a.

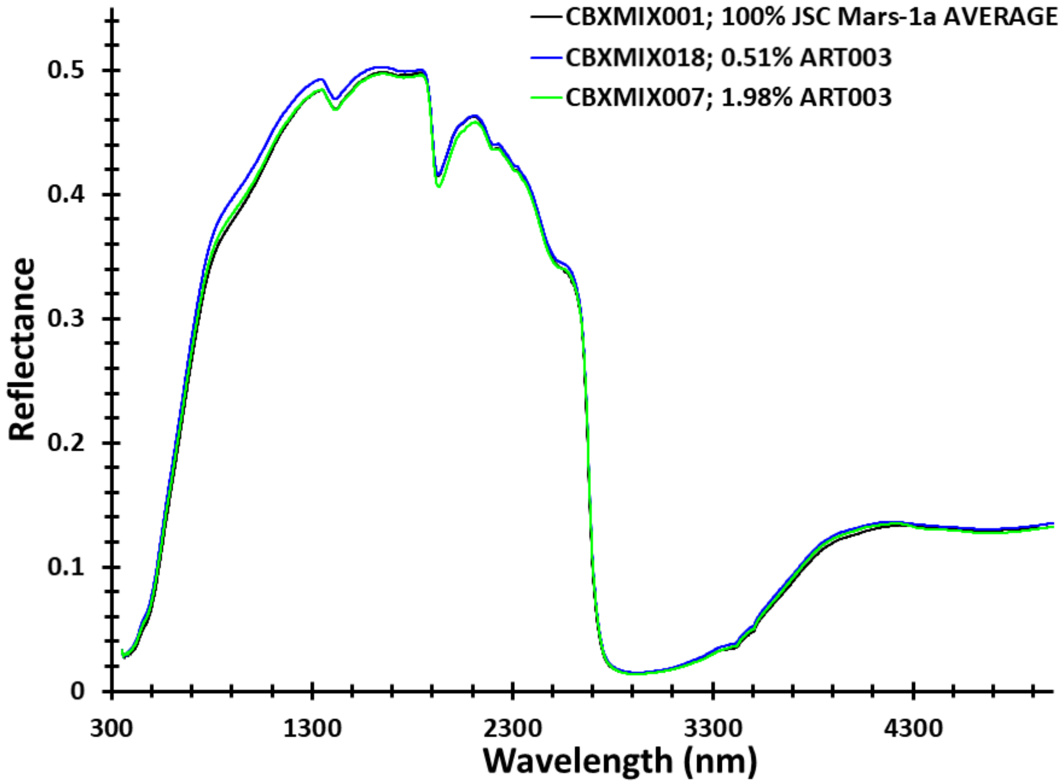

Figure 9k. Reflectance spectra of the whewellite + JSC Mars-1a mixtures compared with pure JSC Mars-1a.

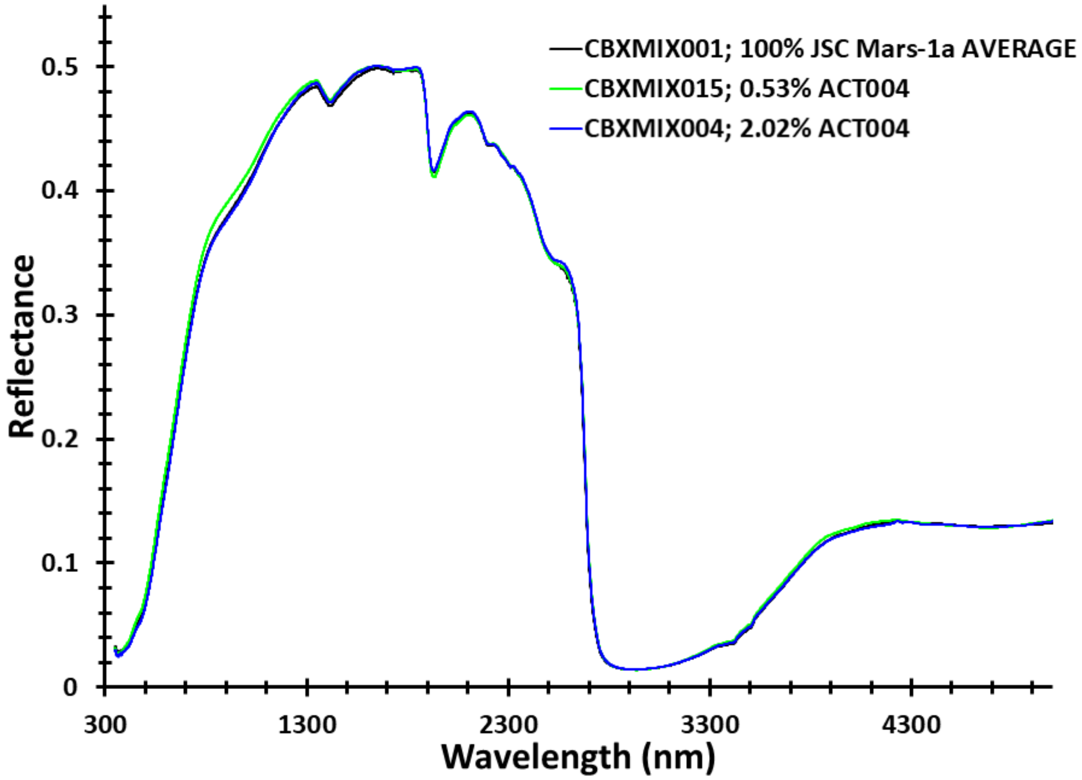

Figure 9l. Reflectance spectra of the Fe^{2+} acetate + JSC Mars-1a mixtures compared with pure JSC Mars-1a.

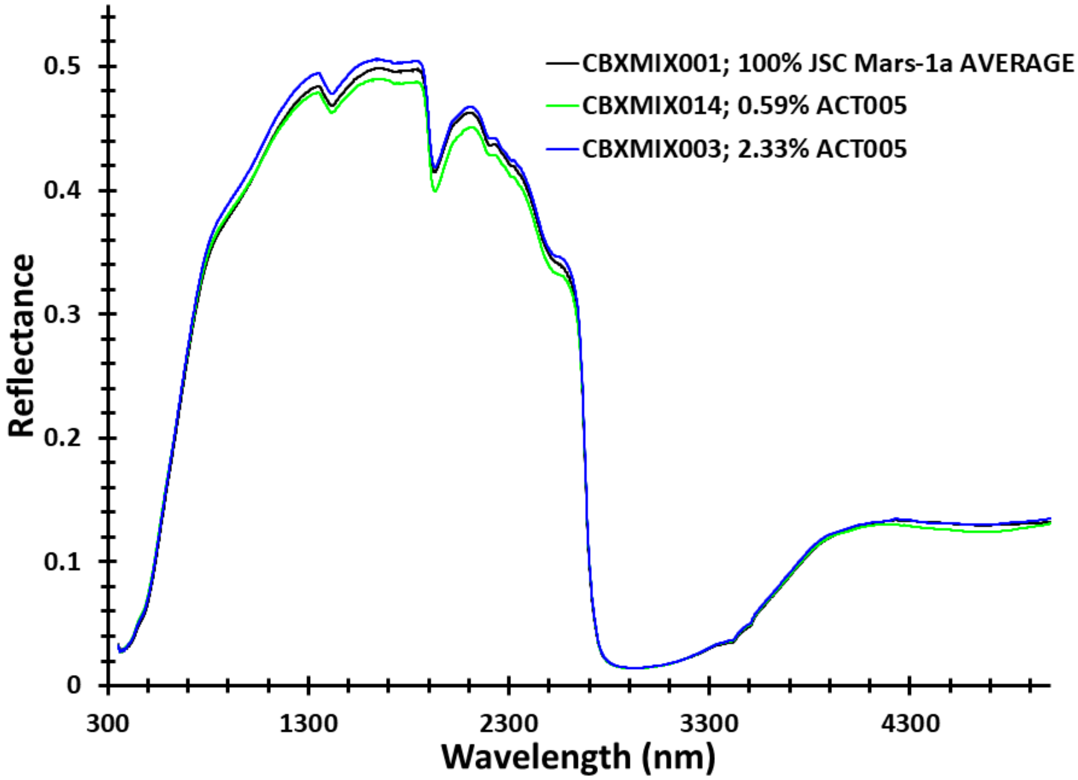

Figure 9m. Reflectance spectra of the magnesium acetate tetrahydrate+ JSC Mars-1a mixtures compared with pure JSC Mars-1a.

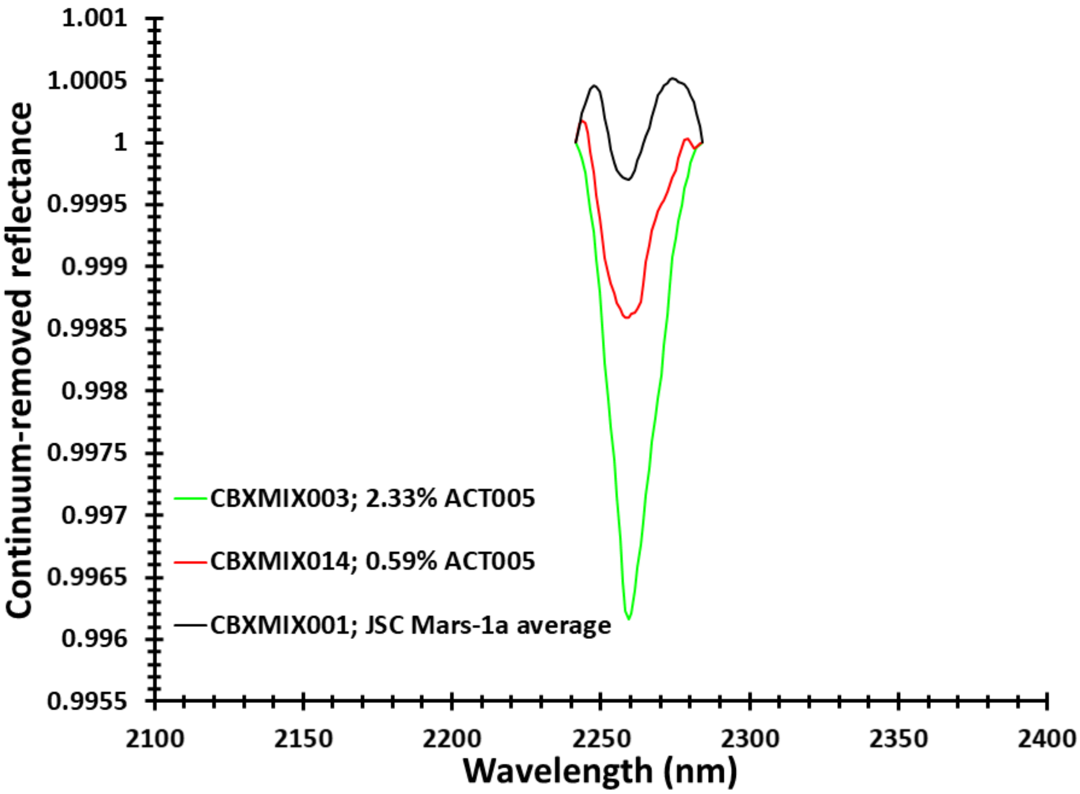

Figure 9n. Continuum-removed reflectance of the MIR band of the magnesium acetate tetrahydrate + JSC Mars-1a mixtures compared with pure JSC Mars-1a.

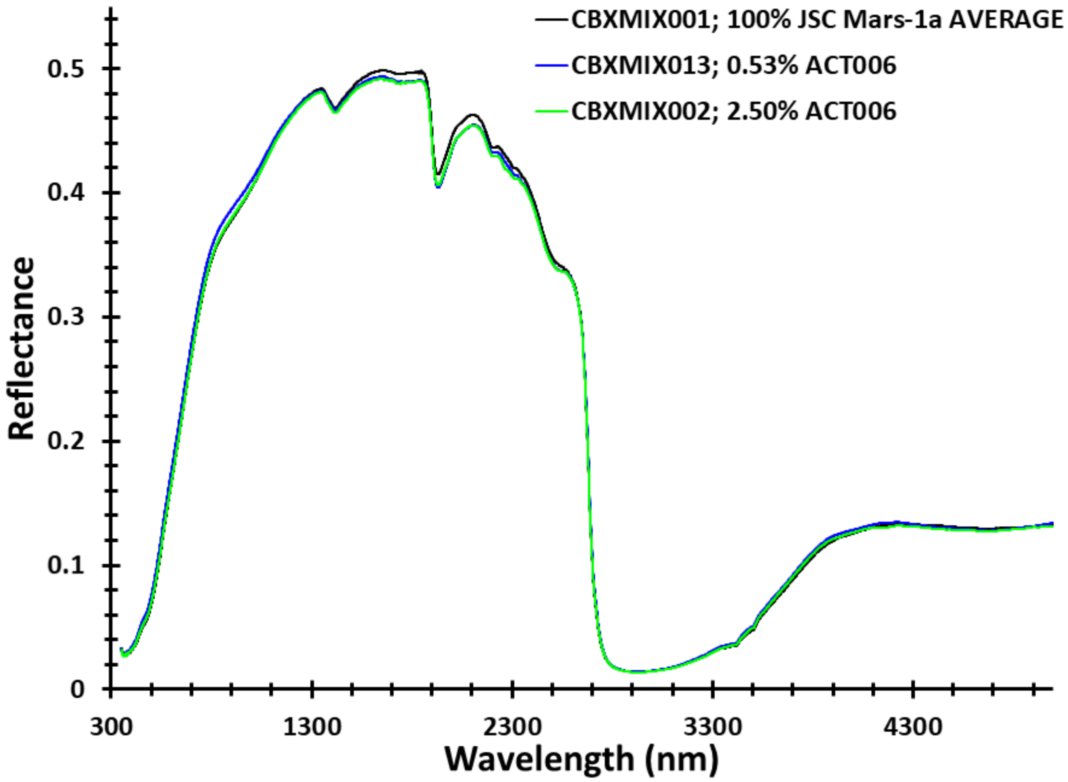

Figure 9o. Reflectance spectra of the calcium acetate monohydrate + JSC Mars-1a mixtures compared with pure JSC Mars-1a.

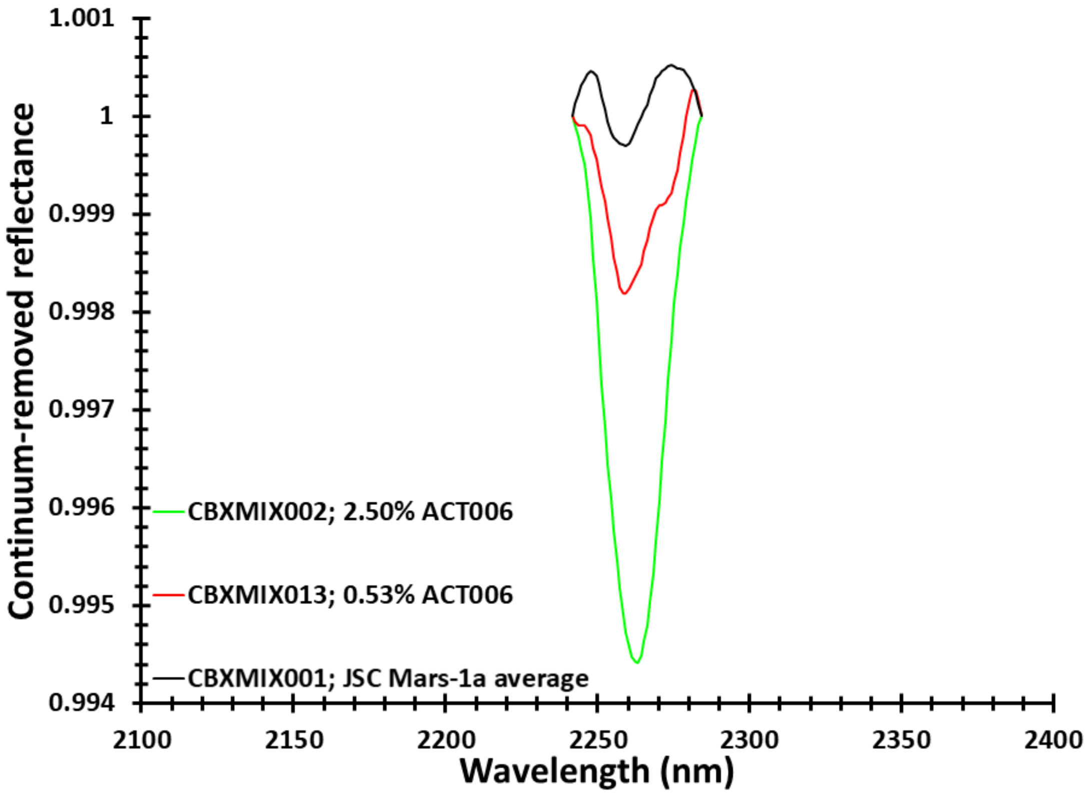

Figure 9p. Continuum-removed reflectance of the MIR band of the calcium acetate monohydrate + JSC Mars-1a mixtures compared with pure JSC Mars-1a.

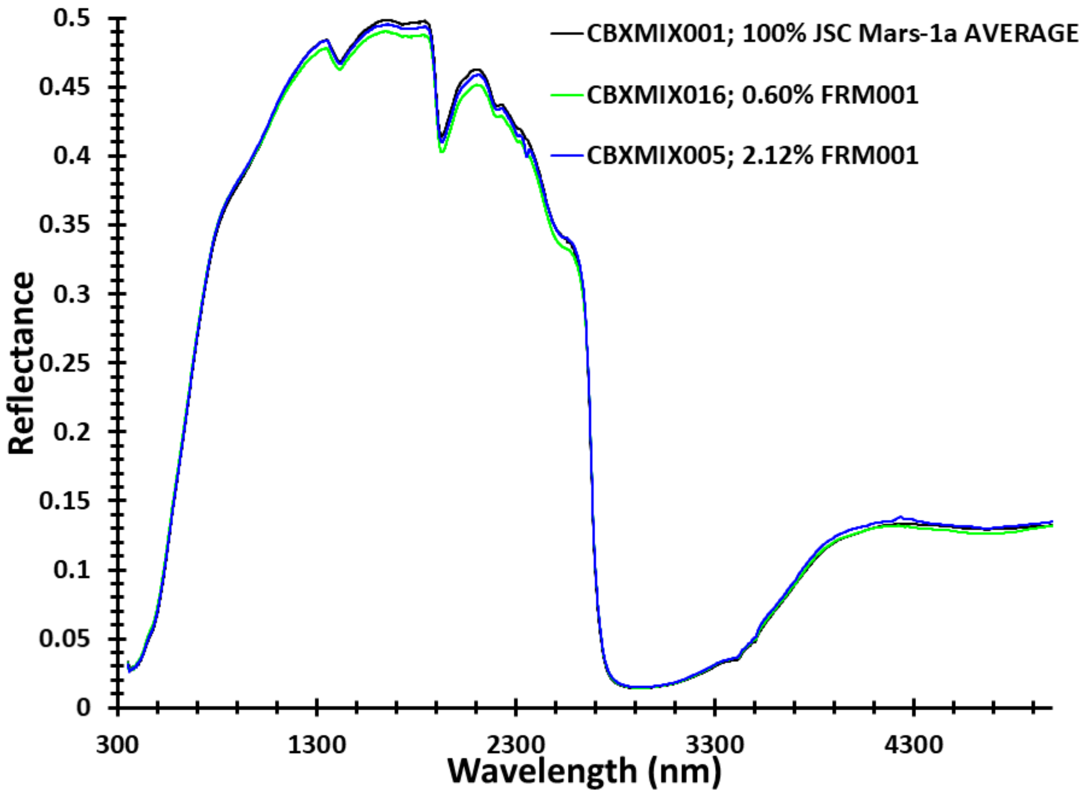

Figure 9q. Reflectance spectra of the calcium formate + JSC Mars-1a mixtures compared with pure JSC Mars-1a.

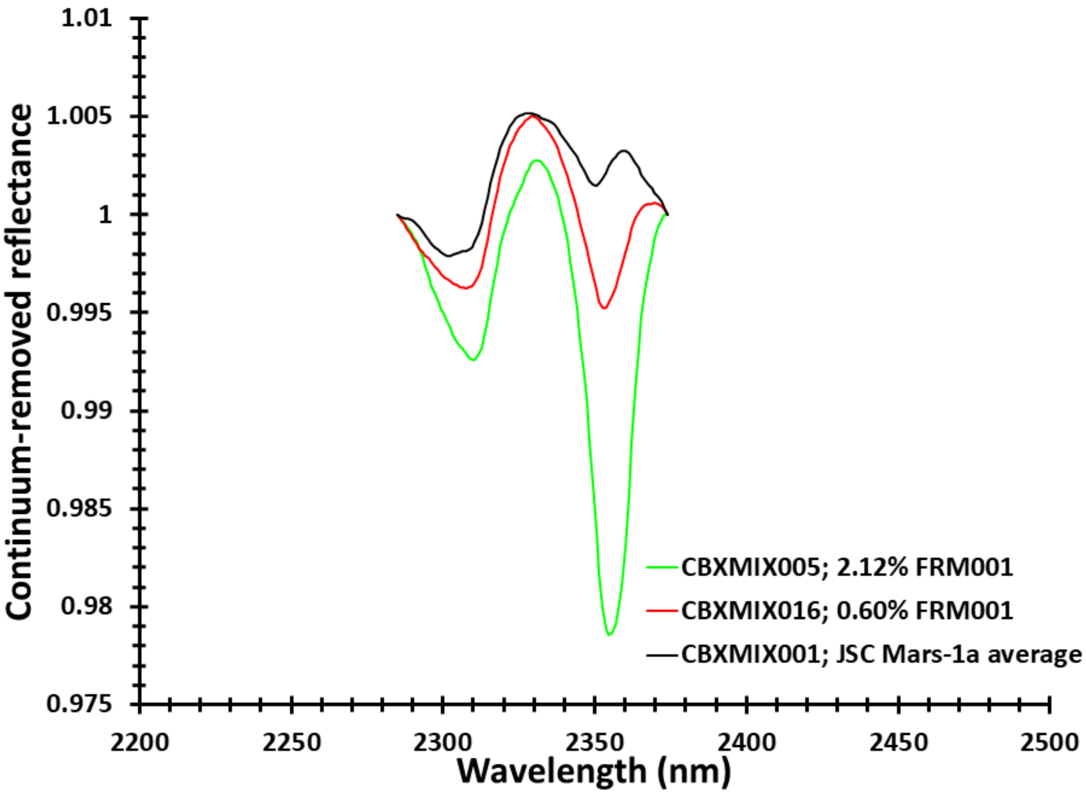

Figure 9r. Continuum-removed reflectance of the MIR band of the calcium formate + JSC Mars-1a mixtures compared with pure JSC Mars-1a.

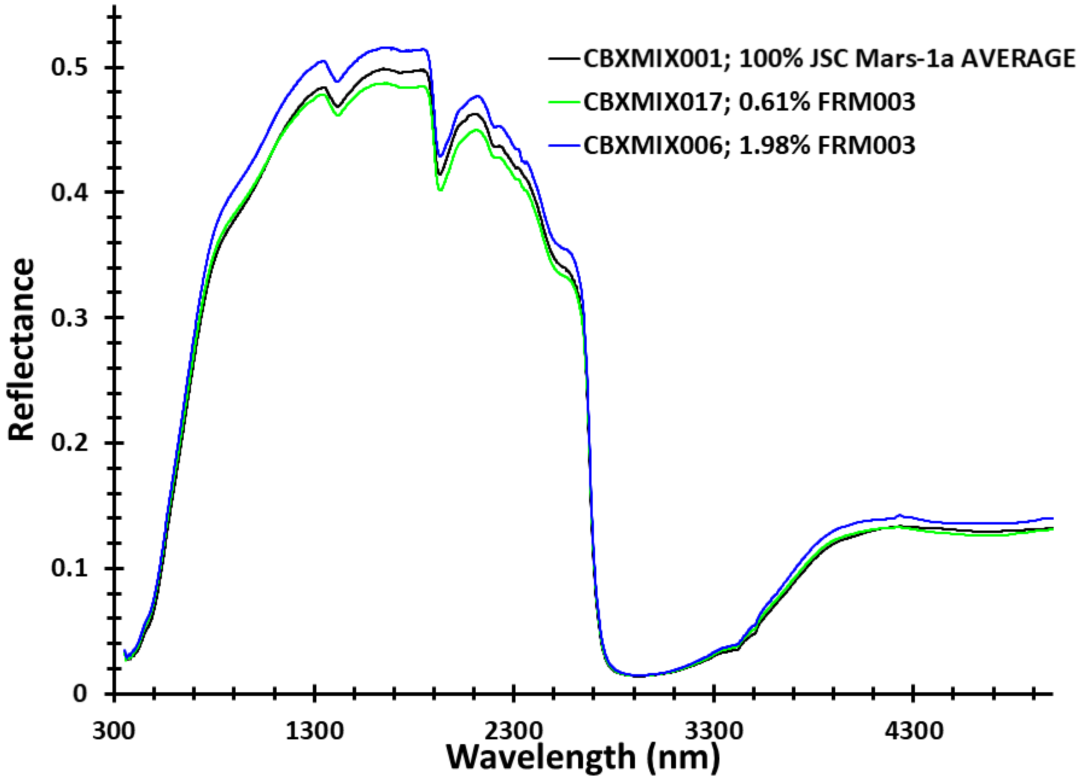

Figure 9s. Reflectance spectra of the magnesium formate monohydrate + JSC Mars-1a mixtures compared with pure JSC Mars-1a.

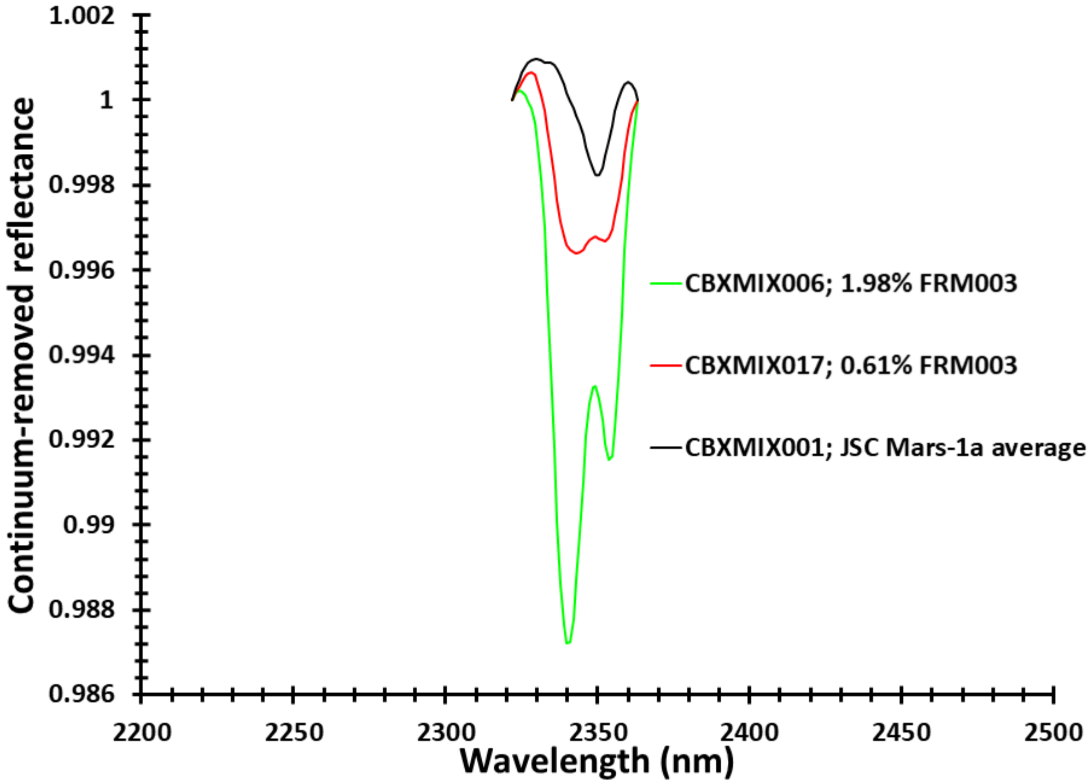

Figure 9t. Continuum-removed reflectance of the MIR band of the magnesium formate monohydrate + JSC Mars-1a mixtures compared with pure JSC Mars-1a.

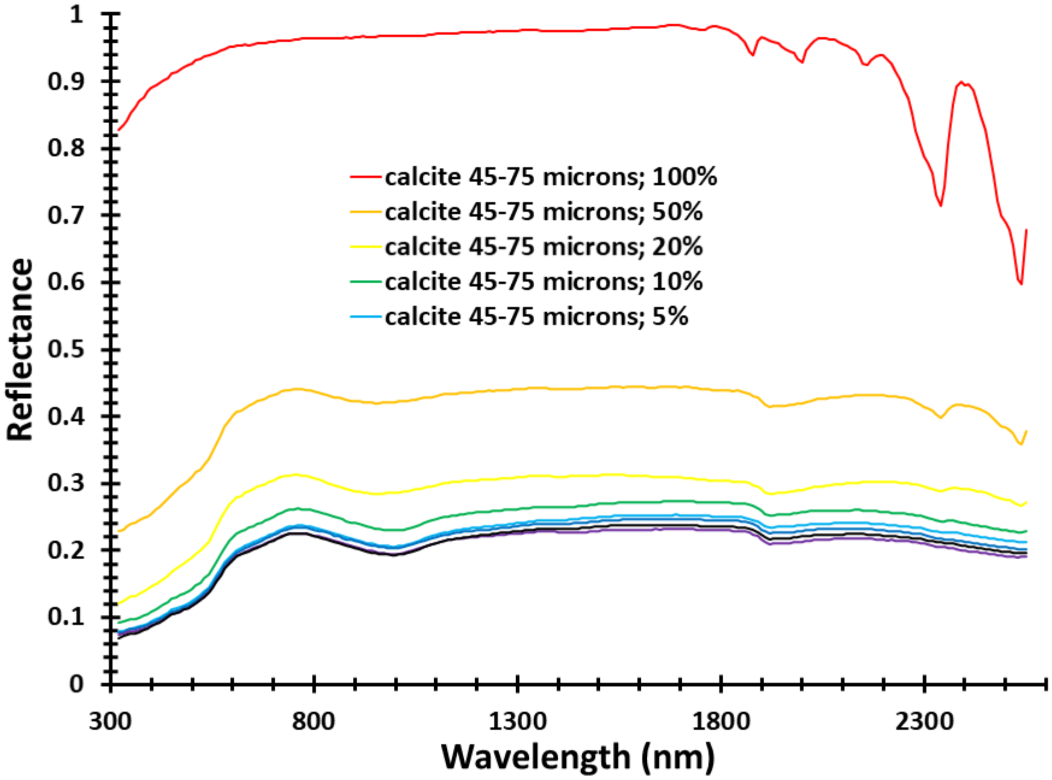

Figure 10a. Reflectance spectra for the 45-75 micron fraction of calcite mixed with the MGS-1 analogue.

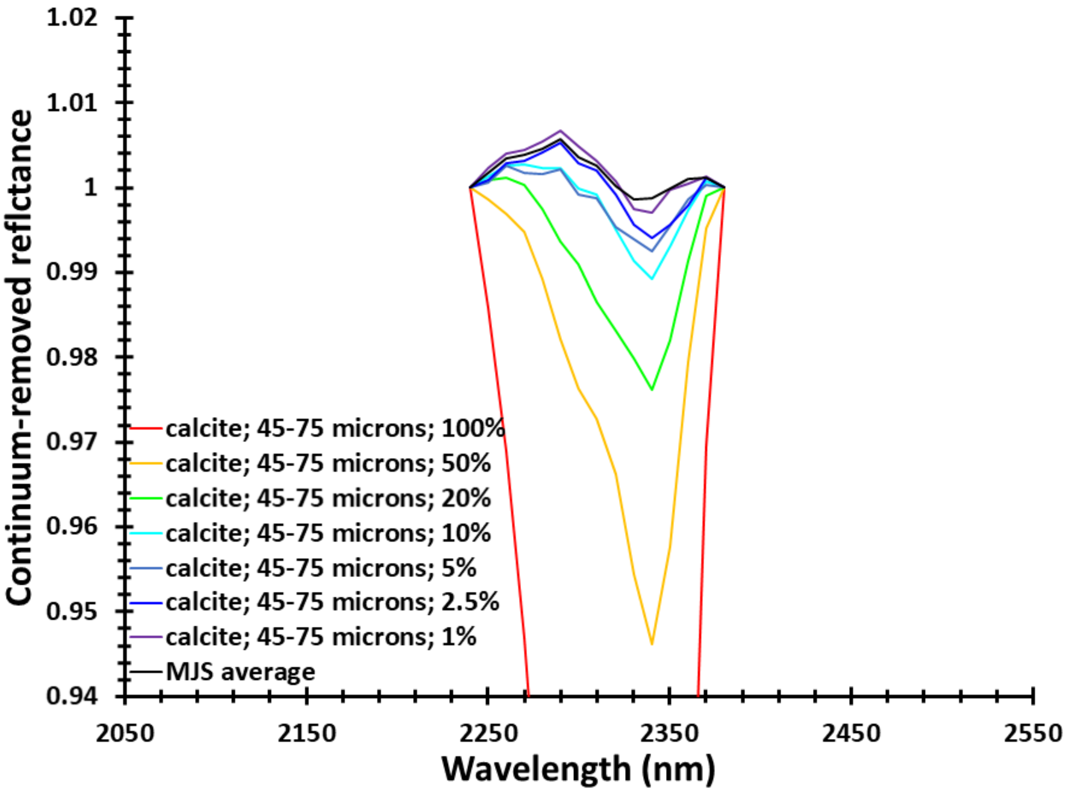

Figure 10b. Continuum-removed reflectance of the 2.3 micron band for the 45-75 micron fraction of calcite mixed with the MGS-1 analogue.

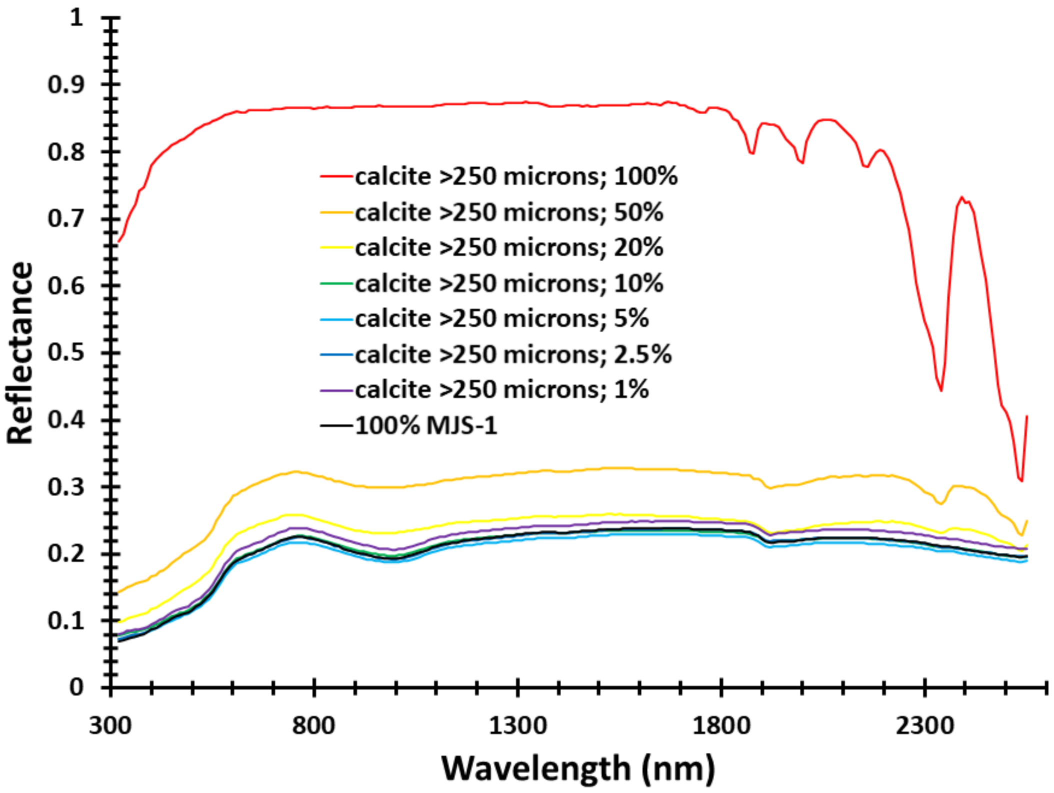

Figure 10c. Reflectance spectra for the 125-250 micron fraction of calcite mixed with the MGS-1 analogue.

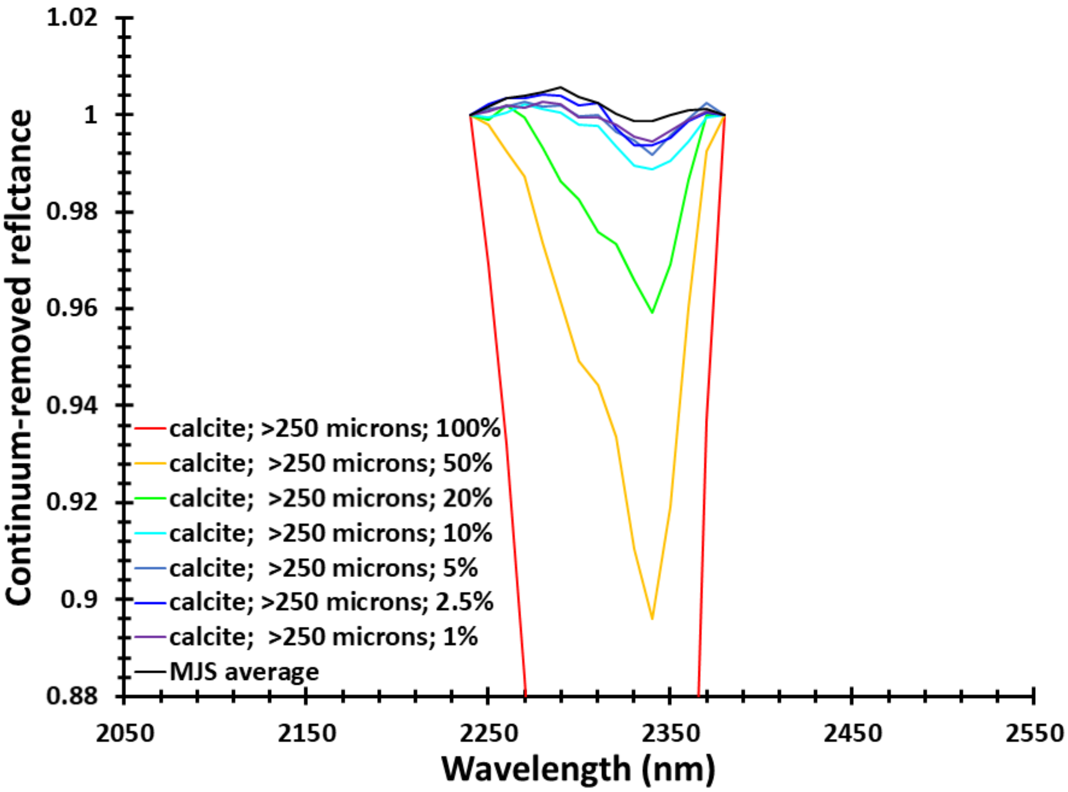

Figure 10d. Continuum-removed reflectance of the 2.3 micron band for the 125-250 micron fraction of calcite mixed with the MGS-1 analogue.

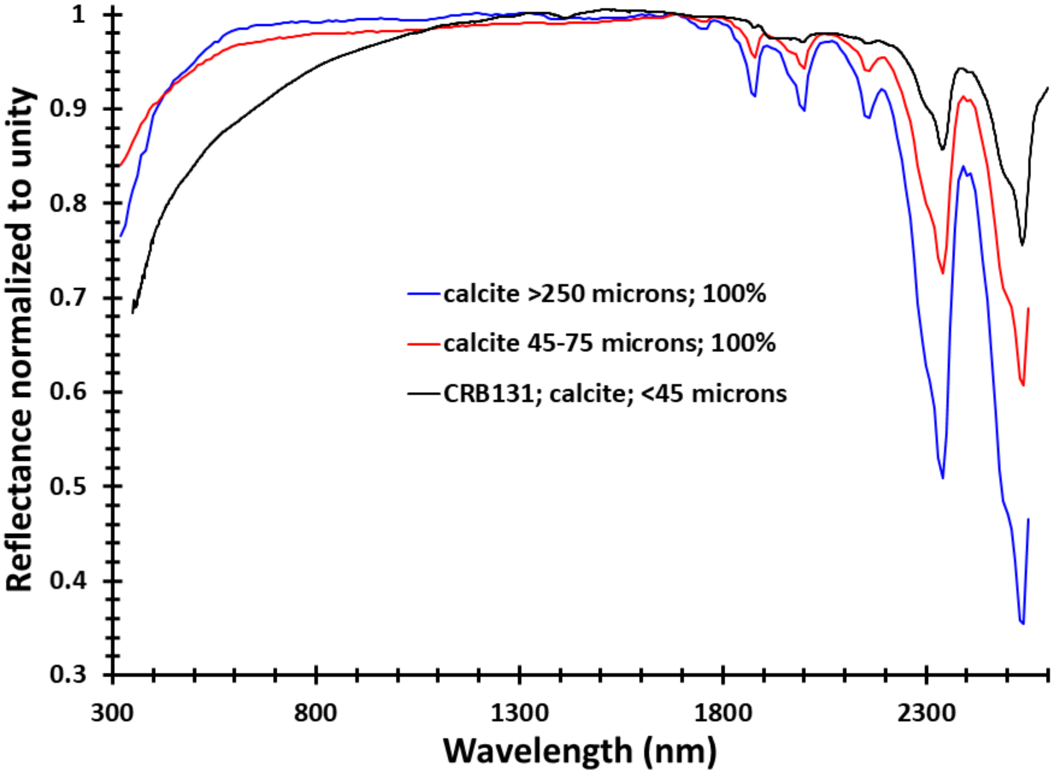

Figure 10e. Reflectance spectra of calcite at different grain size fractions, normalized to unity at 1690 nm.

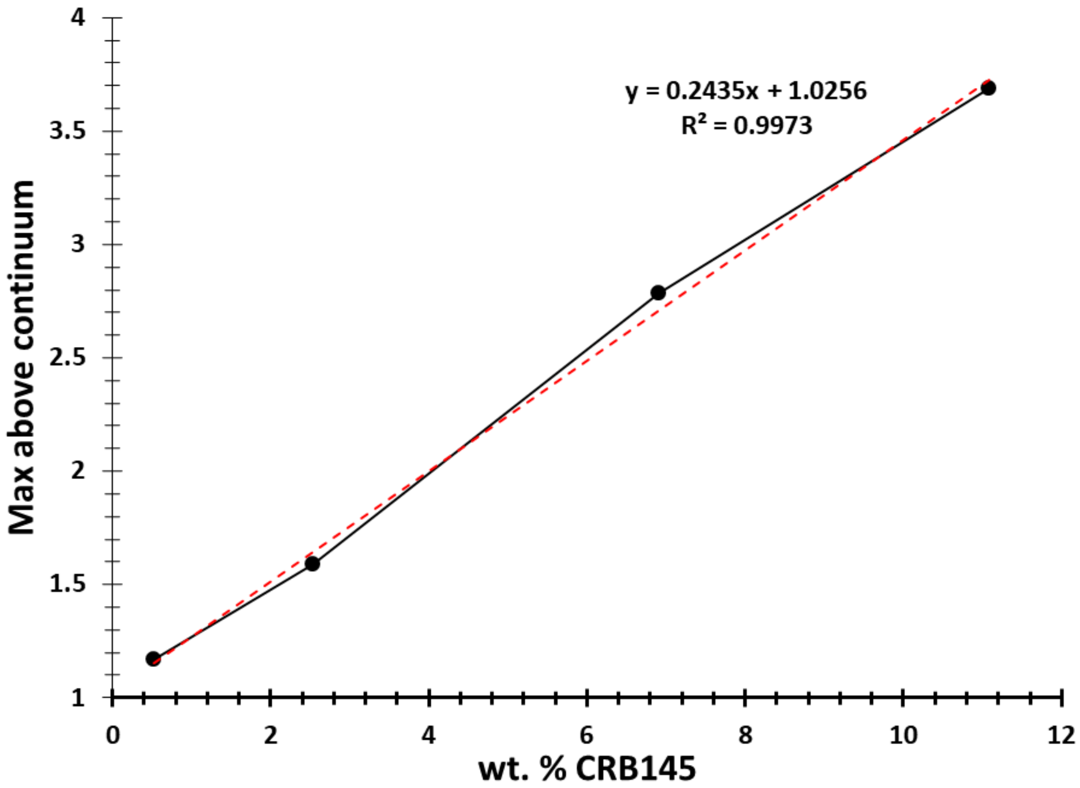

Figure 11a. Linear regression model of the diffraction peak for the JSC Mars-1 with siderite mixtures.

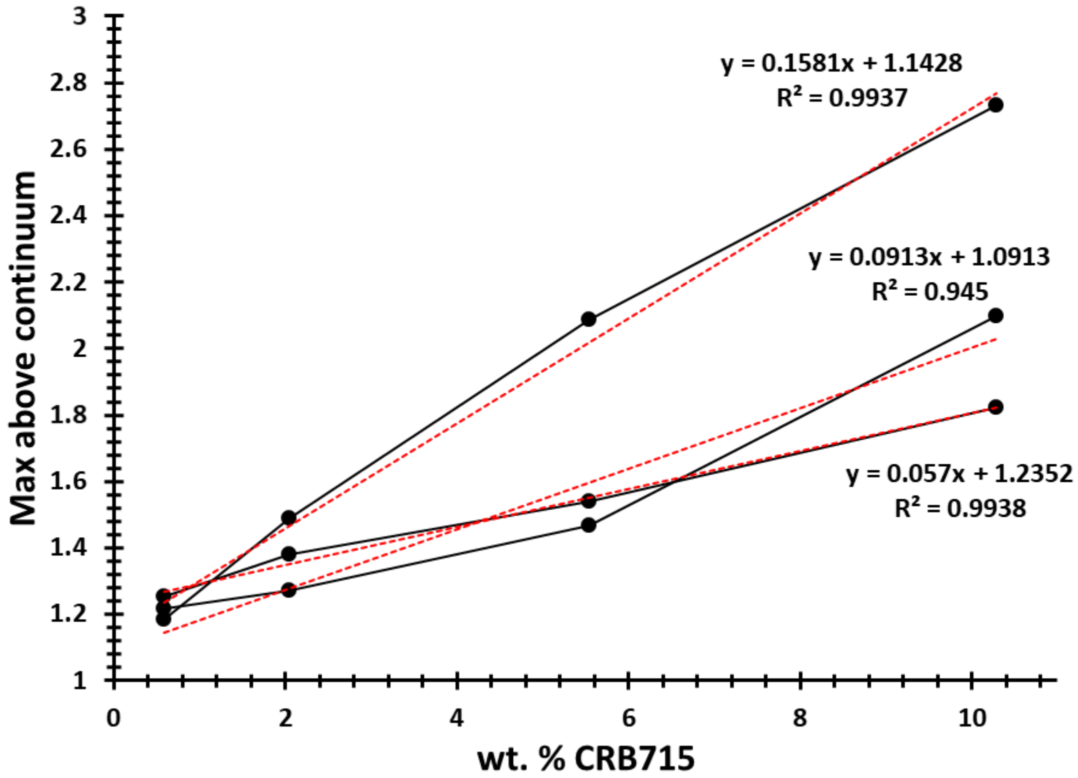

Figure 11b. Linear regression models of the 3 diffraction peaks for the JSC Mars-1 with humboldtine mixtures.

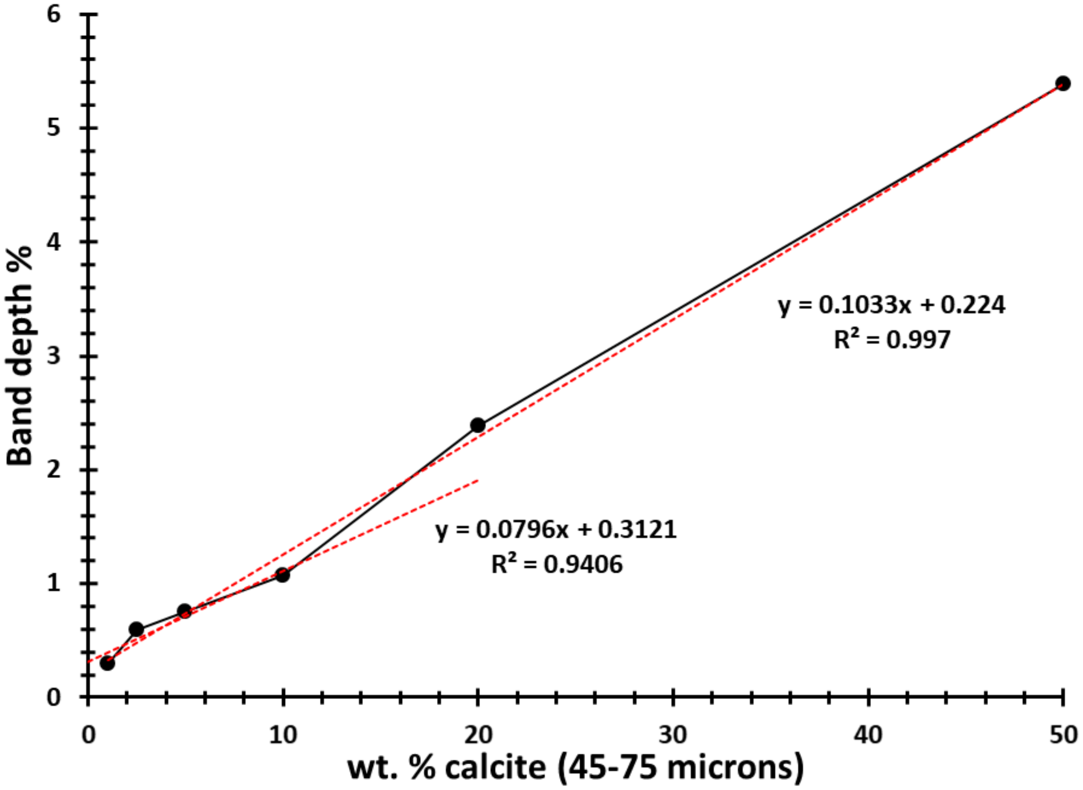

Figure 11c. Linear regression model of the 2.3 micron band for the MGS-1 with calcite mixtures.

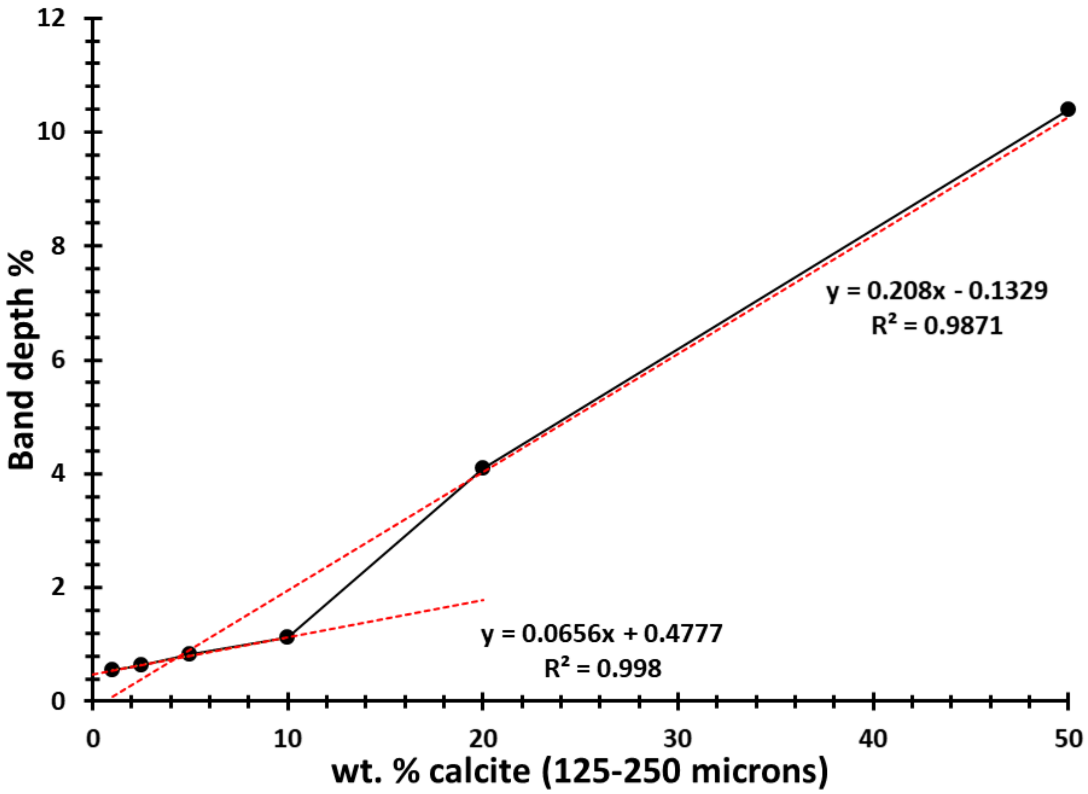

Figure 11d. Linear regression model of the 2.3 micron band for the MGS-1 with calcite mixtures.

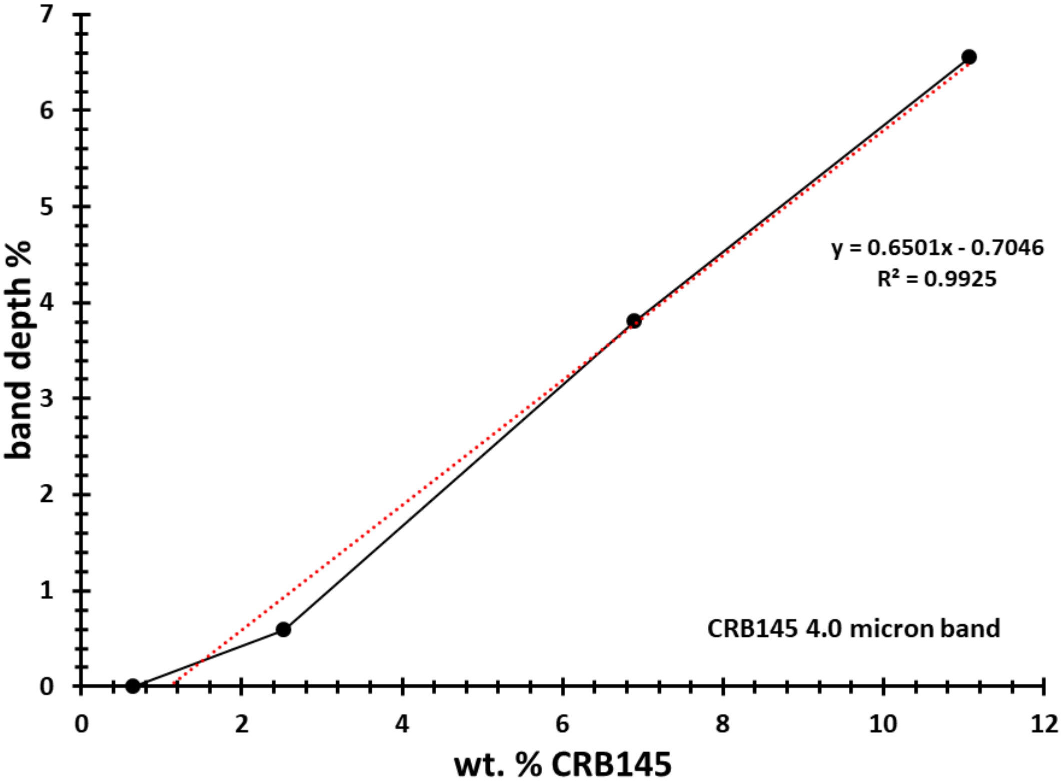

Figure 11e. Linear regression model of the 4.0 micron band for the JSC Mars-1a with siderite mixtures.

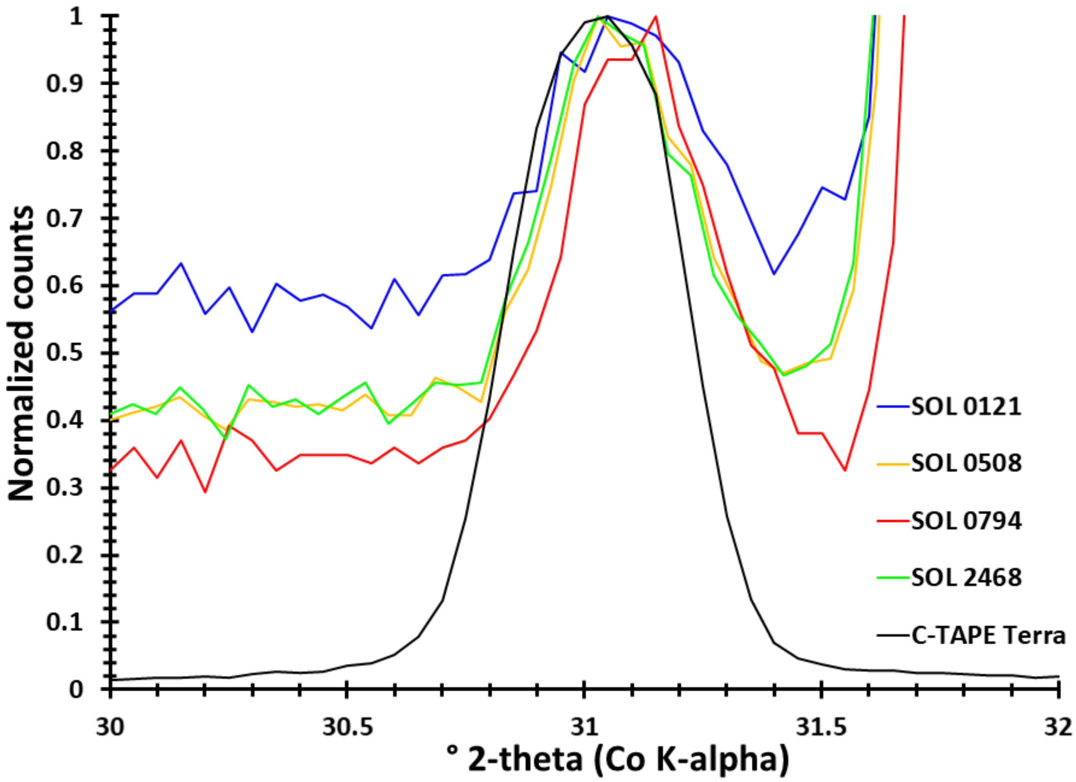

Figure 12a. A comparison of a quartz sample measured with the Terra instrument and the quartz-beryl standard on CheMin. This demonstrates the °2-theta calibration of the Terra instrument and the capability of interpreting CheMin data with that from the Terra.

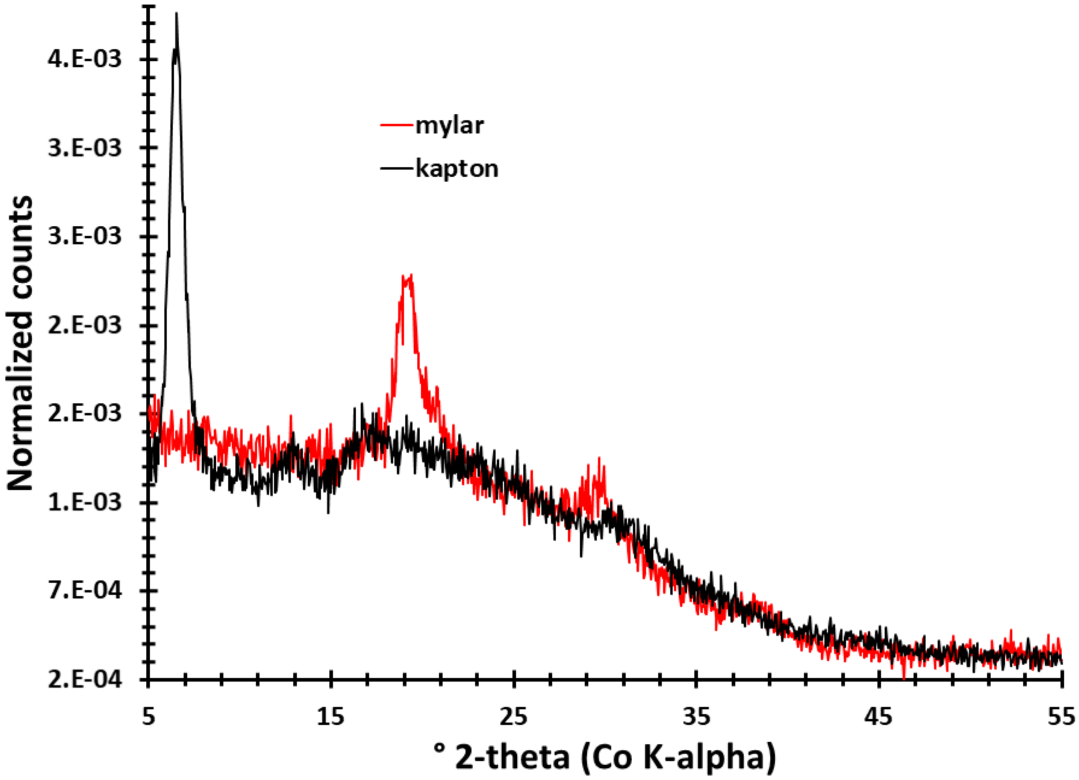

Figure 12b. A comparison of diffraction data from empty mylar and kapton windows in the Terra instrument

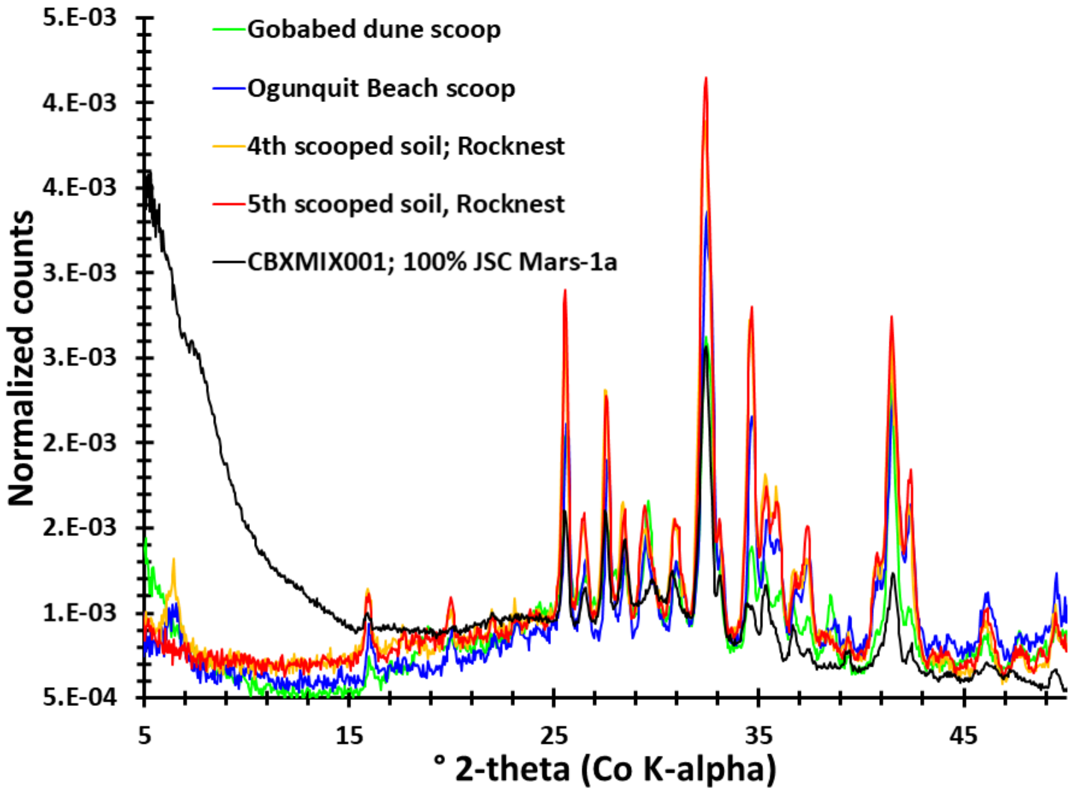

Figure 13a. A comparison of several CheMin datasets analyzed here with the JSC Mars-1a analogue collected with the Terra instrument.

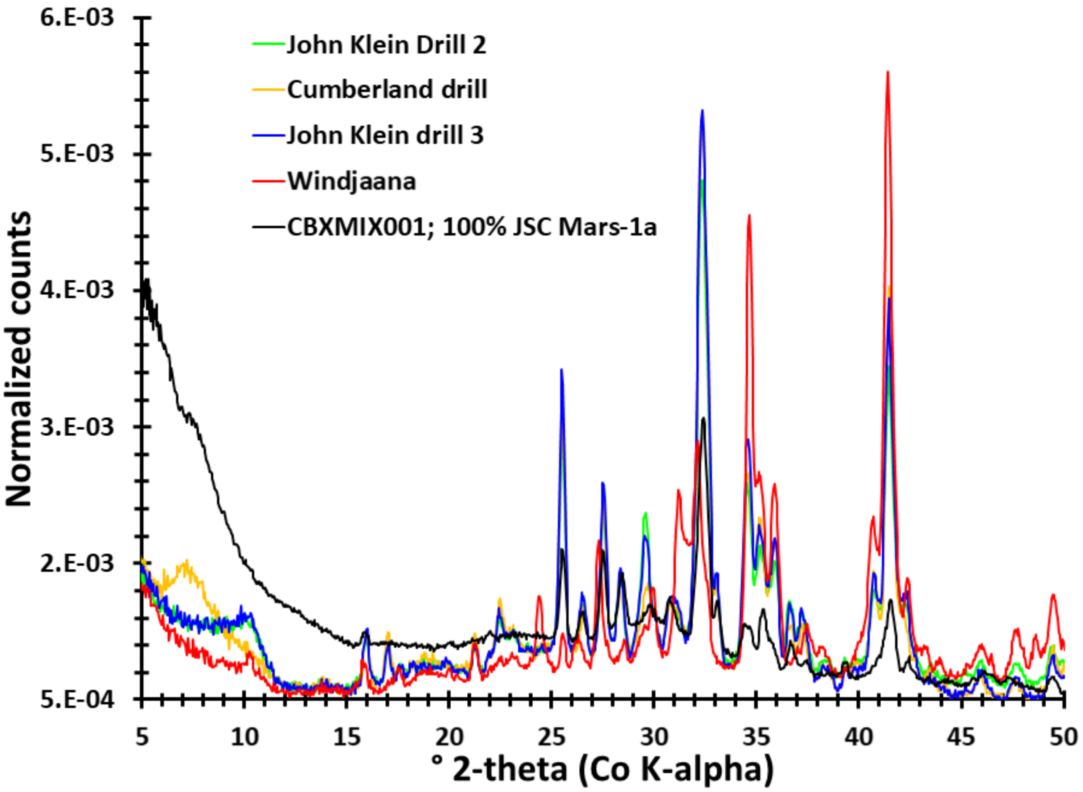

Figure 13b. A comparison of several CheMin datasets analyzed here with the JSC Mars-1a analogue collected with the Terra instrument.

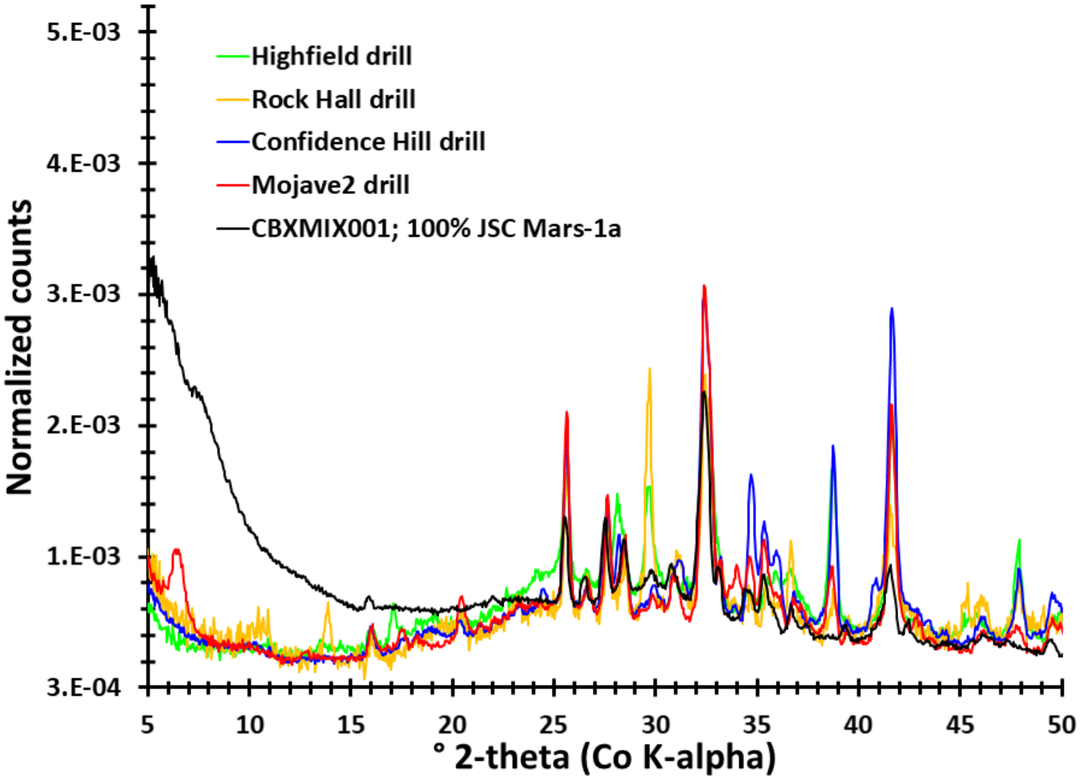

Figure 13c. A comparison of several CheMin datasets analyzed here with the JSC Mars-1a analogue collected with the Terra instrument.

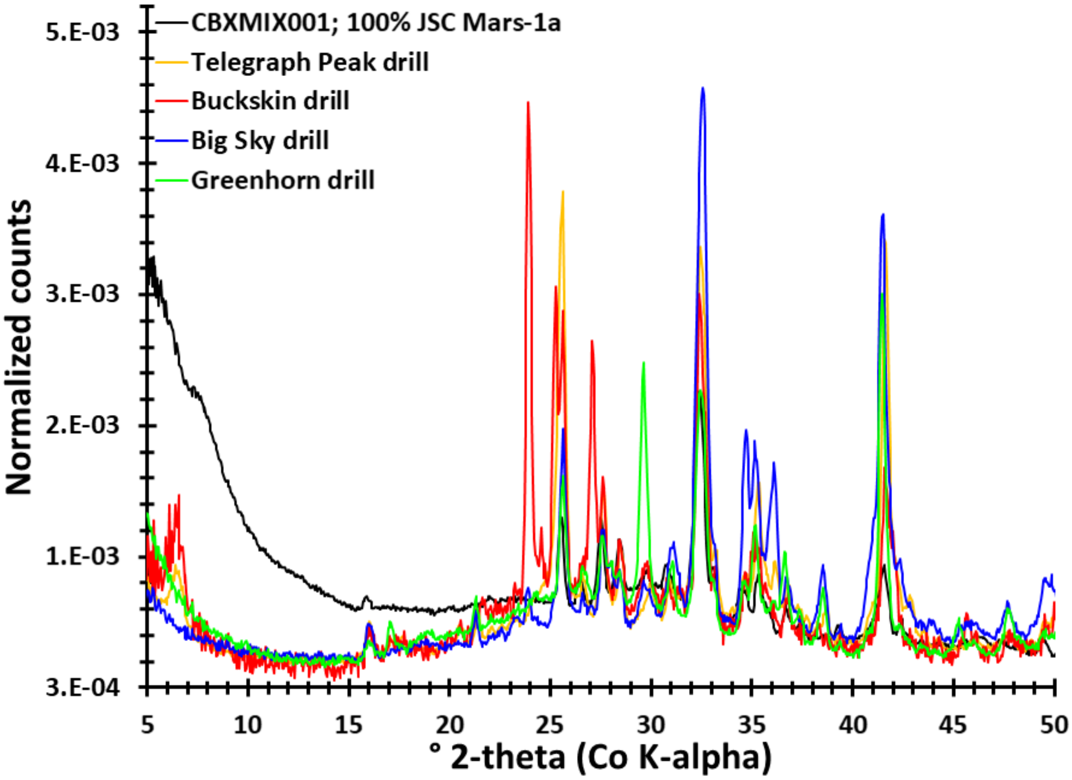

Figure 13d. A comparison of several CheMin datasets analyzed here with the JSC Mars-1a analogue collected with the Terra instrument.

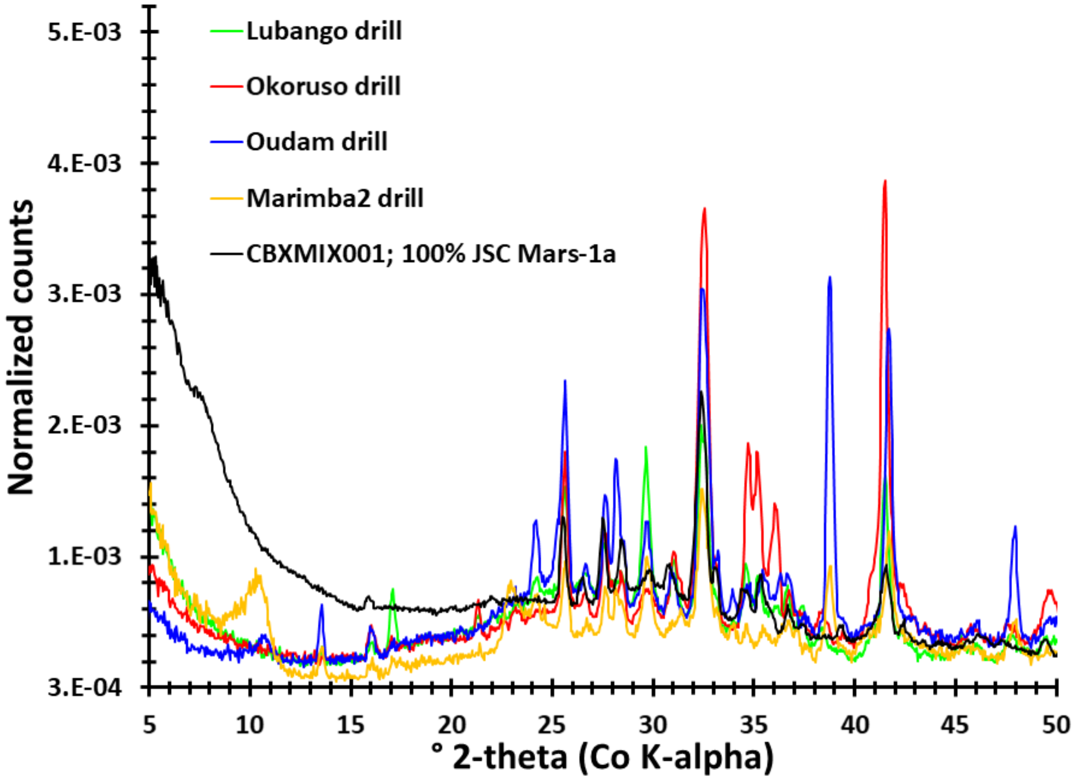

Figure 13e. A comparison of several CheMin datasets analyzed here with the JSC Mars-1a analogue collected with the Terra instrument.

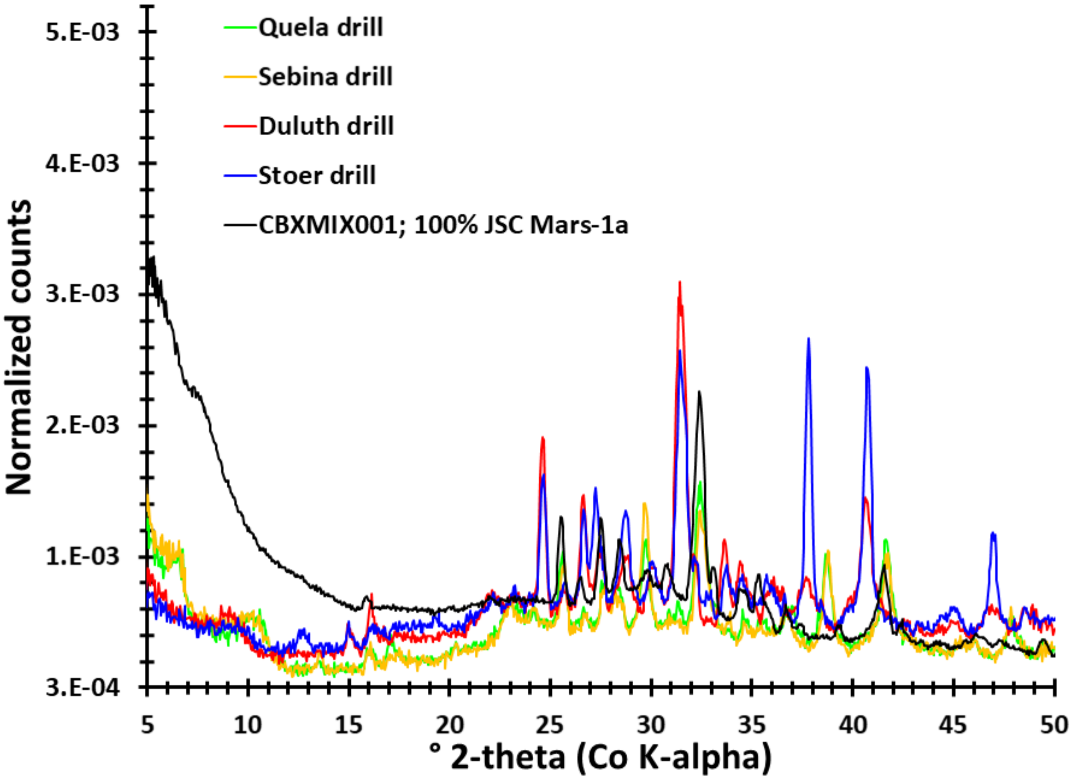

Figure 13f. A comparison of several CheMin datasets analyzed here with the JSC Mars-1a analogue collected with the Terra instrument.

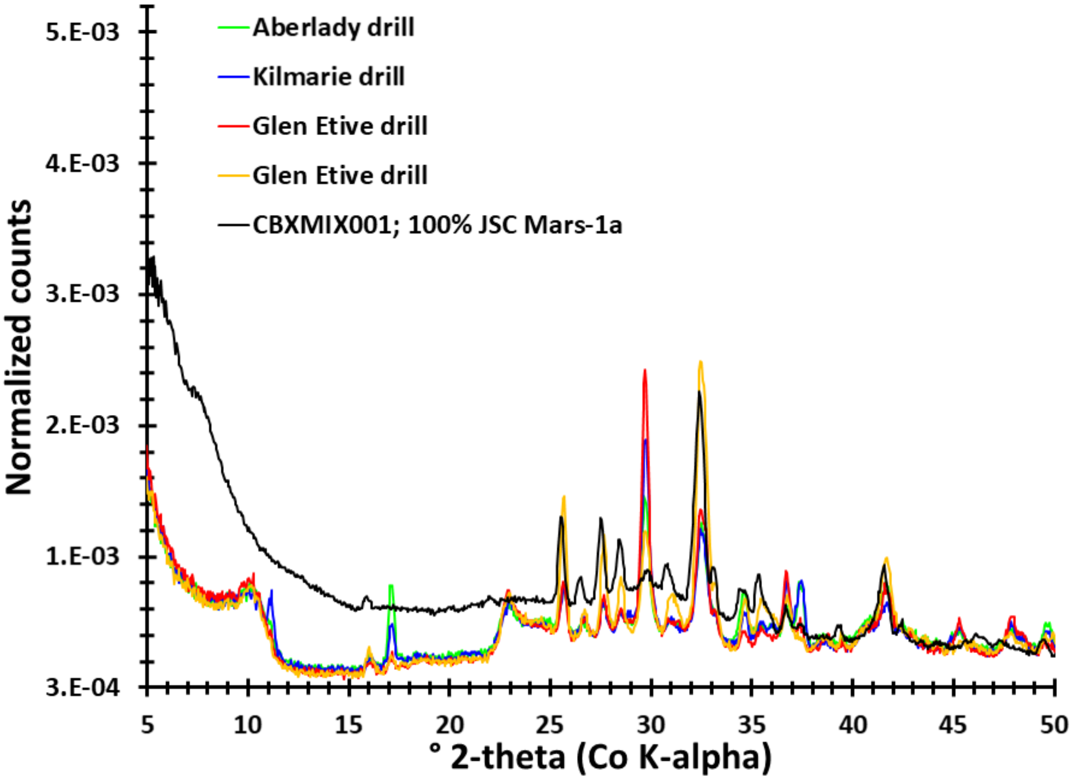

Figure 13g. A comparison of several CheMin datasets analyzed here with the JSC Mars-1a analogue collected with the Terra instrument.

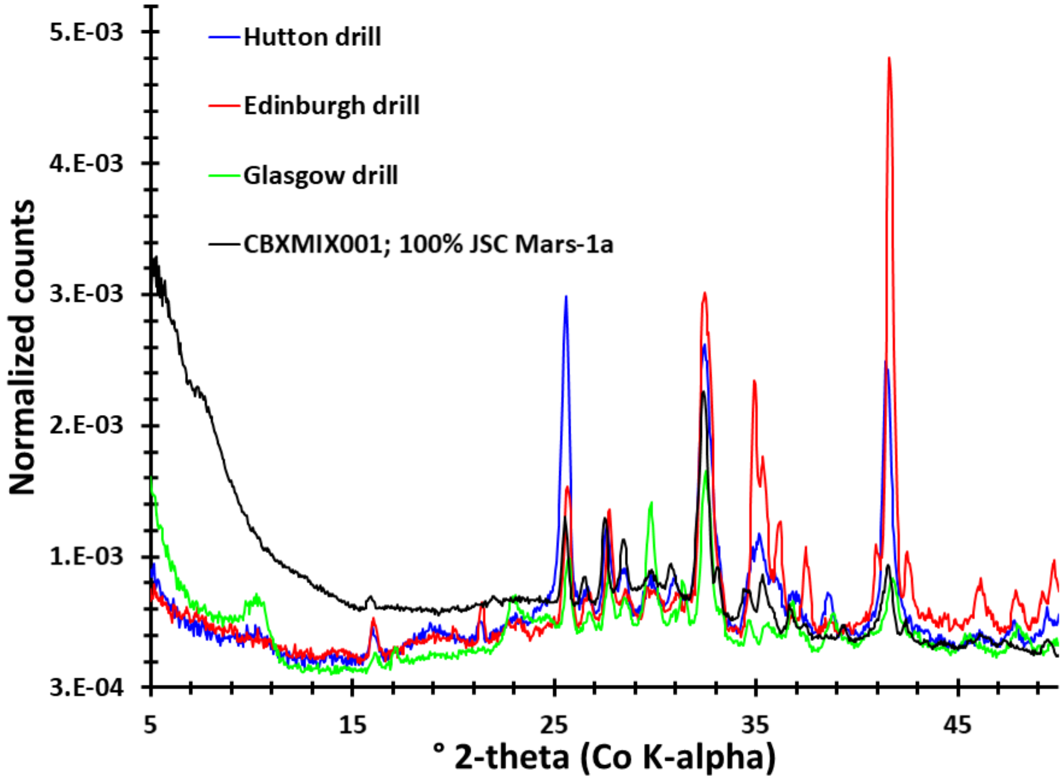

Figure 13h. A comparison of several CheMin datasets analyzed here with the JSC Mars-1a analogue collected with the Terra instrument.

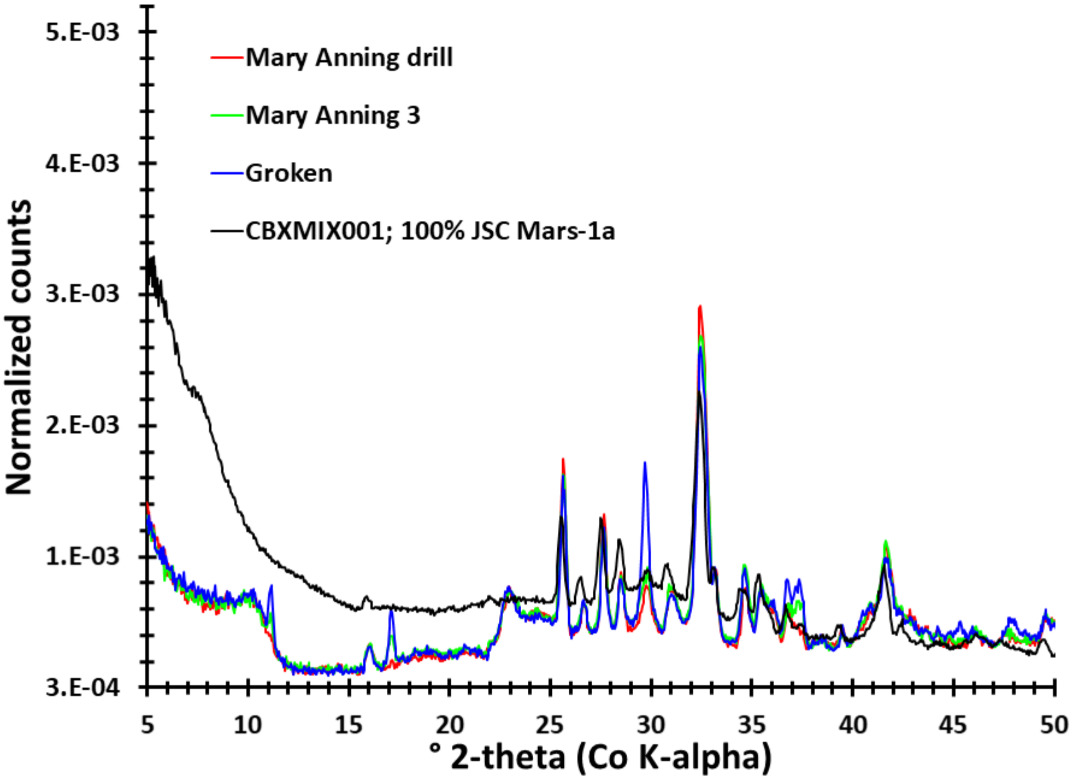

Figure 13i. A comparison of several CheMin datasets analyzed here with the JSC Mars-1a analogue collected with the Terra instrument.

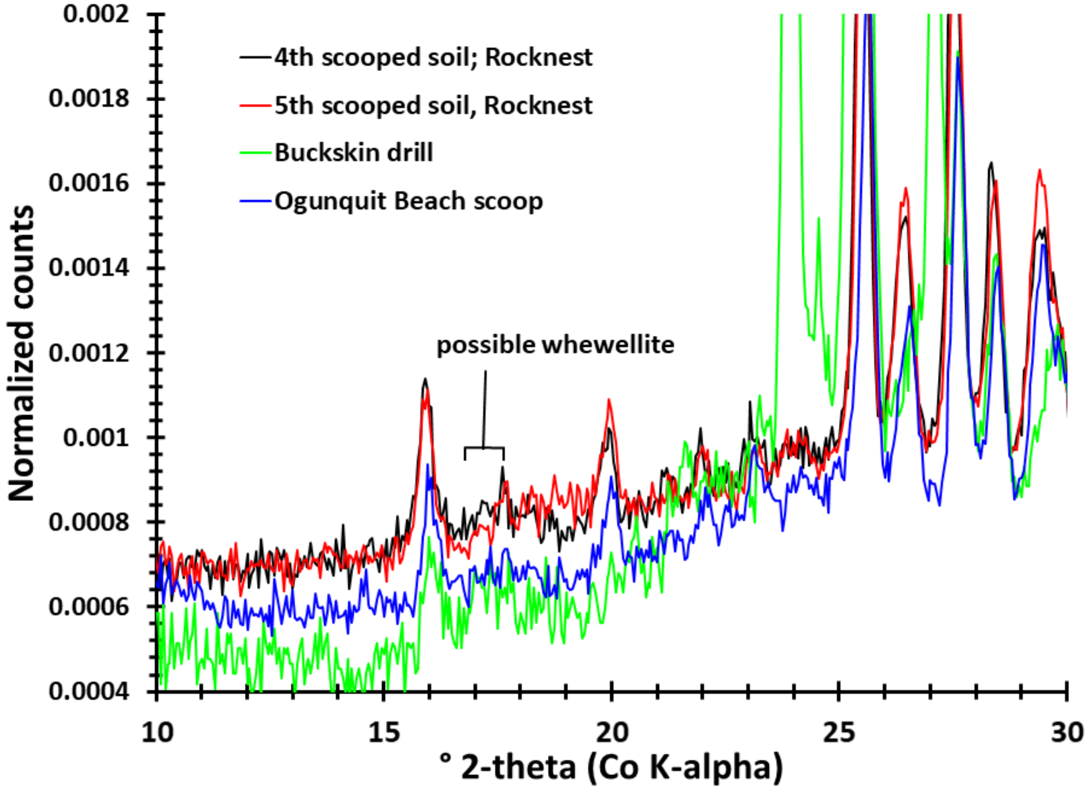

Figure 14a. The weak diffraction peak displayed in some CheMin data that could potentially have contribution from whewellite.

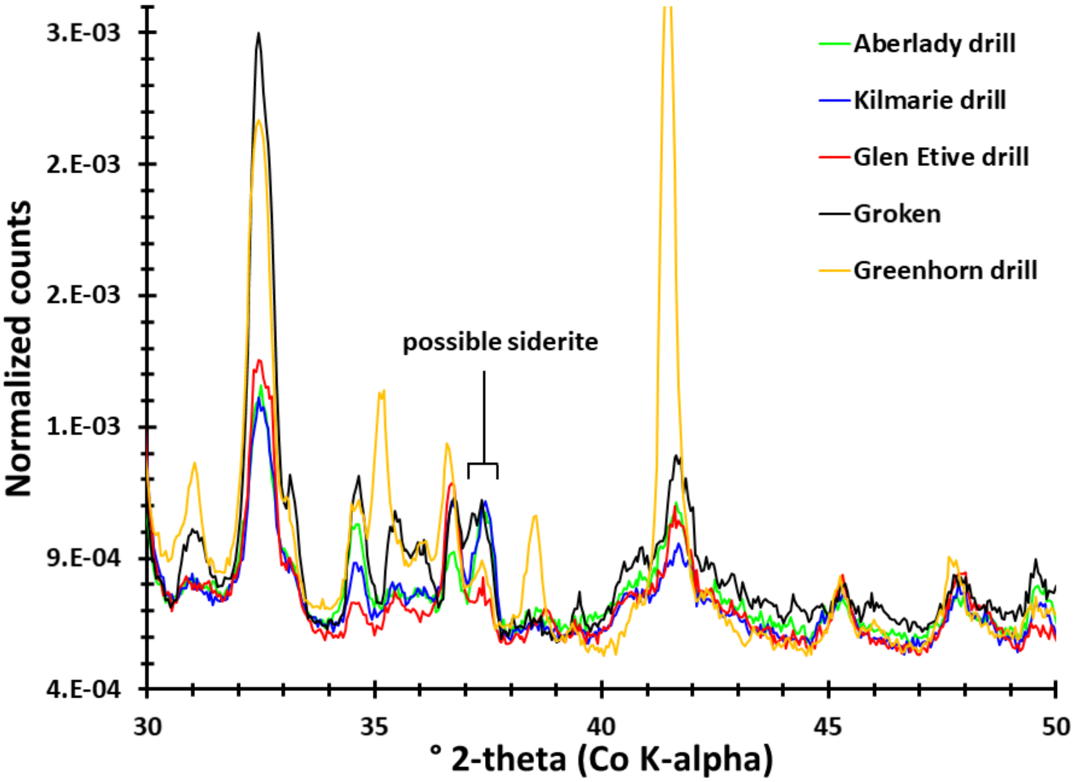

Figure 14b. The diffraction peak in some CheMin data that are likely due to a contribution from siderite.

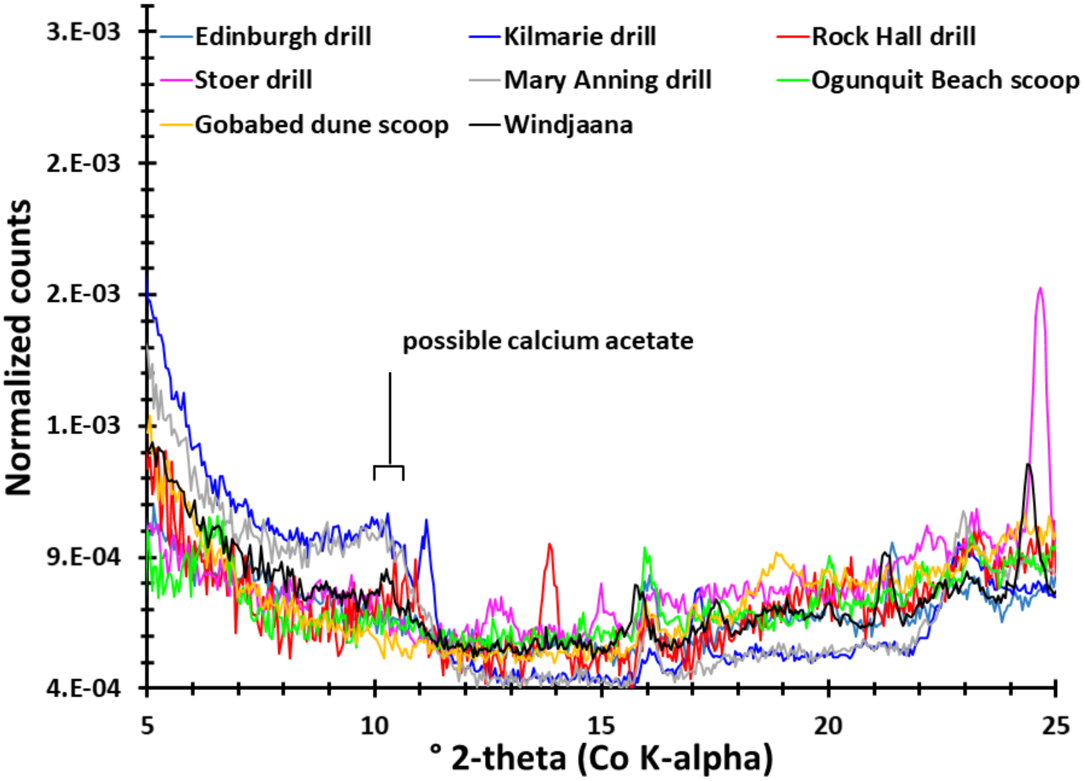

Figure 14c. The weak diffraction peak displayed in some CheMin data that could potentially have contribution from calcium acetate.

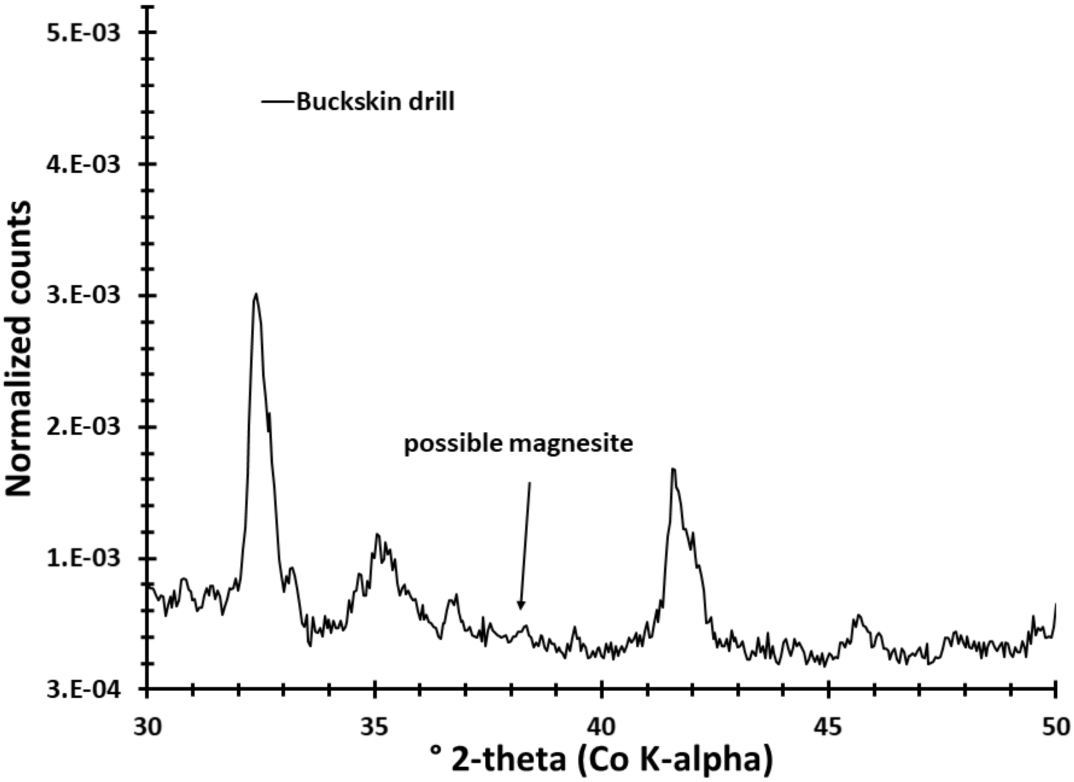

Figure 14d. The weak diffraction peak displayed in the Bucksin Drill CheMin data that could potentially be due to magnesite.

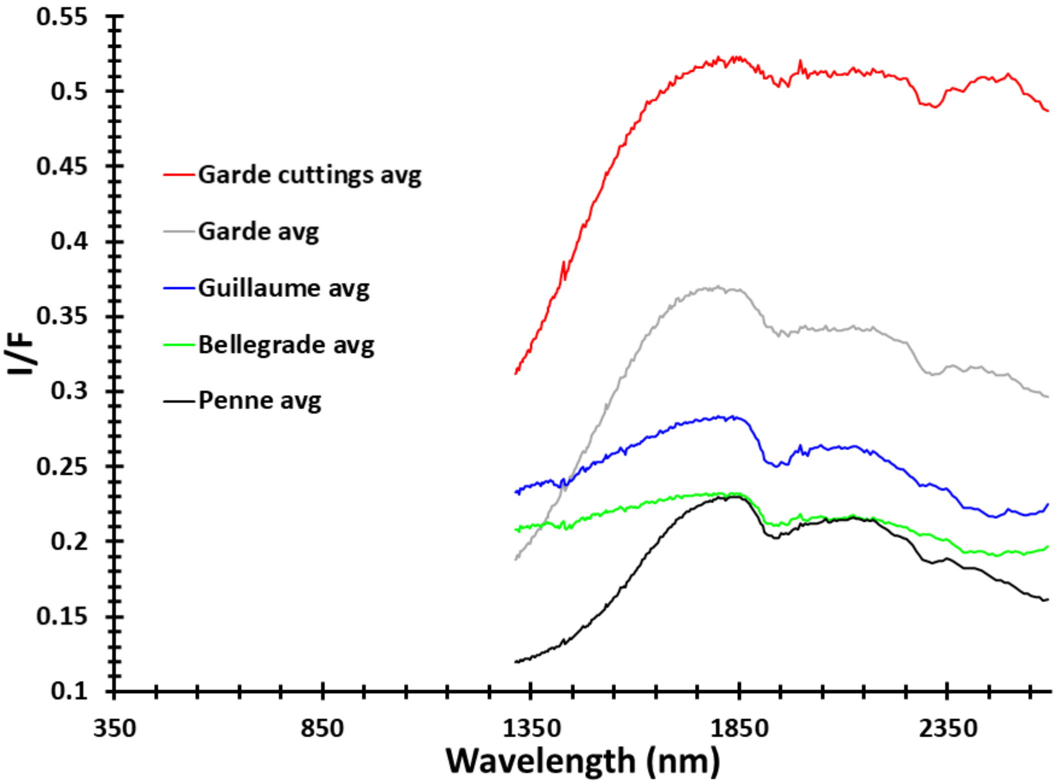

Figure 15a. Average reflectance spectra for the targets from the SuperCam instrument analyzed here.

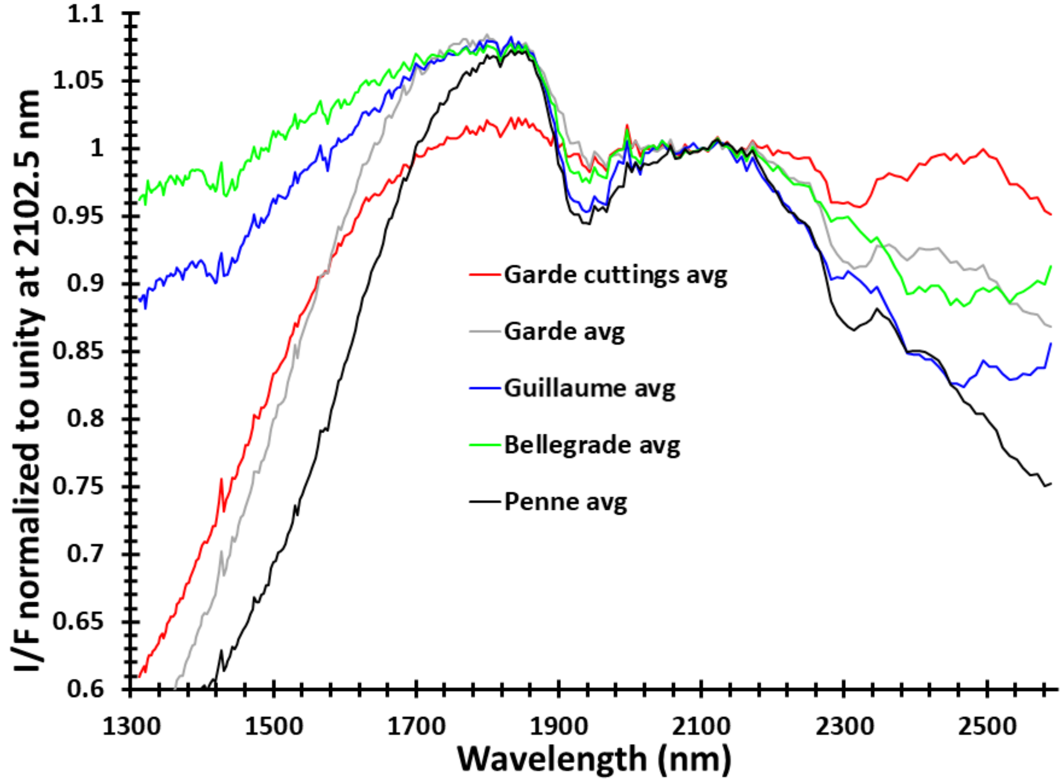

Figure 15b. Normalized reflectance for the targets from the SuperCam instrument analyzed here.

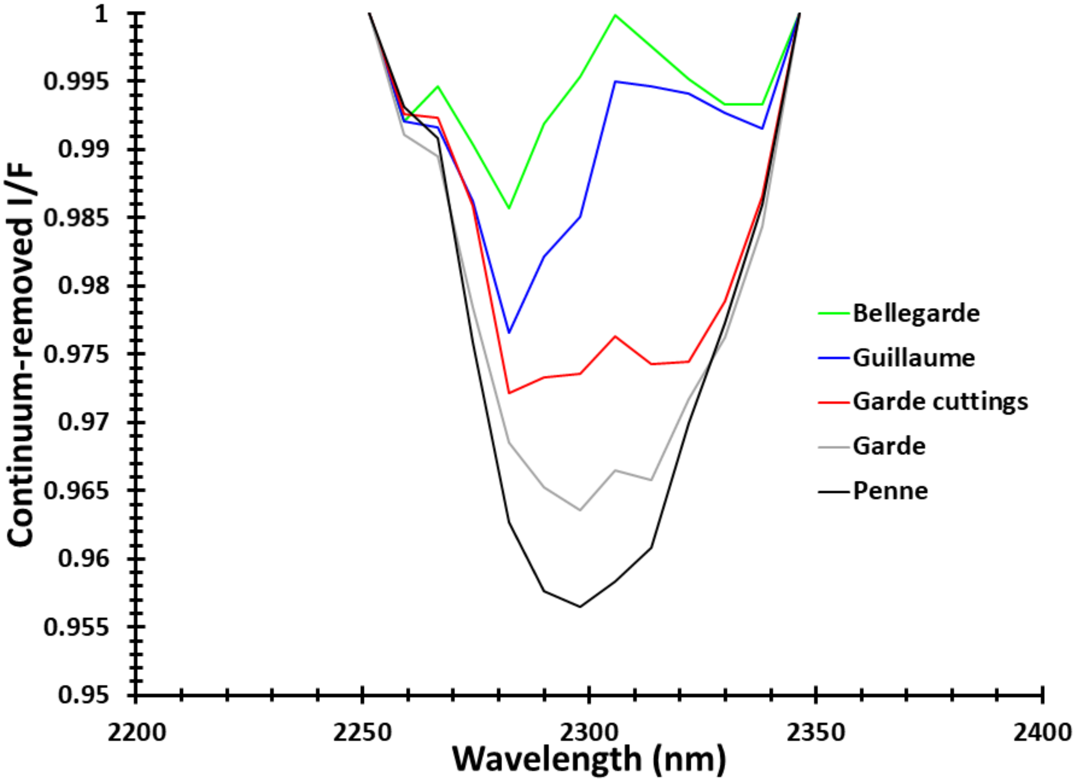

Figure 15c. Continuum-removed reflectance for the targets from the SuperCam instrument analyzed here.

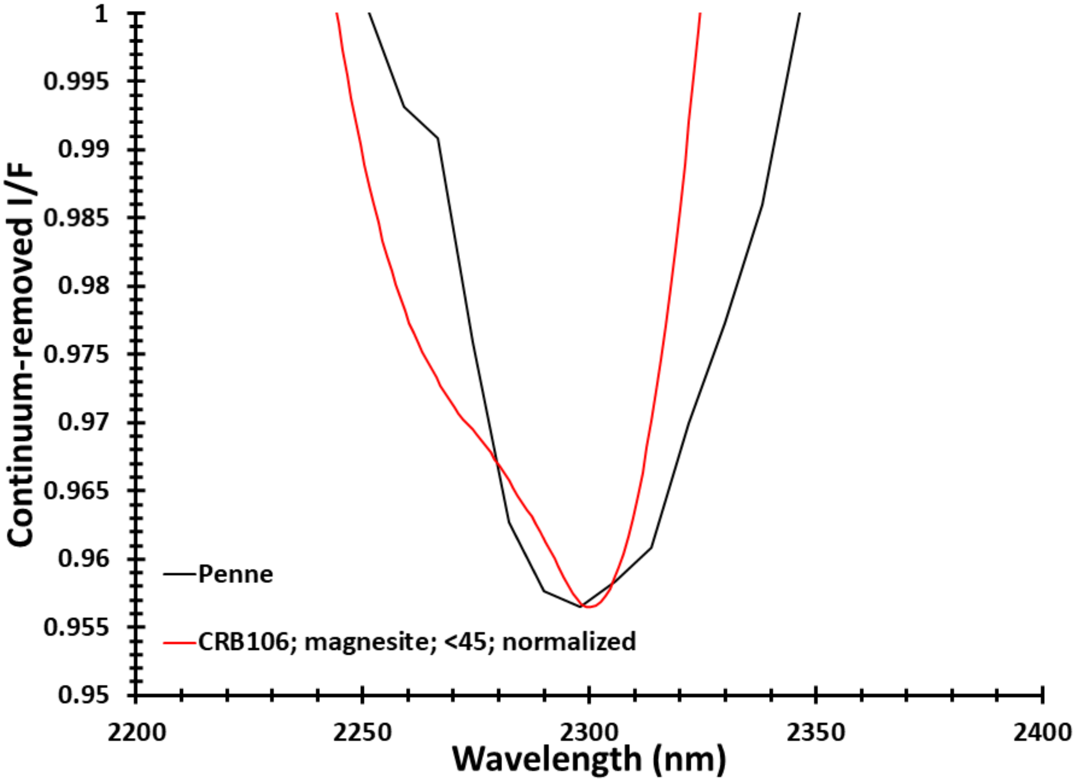

Figure 15d. Comparison of the continuum-removed reflectance for the 2300 nm band between fine grained magnesite and the Penne target measured by SuperCam.